

**Evaluation and prediction method for
solidification cracking during hot-wire laser welding
with a narrow gap joint and GMAW process using
computational simulation**

(数値解析による狭開先ホットワイヤ・レーザ溶接および GMA
溶接における凝固割れの評価並びに発生予測)

March, 2014

Rittichai Phaoniam

Department of Mechanical Science and Engineering
Graduate School of Engineering
Hiroshima University

Table of Contents

Chapter 1	Introduction.....	1
1.1	Research Background.....	1
1.2	Objective and Construction of Thesis.....	3
Chapter 2	Theoretical Background and Literature Review.....	7
2.1	Introduction.....	7
2.2	Research and Development Status of Narrow-Gap Welding.....	7
2.3	Weld Solidification Cracking and its Mechanism.....	13
2.4	Methodology for Solidification Cracking Susceptibility Testing.....	16
2.5	Prediction of Solidification Cracking.....	19
Chapter 3	Development of Hot Wire Laser Welding with a Narrow-Gap Joint.....	23
3.1	Introduction.....	23
3.2	Hot Wire Laser Welding Process with a Narrow Gap Joint.....	24
3.3	Material and Specimen Used.....	26
3.4	Experimental Procedure.....	26
3.5	Effect of Hot Wire Laser Welding Parameters on Weld Characteristics.....	31
3.5.1	Effect of Wire Current.....	31
3.5.2	Effect of the Wire Feeding Position.....	32
3.5.3	Effect of the Angle of Laser Irradiation.....	33
3.6	Mechanism of Weld Bead Formation.....	34
3.6.1	Weld Penetration Shape.....	34
3.6.2	Investigating the Effect of the Reflected Laser Irradiation.....	35
3.7	Weld properties.....	38
3.7.1	Hardness profile.....	38
3.7.2	Tensile Strength.....	38
3.8	Summary.....	39
Chapter 4	Solidification Cracking Susceptibility of Modified 9Cr1Mo Steel in Hot-Wire Laser Welding with a Narrow Gap Joint.....	41
4.1	Introduction.....	41
4.2	Material and Specimen Used.....	42
4.3	Experimental Procedure.....	42
4.3.1	Method and Equipments.....	42
4.3.2	Evaluation Method of Weld Cracking.....	45
4.4	The Investigation of the Occurrence of Solidification Cracking.....	46
4.4.1	Defects in Hot wire Laser Welding with a Narrow Gap Joint.....	46
4.4.2	Identification of Solidification Cracking.....	48
4.5	Solidification Cracking Susceptibility in Modified 9Cr1Mo Steel.....	50
4.5.1	The effect of D/W Ratio on Solidification Cracking Susceptibility.....	50

4.5.2	The Effect of a Groove Width Size.....	50
4.5.3	The Effect of a Laser Spot Shape.....	52
4.5.4	Hot Wire Welding with Laser Scanning.....	56
4.6	Mechanical Properties Evaluation for Welded Joint.....	59
4.7	Summary.....	61
Chapter 5	Evaluation of Solidification Cracking Susceptibility of Cast Steel Welds for Large Scale Parts on Construction Machinery Using U-Groove Weld Cracking Test with GMAW Process.....	62
5.1	Introduction.....	62
5.2	Material Used.....	62
5.3	U-groove Weld Cracking test.....	63
5.3.1	Method and Specimen.....	63
5.3.2	Evaluation Method of Weld Cracking.....	64
5.4	Evaluation of Solidification Cracking Susceptibility.....	65
5.4.1	Effect of the Degree of Constraint.....	65
5.4.2	Relationship between the Type of Filler Wires and Cracking ratio.....	73
5.5	Summary.....	79
Chapter 6	Achievement of High Temperature Ductility Curve in modified 9Cr1Mo Steel and Cast Steel Welds using U-type Hot Cracking Test	80
6.1	Introduction.....	80
6.2	Material and Specimen Used.....	81
6.2.1	Specimen Preparation for Modified 9Cr1Mo Weld Metal.....	81
6.2.2	Specimen Preparation for YM-70A Weld Metal.....	85
6.3	Dilution Evaluation of Welds.....	89
6.4	U-type Hot Cracking Test with In-situ Observation.....	91
6.4.1	Method and Equipments.....	91
6.4.2	Approach to Measuring Local Critical Strains.....	97
6.5	Measurement of Temperature History During Solidification.....	98
6.6	Achievement of High Temperature Ductility Curve.....	99
6.6.1	Solidification cracking in U-type Hot Cracking Test.....	99
6.6.2	Temperature History at the Trailing Edge of the Molten Pool.....	101
6.6.3	High Temperature Ductility Curves.....	103
6.7	Summary.....	107
Chapter 7	Computational Welding Simulation Approach for High Temperature Strain Analysis	109
7.1	Introduction.....	109
7.2	Computational simulation for in Hot-wire Laser Welding with a Narrow Groove Joint.....	110
7.2.1	Experimental Welding Procedure.....	110
7.2.2	Finite Element 3-D Modeling.....	111
7.2.3	Material Properties.....	112
7.2.4	Strategic FEM Approach for Welding Heat Source in Hot-wire Laser Welding.....	113

7.2.5	Experimental Validation of Computation Simulation in Hot-wire Laser Welding with a Narrow Groove Joint.....	118
7.2.5.1	Thermal History Measurement.....	118
7.2.5.2	Deformation and Elastic Strain History Measurement.....	119
7.2.5.3	FEM Model and Boundary Conditions.....	123
7.2.6	Simulation Result of Hot-wire Laser Welding with a Narrow Groove Joint.....	124
7.2.6.1	Thermal Analysis.....	124
7.2.6.2	Thermo-Mechanical Analysis.....	126
7.3	Computational GMAW Simulation of U-Groove Weld Cracking Test.....	129
7.3.1	Computational Simulation Procedure.....	129
7.3.1.1	Material Used and Welding Conditions.....	129
7.3.1.2	3D Finite Element Model.....	130
7.3.1.3	GMAW Heat Source Model.....	131
7.3.1.4	Boundary conditions.....	132
7.3.1.5	Material properties.....	132
7.3.2	Experiment Validation of GMAW Simulation of U-Groove Weld Cracking Test.....	134
7.3.3	Results of Validation in GMAW Simulation of U-Groove Weld Cracking Test.....	135
7.4	Summary.....	137
Chapter 8	Prediction of Solidification Cracking by Integral Approach to Ductility Curves and FEM Analysis.....	139
8.1	Introduction	139
8.2	Prediction of Solidification Cracking in Hot-wire Laser Welding with a Narrow Groove Joint.....	139
8.2.1	Achievement of the Appropriate Temperature for Initial Strain.....	139
8.2.2	Determination of High Temperature Strain and Maximum Strain Rate.....	141
8.2.3	Prediction of Solidification Cracking at Different D/W Ratios.....	145
8.3	Prediction of Solidification Cracking in U-Groove Weld Cracking Test.....	151
8.3.1	Evaluation of High Temperature Strain Dependent on Root Gap Width.....	151
8.3.2	Prediction of Solidification Cracking in U-Groove Weld Cracking Test.....	155
8.4	Summary.....	157
Chapter 9	Summary and Future work.....	159
Acknowledgements	162
Reference	163
Published or Submitted Papers in Regards to this Thesis	170
Presentations	171

Chapter 1

Introduction

1.1 Research Background

For metal joining, it is generally accepted that welding processes have been widely used for fabrication of crucial components in various industries such as shipbuilding, power generation plants, petrochemical refining systems and chemical plants, as well as nuclear and steam power plants and so forth. Nowadays, the conventional welding processes are shielded metal arc welding (SMAW), gas tungsten arc welding (GTAW), gas metal arc welding (GMAW), and flux cored arc welding (FCAW), submerged arc welding (SAW) etc. Each process has unique features, for instance SMAW uses simple equipment at low cost, GTAW is excellent to produce weld quality but both are very slow together with an uneconomic productivity. Semi-automatic methods like GMAW, FCAW, as well as SAW, have been developed for increasing productivity. However, when those welding processes are employed for heavy thick plate, a low production rate, too much weld deposition, and a large distortion are still undesired problems [1-7]. Those problems are relative to the results of general joint preparation.

Recently, many studies have attempted to apply narrow-gap welding for heavy thick plate. Employing a narrow gap joint, this method is a great advantage for reducing undesired shrinkage, residual stress, and improving productivity because of its extreme small groove width compared to general joint preparation [8-12]. Figure 1.1 illustrates the comparison of a welded joint between a general V-groove joint and a narrow groove joint. At this time, the conventional welding processes with a narrow gap joint include SAW, GMAW, GTAW, and laser arc hybrid. Nevertheless, these methods, and particularly SAW, retain the effect of the evolution of metallurgical structures in the vicinity of the weld metal owing to high heat input energy.

Subsequently, a technique requiring lower heat input energy has been developed using a so-called hot wire system. This system is designed to independently control the melting feed wire and the base metal. Nowadays, hot wire-GTAW welding is employed with a narrow gap joint in industries. However, this method is still limited in terms of the efficiency of the process and the quality of the weldment [13-16]. As an alternative to narrow-gap welding, laser and laser-arc hybrid welding are used [17-18]. Although laser processes show the advantage of high welding speeds and no weld spatter, in the case of laser-arc hybrid welding, it has a tendency to induce defects through the arcing phenomenon.

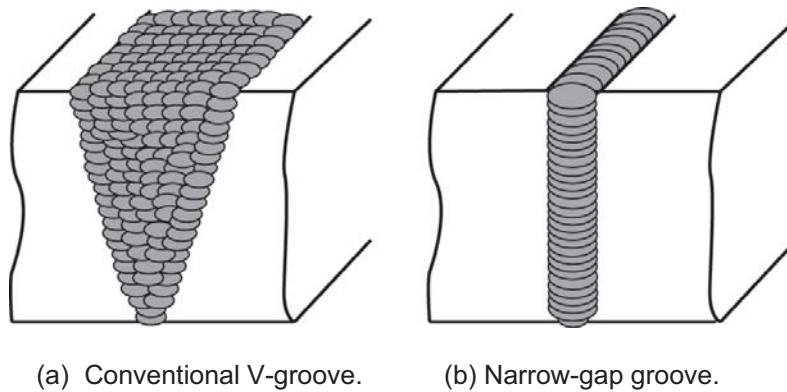


Fig. 1.1 Comparison of a conventional joint and a narrow gap joint.

Narrow-gap welding technology has been extensively used due to it being an effective method to deal with the weld joint of a heavy, thick component. At present, a power generation plant has been required to improve thermal efficiency. An alternative approach to increased efficiency is maximizing temperatures and pressures in a thermal cycle. In recent years, ultra-supercritical (UCS) power plants have been built to serve such requirements of operational pressure 25 MPa with a stream temperature of 600 °C [19, 20]. A heavy thicker wall for critical components such as tubes and pipes is vital to such application. Thus, narrow-gap welding technology is substantially used to deal with such a heavy, thick component. Aspects of heat resistant steel in a power generation plant, modified 9Cr1Mo steel (9Cr-1Mo-V-Nb) commonly known as grade 91 according to ASTM standard is a potential candidate for the application in elevated temperatures. With the addition of vanadium and niobium it has better creep rupture strength than other ferritic CrMo steels. This material is widely used for critical components such as pipes and tubes in a power generation plant.

Generally, it is well known that solidification cracking on welded components is an undesirable discontinuity. By reason of very narrow groove width, solidification cracking is easily induced, especially in a pear-shaped weld bead as shown in Fig. 1.2 [21]. However, in modified 9Cr1Mo steel, there are few studies from the viewpoint of weldability, particularly in solidification cracking susceptibility [22].

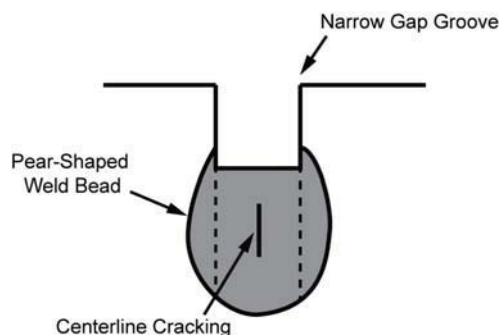


Fig. 1.2 Illustration of pear-shaped bead cracking.

A remarkable application in narrow-gap welding is in heavy construction machinery fabrication. Large scale cast steel is mainly used since it is beneficial to a complex shape and has a high strength property. Such components are effectively fabricated by narrow-gap welding for higher productivity. This method provides low heat input, less deposited metal volume and less deformation. However, it is possible to induce weld cracking particularly in heavy thick plate with a narrow gap joint for the reason that the cast steel contains a large amount of carbon. In practical work using narrow-gap GMAW, cracks usually occur at the first root pass in the weld metal. Presently, the foremost cause of cracking has not been investigated clearly [23-28].

As mentioned earlier, conventional welding processes with a narrow gap joint have not yet met up-to-date requirements of high quality and high productivity. Consequently, an innovative process for narrow-gap welding is required to overcome such circumstances, namely it should combine the benefits of fast welding speed, high weld deposition rate, low deformation as well as good quality weld. Meanwhile, the weldability of the materials such as modified 9Cr1Mo and cast steel is another important issue. There are few studies and a lack of clarity in this area. It is necessary to investigate comprehensively in order to evaluate and predict the occurrence of solidification cracking in narrow-gap welding.

1.2 Objective and Construction of Thesis

An innovative process for narrow-gap welding requires overcoming requirements between quality and productivity. According to narrow-gap welding, few researches have addressed the problem of solidification cracking in the application of materials such as modified 9Cr1Mo and large scale cast steel. The main causes to solidification cracking and its susceptibility between a mechanical factor and a material factor remain unclear.

Therefore, the objective of this research intends to develop an innovative hybrid process of hot wire laser welding for a narrow gap joint. This developing process has focused on such requirements as high weld deposition rate, low deformation as well as low dilution. Solidification cracking during narrow-gap welding was studied. In order to prevent the problems of solidification cracking, an important approach studied by means of experiments and computational welding simulation is addressed for the development of a methodology of systemic evaluation and prediction of the solidification cracking phenomenon and its mechanism.

A modified 9Cr1Mo steel, solidification cracking susceptibility owing to hot wire laser welding was investigated. Additionally, solidification cracking using GMAW for large scale-cast steel in heavy machinery was also studied. A modified 9Cr1Mo steel, solidification cracking susceptibility owing to hot wire laser welding was investigated. Additionally, solidification cracking using GMAW for large scale-cast steel in heavy machinery was also studied. According to solidification cracking theory, solidification cracking occurs in conditions that the weld strain developed exceeds the ductility strength of the weld metal during solidification

temperature range. In order to make clear the material factor, a U-type hot cracking test with in-situ observation is employed to evaluate quantitatively material resistance to cracking at high temperature, the critical local strain to crack initiation at various temperatures during solidification was accurately measured. A high temperature ductility curve was achieved. In mechanical factors, a three dimensional-finite element method (3D-FEM) is simulated to reasonably estimate weld strain during welding. By an integrally systematic approach between a high temperature ductility curve and a calculated weld strain, the occurrence of solidification cracking in practical use was able to be understood comprehensively in both material and mechanical factors. Figure 1.3 shows the flow chart of the construction of the thesis.

Chapter 1 discusses the background of the research as well as the objective and construction of the thesis.

Chapter 2 reviews the theoretical background and the present researches on solidification cracking during narrow-gap welding and related welding processes. Solidification cracking susceptibility tests and computational welding simulation is discussed. The mechanism of solidification cracking in welds is detailed to clearly understand the cracking phenomena and the systematic approach of prediction.

In Chapter 3, the development of hot wire laser welding for a narrow gap joint is introduced. The potential of this method is studied through ASTM A 304 stainless steel welded by tentative nickel-based filler wire. Welding pool phenomena and weld bead formation are investigated by in-situ observation using a high-speed camera. Welding parameters such as wire current, wire feeding position, and wire feeding angle are investigated to determine appropriate conditions. The sufficiency of the bonding strength at the fusion boundary is demonstrated in a tensile test and also a metallurgical examination is performed to confirm the fracture surface with no defects.

In Chapter 4, hot wire laser welding with a narrow gap joint is applied to modified 9Cr1Mo steel. Solidification cracking susceptibility is addressed. In order to understand thoroughly the causes associated with the occurrence of solidification cracking in modified 9Cr1Mo steel, the important factors are experimentally investigated, namely the effect of the depth-to-width (D/W) ratio of a weld shape, groove width, laser spot shape, and welding with a laser scanning method.

Chapter 5 addresses the occurrence of solidification cracking in large-scale cast steel parts with a heavy thick material for construction machineries using narrow-gap GMAW. Particularly the first weld pass of a narrow gap joint is investigated through reproducing cracking behavior by a U-groove weld cracking test. The important factors to solidification cracking susceptibility are studied such as the degree of constraint, the root gap width, and the use of the different filler wires.

In Chapter 6, in order to evaluate the material factor affects on solidification cracking, both modified 9Cr1Mo weld metal and cast steel weld metal are experimented on to obtain high temperature ductility curves by means of a U-type hot cracking test with an in-situ observation method and measurement of temperature history.

Chapter 7 focuses on the developing approach of high temperature strain analysis in weld metal during solidification. Computational welding simulation by means of 3D-FEM with a special subroutine program is employed in order to achieve the thermal distribution and strain calculation. The special heat source model consistent with hot wire laser welding phenomenon is developed and validated based on experimental measurements. All simulation cases such as hot wire laser welding with a narrow gap joint and U-groove weld cracking test using GMAW were validated based on experimental measurements in terms of a cross-sectional weld, temperature history, deformation, and elastic strain.

In Chapter 8, an integrally systematic approach to predicting solidification cracking is performed by comparing a high temperature ductility curve and a calculated strain rate. The mechanical factor to the susceptibility of solidification cracking is investigated. Then, it is verified with the actual experiments. According to hot wire laser welding with a narrow gap joint, high temperature weld strain is computationally calculated in order to make clear the effect of D/W ratios on the susceptibility of solidification cracking. While, FEM analysis of GMAW in U-groove weld cracking test is emphasized to evaluate high temperature strain under the effect of the degree of constraint, together with the root gap width. All cases of prediction are studied to make clearly the effect in terms of both material and mechanical factors on solidification cracking.

Finally, the conclusions of this thesis are summarized in Chapter 9.

Chapter 1

Introduction

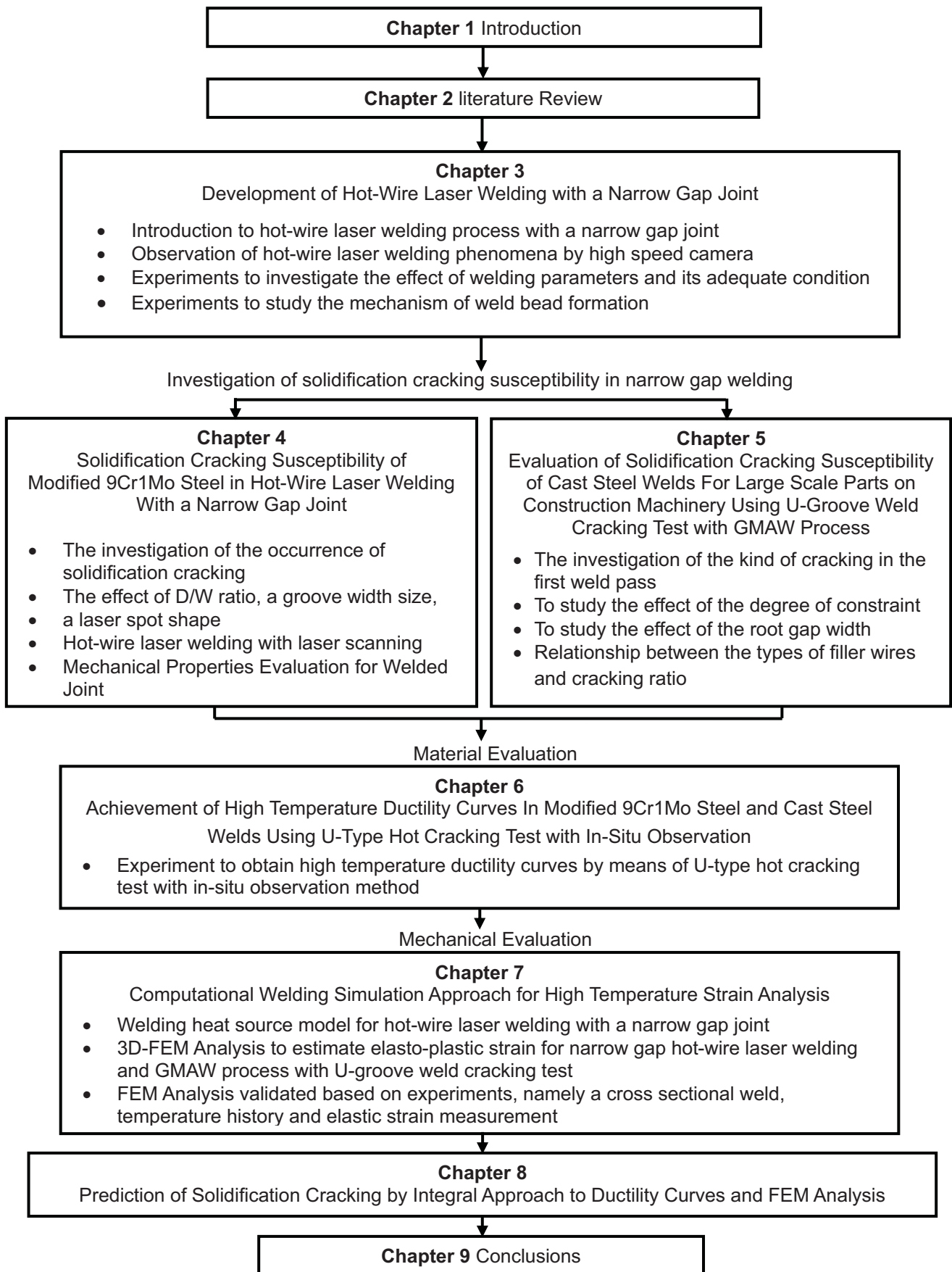


Fig. 1.3 Construction of the thesis.

Chapter 2

Theoretical background and literature review

2.1 Introduction

This chapter discusses the theoretical background and the present researches on solidification cracking during narrow-gap welding and related welding processes. The solidification cracking susceptibility test and computational welding simulation are explained. The mechanism of solidification cracking in welds is detailed to clearly understand cracking phenomena and the systematic approach of prediction.

2.2 Research and Development Status of Narrow-gap Welding

Narrow-gap welding technology has been developed in order to join heavy, thick sections in large structures. The advantages of this technique are able to serve industrial requirements in both productivity and weld quality such as increased productivity, reduced residual stress, and reduced distortion [1, 2, 29-30]. Such advantages are directly related to a small groove joint preparation, which is a parallel sidewall or slightly U-shaped. A typical groove joint in narrow-gap welding is shown in Fig. 2.1. A, traditional welding procedure normally uses a single or double V-groove joint preparation with a groove angle of 30° or larger [1, 2]. A narrow joint preparation for a thick plate leads to a smaller amount of weld metal and less time than traditional welding procedures.

Narrow-gap welding (NGW) was firstly recognized in the USSR by Dudko et al. in 1957 [29]. Meister and Martin [30] additionally developed the method in the United States in 1966. Currently, it is widely used in international welding industries. The development of this process is intended to increase weld deposition efficiency by reducing the volume of the weld metal in a thick plate-welded joint. The welding processes typically used in a narrow-gap joint are SAW, GMAW, and GTAW. Electroslag and electrogas welding are used in some applications [8-12, 31-33]. Furthermore, laser and laser arc hybrid welding has been studied for practical use [17, 18, and 34]. In addition to welding processes with a narrow groove, various approaches to fill the welding wire have been developed in order to achieve a sound weld such as a filler wire feeding technique, arcing manipulation, and number of electrodes etc. In 1984, Nomura and Sugitani [35] proposed the classification of narrow-gap welding in aspects of the welding process, and wire feeding techniques as shown in Fig. 2.2. It was summarized by V.P.Malin [36] in 1987 as presented in Fig. 2.3.

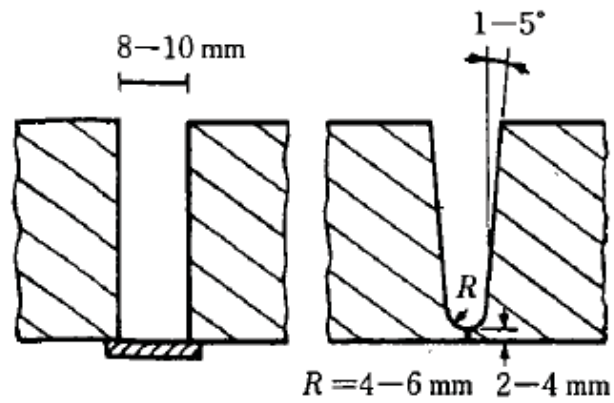


Fig. 2.1 Typical narrow-gap joint [31].

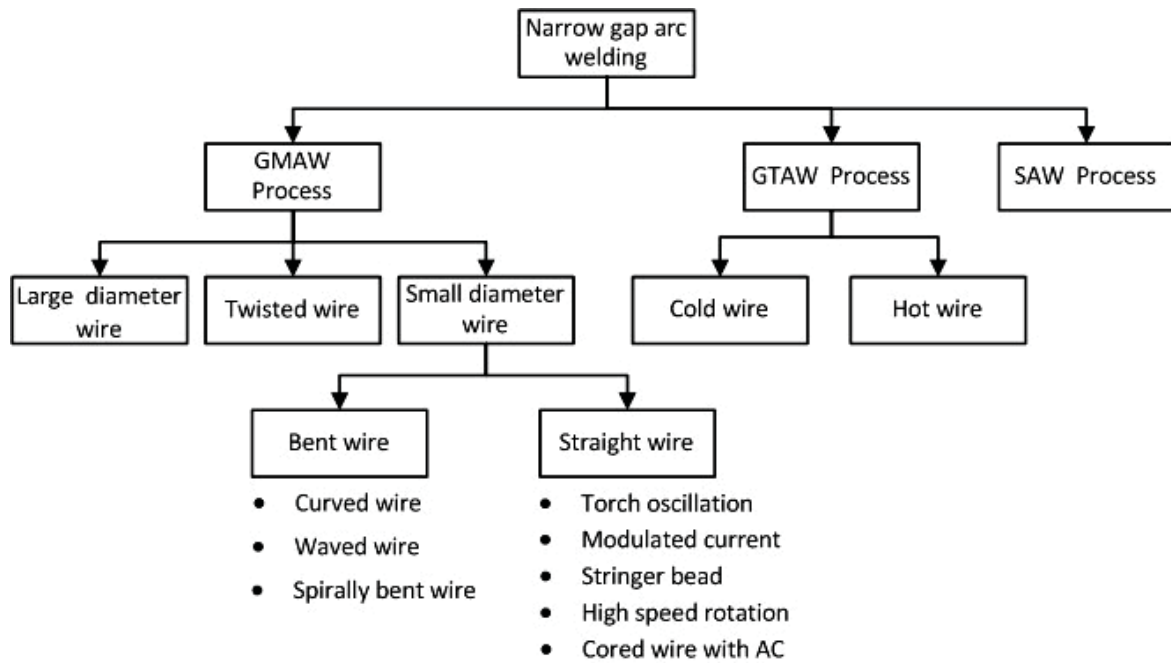


Fig. 2.2 Classification of narrow-gap welding by Nomura and Sugitani [35].

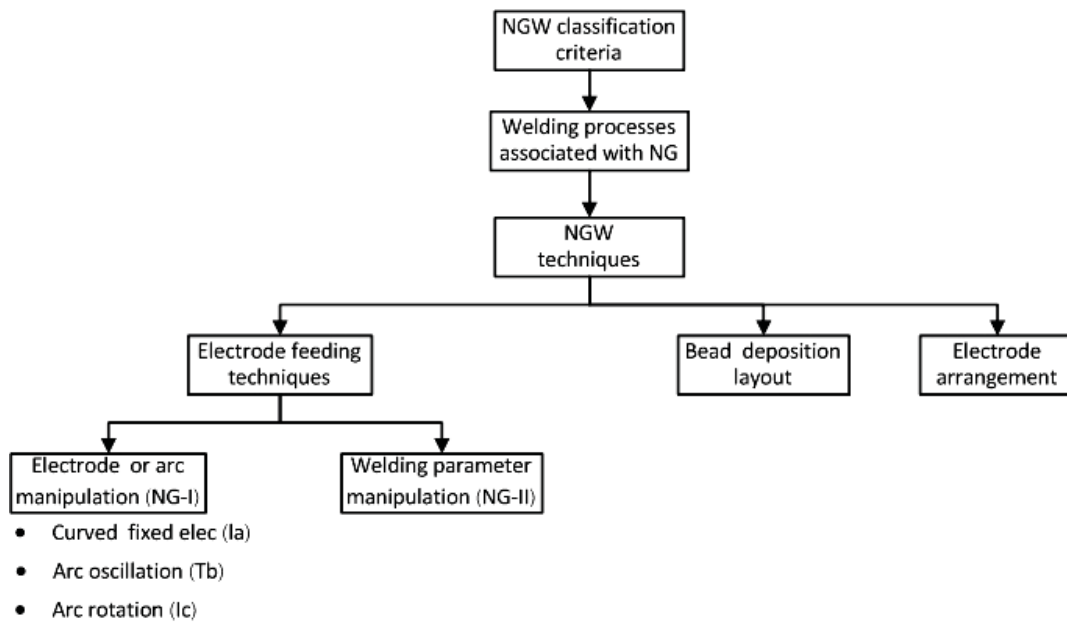
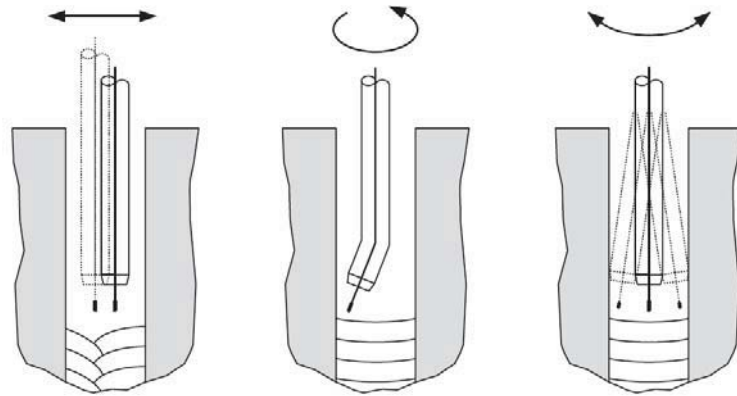


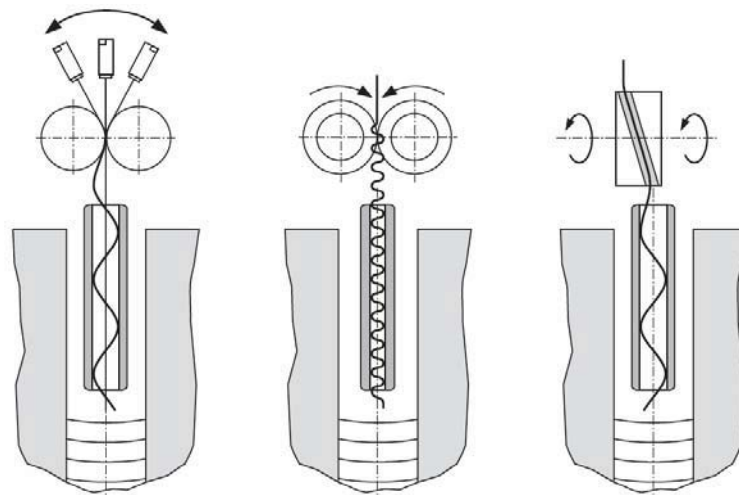
Fig. 2.3 Classification of narrow-gap welding by V.Y.Malin [36].

Some applications, (Electroslag and electrogas welding) are used with a narrow gap joint in order to join a thick plate with a long vertical joint especially in railway welding [37]. This process is able to achieve high quality welds by only single pass welding, which has inclusions and defects. An accuracy of edge preparations is not required. However, such a process contributes to too high dilution in the base metal. Moreover, it induces a coarse grain structure in the weld and heat affected zones (HAZ) which result in low toughness without post weld heat treatment.

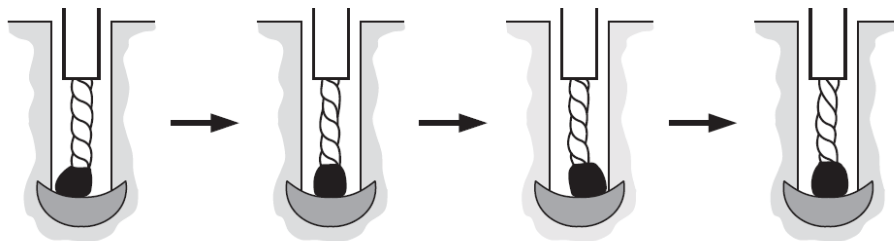
Narrow-gap welding using GMAW (NG-GMAW) was firstly developed by the Battelle Memorial Institute in 1970. This method is one of the most widely used - particularly in Japan [36]. NG-GMAW can provide the ability to weld in all positions with low weld metal hydrogen content; a shielding gas is required. Higher productivity can increase deposition rates drastically by continuously feeding wire and more electrodes. In order to obtain a welding quality, appropriate melting of the sides of the joint is ensured by a specially designed torch that fits into a small gap, whereas the welding arc will be alternately moved to the left and right side of the gap joint. There are different techniques of the feeding wire movement mainly used as illustrated in Fig. 2.4. However, the inherent problems related to lack of sidewall fusion, arc instability to magnetic fields and spattering build-up have to be seriously considered [32, 33, 38, and 39]. Therefore, the range of proper welding conditions to achieve a high quality weld is rather limited and highly skilled welding operator is required.



(a) NG-GMAW process variants - oscillation of straight fed wire.



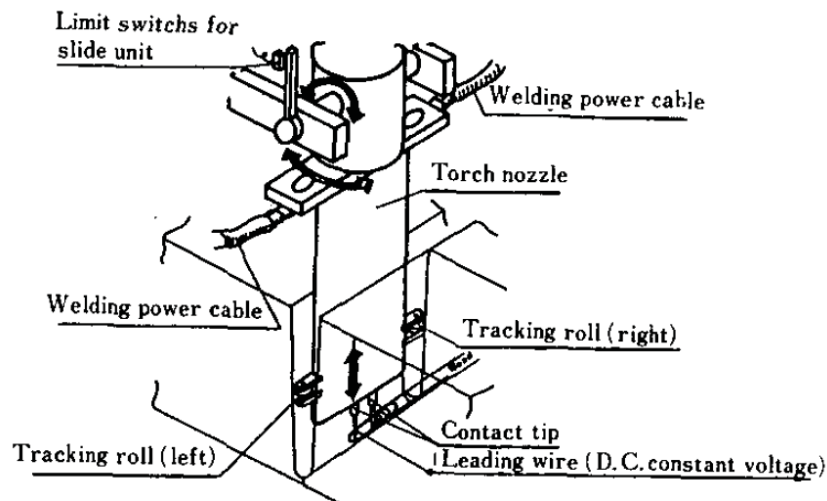
(b) NG-GMAW process variants - corrugation of wire to achieve oscillation.



(c) TWISTARC NG-GMAW variant.

Fig. 2.4 Types of movement of the melting wire in NG-GMAW [32, 40].

Comparing NG-GMAW, SAW with a narrow gap (NG-SAW) provides high deposition rates and major advantages to overcome an inadequate fusion of sidewall and porosity. The wider tolerance of welding conditions to obtain a reliable welded joint is an attractive benefit for practical use. An NG-SAW process needs a suitable flux to produce gases and slag to protect the arc and weld pool. Alloying elements in the flux can be added into the weld pool for improving weld metal properties. Figure 2.5 shows a typical NG-SAW process. Nevertheless, such application is commonly limited in the flat position. Furthermore, an important drawback is the difficulty of slag removal, which leads to defects like slag inclusions [36, 37, 41, and 42].



(a) Schematic illustration of NG-SAW [32].



(b) Tandem twin wire SAW welding head and ancillary equipment [43].

Fig. 2.5 Narrow-gap SAW welding.

Similar to Electroslag welding, NG-SAW gives a high heat input. For this reason, this method still causes a grain growth on HAZ, and reduced strength.

Recently, narrow-gap GTAW (NG-GTAW) method has been developed. The advantages such as low heat input, good arc stability, no spatter, no slag, and high quality weld metal in all welding positions, can be obtained through this method. The process involves the independent control of the heat input and wire feed speed. NG-GTAW provides the benefit of greater melting control on a groove sidewall of butt joints, which has the potential to reduce incomplete fusion defects. NG-GTAW is mostly suitable for use in a narrow-gap joint. However, it has the noted limitation of deposition rate capability. For this method, high quality weld joints are required; however it comes with low productivity. This process is mainly used in welding high strength low alloy steel, stainless steel, and titanium. Figure 2.6 shows typical NG-GTAW welding.

A recent development of a hot-wire system as illustrated in Fig. 2.7, NG-GTAW with a hot-wire filler metal provides an attractive alternative that combines the benefits between increasing deposition rate and independent control of heat input. Good shielding gas protection and ensuring that the arc reaches the groove edges of the joint are the key points to successful welding [40, 44-48]. Due to a small gap preparation of joint and the size limitation of electrode torch heads, there have been different techniques of electrode manipulation developed to achieve a good weld quality as shown in Fig. 2.8. Nevertheless, a special electrode torch head and complicated equipment are required, because of the limited accessibility to a narrow joint preparation.

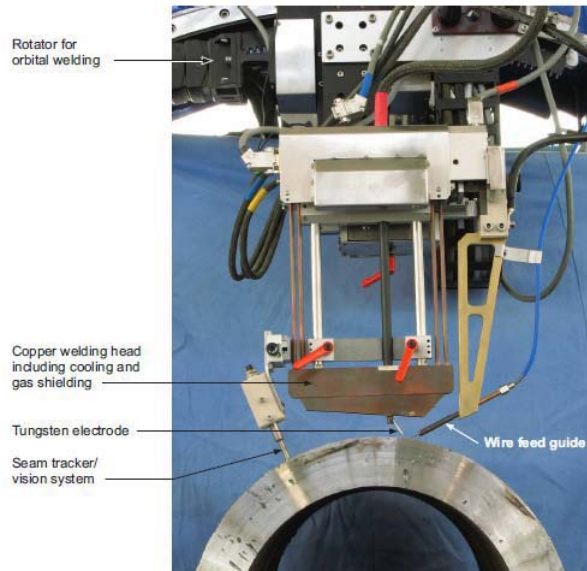


Fig. 2.6 Typical Narrow-gap GTAW welding with an orbital torch.
[Image courtesy of Polysoude]

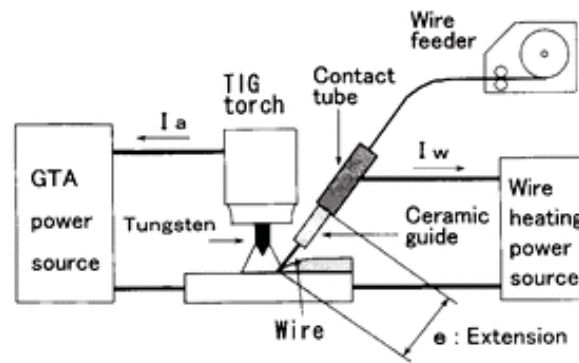


Fig. 2.7 Principle of Hot-wire GTAW [40].

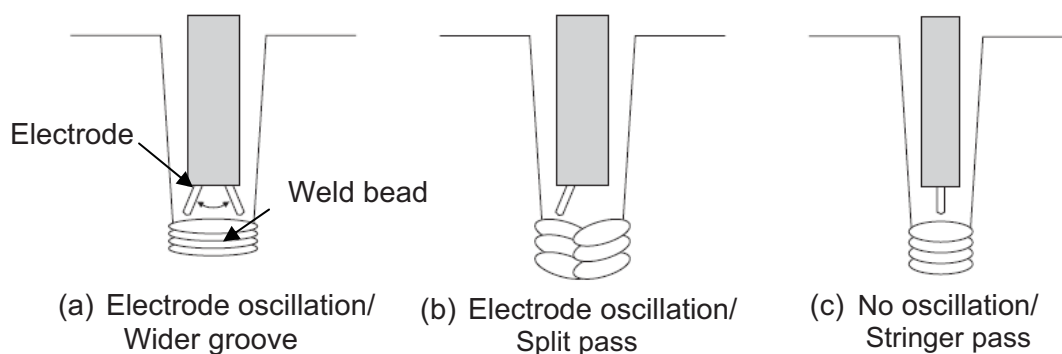


Fig. 2.8 Manipulate modes of welding electrode and weld pass in NG-GTAW [48].

Other processes can be used for narrow-gap welding. Laser and laser-arc hybrid welding are interesting processes [17, 18, and 34]. Even though the laser arc hybrid process provides high welding speed, this method has potential to generate defects and weld spatter because of arcing.

2.3 Weld Solidification Cracking and its Mechanism

There are many studies regarding the phenomena of the occurrence of solidification cracking [49-61]. This is a complicated phenomenon concerning an interaction between thermal, mechanical, and metallurgical causes. A solidification crack in a weld metal usually appears at the centerline weld as shown in Fig. 2.9. Sometimes, it occurs at other locations in the fusion zone or near the HAZ and in the crater. Solidification cracking, also known as hot cracking, consists of the fractures at the interdendritic and/or intergranular grain boundaries in the solidification temperature range, in which the liquid phase of the mushy melt becomes rich in impurities, mainly sulfur (S) and phosphorus (P). This situation causes a drop in the mechanical strength at the grain and dendritic boundaries, which lead to a susceptible to cracking.

The mechanism of solidification cracking is shown in Fig.2.10. Solidification cracks form during the terminal stage of solidification when a liquid film is distributed along interdendritic regions. At this stage, shrinkage strains across the partially solidified boundaries can become appreciable. If the terminal liquid is distributed along the boundaries as a continuous film, the strains cannot be

accommodated and the boundaries separate from a crack. In terms of materials, the solidification temperature range and morphology of the interfacial liquid that exists at the terminal stages of solidification are primary factors that control solidification cracking susceptibility. Solute redistribution plays an important role in solidification cracking as it affects the solidification temperature range and amount of terminal liquid.

Solidification cracking has been divided into four stages by Borland [52-54]. At first, primary dendrite formation, the solid phase is dispersed and the liquid is continuous, both solid and liquid are capable of relative movement, and therefore no crack occurs. Second, dendrite interlocking, both solid and liquid, are continuous but only the liquid is capable of relative movement and is able to circulate freely between interlocking dendrites. In this stage, if the grains are pulled apart by excessive strain, the cracks are refilled and healed by the interconnecting liquid. Third, grain boundary development, the solid crystals are in an advantage of development, and a semi-continuous network of solids restricts the free passage of liquid. This is called the critical solidification range. No healing of cracks is possible if the accommodation strain exceeds critical value, because the remaining liquid volumes are not interconnected. The final stage is complete solidification, the remaining liquid has solidified and no solidification cracks occur.

As an alloy, the solidification temperature range and amount of terminal liquid are controlled primarily by chemical composition, which can manage the susceptibility to hot cracking. Solidification cracks can be minimized by a careful selection of weld metal composition. Weld solidification cracking occurs during the final stages of solidification when tensile shrinkage stress accumulates and liquid films still persist along solidification grain boundaries in the structure. If the imposed shrinkage strain exceeds the inherent ductility of the solidifying weld metal, cracking will occur. The solidification and solidification cracking features in the weld metal are exhibited in Fig.2.11.



Fig. 2.9 Picture of solidification cracking in the centerline related to a pear-shaped bead [21].

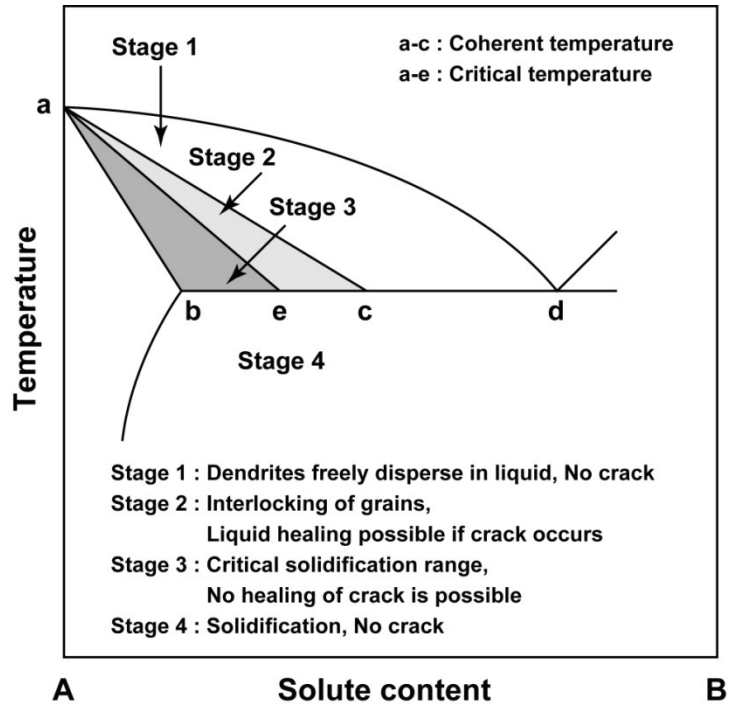


Fig.2.10 General theory of solidification cracking [52].

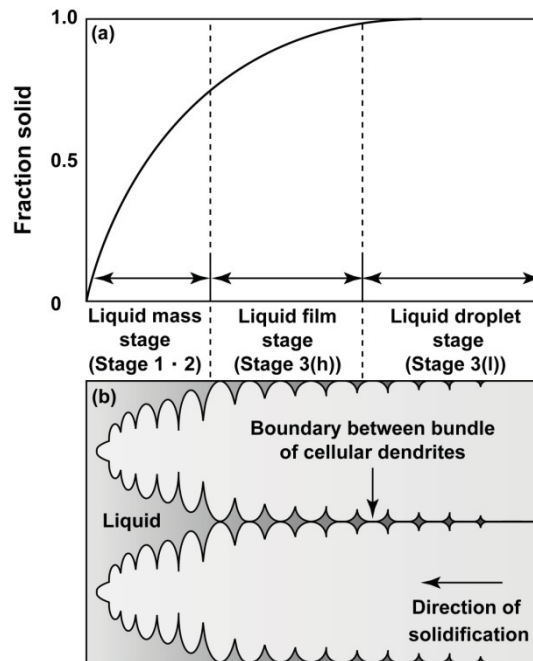
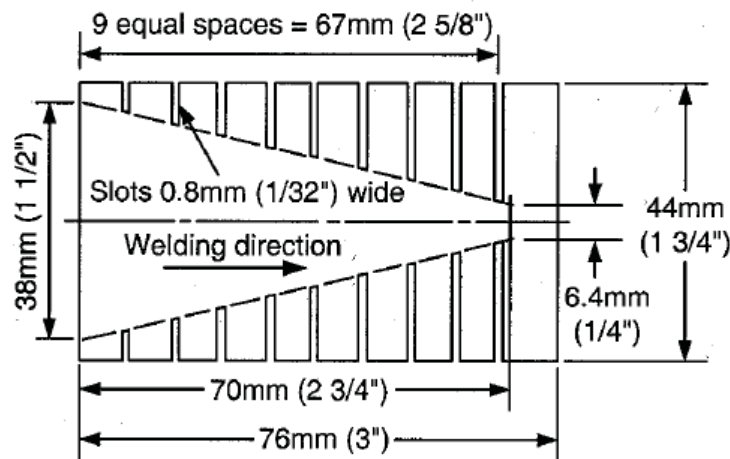


Fig.2.11 Development of solidification cracking proposed by Matsuda.F. [55]

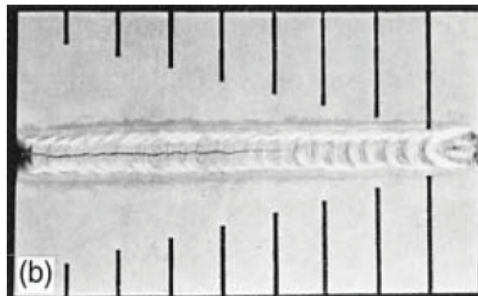
2.4 Methodology of Solidification Cracking Susceptibility Testing

Currently, testing methods of solidification cracking susceptibility have been developed to assess weldability in several materials [1-3, 54]. Those methods can be mainly classified into two types, namely a self-restraint cracking test and an externally loaded-cracking test.

Self-restraint cracking tests are employed to reproduce the actual welding conditions as closely as possible in practical work. The configuration of test specimens and the related fixtures are designed to induce different restraints. The methods widely used include the Houldcroft test, FISCO hot cracking test, and circular patch test. Fig. 2.12 shows the specimen dimensions used for the Houldcroft crack susceptibility test, which is usually used in aluminum. When beginning GTAW welding at the starting edge of the test specimen, solidification cracking is initiated from this point due to a more constraint level. As the weld pool moves inwards along a centerline, the cracking is propagated due to thermal-tensile stresses. The different width of slots allows the inducing of cracking under an amount of tension. A shorter slot width in the specimen is able to bring the cracking to a stop. The length of crack is used to indicate the susceptibility to cracking.



(a) Design specimen.



(b) Cracking in an aluminum alloy

Fig. 2.12 Houldcroft test [3].

Nevertheless, most self-restraint cracking tests are not suitable to reproduce cracking in materials with low cracking susceptibility. Moreover, the mechanical factors to solidification cracking are unclear and not separated from the material factors.

According to externally loaded-cracking tests, an external augmented strain or stress is applied during welding. By this means, the material factor such as the effect of metallurgical and composition associated with solidification cracking can be distinguished from the mechanical factors. Consequently, an externally loaded-cracking test can be defined as quantitative evaluation of cracking susceptibility as a result of providing a comprehensive order ranking of families of alloys.

There are many types of externally loaded-cracking tests such as Varestreint test, Sigmajig test, Rapid tensile test, U-type test etc. A Varestreint test is one example in these test types, which is commonly used in the present. The Varestreint test was developed by Savage and Lundin as illustrated in Fig 2.13.

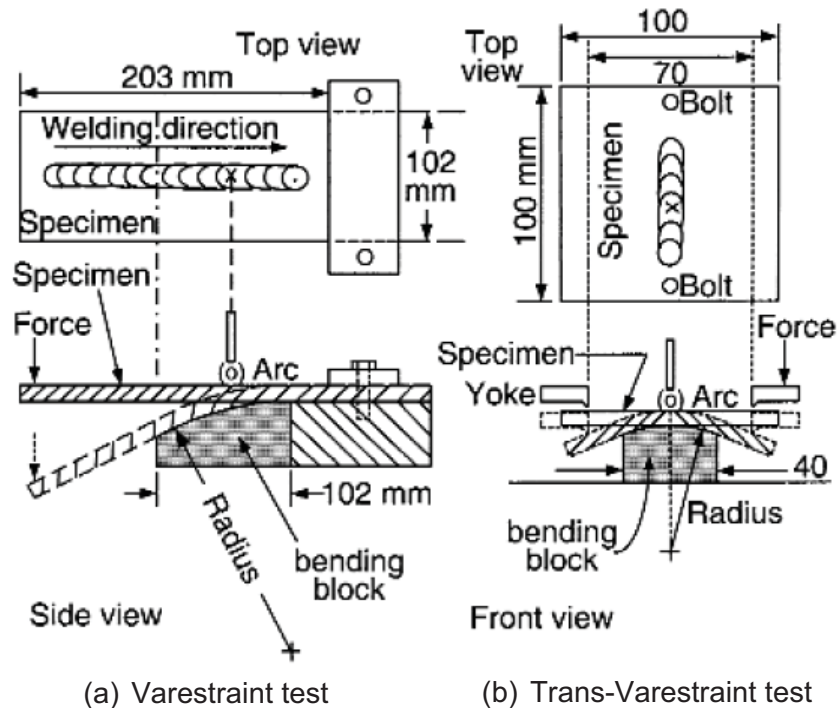
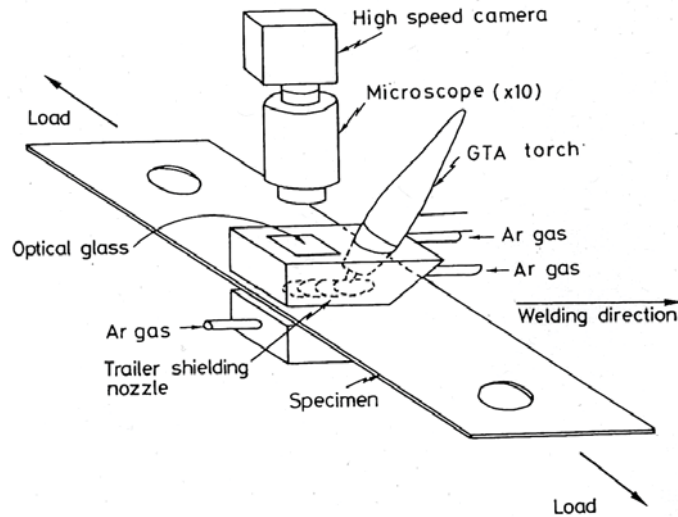


Fig. 2.13 Externally loaded-cracking test [3].

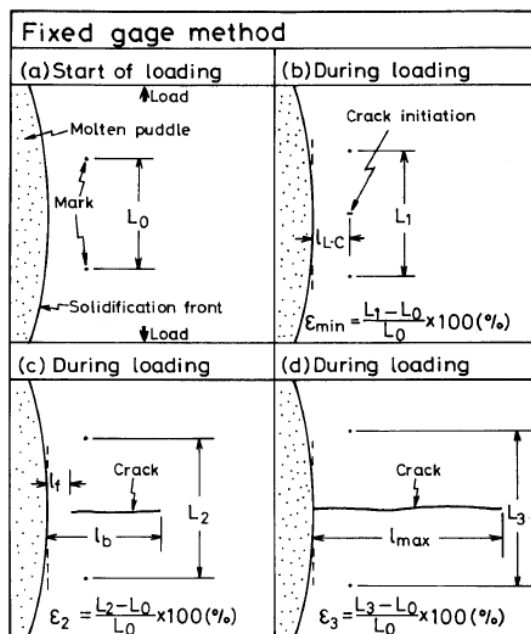
Strain is applied to a test specimen by bending it with a designated radius at an appropriate time during welding. Quantitative evaluation of cracking susceptibility includes indexes such as the amount of applied strain, total crack length, maximum crack length, and total number of cracks.

Matsuda et al. [55-64] reported regarding a reduced amount of ductility of a solidifying weld metal by using in-situ observation (MISO). Figure 2.14 shows a hot cracking test by means of in-situ observation. In that study, an optical microscope and a high speed camera are utilized to measure the dynamic

movement of reference points nearby solidification cracking tips during crack initiation and propagation. Therefore, the local strain to crack initiation can be calculated accurately. The relationship between measured local strain to crack initiation and temperature history along the tail edge of the molten pool is used to determine so-called ductility curve. Figure 2.15 exhibits the example of the ductility curves for some stainless steels and Inconel600 obtained by using MISO.



(a) Hot cracking test by external load and high speed camera observation.



(b) Procedure to determine local strain.

Fig.2.14 Hot cracking test by means of in-situ observation [63].

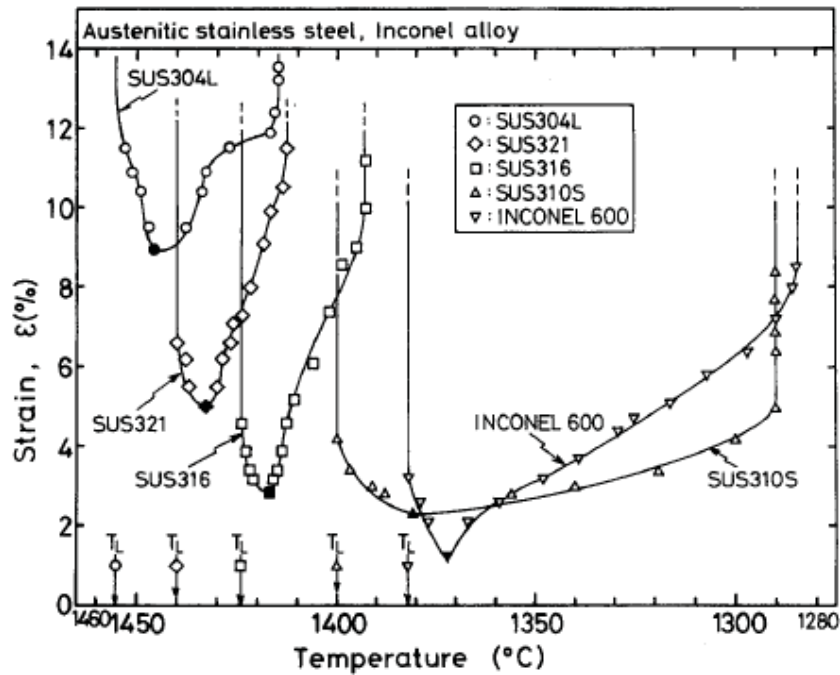


Fig.2.15 Ductility curves of austenitic stainless steels and Inconel alloy [64].

2.5 Prediction of Solidification Cracking

Generally, it is well known that solidification cracking on weld components gives undesirable defects during welding processing. There are many literatures attempting to study the mechanism and prediction of the occurrence of solidification cracking [65-76]. According to Prokhorov's theory [65], the integral approach between a ductility curve and a driving force during solidification, the formation of weld metal solidification cracking results from the competition between the material resistance to cracks and the driving force to cracks (strain rate) during term solidification of weld metal. That is, the accumulated tensile strain during solidification of a weld pool is considered to be the mechanically driving force of solidification cracking. The deformability of the liquid-solid region or the high temperature ductility is regarded to be the material factor, which is obtained by hot cracking test [63-64]. When the accumulated tensile strain exceeds the critical strain of the ductility curves, weld metal solidification cracking is initiated.

According to the theory of prediction of solidification as mentioned above, there are many researches regarding welding application. Fig. 2.16 represents the schematic illustration of weld solidification crack mechanism. Cracking occurs only when the strain rate (red solid line) exceeds the material resistance to cracks (ductility curve) in the entire brittle temperature range (BTR). The fundamental parameter representing the material resistance is its ductility curve in the BTR during weld metal solidification, which is not constant but a function of temperatures, while the mechanical strain accumulated in the BTR is considered as the driving force, which is also a function of temperatures.

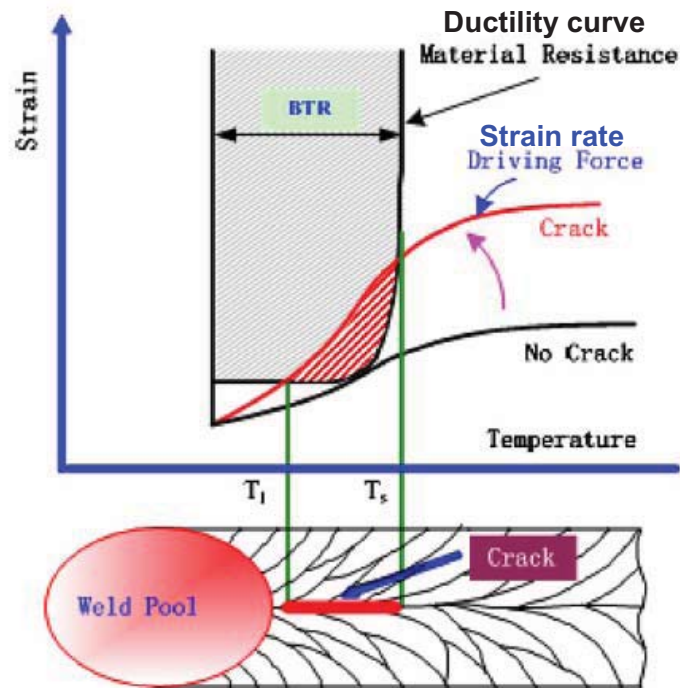


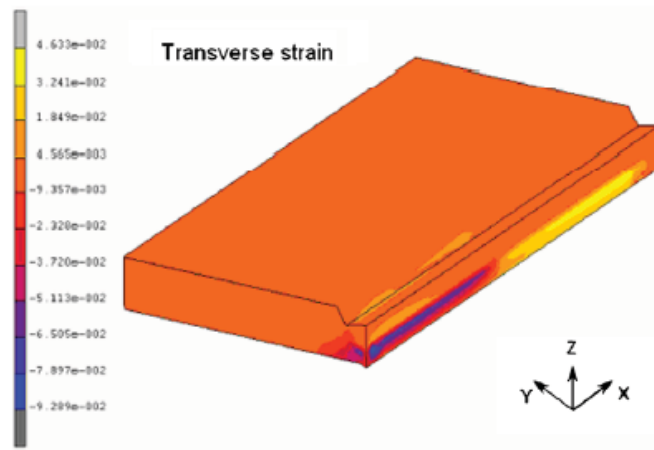
Fig.2.16 Ductility curve and the occurrence of solidification cracking [69].

By developing the numerical method and increasing the computational simulation performance, the finite element method (FEM) is very powerful to calculate the simultaneous couple problems between thermal and mechanical. Consequently, the mechanical driving force or strain due to non-uniform temperature distribution is able to be estimated accurately during welding.

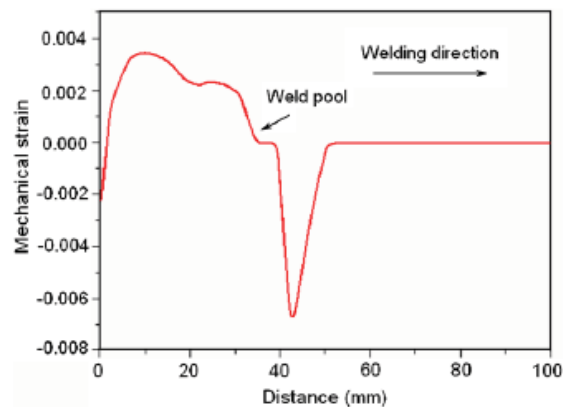
In general, the procedure of computational welding simulation is always divided into two parts, namely, thermal analysis for temperature distribution and elasto-plastic strain analysis for mechanical response. The thermal analysis calculates the temperature distribution during welding. After this, the results of the temperature distribution are used to input in a database in order to calculate elasto-plastic strain analysis. In this step, mechanical accumulated strain during solidification of a weld pool can be estimated precisely. Therefore, the occurrence of solidification cracks can be reasonably predicted by comparing the calculated strain and the high temperature ductility curve as explained before.

For example, the study of Zhibo Dong, et al. [75] utilizes the 3D-FEM analysis of SUS310 stainless steel welded by SMAW, in which 3D-strain distributions are calculated during the first pass welding as shown in Fig.2.17. In another study, Wei Y.H. and Liu R.P [76] presents the approach of predicting weld solidification cracking during GTA welding as exhibited in Fig.2.18. This study explains the ductility curve was obtained by a Trans-Varestraint test, while the strain curve was calculated with the moving heat source model for GTA welding. The results reveal that no solidification cracking is predicted, for the reason that the local critical strain does not appear over the used ductility curve.

In welding simulation using FEM, the appropriate model of welding heat source relative to the kind of welding processes is an important viewpoint to obtain the precise result, in which there are several models of heat source [77-83]. They have been developed to attain the accuracy of temperature distribution on welded components and explain the welding phenomena in the thermal field. However, especially in narrow-gap welding with hot wire system, it still has not been studied clearly [21, 84, and 85].



(a) 3D-plastic strain distributions



(b) the mechanical strain distribution in the weld centerline

Fig.2.17 Calculated strain distributions in 3D-FEM [75].

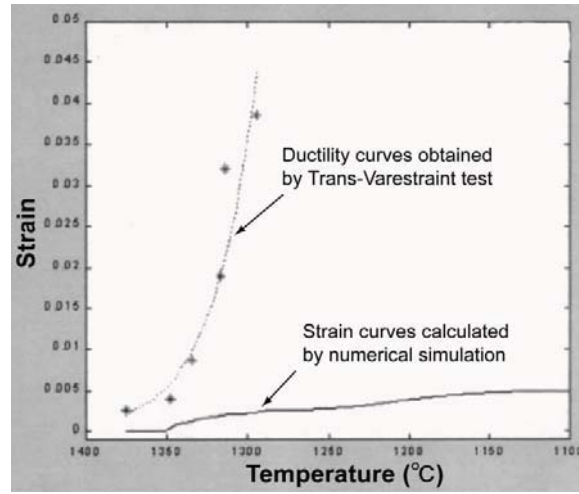


Fig.2.18 Prediction of solidification cracking made by Wei Y.H. during GTAW [76].

Chapter 3

Development of Hot wire Laser Welding with a Narrow Gap Joint

3.1 Introduction

Many recent studies have attempted to apply conventional welding processes with a narrow gap joint to reduce large shrinkage and residual stress and improve productivity relative to the results of general joint preparation. Applications of such processes with a narrow gap joint include submerged arc welding, gas metal arc welding, gas tungsten arc welding (GTAW), and plasma welding [1, 2, 8-12, 31-33]. These methods and particularly submerged arc welding retain the effect of the evolution of the metallurgical structure in the vicinity of the weld metal owing to high input heat energy. A wire preheating system was designed to independently control the melting feed wire and the base metal, and lower heat input energy. Conversely, hot-wire-GTAW is currently the modern combination method with a narrow gap joint most employed for fabrication. This hybrid process is capable of realizing a weld joint with high integrity.

As mentioned above, even if hot-wire-GTAW is useful for a narrow gap joint, such technology is still limited in terms of traveling speed and production rate. An alternative to narrow-gap welding is laser-arc hybrid welding, which has a tendency to induce defects due to arcing - although such a process has the advantage of a high traveling speed. Consequently, an innovative hybrid process of hot wire laser welding has been designed. This novel hybrid process combines the advantages of high weld deposition, no electric arc, and a low dilution ratio [17, 18, and 34]

The first part this chapter presents the methodology of hot wire laser welding with a narrow gap joint. The phenomenon of the melting pool is observed using an in-situ observation technique in order to make clear the mechanism of weld bead formation. In addition, a particular experiment is carried out to explain the effect of the reflected laser irradiation - especially in terms of melting the side groove wall of the base metal.

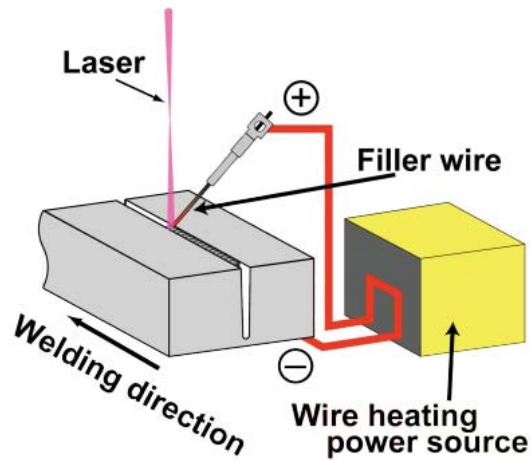
The second part includes the investigation of welding variables which affect the sound welding in a narrow gap joint such as wire current, and wire feeding position, as well as the angle of laser irradiation. Finally, mechanical weld properties that include hardness profile and tensile strength are tested.

3.2 Hot Wire Laser Welding Process with a Narrow Gap Joint

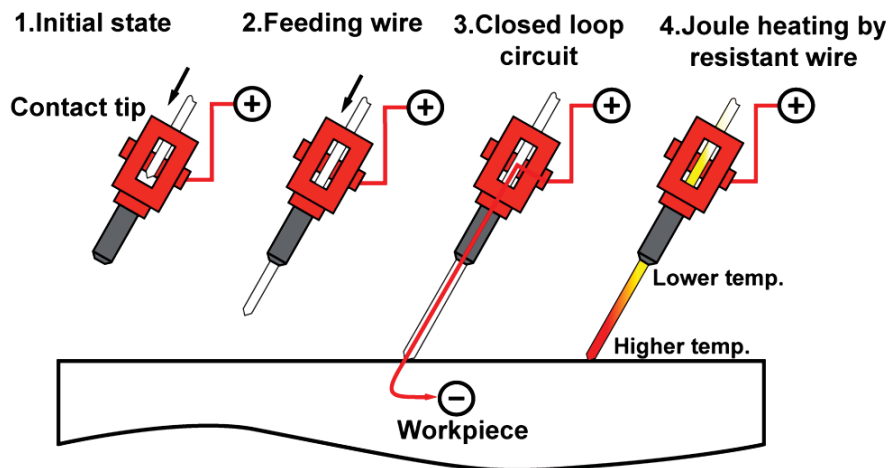
In the present work, this novel hot wire laser process includes crucial components between a wire heating power source and a defocused laser beam. Figure 3.1 (a) presents the schematic illustration of a hot wire laser welding system. Based on the joule heating's principle, the electric power source plays an important role in the function to heat a filler wire up to near the melting point. The amount of electric current flowing through a filler wire is adjusted in order to obtain an adequate melting of a filler wire during feeding into the molten pool. The defocused laser beam is a further heat input to develop the complete weld pool.

As for a wire heating power source, known as a "hot wire system", a filler wire is electrically heated through a pulsed-direct current power source in order to provide a mushy state close to liquid phase just before reaching a molten pool. Figure 3.1 (b) illustrates the sequential steps of initially generating heat in a fed filler wire. At first the distance span between a copper contact tip and a work piece is specified. When a filler wire is fed through the copper contact tip till it touches the work piece the electric current flows through a fed filler wire and a closed loop circuit is complete. Based on the joule heating law, heat is generated due to having a higher value of electrical resistance in a filler wire.

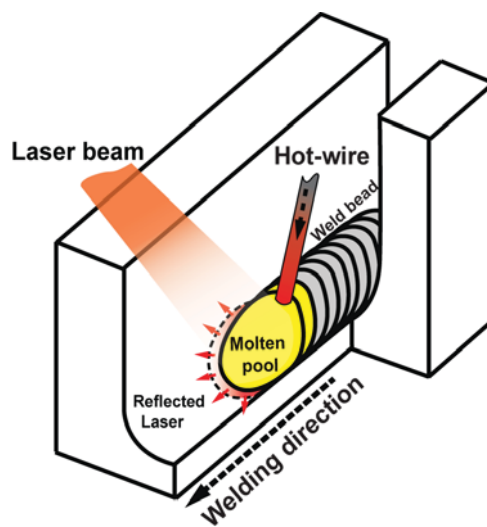
At the same time, a defocus laser beam serves a role to encourage the amount of thermal volumetric energy in a hot wire slightly in excess of the melting temperature. Therefore, a complete weld pool is achieved by very low heat energy while a hot wire is still fed into the weld pool continuously at a rear laser beam. In addition, Fig. 3.1 (c) represents a schematic illustration of the application of hot wire laser welding in a narrow groove. This developed hybrid process has a particular feature for independently controlling melting between a hot wire and a base metal.



(a) Hot wire laser welding system.



(b) Generating heat in a fed filler wire.



(c) Characteristic of hot wire laser welding in a narrow groove.

Fig. 3.1 Schematic illustration of hot wire laser welding with a narrow gap joint.

3.3 Material and Specimen Used

The efficiency of hot wire-laser welding has been investigated in terms of application to thick plates widely used in power generation plants; e.g., study of the application to piping and boilers with respect to elevated-temperature service. The specimen used in the present study was ASTM A 304 austenitic stainless steel welded with tentative nickel-based filler metals made of Inconel 600 alloy. Such filler metals were used to investigate adequate welding conditions. In a real application of welding A-USC boilers, a specimen welded with candidate filler wire ER NiCrCoMo-1 according to AWS classification was used for hardness and tensile testing. Both filler metal types have diameter of 1.2 mm. Chemical compositions of each material are given in Table 3.1. For joint preparation, a U groove weld joint with a gap width of 3 mm was applied. The test plate had dimensions of 120 mm × 23 mm × 10 mm as shown in Figure 3.2.

Table 3.1 Chemical composition of used materials (mass %)

Material	C	Si	Mn	P	S	Ni	Cr	Fe	Cu	Mo	Ti	Co
A 304	0.04	0.49	0.91	0.035	0.002	8.26	18.23	Bal.	-	-	-	-
Inconel 600 (ϕ 1.2 mm)	0.04	0.24	0.25	0.006	<0.001	77.15	15.68	6.4	-	-	-	-
ER NiCrCoMo-1 (ϕ 1.2 mm)	0.08	0.09	0.05	0.004	0.001	Bal.	21.37	0.47	0.03	9.54	0.31	12.21

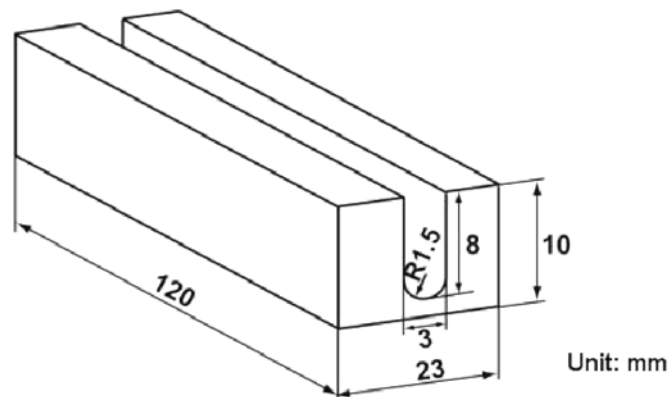


Fig. 3.2 Geometry of joint and test plate.

3.4 Experimental Procedure

The experimental setups included fiber laser welding equipment as shown in Fig. 3.3. Sample plates were automatically welded using a Yb:YAG fiber laser power source (YLR-3000S IPG-Laser), maximum output 3kW, with a six-axis robotic welder (Kawasaki FA10N). The wavelength of the operating laser was 1070 nm, and the beam parameter product of the beam quality was 5.4 mm·mrad. Spot size is 0.436 mm in diameter and 400 mm in length at the just focus. 3. 4 illustrates the comparison of the beam profile between at the just focus and the defocused length. It is noted that the defocused beam profile provides more homogenous concentration of laser energy input to the molten pool. The hot wire feeding system is supplied by pulsed-direct current with Assist IV-662 power source manufactured from BABCOCK-HITACHI. Figure 3.5 (a) shows the picture

of hot wire supplier, while Fig. 3.5 (b) presents the examples the pulsed shape of direct current during welding. Due to the pulsed-direct current of hot wire supplier, the wire current setting is explained in terms of root mean square (RMS) current related to a sampling rate. The proper sampling rate is not less than 120 to obtain the accurate value of wire current.

Figure 3.6 shows the experimental setup. In terms of the welding conditions, Fig. 3.7 illustrates the essential welding variables related to the position and orientation of the filler wire and laser beam, namely the laser irradiation angle, wire feeding angle, and wire feeding position. Table 3.2 gives the changes in welding variables (i.e., wire current, wire feeding position, wire feeding and laser irradiation angle). Figure 3.8 presents the particular chamber which provides the local and gross shielding gas distribution. Argon was employed as a shielding gas to protect from an undesired reaction with the outside atmosphere.

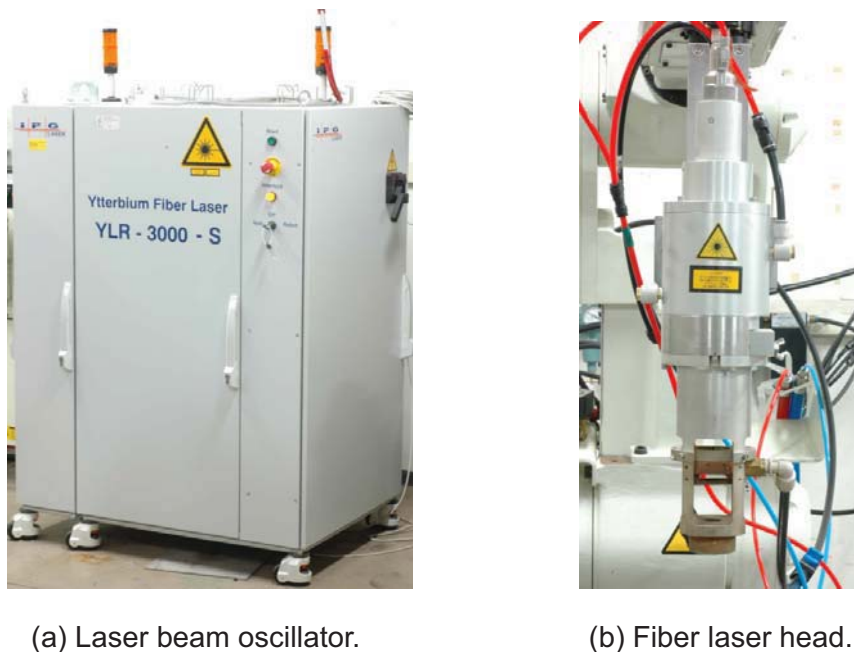


Fig. 3.3 Image of fiber laser welding equipment.

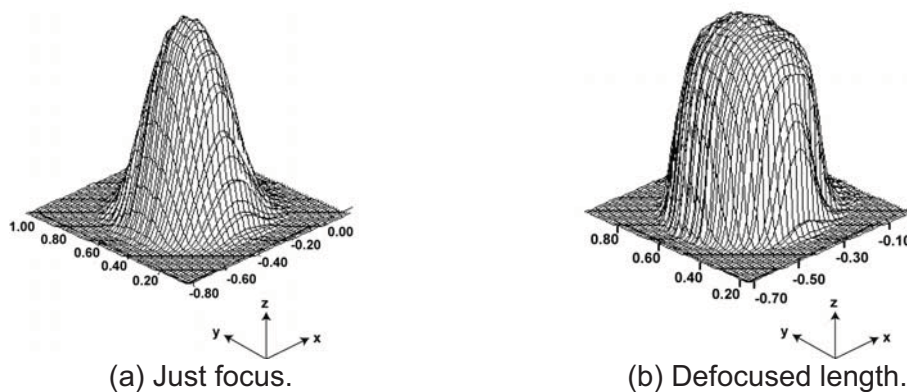
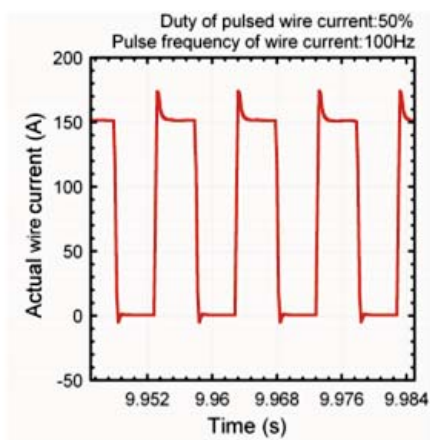


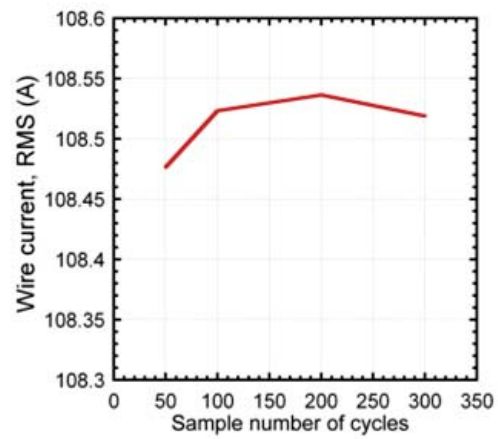
Fig. 3.4 Fiber laser beam profile.



(a) Power source equipment.



(b) Pulsed-direct current waveform.



(c) RMS current and sampling rate.

Fig. 3.5 Image of a wire heating power source.

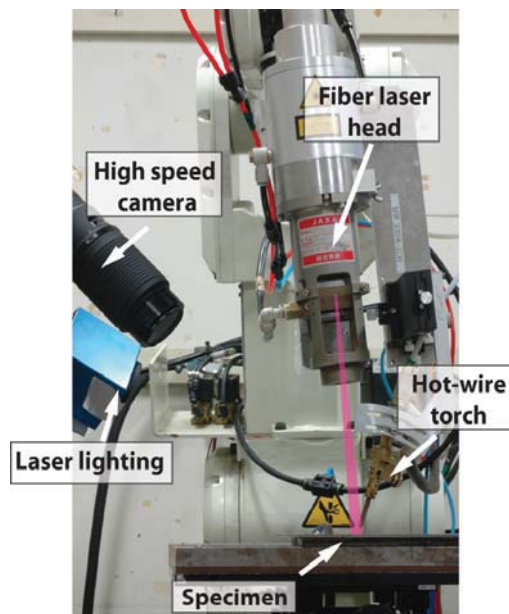


Fig. 3.6 Experimental setup of hot wire laser welding.

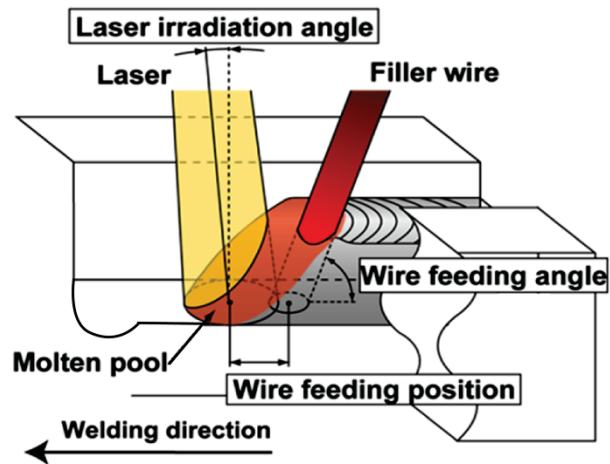
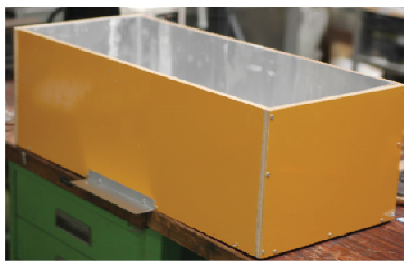


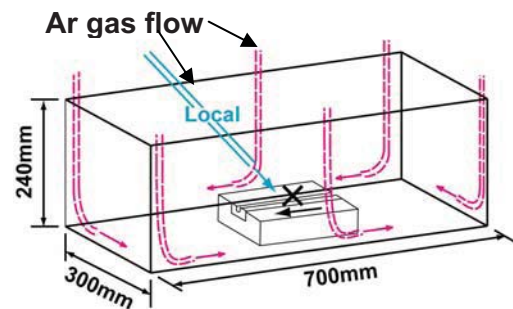
Fig. 3.7 Positional relationships of the essential welding variables in the hot wire laser process.

Table 3.2 Utilized welding parameters

Laser type	Fiber laser
Laser power (kW)	3
Welding speed (m/min)	0.5
Defocus length (mm)	60
Laser spot diameter (mm)	3
Irradiation angle (deg.)	5, 30, 45, 60
Wire feeding speed (m/min)	6, 8
Wire feeding angle (deg.)	70, 80
Wire feeding position (mm)	0, 1, 2, 3
Wire current (A)	125, 137, 144
Argon shielding gas (l/min)	10(hold15 min)
Chamber box	5
Local place	5



(a) Image of chamber.



(b) Illustration of shielding gas flow.

Fig. 3.8 Shielding gas chamber.

The phenomenon of molten pool behavior and bead formation during welding was visually monitored by in-situ observation using a high-speed camera (FASTCAM-1024: Photron) located in front of the molten pool. Conditions of the in-situ observation are given in Table 3.3. Furthermore, the joint was illuminated with a lighting laser having a wavelength of 980 ± 5 nm to acquire bright images. As for protecting the too strong laser irradiation reflected from the molten pool, a band pass filter (Band pass 10 nm FWHM 980-10) with transmitted wavelength of 980 nm was installed with an optical lens. Figure 3.9 shows the transmission conditions of band-pass filter. A protect lens was used to protect the outside filter from damage of spatter and metal vapor.

Table 3.3 Observation conditions of high speed camera

Shutter speed (s)	1/1000
Frame rate (fps)	250
lighting laser (nm)	980 ± 5 nm
a band pass filter (nm)	980 nm

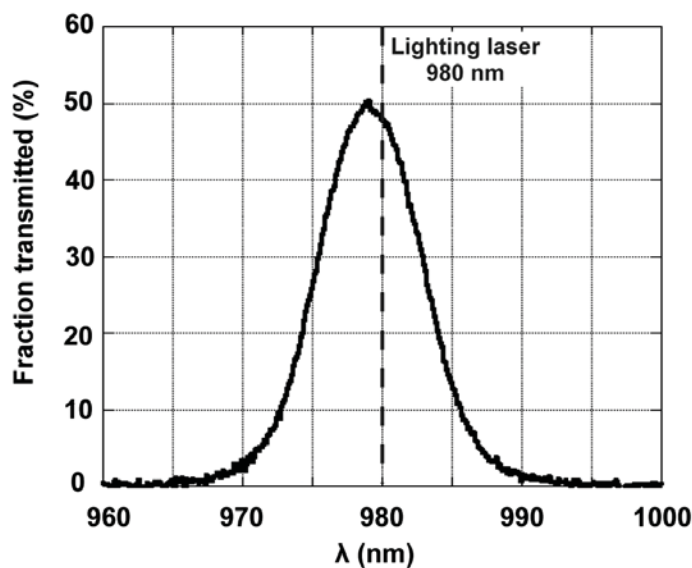
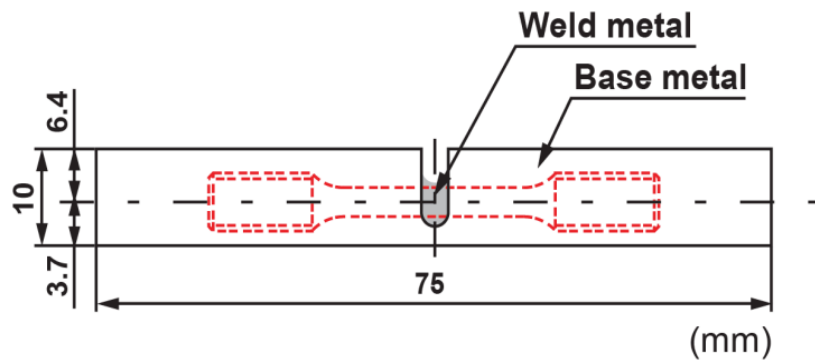


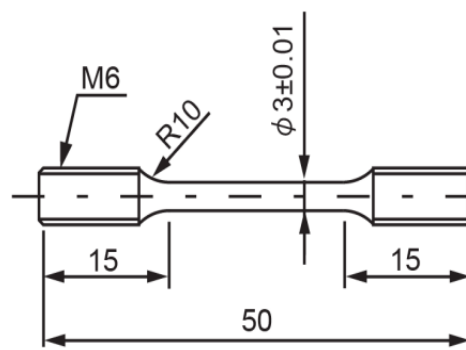
Fig. 3.9 Transmission conditions of band-pass filter.

The welded sample plates were sectioned transversely relative to the welding direction and prepared for metallurgical examination for an adequately sound weld deposit together and to examine microstructure.

The weld property was evaluated in a hardness test. Additionally, because the hot wire laser welding process resulted in slight penetration of the base metal, the adequacy of bonding strength at the fusion boundary was tested in a tensile test condition. That is, tensile load was 10 kgf and the speed rate was 5 mm/min. The dimension of the tensile specimen and the cutting location is shown in Fig. 3.10. The fracture surface was confirmed with a scanning electron microscope (SEM).



(a) Position of a machined specimen.



(b) Dimension of a tensile specimen.

Fig. 3.10 Tensile testing.

3.5 Effects of Hot Wire Laser Welding Parameters on Weld Characteristics

From experimental results, the essential welding variables were diagnosed for their effects on the wire melting phenomenon and the quality of the weld beads as described below.

3.5.1 Effect of Wire Current

Figure 3.11 compares the observation images captured using the high-speed camera for different wire currents, namely 125, 137, and 144 A, and their cross section views. Constant welding conditions were output laser power of 3 kW and spot beam diameter of 3 mm, welding speed of 0.5 m/min and wire feeding speed of 8.0 m/min, and a wire feeding angle of 70° and wire feeding position of 0 mm. The dotted line represents the molten pool region and the solid line indicates the hot wire feeding. Wire current had a significant effect on the melting behavior of the inserted wire. In other words, increasing the current resulted in more melting of the wire. However, an unstable melting phenomenon results from an inappropriate current value, eventually leading to undesired defects. In this case, an adequate weld bead was achieved for current of 137 A.

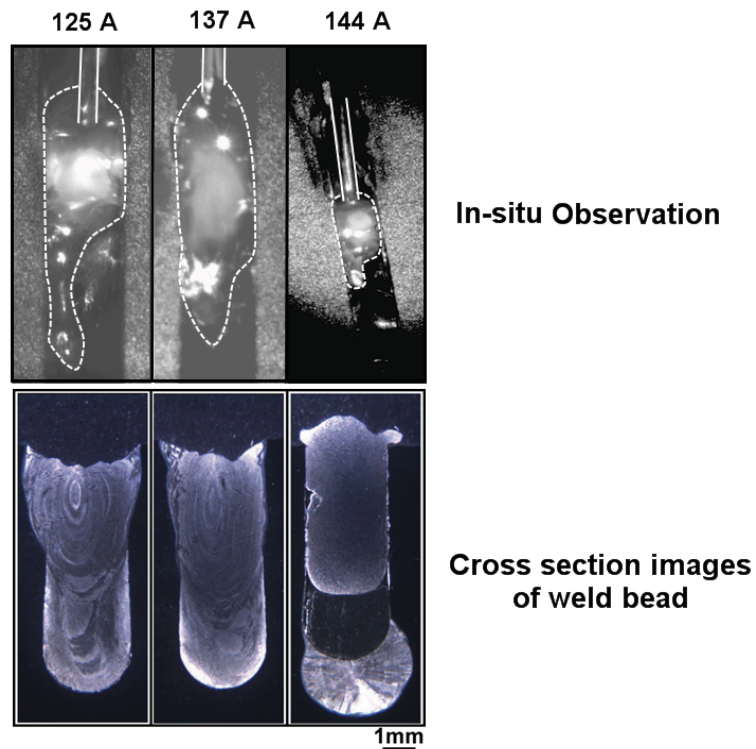


Fig. 3.11 Melting phenomenon and cross section images for varied wire current.

3.5.2 Effect of the Wire Feeding Position

The location where a hot wire is inserted into the molten pool is another important welding condition affecting the stability of melting phenomena. This parameter is related to the distance between the center of an applied laser beam and the wire feeding point. In this experiment, the wire feeding position was varied as 0, 1, and 3 mm, while the constant welding conditions were output laser power of 3 kW and a spot beam diameter of 3 mm, welding speed of 0.5 m/min and wire feeding speed of 8.0 m/min, wire feeding angle of 70° and wire current of 137 A.

Figure 3.12 presents the observation images of the melting phenomenon for which the feeding points are varied and their cross sectional views. The dotted line represents the molten pool region while the solid line is the feeding wire. It is clear that a wire feeding position of 0 mm is inappropriate because it results in the uneven melting of the feeding wire by the laser beam before the wire is dipped into the weld pool. In contrast, when the feeding wire was located at 3 mm and thus outside the melting region, the feeding wire tends to be distorted because of inadequate melting. The optimum condition was found to be a wire feeding position of 1 mm, which produces stable melting and a sound weld.

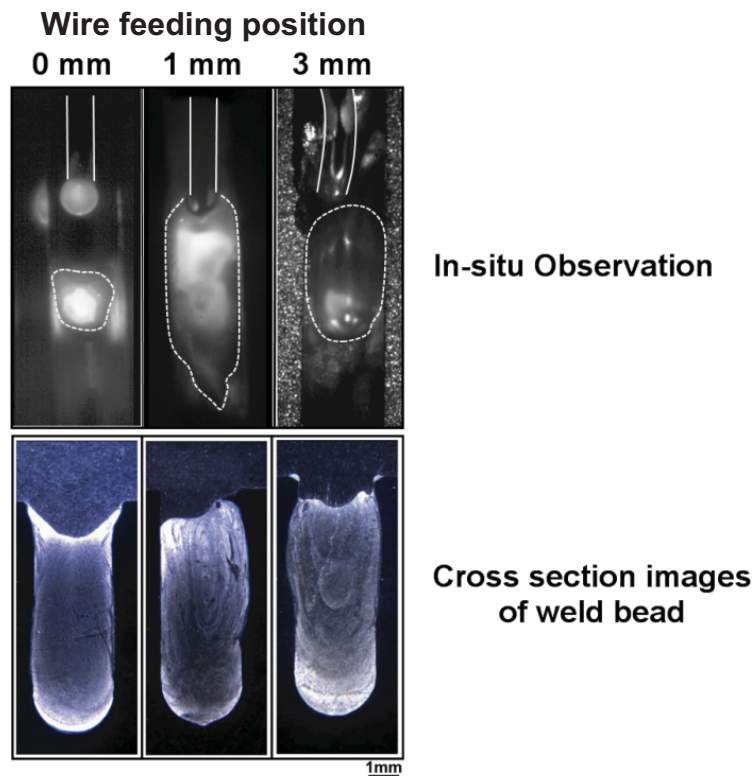


Fig. 3.12 Melting phenomenon and cross section for varied wire feeding position.

3.5.3 Effect of the Angle of Laser Irradiation

An experiment was carried out to determine the effect of the laser irradiation angle on the melting phenomena. The angle of laser irradiation was set as 5°, 30°, 45°, and 60°, while the constant welding conditions were output laser power of 3 kW and spot diameter of 3 mm, welding speed of 0.5 m/min and wire feeding speed of 8.0 m/min, a wire feeding angle of 80° and wire feeding position of 0 mm. The laser irradiation angle had a substantial effect on the integrity of the weld deposition. Figure 3.13 shows that a laser irradiation angle of 45° or 60° contributed to incomplete fusion between weld passes, at the root in particular, while a laser irradiation angle of 5° provides a sound weld.

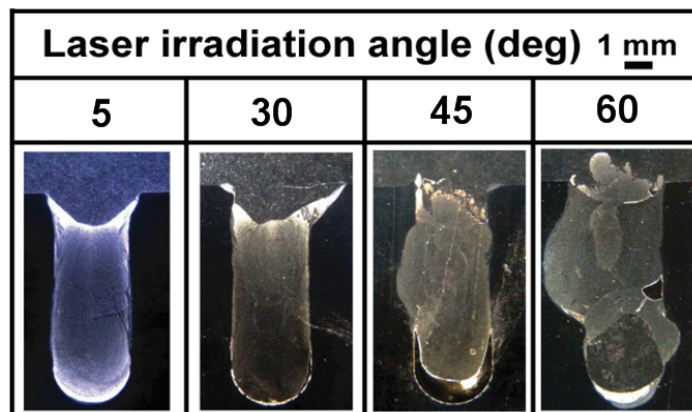
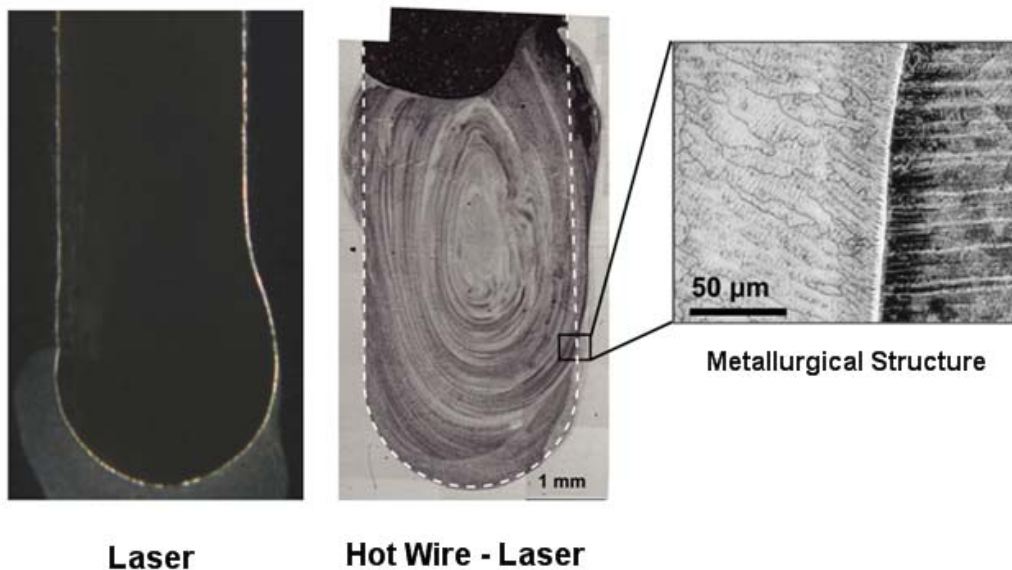


Fig. 3.13 Cross section views for varied the laser irradiation angle.

3.6 Mechanism of Weld Bead Formation

3.6.1 Weld Penetration Shape

Figure 3.14 shows the cross sections of the weld bead under the applied welding conditions. After welding, the cross sections of the weld beads produced only the laser without a filler wire and those produced with a hot wire laser were compared. The results reveal that the combined technique of using a preheating wire and defocused laser beam yielded a sound weld joint with a very low dilution rate of about 10.7%.



Laser power=3 kW, irradiation angle=5°, welding speed=0.5 m/min, wire feeding speed =6.0 m/min, wire feeding angle= 80°, wire feeding position= 2 mm, wire current= 125 A

Fig. 3.14 Comparison of the cross section images between laser and hot wire laser welding.

In the case of laser radiation without a filler wire, the base metal melts only at the bottom of the U-groove where it is directly irradiated by the laser beam. In contrast, in the case of the hot wire laser, the wall of the groove also melts, even though the laser beam does not irradiate on the wall directly. It was supposed that laser light reflected from the molten pool irradiated on the wall of the groove because a defocused laser was used in hot wire laser welding. Therefore, a particular experiment was carried out to investigate whether the reflected laser light can melt the wall of a groove.

3.6.2 Investigating the Effect of the Reflected Laser Irradiation

The phenomenon of the reflection of laser irradiation was investigated in order to clearly explain the formation of the weld bead, especially in terms of melting the side groove wall of the base metal. Figure 3.15 shows the experimental setup included a lap joint of mild steel plates with a thickness of 9 mm was provided to incline 45° from the horizontal, while the laser beam was applied to the other side as illustrated in Fig 3.15. In this case, the welding conditions are given in Table 3.4.

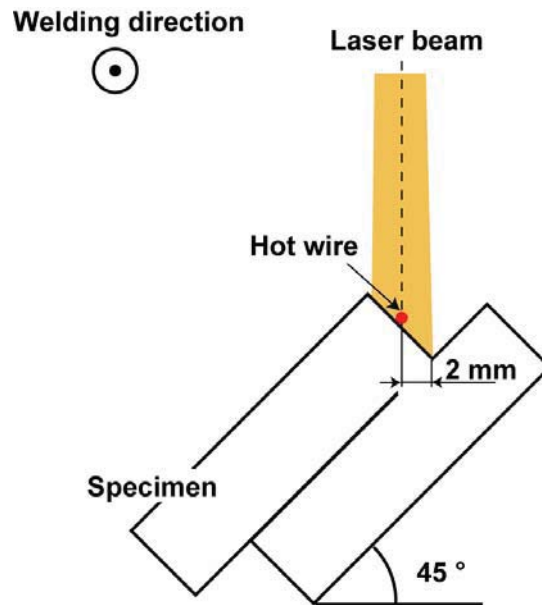


Fig. 3.15 Schematic illustration of the experimental setup for laser beam reflection.

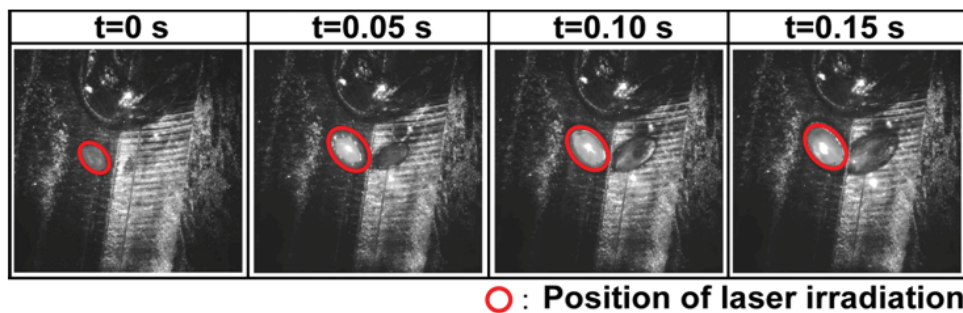
Table 3.4 Utilized welding parameters for the reflection of laser irradiation

Welding method	Hot wire laser	Laser
Laser power (kW)	3	3
Welding speed (m/min)	0.3	0.3
Laser spot diameter (mm)	4	4
Irradiation angle (deg.)	5	5
Wire feeding speed (m/min)	1.1	-
Wire feeding angle (deg.)	70	-
Wire feeding position (mm)	1.5	-
Wire current (A)	87	-

The experimental results revealed that reflection of the laser beam significantly affects the melting phenomenon especially on the wall of the groove. Figure 3.16 represents the sequential images during welding obtained by high speed camera. The different melting phenomena between only laser irradiation and laser with a feeding wire are compared. In the case of laser irradiation with the feeding of a hot wire shown in 3.17, the dotted line represents the melting region, it is observed that the indirect laser irradiation (the effect of laser light reflects from the weld pool) melts early on the area around the weld pool prior to

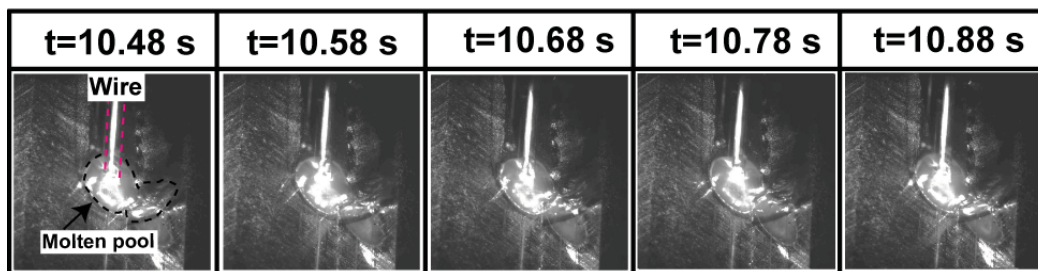
deposition by the liquid metal from the weld pool in the subsequent step. Additionally, the images of the microscale appearance and the weld bead cross section are examined, as presented in Fig. 3.18. It is seen that the metallurgical structure and wall shape is changed substantially. This is remarkable evidence explaining why the energy of scattering laser irradiation can increase the penetration depth at the groove side wall and the melting of the feeding wire in narrow-gap welding.

Mechanism of Weld Bead Formation



(a) Only laser radiation

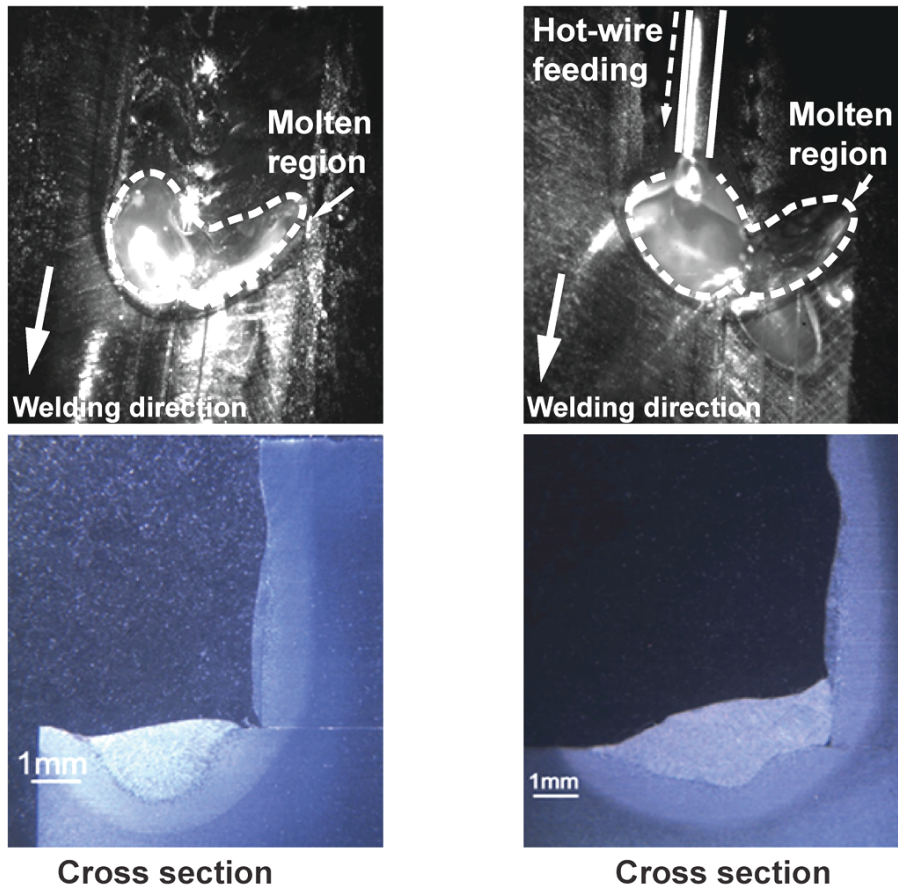
Laser power=3kW. Welding speed=0.3 m/min. Laser spot size=4 mm



(b) Laser welding with feeding of a hot-wire

Laser power=3kW, Welding speed=0.3 m/min, Laser spot size=4 mm,
Wire feeding speed=1.1 m/min, Wire current=87 A, Wire feeding angle=70°,
Wire feeding position=1.5 mm

Fig. 3.16 Images obtained by high speed camera.



(a) Only laser radiation.

(b) Hot wire Laser welding.

Fig. 3.17 Captured image of influence of laser beam reflection.

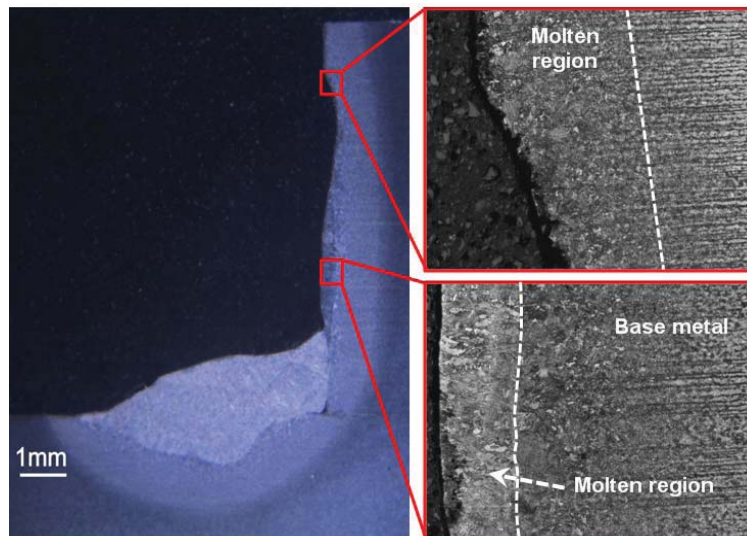


Fig. 3.18 Cross section images of sample welded by a laser with the feeding of filler metal.

3.7 Weld properties

3.7.1 Hardness profile

Figure 3.19 shows the Vickers hardness profile of the weld bead for a wire feeding angle of 80° , wire feeding position of 2 mm, and wire current of 125 A. The Vickers hardness was measured along the transverse direction of the weld bead at the center of the groove width. The test was performed under the applied load of 1 kgf for the dwell time of 10s. It is seen that the average hardness was around 200 HV, and there was no great difference in the distribution between the weld metal and base metal.

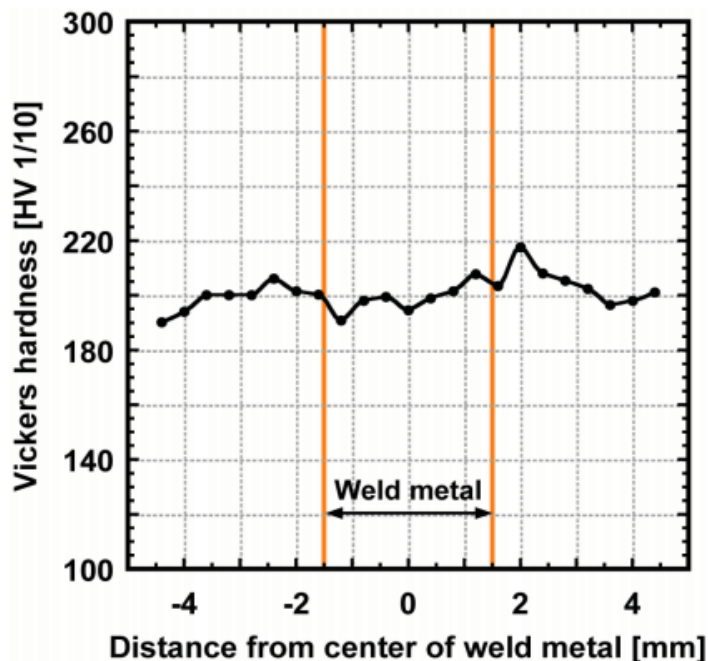
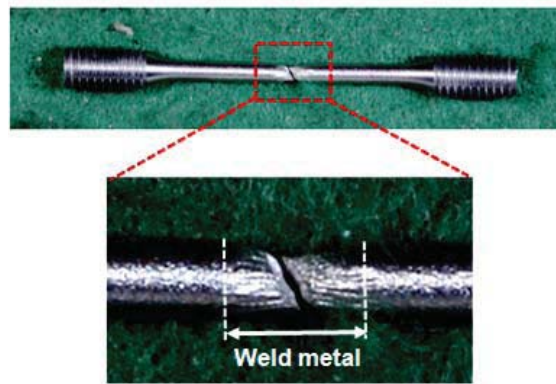


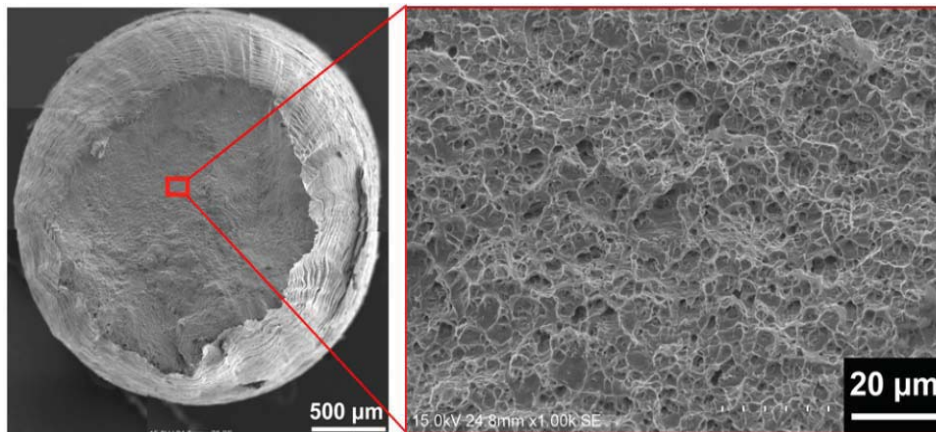
Fig. 3.19 Vickers hardness profile.

3.7.2 Tensile strength

To confirm the adequate strength at the fusion boundary in hot wire laser welding, a tensile test was carried out. A round specimen with a diameter of 3 mm taken from a welded test plate was used. Rupture occurred at the center of a specimen on the weld metal. Tensile strength was 640.5 MPa. In addition, a scanning electron microscope was employed to metallurgically examine the fracture surface and validate the weld metal location. Figure 3.20 shows the fracture surface of the specimen. Although fracture occurs at the weld metal, a dimpled fracture surface is visible and there are no defects on the surface. Therefore, it is evident that hot wire laser welding was capable of producing a strong weld joint at the fusion interface as good as the weld metal.



(a) Tested specimen



(b) Fracture surface

Fig. 3.20 Tensile testing.

3.8 Summary

On the basis of the principle of hot wire laser welding, hybrid technology has the strong potential to simultaneously optimize high efficiency and low heat input. The two merits improve capital productivity and efficiency, and affect material properties less when compared to conventional welding. Generally speaking, the hybrid technology is capable of not only low dilution and a narrow HAZ but also a sound weld with a high deposition rate. The results of this work show the potential of narrow-gap hot wire laser welding in terms of the melting phenomena in a weld pool and the following adequate characteristics.

1. The results thus seen indicated that the essential welding variables affecting the melting phenomena were the wire current, wire feeding position, and wire feeding angle. For a narrow-gap joint having a gap width of 3 mm, the complete deposition of the weld joint was achieved with adequate welding variables such as output laser power of 3 kW, spot size of 3 mm in diameter, laser irradiation

angle of 5°, welding speed of 0.5 m/min, wire feeding speed of 8.0 m/min, wire feeding angle of 80°, wire current of 137 A, and wire feeding position of 1 mm.

2. Welding phenomena of the hot wire laser process were observed in situ using a high-speed camera. The observations revealed that with the low energy density of a defocused laser beam and the pre-heated wire (hot wire) was highly efficient in producing a stable molten pool and excellent integrity of weld bead formation.

3. In addition, one unique feature for this process is the effect of laser beam reflection on a molten pool. The reflection of the laser beam had a substantial effect in melting the sidewall of a groove and nearby areas. For this reason, a low dilution ratio and little evolution of microstructure in the HAZ could be achieved.

4. In terms of the quality of joints, the adequacy of the strength at the fusion boundary was demonstrated in tensile testing. Employing a scanning electron microscope to inspect the metallurgical fracture surface confirmed that rupture occurred at the weld metal and there were no defects on the fusion boundary, even though the weld penetration depth was so small.

Chapter 4

Solidification cracking susceptibility of modified 9Cr1Mo steel in hot wire laser welding with a narrow gap joint

4.1 Introduction

One type of heat resistant steel, which is a potential candidate for application in elevated temperatures and with a better creep rupture strength than other ferritic CrMo steels is modified 9Cr1Mo steel, commonly known as grade 91 according to the ASTM standard [86-88]. This material is used for critical components such as pipes and tubes in a power generation plant [89-90].

In a boiler tube fabrication, an up-to-date process, which is efficiently employed to joint components, is narrow-gap welding. This method is attractive due to reducing large shrinkage and residual stress and improving productivity for joint preparation. Many studies have attempted the application of conventional welding processes with a narrow gap joint. Lower heat input energy is accomplished by a hot wire system which is designed to independently control the melting feed wire and the base metal. Nowadays, hot wire-GTAW is employed with a narrow gap joint in industries. However, such a method is still limited for high efficiency in process and production rates.

Consequently, modern technology of a hot wire laser welding process with a narrow groove is proposed in this thesis. This dominant hybrid process serves such requirements as fast welding speed, high weld deposition, low deformation as well as a low dilution ratio. Furthermore, the reflected laser beam on the molten pool heats and melts base material in front of the molten pool, thus, the dilution of base material can be reduced significantly (less than 10 %).

In addition to the capability of the hot wire laser process, the occurrence of solidification cracking is an important issue to be considered. There are many reports regarding the evaluation and the prevention of weld metal solidification cracking in heat resistant steels [90-96]. However, currently, there is only one report presenting the hot cracking susceptibility of modified 9Cr1Mo steel using a vareststraint test with arc welding, and suggests prevention of hot cracking by selecting appropriate filler wires in terms of the required chemical composition [22].

However, solidification cracking is substantially induced by different causes in a narrow gap joint welded with a hot wire laser process, especially from the viewpoint of mechanical factors. Therefore, this chapter regards the occurrence of solidification cracking of modified 9Cr1Mo steel due to the application of hot wire laser welding with a narrow gap joint. In order to understand thoroughly the causes associated with solidification cracking susceptibility, the important factors

were investigated experimentally, namely weld shape, size of groove width, laser spot shape, and welding with laser scanning.

4.2 Material and Specimen Used

Modified 9Cr1Mo material according to ASTM standard Grade 91 was used as a base metal welded with a filler wire; TG-S9Cb (KOBE steel manufacture), according to AWS classification A5.28 ER90S-G. The dimension of the test plate was 120 mm x 75 mm x 21 mm as shown in Figure 4.1. For narrow gap joint preparation, a U-shaped groove joint with 3, 4, and 5 mm in gap width was applied. A groove angle of 2.8° was provided. The diameter of the filler wire was 1.0 and 1.2 mm. The chemical compositions of each material are given in Table 4.1.

Table 4.1 Chemical composition of used materials (mass %)

Material	C	Si	Mn	P	S	Fe	Cr	Mo	Nb	V	Cu
Base metal : Modified 9Cr1Mo	0.01	0.37	0.43	0.014	0.002	Bal.	8.55	0.98	0.08	0.19	0.02
Filler wire : ER90S-G	0.08	0.12	1.02	0.005	0.004	Bal.	8.99	0.90	0.04	0.18	0.12

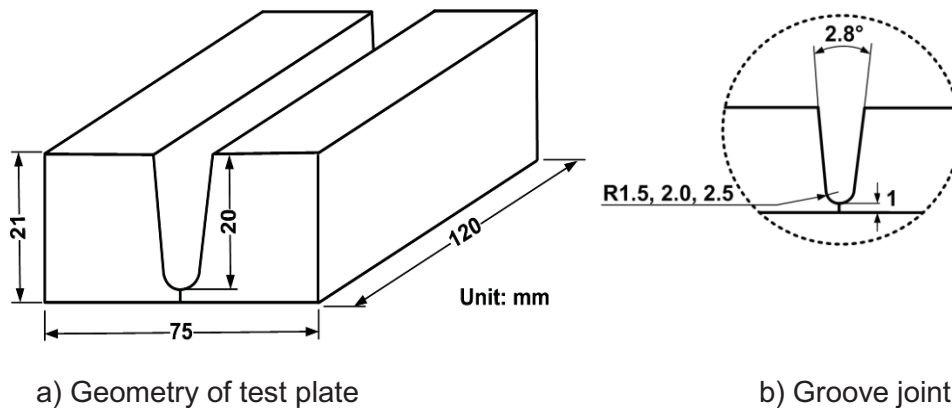


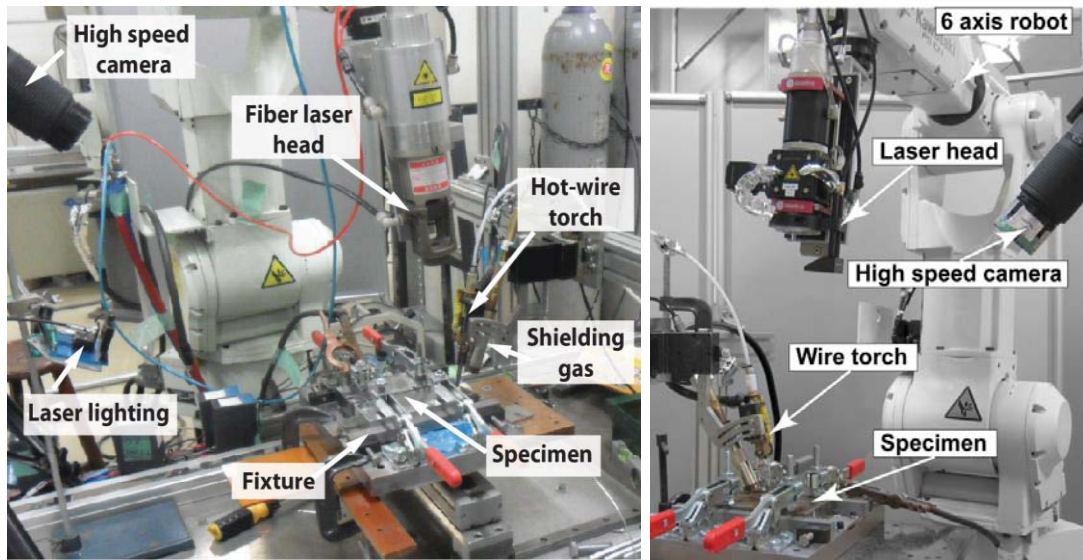
Fig. 4.1 Geometry of joint and test plate.

4.3 Experimental Procedure

4.3.1 Method and Equipment

In the present work, a hot wire laser welding process was incorporated to attain a sound weld in a narrow gap joint. Figure 4.2 shows the image of the experimental setup. The illustration of the essential welding variables related to the position and orientation of the filler wire and laser beam as presented in Fig. 4.3, namely the laser irradiation angle, wire feeding angle, and wire feeding position. Test plates were automatically welded using a Yb: YAG fiber laser power source with a six-axis robotic welder, and a hot wire feeding system. Laser beam characteristics consisted of the operating wavelength of 1070 nm, and the beam parameter product of the beam quality of 5.4 mm·mrad. Table 4.2 shows the welding conditions and gives the changes in wire current and wire feeding speeds in order to produce different rates of a weld deposition. Argon as a shielding gas was employed to protect from an undesired reaction with the outside atmosphere.

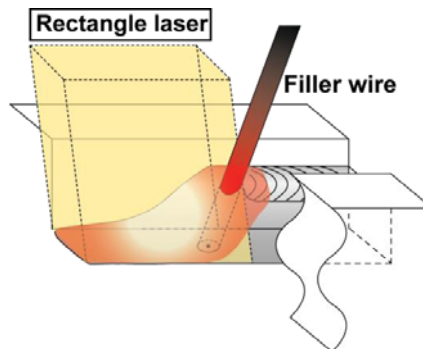
Solidification cracking susceptibility of modified 9Cr1Mo steel in
Hot wire laser welding with a narrow gap joint



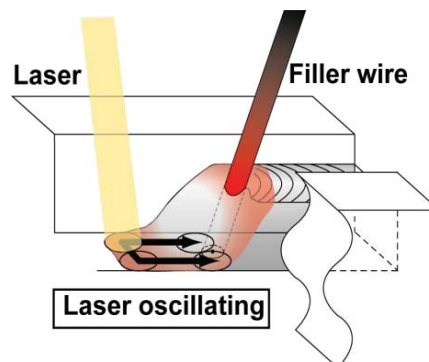
(a) Fiber laser

(b) Diode Laser (LD)

Fig. 4.2 Experimental setup of hot wire laser welding.

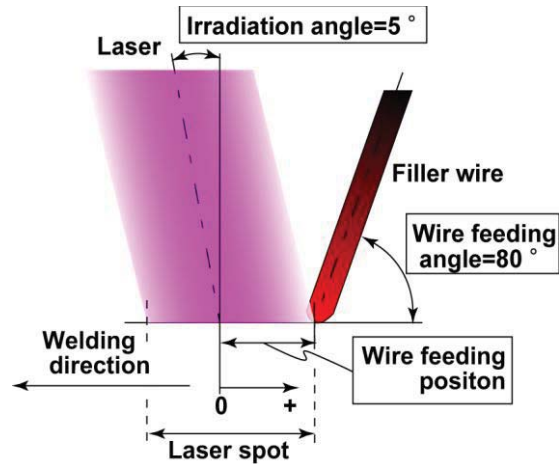


(a) Rectangle laser spot shape.



(b) Wobbling pattern of laser spot laser using scanning.

Fig. 4.3 Schematic illustrations of laser beam characteristic during welding.



(c) Positional relationships of the essential welding variables in the hot wire laser process.

Fig. 4.3 Schematic illustrations of laser beam characteristic during welding.
(Continue)

Table 4.2 Utilized welding parameters

Laser type	Fiber laser	Diode Laser
Laser power (kW)	3	3,5,6
Welding speed (m/min)	0.3,0.4	
Laser spot diameter (mm)	3, 4, 5	
Irradiation angle (deg.)	5	
Wire feeding speed (m/min)	2.3-6.8	
Wire feeding angle (deg.)	80	
Wire feeding position (mm)	-1,0,1,2	
Wire current (A)	65-118	
Argon shielding gas (l/min)	10-15	

The phenomenon of molten pool behavior and bead formation during welding was visually monitored by in-situ observation using a high-speed camera (FASTCAM-1024: Photron) located in front of the molten pool. Conditions of the in-situ observation, given in Table 4.3, were a frame rate of 250 fps and a shutter speed of 1/1000 s. Furthermore, the joint was illuminated with a lighting laser having a wavelength of 980 nm to acquire bright images. As for protecting the too strong laser irradiation reflected from the molten pool, a band pass filter (Band pass 10 nm FWHM 980-10) with a transmitted wavelength of 980 nm was installed with an optical lens. A protection lens was used on the outside filter against damage from spatter and metal vapor.

Table 4.3 Observation conditions of high-speed camera

Resolution (Pixel)	256x1024
Shutter speed (s)	1/1000-1/2000
Frame rate (fps)	250, 500, 2000
lighting laser (nm)	980
a band pass filter (nm)	980

4.3.2 Evaluation Method of Weld Cracking

Following this, welded specimens were sectioned transversely relative to the welding direction and prepared for metallurgical examination for an adequately sound weld and weld cracking. A cracking specimen was frozen by immersing in liquid nitrogen and broken to examine the fracture surface as illustrated in Fig. 4.4. The solidification cracking surface was confirmed by a scanning electron microscope. The relationship of the ratio of D/W on solidification cracking was studied. The solidification cracking surface was confirmed by a scanning electron microscope.

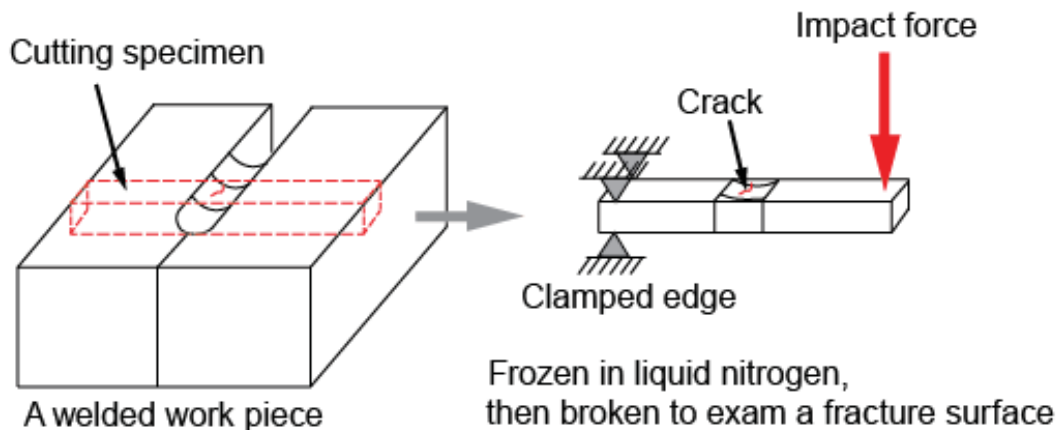


Fig. 4.4 Method of fracture surface observation.

The welded specimens were transversely cut in the welding direction. The cutting location was designated as illustrated in Fig.4.5. A metallurgical examination at the cross sections of weld bead was performed using an optical microscope. Cracks were observed and crack length was measured. Cracking ratio was defined in order to quantitatively evaluate weld cracking susceptibility. Cracking ratio is the relationship of the value of the penetration weld depth divided by a crack length as expressed in equation (4.1). An average value of five cross sections was used to evaluate the cracking ratio. Figure 4.6 presents a measurement of cracking ratio.

$$\text{Cracking Ratio} = \frac{\text{Crack length}}{\text{Penetration depth}} \times 100\% \quad (4.1)$$

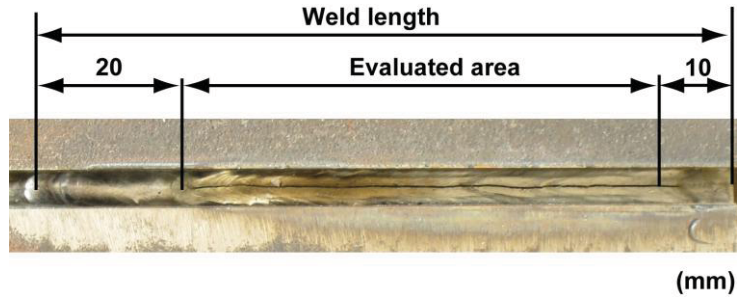


Fig. 4.5 Evaluated area of hot wire laser welding.

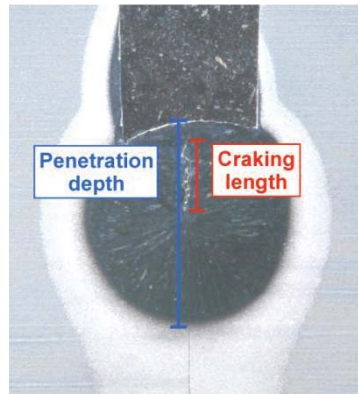


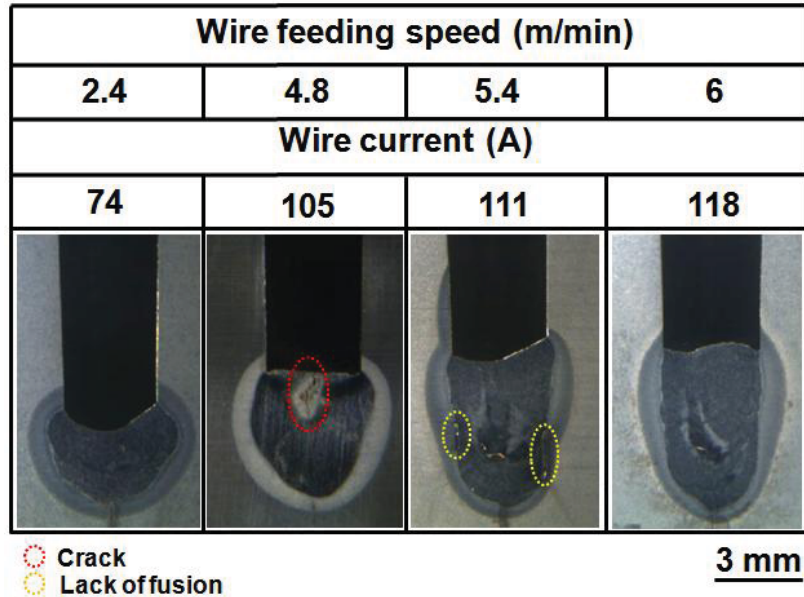
Fig. 4.6 Illustration of cracking ratio measurement.

4.4 The Investigation of the Occurrence of Solidification Cracking

4.4.1 Defects in Hot-wire Laser Welding with a Narrow Gap Joint

After hot wire laser welding of a single layer weld, the welded specimens were observed for an adequately sound weld and the types of discontinuity in the weld bead. The welded specimens were sectioned transversely relative to the welding direction and prepared for metallurgical examination. Figure 4.7 represents the cross sections of the weld beads depending on welding variables as a wire feeding speed and a wire current. Wire feeding speed varied from 2.4, 4.6, 5.4, and 6 m/min, while the wire current was set up as 74 A, 105 A, 111A, and 118 A, respectively.

**Solidification cracking susceptibility of modified 9Cr1Mo steel in
Hot wire laser welding with a narrow gap joint**

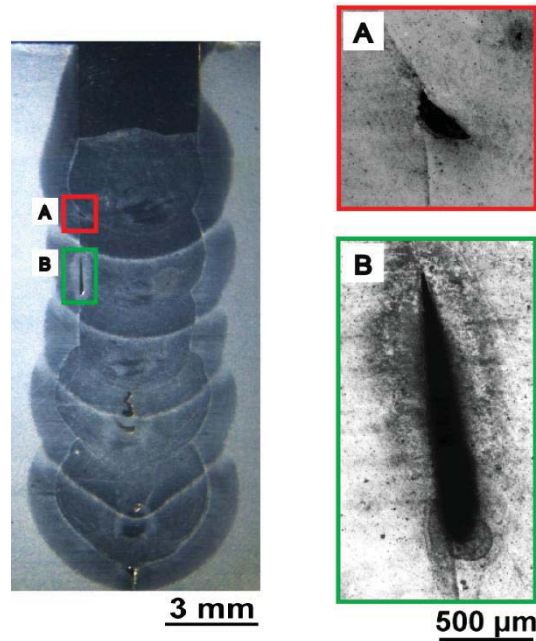


Fiber Laser power=3 kW, Spot type=Round, Groove width=3 mm, Welding speed=0.4 m/min, irradiation angle=5°, Wire feeding angle= 80°, Wire feeding position= 2 mm

Fig. 4.7 The occurrence of welding defects.

A higher weld deposition can be achieved with an increase in the wire feeding speed, while the wire current served a function as heating the temperature of a fed wire to be an adequate and stable melting before dipping into the molten pool. Particularly in the case of a wire feeding speed of 2.4 m/min and wire current of 74 A the cross section of a weld shows a lower bead height but deeper penetration in the sidewall. Conversely, a wire feeding speed of 6 m/min and wire current of 118 A shows a higher weld bead height with a little penetration of fusion.

However, defects in welds were found. The defects can be mainly classified into two types, namely crack, and lack of fusion. In Fig. 4.7 the red dash line shows the center line cracking at the wire feeding speed of 4.8 m/min and the yellow dash line indicates the lack of fusion at the side wall when the wire feeding speed increases up to be 5.8 m/min. Also, the multiple-pass welding with five layers was performed with welding conditions included laser power output of 3 kW, groove width of 3 mm, filler wire diameter of 1.0 mm, welding speed of 0.3 m/min, wire feeding speed of 3.6 m/min, and wire current of 81 A. The multi-pass welds were inspected in the macro-sectional weld as shown in Fig. 4.8. The enlarged images of defects are further presented as Fig. 4.8 (a) and (b). As a result, the lack of fusion can occur at the sidewall of grooves and between layer number 4 and 5.



Fiber Laser power=3 kW, Spot type=Round, Groove width=3 mm, Welding speed=0.3 m/min, Wire feeding speed=3.6 m/min, Wire current=81 A, irradiation angle=5°, Wire feeding angle= 80°, Wire feeding position= 2 mm, Layer number=5 layers

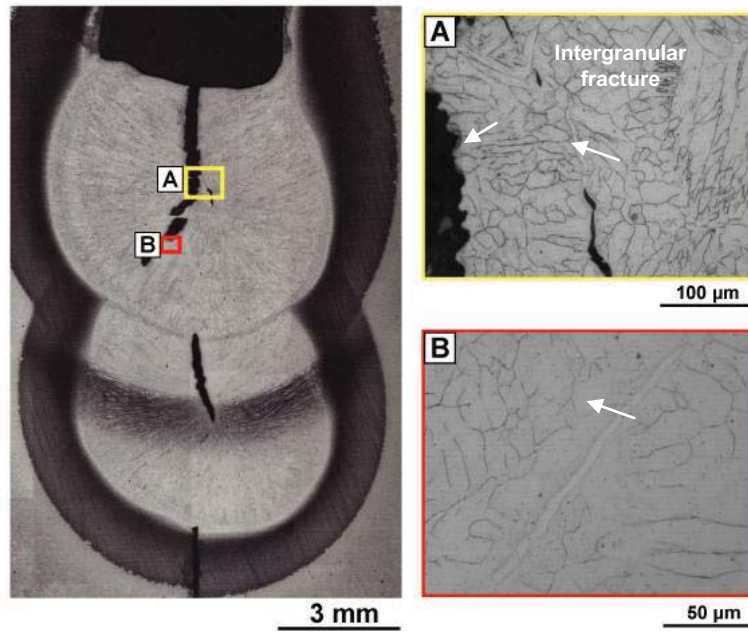
Fig. 4.8 Lack of fusion in multiple-pass welding.

4.4.2 Identification of Solidification Cracking

From the previous sections, in order to make clear the kind of cracking in modified 9Cr1Mo steel from hot wire laser welding with a narrow gap joint the cracks in welds were observed in the metallurgical structure. Figure 4.9 presents the enlarged images of a cracking weld in two layers. Cracking substantially arose in the center of the weld bead. The zigzag shape or intergranular fracture took place along the grain boundary as seen in Fig. 4.9 (a) and also the fissure cracks evenly distributed around main fracture. Furthermore, Fig. 4.9 (b) shows the trace evidence of a remaining structure between grain boundaries during solidification, where it seems to affect cracking.

Figure 4.10 (a) presents the cross-section of a weld bead with a crack and (b) higher magnified views examined by a scanning electron microscope. The microstructure of the fusion zone of cracking surface as Figure 4.10 (c) shows a dendritic fracture surface, this is regarded as solidification cracking.

Solidification cracking susceptibility of modified 9Cr1Mo steel in Hot wire laser welding with a narrow gap joint



Groove width=3 mm, Laser type=LD laser, Spot type=Round, Laser power=6 kW
 Welding speed=0.3 m/min, Wire feeding speed=5.3m/min, Wire feeding angle=80°,
 Irradiation angle=5°, Wire feeding position=2 mm, Wire current=109 A,
 Layer number=2 layers

Fig. 4.9 Macro and microstructure close to a crack.

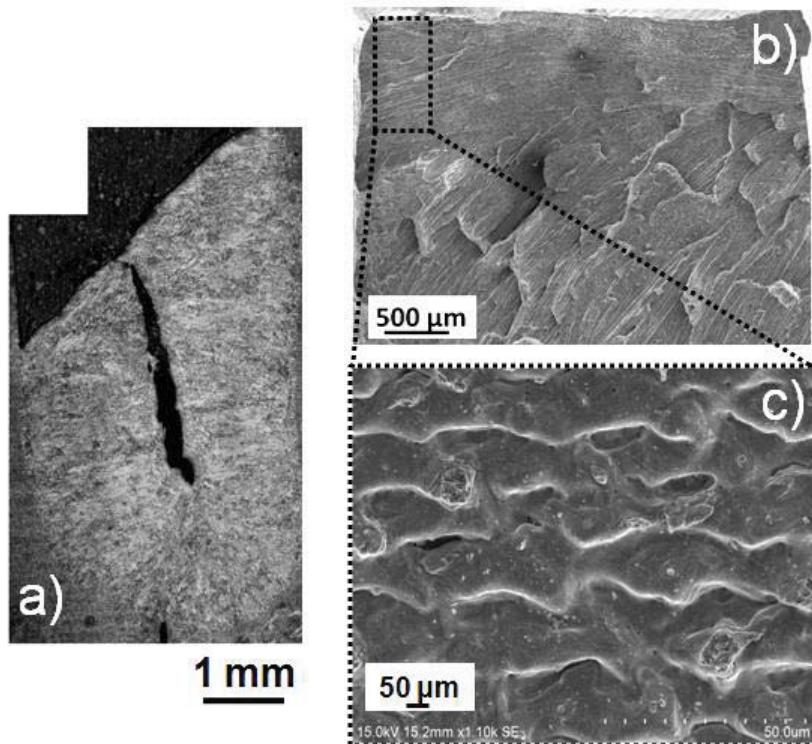


Fig. 4.10 Fracture surface observation.

4.5 Solidification Cracking Susceptibility in Modified 9Cr1Mo Steel

4.5.1 The Effect of Depth to Width Ratio (D/W)

In this part, the various weld shapes with single layer were built up by hot wire laser welding. The wire feeding speed was adjusted to achieve different deposition rates and bead height. Welding conditions mainly included fiber laser power of 3 kW, welding speed of 0.3 m/min, wire feeding angle of 80° , wire feeding point of 2 mm. Groove width of 3 mm was applied. As a result, it was found that hot wire laser welding with a narrow gap joint for modified 9Cr1Mo steel could produce various weld shapes. The relation to the variation of weld shapes in terms of D/W ratios was investigated to evaluate the susceptibility of solidification cracking. Figure 4.11 presents the relationship between the occurrences of solidification cracking and D/W ratios. The red-cross marks show cracking conditions and the blue dot marks indicate no cracking. From the results, it was revealed that solidification cracking occurred in the case of a D/W ratio higher than 0.6. Nevertheless, solidification cracking did not occur especially when the D/W ratio was more than 1.2.

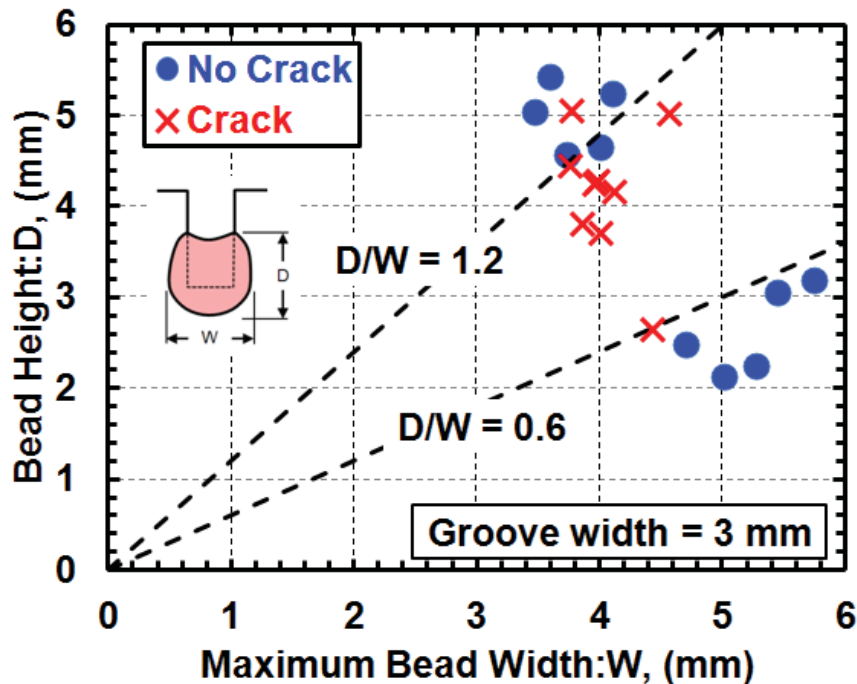


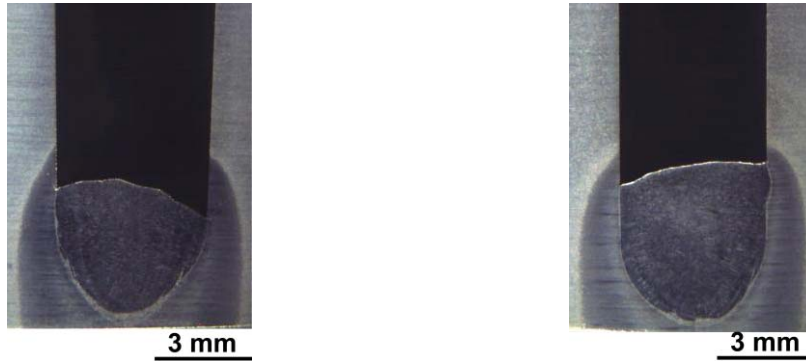
Fig. 4.11 Relationship between D/W and susceptibility of solidification cracking.

4.5.2 The Effect of Groove Width Size

As the previous results revealed, with a groove width of 3 mm with D/W ratio between 0.6 and 1.2 solidification cracking occurred. However, in order to make clear the effect of the size of the groove width on solidification cracking, a specimen with a groove width of 5 mm was employed to build up the different weld shapes in the same D/W range as the groove width of 3 mm, namely D/W between 0.6 and 1.2. Figure 4.12 represents the images of cross section weld beads with a groove width of 5 mm in single layer. It is noted that the cracking does not occur in welds. In addition, Fig. 4.13 shows the comparison of solidification cracking between a groove width of 3 mm and 5 mm. The green

Solidification cracking susceptibility of modified 9Cr1Mo steel in
Hot wire laser welding with a narrow gap joint

triangle marks indicate no cracking in the groove width of 5 mm. As a result, it is obvious that hot wire laser welding with a groove width of 5 mm does not contribute to solidification cracking.



(a) Wire feeding speed =3.6 m/min, Wire current=96 A
(b) Wire feeding speed =4.8 m/min, Wire current=107 A

Groove width=5 mm, Laser type=Fiber laser, Spot type=Round, Laser power=3 kW
Welding speed=0.3 m/min, Wire feeding angle=80°, Irradiation angle=5°,
Wire feeding position =2 mm

Fig. 4.12 Cross section weld bead with a groove width of 5 mm.

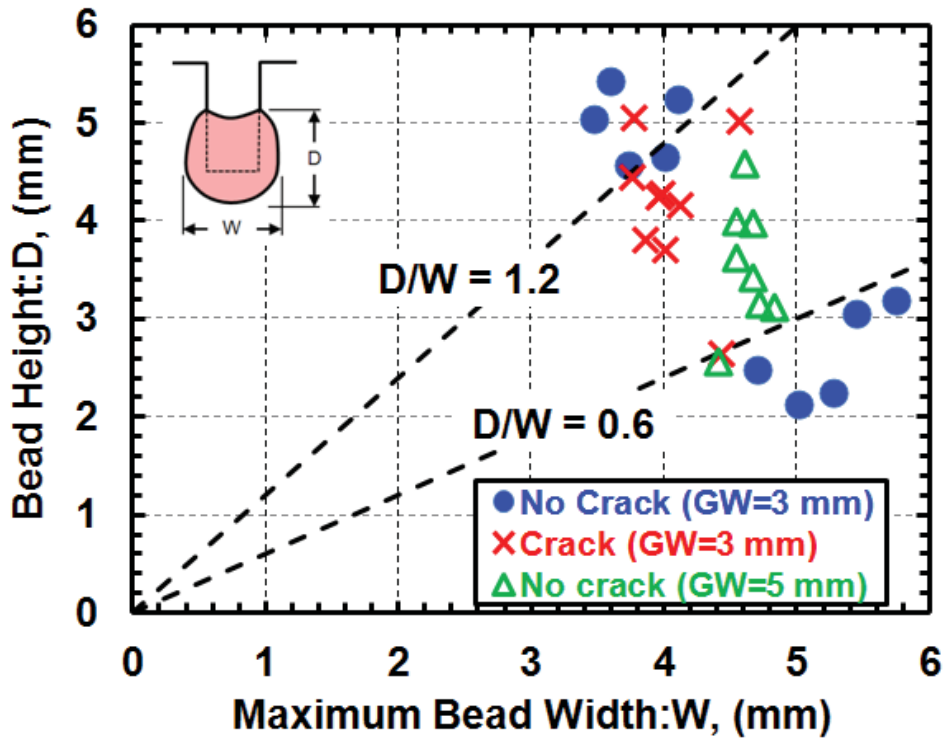


Fig. 4.13 Relationship between D/W and susceptibility of solidification cracking, Groove width (GW) = 3, 5 mm.

4.5.3 The Effect of a Laser Spot Shape

It is generally well known that the amount of heat input relates to solidification cracking, as well as a weld bead shape. In laser welding, a laser beam is able to form in different shapes even though the same heat input is applied. The diverse shapes of a laser beam contribute to different heat energy densities. In this part, three different shapes of a laser beam were applied to investigate its effect on solidification cracking, namely a round spot of 4 mm in diameter, a rectangular spot of 4x11mm and a longer rectangular spot of 4x17 mm. The same laser power of 6 kW was employed in all cases. Table 4.4 shows laser beam shapes used and a calculated energy density. It can be seen that the bigger laser spot area has a decreasing power density.

Table 4.4 Energy density in each laser beam shape


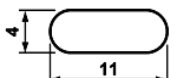
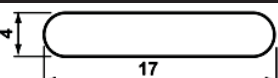
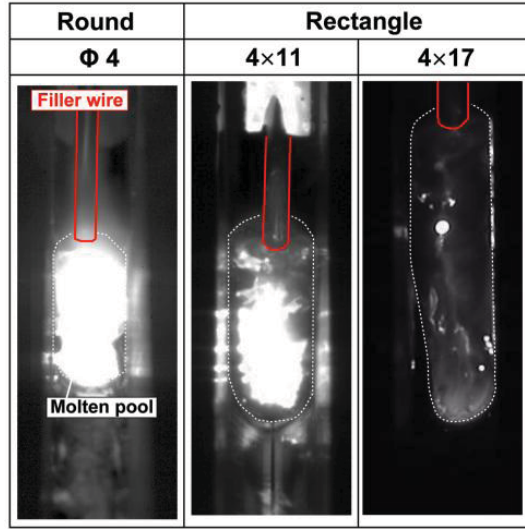
Laser beam shape (mm)	Laser spot area (mm ²)	Laser power (kW)	Power density (kW/mm ²)
	12.6	6	0.477
	40.6	6	0.148
	64.6	6	0.093

Figure 4.14 represents the comparison of the molten pool images in each spot shape, captured by high-speed camera. It is obvious that the molten pool length increases with a longer laser spot shape. The cross sectional welds were examined in order to observe solidification cracking as shown in Fig. 4.15. When comparing between the laser spot shapes, it is found that the rectangle laser beam can provide a smaller weld penetration. In quantitative evaluation to solidification cracking, Fig. 4.16 shows the comparison of cracking ratio between laser spot shapes. As a result, it reveals that the cracking ratio of a first weld pass is 30-40 % and two-weld pass welding is 40-50%. With similar welding conditions, there is insignificant difference of cracking ratio due to the kind of a laser spot shape.

However, a rectangle laser spot of 4x11 mm, a wire feeding position of -1 and +1 mm was applied as illustrated in Fig. 4.17. When the cross sectional welds were observed as shown in Fig. 4.18, solidification cracking occurs at the center weld observed in the case of a wire feeding position of -1 mm. Weld shape in the term of D/W is 1.33 with a crack length of 2.9 mm. In case of a wire feeding position of +1 mm, it is found that it is able to provide a smaller cracking length than a wire feeding position of -1 mm. There is D/W ratio of 1.52 with a crack length of 0.7 mm.

Solidification cracking susceptibility of modified 9Cr1Mo steel in Hot wire laser welding with a narrow gap joint



Groove width=4 mm, Laser type: LD laser, Spot type: Round Φ4 (Lens: f: 400), Rectangle 4X11 (Lens: f: 400, Beam-homoginizer: LL6), Rectangle 4X17 (Lens: f: 400, Beam-homoginizer: LL4), Defocus=0 mm, Laser power=6 kW, Welding speed=0.3 m/min, Wire feeding angle=80°, Irradiation angle=5°, Wire feeding position = -1, 0, +2 mm, Wire feeding speed=4.2 m/min, Wire current=96 A

Fig. 4.14 Image captures of a molten pool in each spot shape.

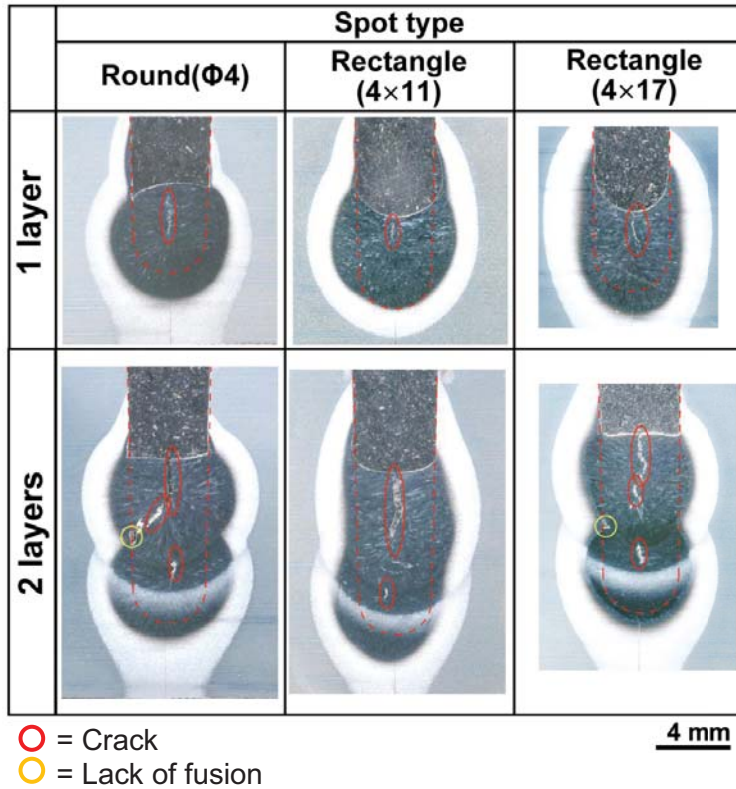


Fig. 4.15 Comparison of cross-sectional welds in each laser spot shape.

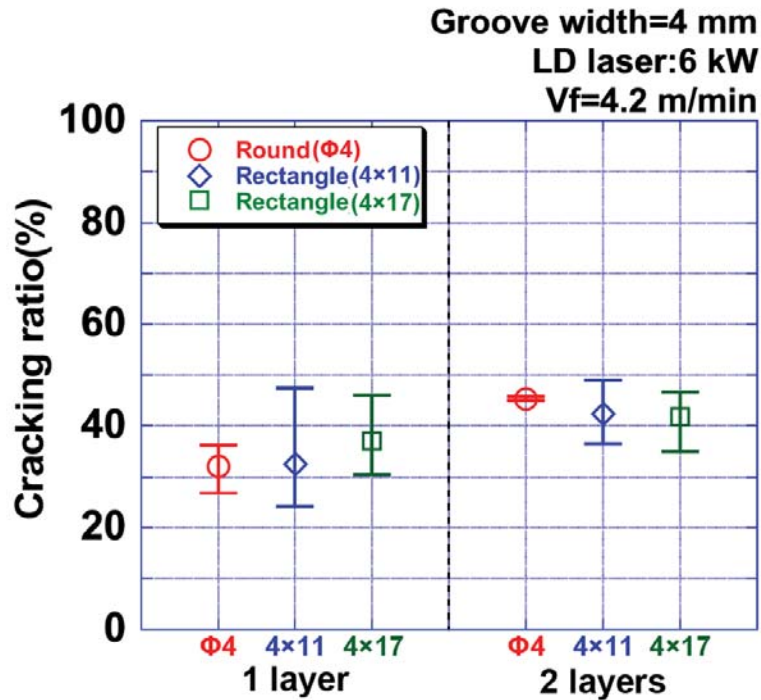


Fig. 4.16 Relationship between cracking ratio and laser beam shapes.

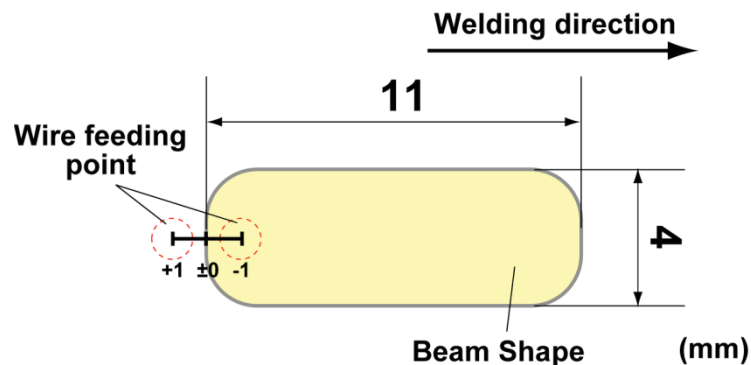
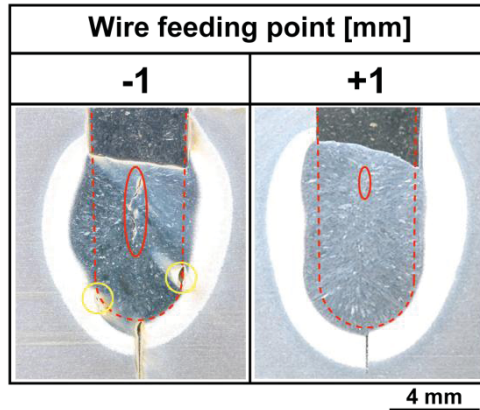


Fig. 4.17 Wire feeding position with a rectangle laser spot.

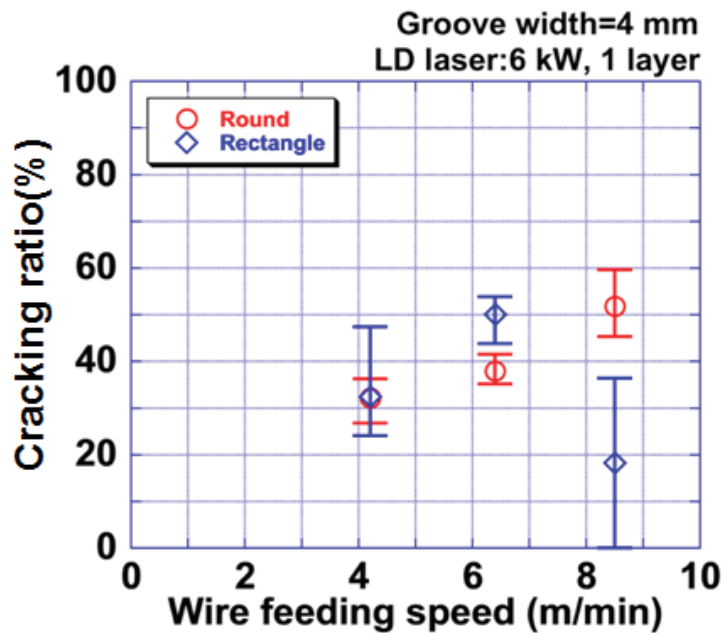
Figure 4.19 exhibits the comparison of cracking ratio in the first weld pass between cracking ratio and wire feeding speed. The different weld bead height was provided with a variety of wire feeding speeds. When the wire feeding speed increases up to 8.5 m/min, it is found that the rectangle laser spot can reduce solidification crack length substantially, which is smaller than the round laser spot. Also, as in Fig. 4.20, in the case of welding with two weld layers exhibits the rectangle laser spot has a potential to significantly decrease the cracking ratio with a wire feeding speed of 6.5 m/min. As a result, it indicates that the rectangle laser spot is rationally suitable to decrease solidification cracking.

Solidification cracking susceptibility of modified 9Cr1Mo steel in Hot wire laser welding with a narrow gap joint



Groove width=4 mm, Laser type: LD laser, Spot type: Rectangle 4 × 11 (Lens: f: 400, Beam-homoginizer: LL6), Defocus=0 mm, Laser power=6 kW, Welding speed=0.3 m/min, Wire feeding speed=8.5 m/min, Wire feeding angle=80°, Irradiation angle=5°, Wire current=108, 133 A, 1 layer

Fig. 4.18 Cross-sectional welds when using a wire feeding position of -1, and +1 mm.



Groove width=4 mm, Laser type: LD laser Spot, type: Round, Rectangle (4×11), Laser power= 6 kW, Welding speed=0.3 m/min, Wire feeding angle=80°, Wire feeding position=-1, 0, +2, +1 mm, Wire current=96, 108, 123 A

Fig. 4.19 Comparison of a cracking ratio between a laser spot shapes and a wire feeding speed. (One weld layer)

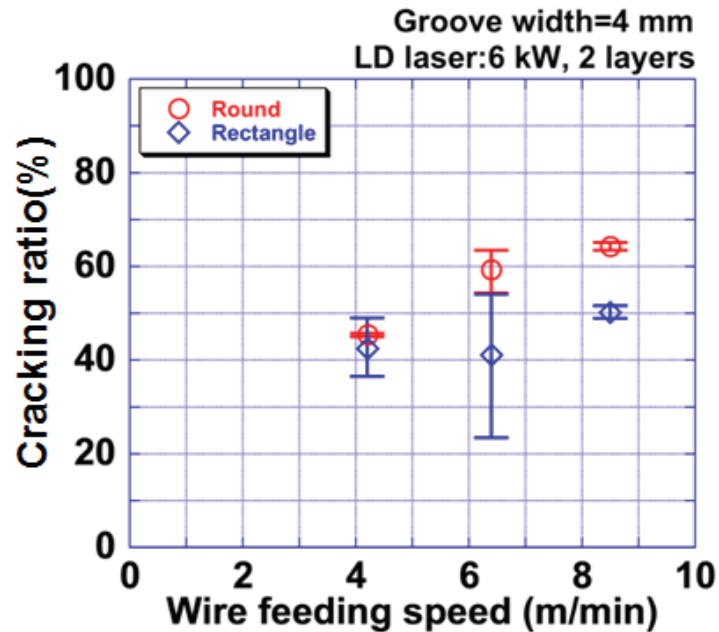


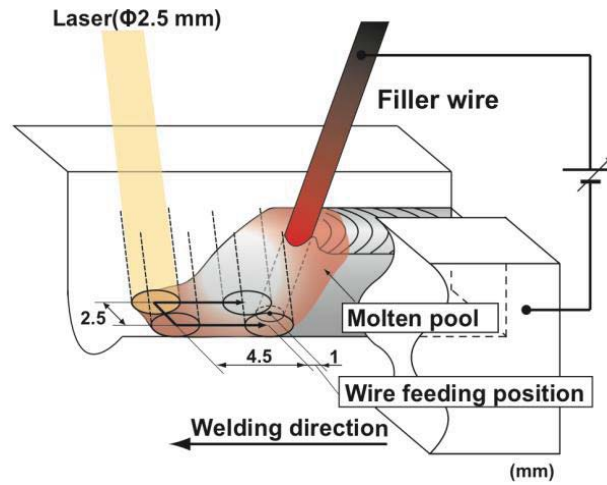
Fig. 4.20 Comparison of a cracking ratio between a laser spot shapes and a wire feeding speed. (Two weld layers)

4.5.4 Hot wire laser welding with laser scanning

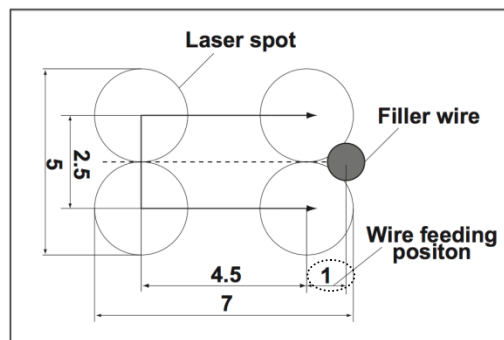
In this part, the hot wire laser welding method using a laser scanner system was proposed and applied to a thick narrow-gap joint in order to obtain a welded joint without lack of fusion defects between layers by relatively low laser power. The observation of welding phenomena using the laser scanning and mechanical property evaluations for the weld joint were carried out. A specimen 50 mm thick with a U-shape groove having a 2.8° groove angle and a 47 mm groove depth was employed. Groove width was 5 mm. Welding conditions are shown in Table 4.3. A disc laser oscillator was used as a main heat source. Laser power was 3 kW and laser spot diameter was 2.5 mm. Figure 4.21 shows a schematic illustration of the experimental setup and the scanning method.

Table 4.3 Utilized welding parameters for welding with laser scanning

Laser power (kW)	3
Laser spot diameter (mm)	2.5
Scanning shape (mm)	U (2.5x4.5)
Scanning speed (mm/s)	200
Welding speed (m/min)	0.3
Wire feeding angle (deg.)	80
Wire feeding position (mm)	1
Wire feeding speed (m/min)	4.8
Wire current (A)	66
Argon shielding gas (l/min)	10



(a) Hot wire laser welding with laser scanning.



(b) Scanning pattern and wire feeding position

Fig. 4.21 Schematic illustration of hot wire laser welding with laser scanning.

Figure 4.22 shows the molten pool images during the half-scanning cycle by a high-speed camera. The white solid line and white broken line indicates a filler wire and molten pool respectively. The bright laser spot on the molten pool surface moved in a U-shape path. The images clearly show that laser scanning creates the growth of the molten pool in front toward the sidewall. The bead surface shape was also improved from a convex shape to a concave shape.

Figure 4.23 represents the cross section of the welded joint with the laser scanning method. This joint has 23 layers in the 47 mm groove depth. It is obvious that there is no solidification cracking and the lack of fusion between layers became smaller than that without laser scanning. The quite narrow heat-affected zone (HAZ), (about 2 mm width), was achieved. Moreover, a stable and small penetration to the sidewall was obtained.

As a result, it was considered that the laser scanning method contributed to reducing the solidification cracking. Some lack of fusion defects remains between

**Solidification cracking susceptibility of modified 9Cr1Mo steel in
Hot wire laser welding with a narrow gap joint**

layers, however; such welding defects will be reduced by promoting penetration into the sidewall with a higher laser power and optimum laser-scanning pattern.

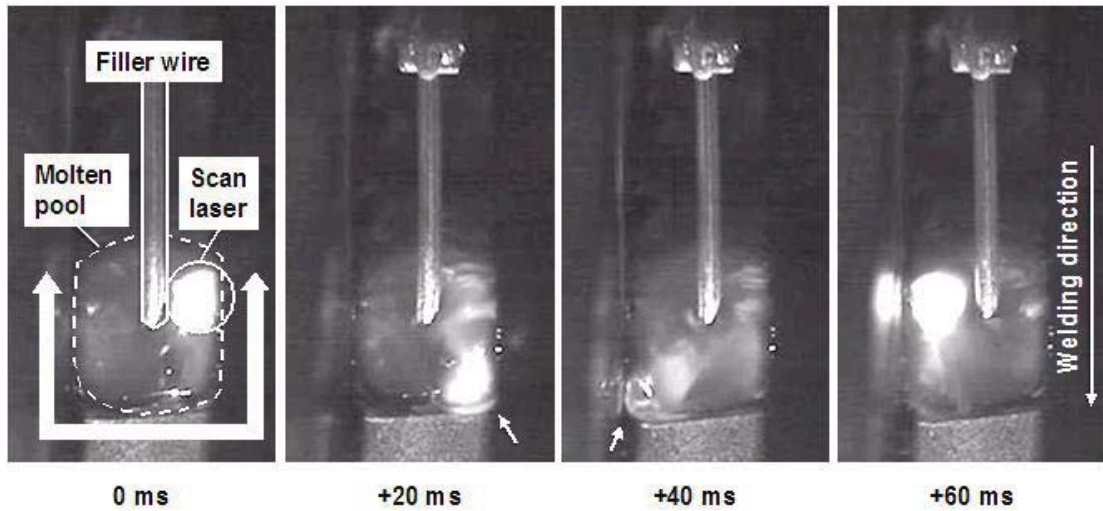


Fig.4. 22 High speed camera image during hot wire laser welding with laser scanning method

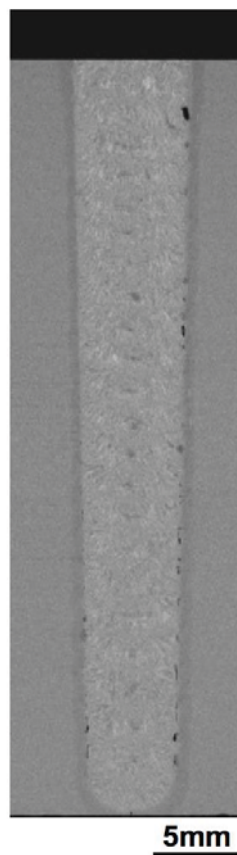


Fig. 4.23 Cross sectional weld produced by hot wire laser welding using laser scanning method.

4.6 Mechanical Properties Evaluation for Welded Joint

Hot wire laser welding using the laser scanner system, a tensile test, and creep rupture test were carried out. The tensile test was performed at room temperature (23 °C) and 600 °C. The specimens after the tensile test are shown in Fig. 2.24. The specimens of both testing temperature conditions fractured in the base metal region. The welded joint had good tensile strength.

The creep rupture test was carried out under the following three conditions: 160 MPa, 140 MPa at 600 °C and 80 MPa at 650 °C. The test specimens were machined from the region without defects of the welded joint. The tested specimens were shown in Fig.2.25. Two specimens under the conditions of 160 MPa at 600 °C and 80 MPa at 650 °C ruptured in the HAZ in about 900 hr. One specimen under conditions of 140 MPa at 600 °C did not rupture in 1800 h. All specimens fractured at HAZ whose width was about 2 mm.

Figure 2.26 shows the test result with reference data of conventional arc welded joints [28]. The results of creep rupture tests showed that the welded joint produced by the proposed hot-wire laser welding process using the laser scanning method had equal or higher creep rupture strength compared with that of conventional arc welded joints. It was thought that the lower heat input contributed to narrow softened zone in HAZ and sequentially good creep strength.



(a) Test at R.T(23 °C).



(b) Test at 600 °C.

Fig. 2.24 Specimens after Tensile Test.

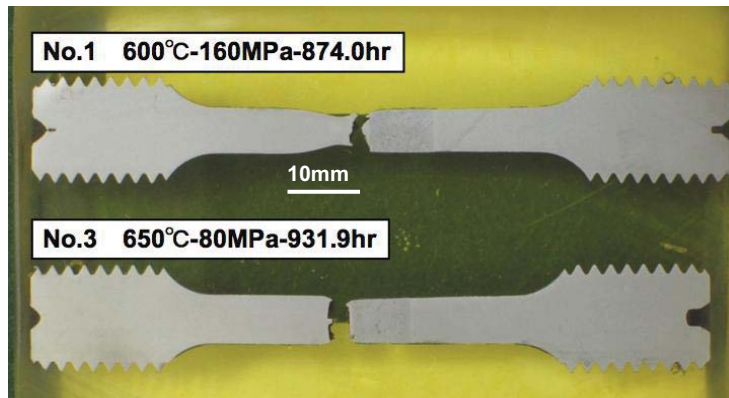


Fig. 25 Specimens after Creep Rupture Test.

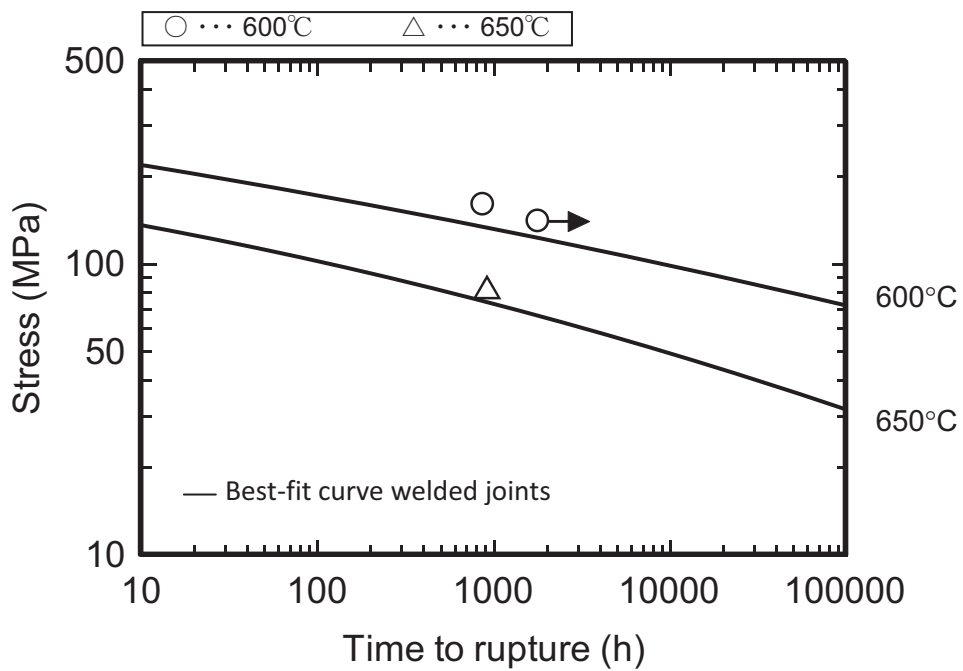


Fig. 2.26 Creep Rupture Test Results with Reference Data [28].

4.7 Summary

This chapter addressed investigating solidification cracking susceptibility of modified 9Cr1Mo steel in a narrow-gap joint using hot wire laser welding.

Conclusions can be drawn as follows:

1. The defects during hot wire laser welding with a narrow gap joint are mainly divided into the solidification cracking at the center weld and the lack of sidewall fusion. Particular in the occurrence of solidification cracking was confirmed by metallurgical fracture surface. The lack of sidewall fusion was caused by inadequate heat input.

2. It was found that welding variables including a wire current and a wire feeding speed affected adequate weld shape and deposition. A hot wire laser welding process was able to produce a special weld shape without solidification cracking at a higher D/W ratio. This was particularly noted in the case of a D/W ratio greater than 1.2 and less than 0.6; solidification cracking did not occur with a groove width of 3 mm.

3. The effect of a groove width on the tendency of solidification cracking exhibits that having the possibility to apply such a process in an ultra narrow gap application is favorable. However, it is prone to solidification cracking in the range of D/W between 0.6 and 1.2 with groove width of 3 mm. In contrast, groove width of 5 mm does not.

4. According to the effect of a laser beam shape, a round and a rectangle laser spot were applied. As a result, it revealed that a rectangle laser spot of 4x11 mm, which is a lower power density, is mainly effective to reduce the cracking ratio of solidification cracking.

5. The hot wire laser welding process with laser scanning method under the conditions that travel speed was 0.3 m/min produced narrow-gap welded joint and welding layers were 23 for 50mm thick plate. The laser scanning method contributed to the formation of a concave bead surface and free solidification cracking. However, a small lack of fusion between layers remained. Such welding defects will be reduced by promoting penetration into the sidewall with a higher laser power and optimum laser-scanning pattern.

6. The tensile tests showed that the welded joints made by hot wire laser welding had sufficient joint strength and the creep rupture tests showed that the welded joints had equal or higher creep strength compared with that of conventional arc welded joints. It was thought that the lower heat input contributed to a narrow softened zone in HAZ and sequentially good creep strength.

Chapter 5

Evaluation of solidification cracking susceptibility of cast steel welds for large scale parts on construction machinery using U-groove weld cracking test with a GMAW process

5.1 Introduction

In heavy construction machinery, large scale cast steel is beneficial to complex shaped parts with high strength properties. Such components are effectively fabricated by narrow gap welding for higher productivity. Narrow gap welding provides low heat input, smaller deposited metal volume and less deformation; however, the cast steel contains a large amount of carbon. It is possible to induce weld cracking particularly in heavy thick plate with a narrow groove. In practice, cracks usually occur at the first root pass in weld metal.

This chapter describes the investigation of weld cracking in large-scale cast steel parts with a heavy thickness for construction machinery. This work attempts to make clear the crucial causes of cracking, as well as prevention. A U-groove weld cracking test was carried out in order to reproduce the first pass-weld cracking in heavy thick plate. The same welding conditions as in practical work were reproduced.

After the completion of welding, the type of cracking such as solidification cracking and clod cracking was examined by metallurgical fracture surface. Weld cracking susceptibility was evaluated quantitatively in terms of cracking ratio. The influence factors to induce cracking were investigated such as a degree of constraint, root gap width, different filler wires and their hardness profiles, and preheating. Then, suggestions practical use for avoiding solidification cracking was proposed.

5.2 Material Used

The material used in this study is typical cast steel of SCMn3B. This base metal is welded by two kinds of high strength filler wire as JIS Z 3312 G69A3UMN4M3 (G69A3UMN4M3) and JIS Z 3312 YGW-11 (YGW-11). Table 5.1 shows chemical composition and mechanical properties of each material.

Table 5.1 Chemical composition of used materials (mass %) and mechanical properties

Material	C	Si	Mn	P	S	Ni	Cr	Mo	Cu	V	0.2%yield strength (MPa)	Tensile strength (MPa)
SCMn3B	0.32	0.43	1.17	0.027	0.009	0.05	0.11	0.01	0.1	-	490	690
G69A3UMN4M3	0.07	0.33	1.11	0.010	0.005	1.77	-	0.44	-	0.44	660	740
YGW-11	0.02	0.55	1.40	0.030	0.030	-	-	-	0.5	-	490	580

5.3 U-Groove Weld Cracking Test

5.3.1 Method and Specimen

A U-groove weld cracking test in accordance with JIS Z 3157 standard was carried out. SCMn3B steel was used as a specimen. A dimension of the specimen as shown in Fig. 5.1 was a 150 x 200 x 80 mm, U-shape groove with a radius of 6 mm, a groove angle of 20°, a root gap of 0 mm and 2 mm. In order to study the influence of the constraint conditions during welding, specimen geometry was divided into two types of constraint conditions; full constrain and spot constrain as illustrated in Fig 5.1(a) and (b). Two kinds of high strength filler wire were used to compare for weldability, namely JIS Z 3312 G69A3UMN4M3T and JIS Z 3312 YGW-11. GMAW with Ar-20%CO₂ shielding gas was automatically operated by robotic welder (KOBELCO manufacture, ARCMAN-RON). Welding conditions as given in Table 5.2 were set to an arc current of 280 A, arc voltage of 29 V, a welding speed of 0.22 m/min, a filler wire diameter of 1.2 mm, a feeding speed of 8 m/min, weaving width of 6 mm, and weaving frequency of 1 Hz. Local preheating temperature of 200 °C to avoid cold cracking was carried out by a gas burner. Temperature was monitored by a radiation thermometer.

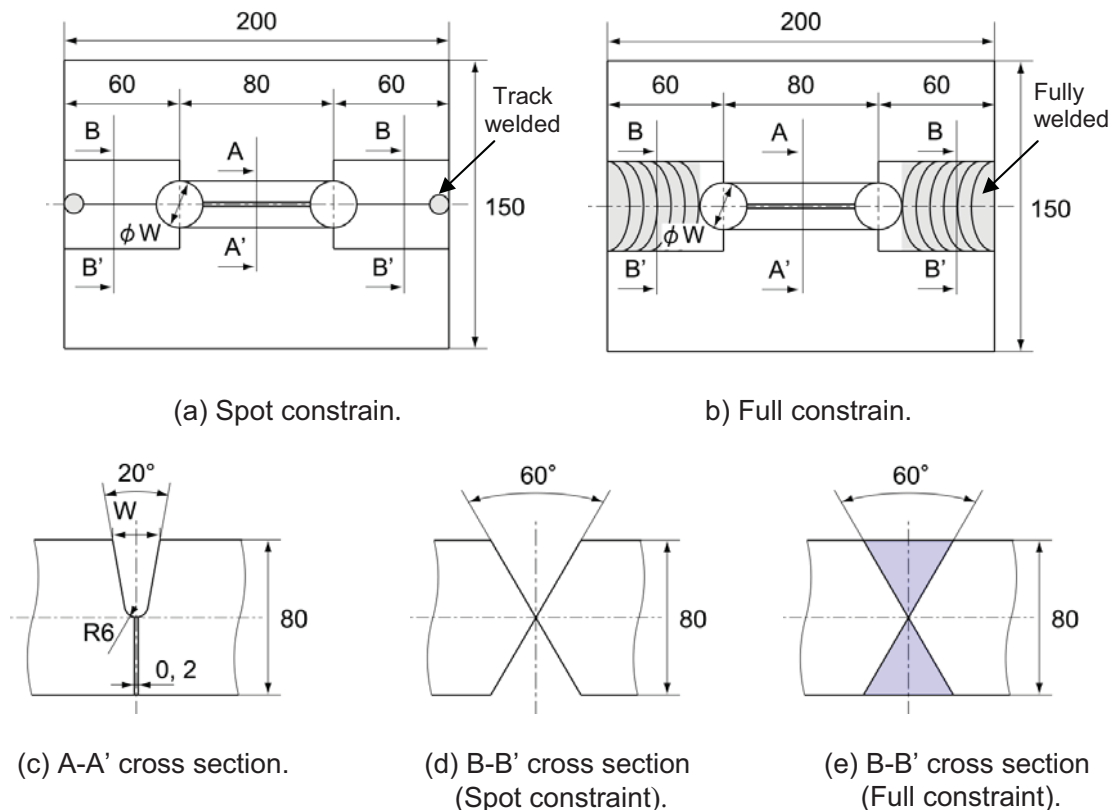


Fig. 5.1 Specimen geometry of U-groove weld cracking test.

Table 5.2 Utilized welding parameters

Arc current, A	280
Arc voltage, V	29
Welding speed (m/min.)	0.22
Wire feeding speed (m/min.)	8
Weaving width, mm	6
Weaving frequency, Hz	1
Preheat temperature (°C)	0, 200

5.3.2 Evaluation Method of Weld Cracking

The welded specimens were transversely cut in the welding direction. The cutting location was designated for five positions at intervals of 5 mm from the rear of the weld crater as illustrated in Fig.5.2. After cutting, the cross sections of weld bead specimens were polished by an emery paper from No. 200 until No.1500. All cross sections of weld bead were etched using a solution of 5% Nital acid. Etching time was 20 seconds. Then, metallurgical examination at the cross sections of weld bead was performed using an optical microscope. Cracks were observed and crack length was measured as well. Also the cracking ratio was defined in order to evaluate quantitatively weld cracking susceptibility. Cracking ratio is the relationship of the value of the weld bead height (L_0) divided by crack length (L_1) as expressed in equation (5.1). An average value of five cross sections was used to evaluate the cracking ratio. Figure 5.3 illustrates how to identify the cracking ratio in the different cracking patterns. Figure 5.3 (a) presents the case when a crack occurs from a root weld at the weld center, whereas Fig. 5.3 (b) cracks locate out of weld center and the longest crack is assigned as crack length (L_1).

$$\text{Cracking Ratio} = \frac{\text{Crack length (L1)}}{\text{Weld bead height (L0)}} \times 100\% \quad (5.1)$$

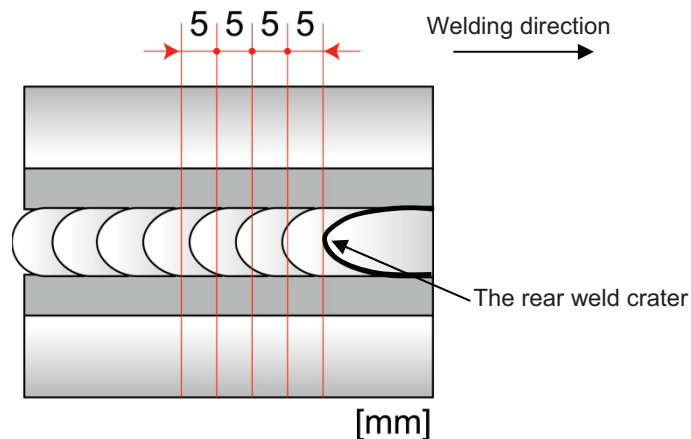
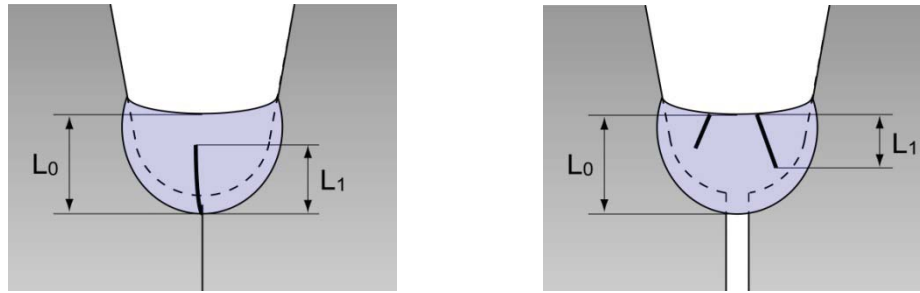


Fig. 5.2 Illustration of cutting location for cracking ratio measurement.



(a) Crack at the weld centerline

(b) Crack at out of the weld centerline

Fig. 5.3 Illustration of cracking ratio measurement.

5.4 Evaluation for Solidification Cracking Susceptibility

In this section, the cracking welds have been examined to observe their fracture surfaces by SEM. The cracking modes were distinguished between solidification cracking and cold cracking. The cracking ratio of each cracking mode was evaluated in every experimental condition. Solidification cracking susceptibility was investigated through the cracking ratio. Aspects of the influence of welding conditions on cracking susceptibility such as the degree of constraint, the root gap width, preheating before welding, welding speed, and the different kinds of filler wires were discussed and evaluated.

5.4.1 Effect of the Degree of Constraint

Based on practical use, a U-groove weld cracking test with a full and spot constraint type was carried out to reproduce occurrences of the cracking weld in real fabrication work. The root gap width of 0 and 2 mm was considered as well. The filler wire was G69A3UMN4M3, which is currently used in real fabrication work. Experimental conditions included the arc current of 280 A, arc voltage of 29 V, a welding speed of 0.22 m/min, and a preheating temperature of 200 °C. From the results, Fig. 5.4 shows the observation images of weld beads and cross sections on a full constraint, as well as spot constraint conditions. It is noticed that the surface cracks can be obviously seen in the welding with a full constraint as presented in Fig. 5.4 (a), while other cracks can be detected from the cross-sectional welds as shown in Fig. 5.4 (b). In the case of a root gap of 2 mm induced the oblique cracks out of the centerline weld and nearby bead surface. On the other hand, the centerline cracks occurred at the weld root under welding with a root gap of 0 mm.

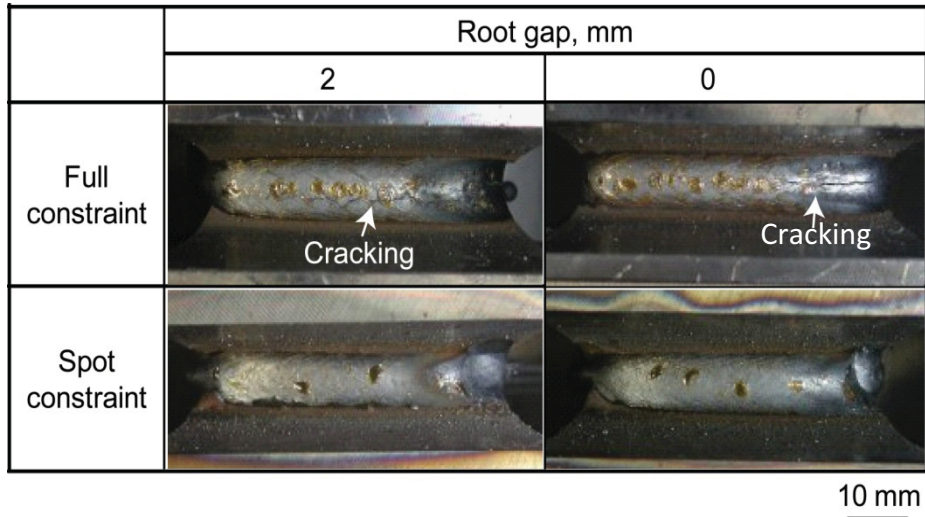
Fractographic examination was carried out to identify the cracking modes. The exam location was selected from the longest crack due to expecting more information. After SEM fractographic observation, Fig. 5.5 to Fig. 5.8 show the SEM magnifying images of a fracture surface in each welding condition. Figure 5.6 shows the SEM fractography from the welding with a full constraint condition and a

root gap width of 2 mm. The fracture surface was investigated outward to the heat affected zone (HAZ). It is found that the fracture surface in the weld metal, Fig. 5.5 (c), reveals the existing dendritic structure with a smooth undulating surface. This evidence indicates there is currently a liquid phase during the occurrence of cracking. Thus, it is well thought-out as solidification cracking. Furthermore, the fracture surface at the HAZ presents a dimple pattern which looks like a ductile overload fracture as shown in Fig. 5.5 (d). It is contemplated that cracking was caused by applying a force to open the crack surface during testing.

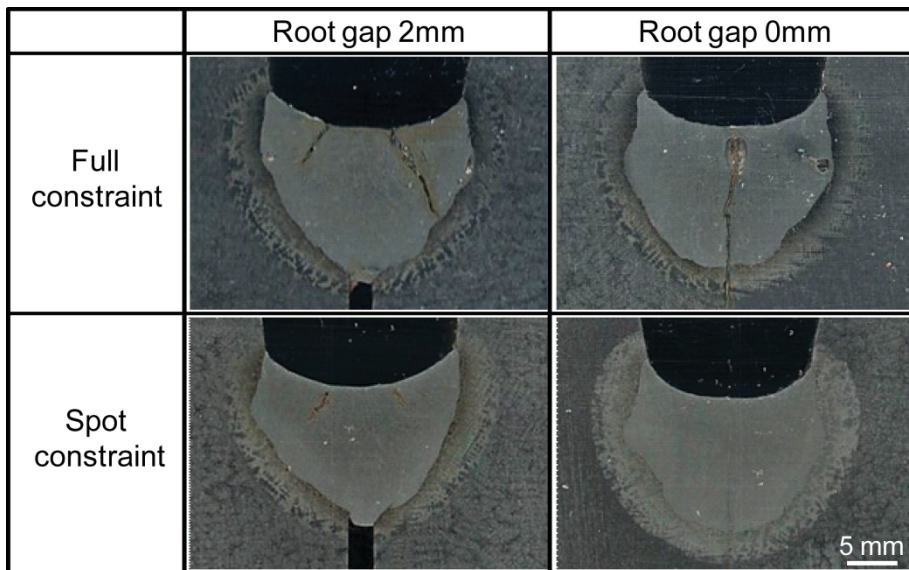
Figure 5.6 shows the results of the fracture surface observation from the welding with a full constraint condition and a root gap width of 0 mm. At this time, the crack was not detected after welding. The SEM fractographic examination exhibits the presence of an intergranular fracture with a faceted appearance along the grain boundaries. Therefore, it is regarded as cold cracking.

Besides this, welding with a less constrained degree was studied further. Figure 5.7 shows a SEM fractography of welding with spot constraint and a root gap width of 2 mm. The metallographic results reveal a dendrite feature on the fracture surface. Such a crack is characterized as solidification cracking. When comparing with a full constraint condition, in this case the crack length is shorter than welding with a full constraint. In the case of the root gap width of 0 mm, as shown in Fig. 5.8, reveals an intergranular crack with a faceted fracture surface which is defined as cold cracking.

As described earlier, the fractographic results reveal solidification cracking always occurs under the welding with a root gap of 2 mm in both of the constraint conditions, while cold cracking takes place in a root gap width of 0 mm under both constraint conditions.



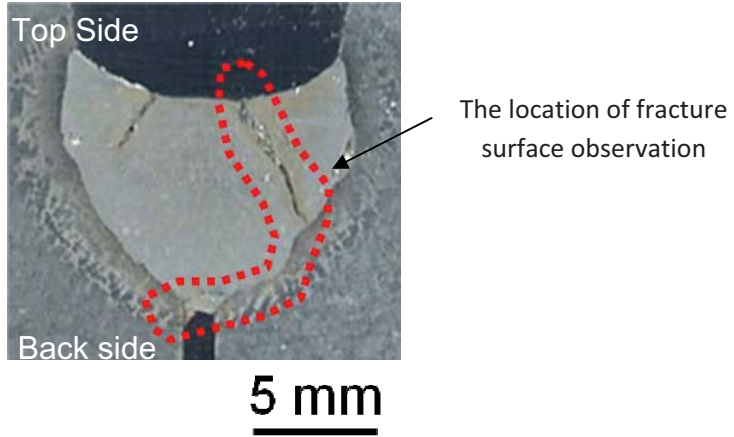
(a) Top view of weld bead appearances.



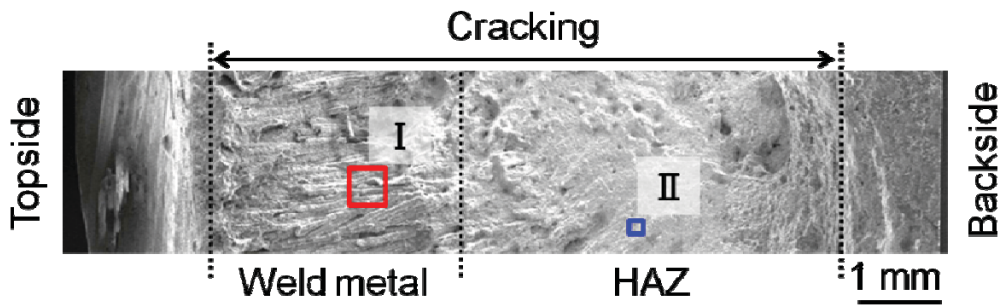
(b) Cross-sectional welds.

(Welding speed= 0.22 m/min, arc current= 280 A, arc voltage= 28 V, filler wire = G69A3UMN4M3, preheating= 200°C)

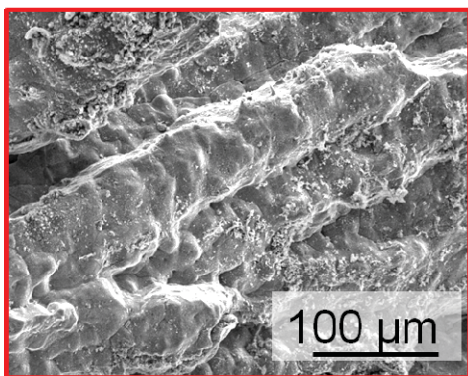
Fig. 5.4 Observation of cracking weld on each constraint condition. (Using G69A3UMN4M3 filler wire)



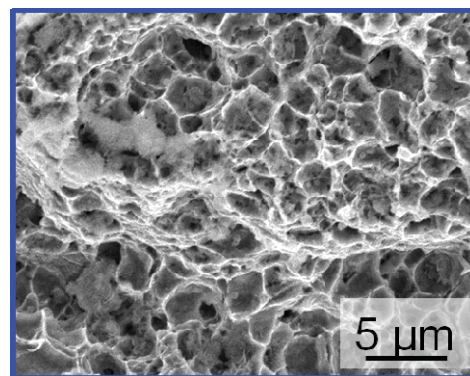
(a) Location of fractographic examination.



(b) Fractography of cracking in each zone



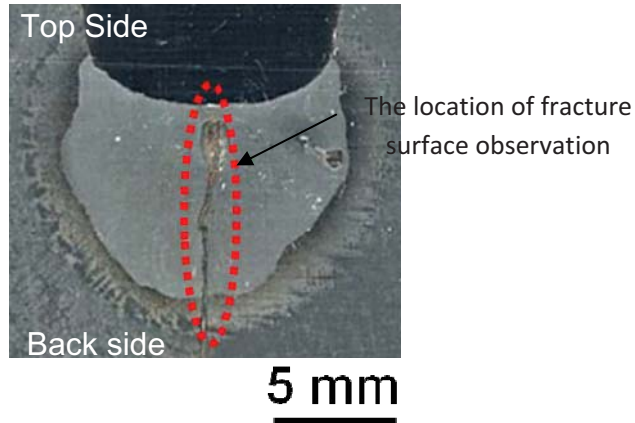
(c) Fracture surface at the point (I)



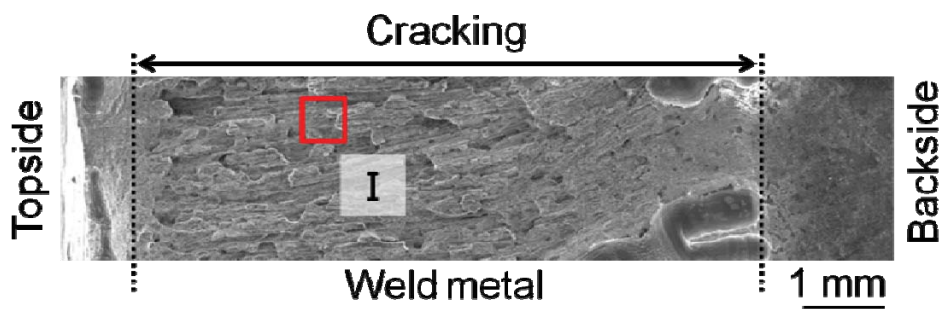
(d) Fracture surface at the point (II)

(Welding speed= 0.22 m/min, arc current= 280 A, arc voltage= 28 V, root gap= 2 mm, full constraint, filler wire = G69A3UMN4M3, preheating= 200 °C)

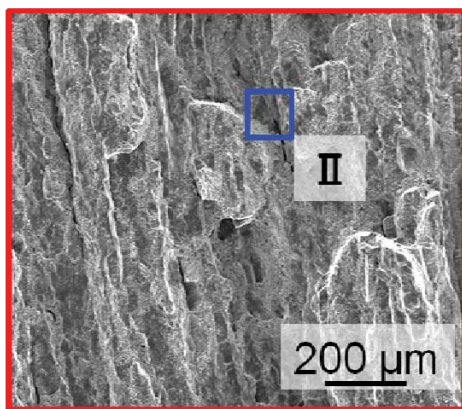
Fig. 5.5 SEM fractographic examination of the welding test with full constraint and a root gap width of 2 mm.



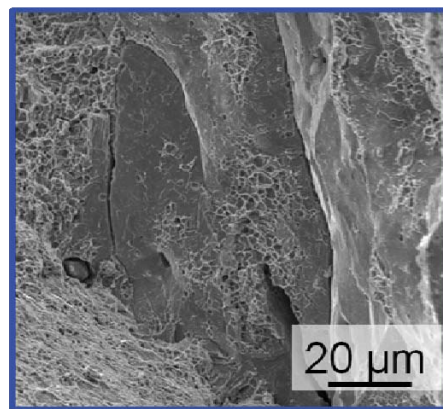
(a) Location of fractographic examination.



(b) Fractography of cracking



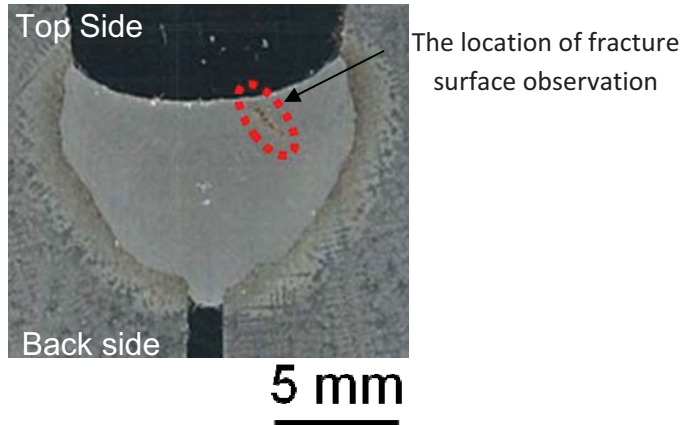
(c) Fracture surface at the point (I)



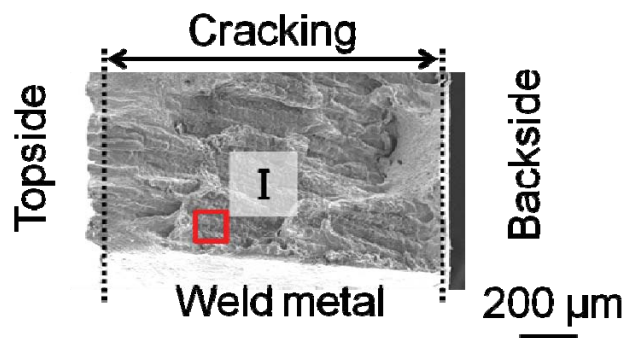
(d) Fracture surface at the point (II)

(Welding speed= 0.22 m/min, arc current= 280 A, arc voltage= 28 V, root gap= 0 mm, full constraint, filler wire = G69A3UMN4M3, preheating= 200 °C)

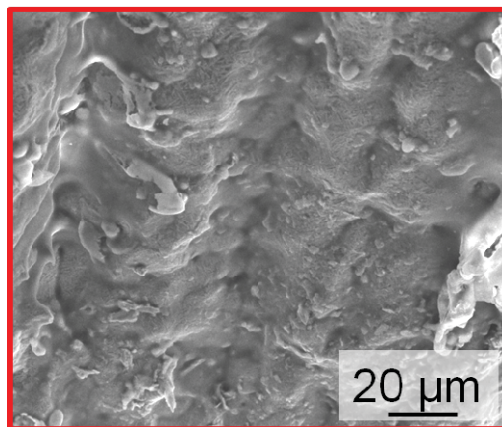
Fig. 5.6 SEM fractographic examination of the welding test with full constraint and a root gap width of 0 mm.



(a) Location of fractographic examination.



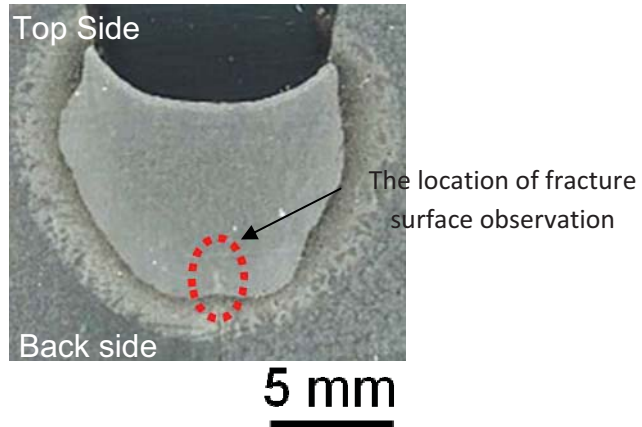
(b) Fractography of cracking



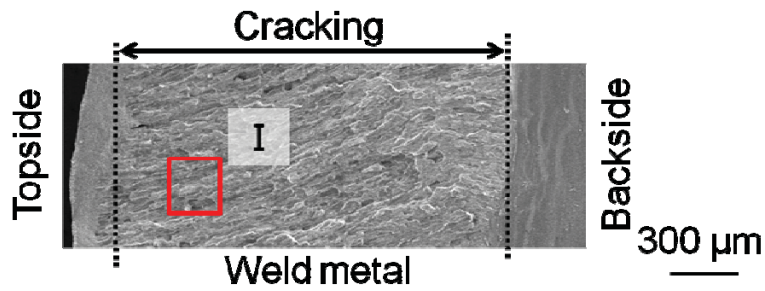
(c) Fracture surface at the point (I)

(Welding speed= 0.22 m/min, arc current= 280 A, arc voltage= 28 V, root gap= 2 mm, spot constraint, filler wire = G69A3UMN4M3, preheating= 200 °C)

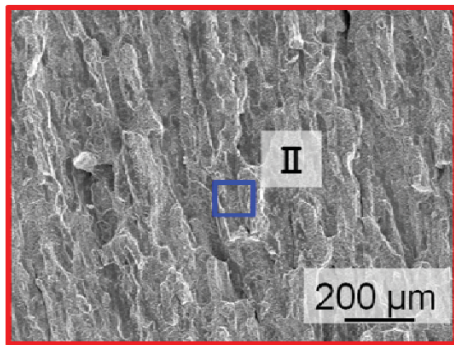
Fig. 5.7 SEM fractographic examination of the welding test with spot constraint and a root gap width of 2 mm.



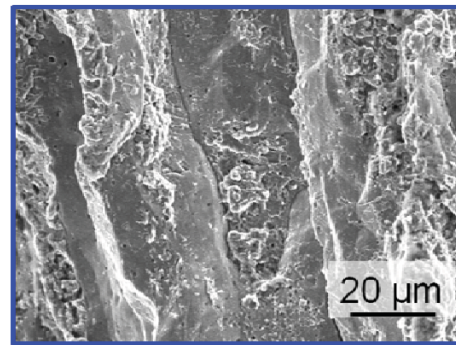
(a) Location of fractographic examination.



(b) Fractography of cracking



(c) Fracture surface at the point (I)

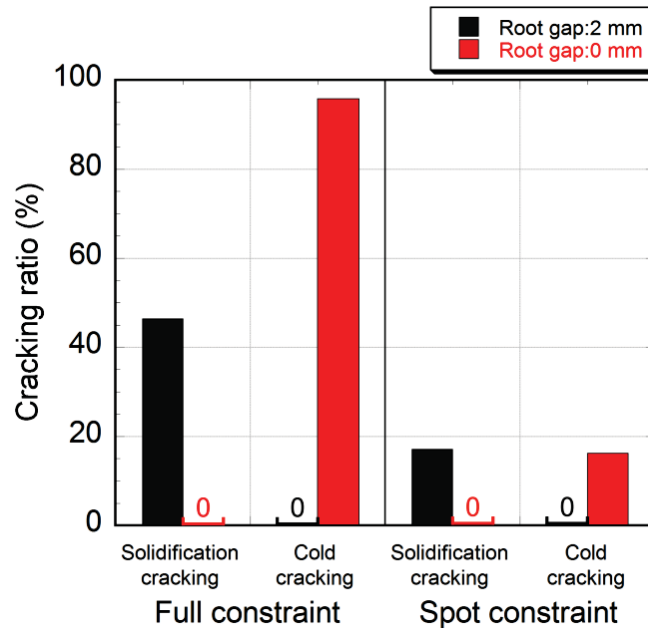


(d) Fracture surface at the point (II)

(Welding speed= 0.22 m/min, arc current= 280 A, arc voltage= 28 V, Root gap= 0 mm, spot constraint, filler wire = G69A3UMN4M3, preheating= 200 °C)

Fig. 5.8 SEM fractographic examination of the welding test with spot constraint and a root gap width of 0 mm.

From this, the effect of the degree of constraint on solidification cracking and cold cracking susceptibility is evaluated from the standpoint of the cracking ratio. Figure 5.9 presents the comparison of cracking ratio between a full constraint and a spot constraint. It is found that the cracking ratio in solidification cracking occurs merely in the root gap width of 2 mm. On the other hand, cold cracking takes place just in the root gap width of 0 mm. As a result, welding with a full constraint condition is more susceptible to cracking than a spot condition. That is, the spot constraint condition is able to reduce the cracking ratio of cold cracking from 96% to 17%. When focused on solidification cracking, the spot constraint condition can also decrease the cracking ratio from 46% to 17%. By this means, the less restraint of a joint fit-up has a significant influence to reduce the cracking ratio. Conversely, a too high restraint due to a joint fit-up is a mechanical factor that induces the weld metal to crack, particularly in the first weld pass of a narrow groove joint.



(Welding speed= 0.22 m/min, arc current= 280 A, arc voltage= 28 V,
filler wire= G69A3UMN4M3, preheating= 200°C)

Fig. 5.9 Relationship between constraint conditions and cracking ratio.

5.4.2 Relationship Between the Type of Filler Wires and Cracking Ratio

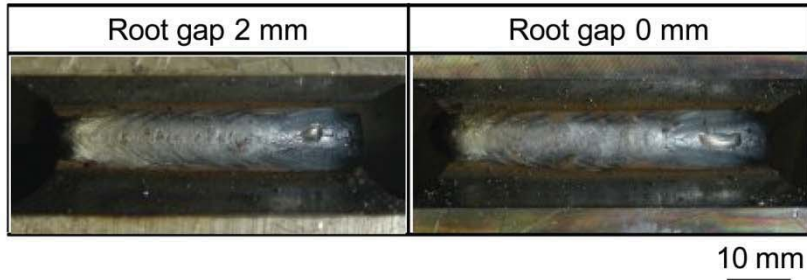
As discussed previously, a G69A3UMN4M3 filler wire for high tensile strength steel (Min.690 MPa) was employed in a U-groove cracking weld test. The experimental results showed cold cracking and solidification cracking had rather high susceptibility. A lower high tensile strength of a filler wire (Min.580 MPa) such as YGW-11 was employed to investigate the cracking susceptibility.

Using YGW-11 filler wire a U-groove cracking weld test with a full constraint, together with a root gap width of 0 and 2 mm was applied. Welding conditions were set as arc current of 280 A, arc voltage of 29 V, a welding speed of 0.22 m/min, and a preheating temperature of 200 °C. Figure 5.10 shows the observation of weld appearances and their cross sections. The weld appearances do not show the surface cracking. However, the cracks at the weld root are detected by the observation of the cross-sectional welds in the both root gap width of 0 and 2 mm.

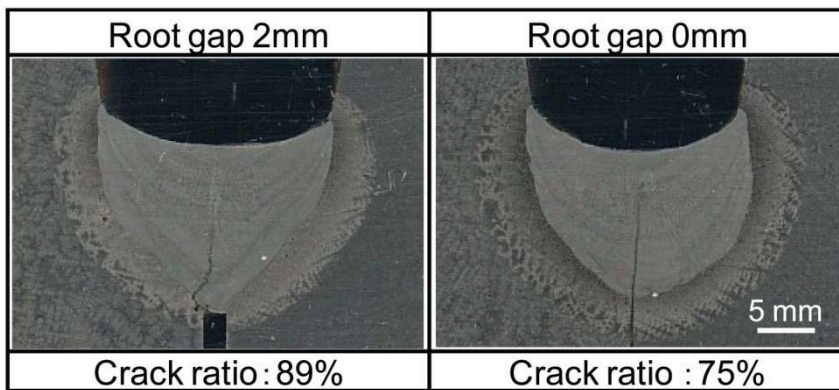
Moreover, Fig. 5.11 and Fig. 5.12 present the SEM fractographic examination to identify the cracking mode. In the case of a root gap width of 2 mm, Fig. 5.11 (b) shows the cracking in the root gap width of 2 mm propagates to the HAZ. The fracture morphology at the upper weld metal exhibits a rather faceted surface as presented in Fig. 5.11 (c). Whereas, fracture surface at the middle of the weld metal has a mixed cracking mode between the dimple and cleavage pattern as Fig. 5.11 (d). In addition, a quasi-cleavage pattern is observed at the HAZ. The faceted fracture surface in the HAZ exhibits obviously an intergranular characteristic separating at grain boundaries as shown in Fig 5.11 (e). This evidence suggests that it was caused by hydrogen embrittlement. For this reason, it is identified as cold cracking. Also, the root gap width of 0 mm, the fracture morphology as Fig. 5.12 (d) reveals a quasi-cleavage fracture in the weld metal which is interpreted as cold cracking too.

As a result, the whole cracks using YGW-11 filler wire are defined as cold cracking. It is noteworthy that when compared with using the G69A3UMN4M3 filler wire, the cold cracking from G69A3UMN4M3 filler wire does not occur in the case of a root gap width of 2 mm.

Full Constraint



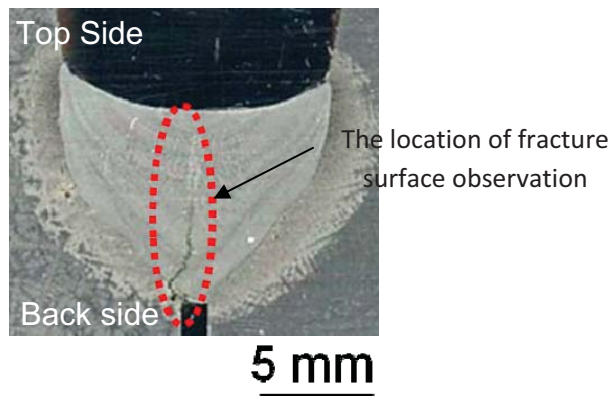
(a) Top view of weld bead appearances



(b) Cross-sectional welds

(Welding speed= 0.22 m/min, arc current= 280 A, arc voltage= 28V, full constraint, filler wire= YGW-11, preheating= 200°C)

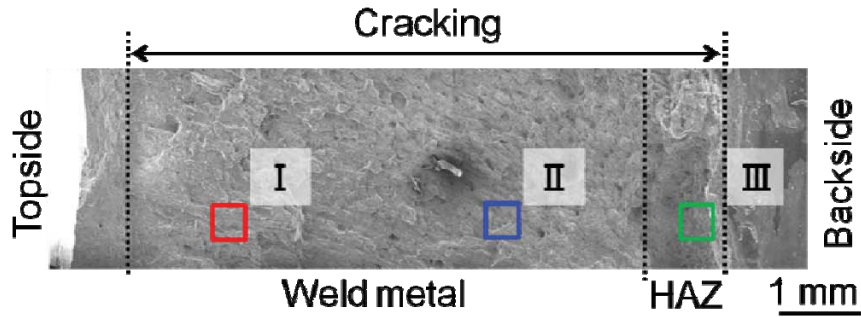
Fig. 5.10 Observation of cracking weld with YGW-11 filler wire.



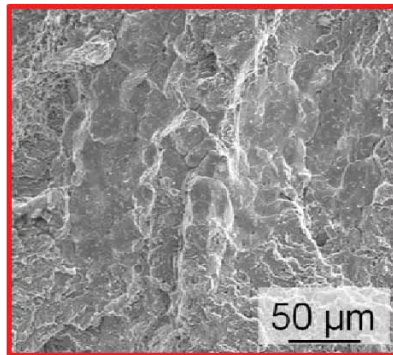
(a) Location of fractographic examination.

(Welding speed= 0.22 m/min, arc current= 280 A, arc voltage= 28V, full constraint, root gap= 2 mm, filler wire= YGW-11, preheating= 200°C)

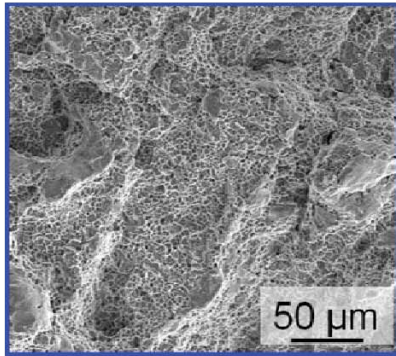
Fig. 5.11 SEM Fractographic examination of the welding test with YGW-11 filler wire, full constraint, and a root gap width of 2 mm.



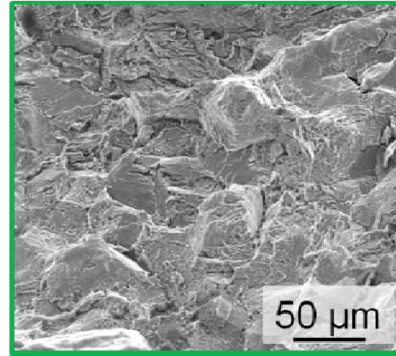
(b) Fractography of cracking



(c) Fracture surface at the point (I)



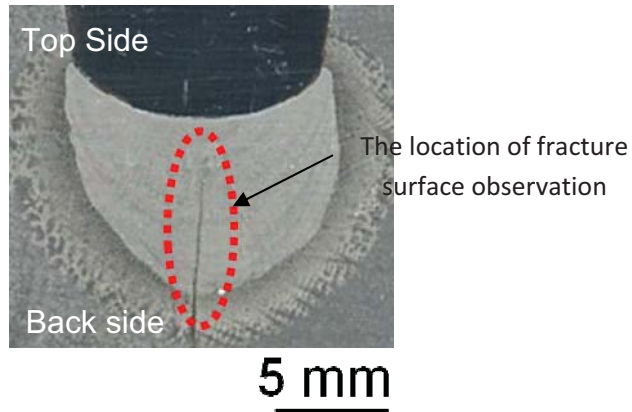
(d) Fracture surface at the point (II)



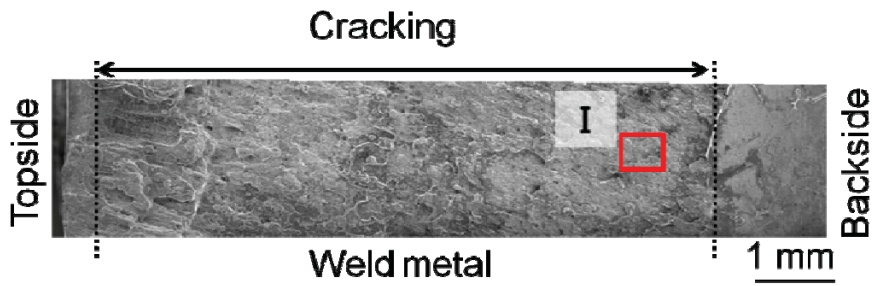
(e) Fracture surface at the point (III)

(Welding speed= 0.22 m/min, arc current= 280 A, arc voltage= 28V, full constraint, root gap = 2 mm, Filler wire= YGW-11, Preheating= 200°C)

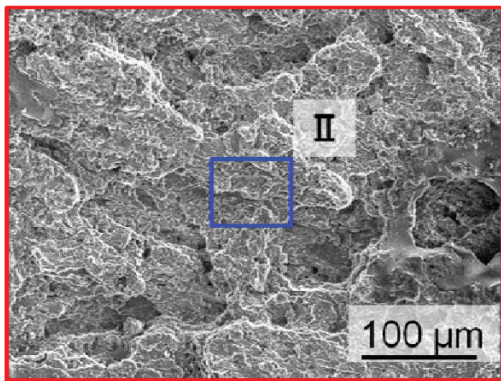
Fig. 5.11 SEM fractographic examination of the welding test with YGW-11 filler wire, full constraint, and a root gap width of 2 mm. (Continue)



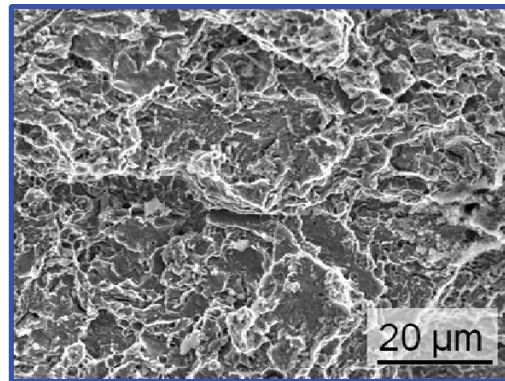
(a) Location of fractographic examination.



(b) Fractography of cracking



(c) Fracture surface at the point (I)

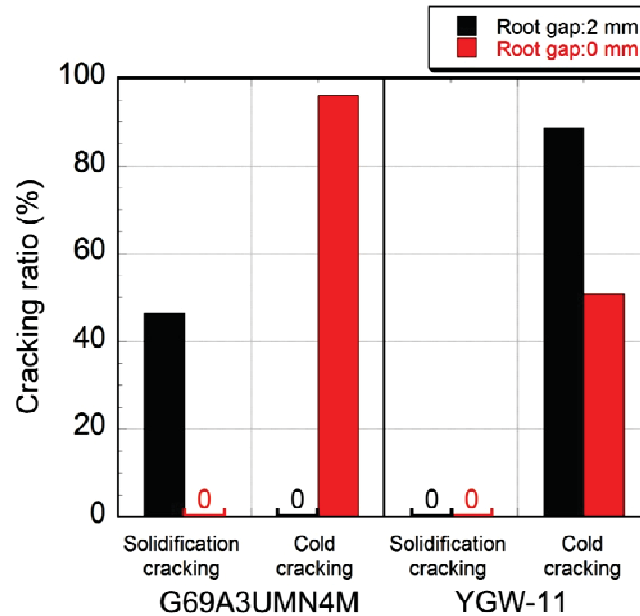


(d) Fracture surface at the point (II)

Welding speed= 0.22 m/min, arc current= 280 A, arc voltage= 28V,
full constraint, root gap = 0 mm, filler wire= YGW-11, preheating= 200°C)

Fig. 5.12 SEM Fractographic examination of the welding test with YGW-11 filler wire, full constraint, and a root gap width of 0 mm.

From this, the quantitative evaluation of cracking ratio between the different filler wires can be discussed. Figure 5.13 presents the comparison of cracking ratio between a filler wire of G69A3UMN4M3 and YGW-11. Under the experimental setup imitating practical work based on solidification cracking, it is found that welding using G69A3UMN4M3 filler wire induces a cracking ratio of 46% in the root gap width of 2 mm, while welding using YGW-11 filler wire can provide a cracking ratio of 0% or no solidification cracking in both the root gap widths. Cold cracking exhibits that the cracking ratio of G69A3UMN4M3 filler wire is 96% only in a root gap width of 0 mm, whereas the cracking ratio of YGW-11 filler wire occurs in both the root gap widths too. That is the cracking ratio of 89% in the root gap width of 2 mm and 51% in the root gap width of 0 mm.

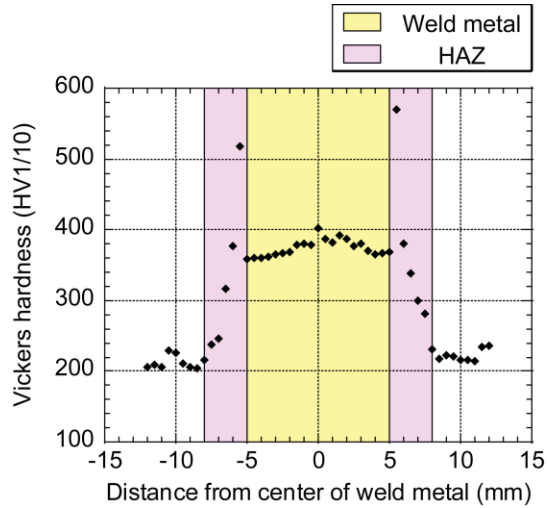


Welding speed= 0.22 m/min, arc current= 280 A, arc voltage= 28V,
full constraint, preheating= 200°C)

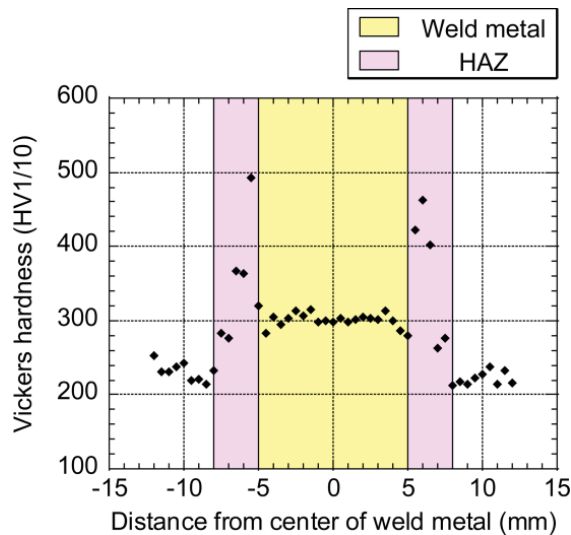
Fig. 5.13 Relationship between the kinds of filler wires and cracking ratio.

Additionally, a micro hardness test was carried out to investigate the mechanical property between two types of filler wire. A micro hardness tester (Matsuzawa Seiki Co., MHT-1) was utilized. An applied load of 9.8 N and a holding time of 10 s was performed. The interval of measuring points was 0.5 mm and the measurement procedure was operated in accordance with JIS Z 2244. Figure 5.14 shows the comparison of micro Vickers hardness profiles between the filler wire of G69A3UMN4M3 and YGW-11. From the results, the hardness value of the SCMn3B base metal is approximately 220 HV and increases up to about 500 HV at the HAZ in either filler wire. The G69A3UMN4M3 weld metal provides the hardness value of about 380 HV, which is much higher than the base metal,

whereas the YGW-11 weld metal gives a hardness value of about 300 HV that relatively matches to the base metal. It is suggested that the G69A3UMN4M3 weld metal has more joint strength than the SCMn3B base metal, which leads to easier solidification cracking than in YGW-11 weld metal; while the joint strength of YGW-11 weld metal is satisfied. However, the high hardness value of YGW-11 weld metal is enough to induce cold cracking.



(a) G69A3UMN4M3



(b) YGW-11

(Welding speed= 0.22 m/min, arc current= 280 A, arc voltage= 28 V, root gap= 0 mm, full constraint, preheating= 200 °C)

Fig. 5.14 Comparison of micro Vickers hardness profiles.

As a result, it is suggested that welding with a filler wire of YGW-11 with a lower tensile strength than the high strength filler wire of G69A3UMN4M3 has potential to prevent the occurrence of solidification cracking in the first weld pass particularly in a narrow groove joint. Nevertheless, cold cracking has to be carefully considered for use such as in filler wire.

5.5 Summary

In this study, solidification cracking in large-scale cast steel parts with a heavy thickness for construction machineries, especially in the first weld pass of a narrow groove joint, was investigated through reproducing cracking behavior by employing a U-groove weld cracking test. The important factors to solidification cracking susceptibility were studied such the degree of constraint, the root gap width, and the use of the different filler wires. The conclusions can be summarized as follows:

1. Based on the degree of constraint, experiments were carried out to make clear the effect of the restraint of a joint fit-up during welding. A specimen with full and spot constraint condition was employed to imitate over rigidity of joint and more flexible joint, respectively. From the results, welding with the G69A3UMN4M3 filler wire which is similar to practical welding work produced solidification cracking in the case of the full constrained condition, as well as a root gap width of 2 mm. The solidification cracking ratio was rather high. On the other hand, the welding with the spot constraint condition was substantially able to reduce the solidification cracking ratio. By this means, the less restraint of a joint fit-up that allows more flexibility during welding has a significant influence to decrease the solidification cracking susceptibility particularly in the first weld pass.

2. In the issue of the width of the root gap, the results showed that welding with a root gap width of 2 mm, as well as the G69A3UMN4M3 filler wire caused solidification cracking. While welding with the root gap width of 0 mm resulted in only cold cracking in both the cases of constraint conditions. It is suggested that the wider root gap has a tendency to induce solidification cracking during welding.

3. Due to severe solidification cracking whilst using high tensile strength class filler wire (G69A3UMN4M3), the lower tensile strength class filler wire (YGW-11) was employed to study preventing solidification cracking. As a result, the YGW-11 filler wire has significant potential to eliminate solidification cracking in all cases. Besides, the result of hardness profile exhibited relatively corresponded to the base metal. Therefore, it is suggested that the YGW-11 filler wire is strongly feasible to avoid solidification cracking. Nevertheless, such a filler wire enables production of cold cracking as well. The appropriate temperature level of preheating should be used to prevent such a problem.

Chapter 6

Achievement of high temperature ductility curves in modified 9Cr1Mo steel and cast steel welds using U-type hot cracking test with In-situ observation

6.1 Introduction

In the previous chapters, solidification cracking susceptibility of modified 9Cr1Mo and cast steel welding was studied. The solidification cracking tendency was presented in terms of the D/W ratio and cracking ratio. Nevertheless, a more quantitative approach is necessary to understand clearly the solidification cracking behavior in the weld metal. According to Nakata and Matsuda's study [63-64] on the theory of reduced ductility of a solidifying weld metal, the mechanism of solidification cracking has been explained through the aspect of the dynamic between the material resistance at an elevated temperature, or high temperature ductility curve, and a rising strain rate along the solidification temperature range. Such a high temperature ductility curve is very useful not only for understanding a material factor but also for evaluation and the prediction of solidification cracking.

In this study, the development method, the so-called U-type hot cracking test [97], was employed to achieve a high temperature ductility curve. The U-type hot cracking test combines the merits of the in-situ observation method and U-type jig. Due to the development of the in-situ observation method using a high speed camera, this method has the potential to quantify the minor deformation behavior of the weld bead at high temperatures. Therefore, a critical local strain in the solidification cracking can be accurately measured. When developing a U-type jig in order to apply a tensile force variably to a specimen during welding and measure the temperature history for the duration of solidification, the critical local strain as a function of temperature can be accomplished. Consequently, the high temperature ductility curve can be precisely provided by means of this approach.

This chapter will describe the achievement of high temperature ductility curves through the U-type hot cracking test, which can be divided into two parts as follows.

The first part is associated with the modified 9Cr1Mo weld metal. The modified 9Cr1Mo weld metal specimen was provided through the hot-wire laser welding method. In the U-type hot cracking test, a tensile force was applied to the specimen using the U-type jig and then a fiber laser welding was performed to generate a molten pool, as well as a full penetration. At the same time, a high speed camera with a high magnified lens setting was used to record the real-time deformation at the trailing edge of the molten pool. When varying the amount of tensile force in each experiment, solidification cracking could be observed. Then, the special image processing was performed so as to determine the critical local strain at the initiation of solidification cracking. With an identical welding condition,

the temperature history at the trailing edge of the weld pool was measured. By these means, the high temperature ductility curve of modified 9Cr1Mo weld metal was achieved and also compared with other high resistance steel such as A310S and Inconel 600.

The second part involves the cast steel weld metal, in particular G69A3UMN4M3 weld metal. Due to the fact that the U-groove weld cracking test in Chapter 5 revealed solidification cracking susceptibility in G69A3UMN4M3, the weld metal is remarkably high. Furthermore, the examination of the dilution ratio exhibited typically about 40% base metals. In order to make clear the material factor in solidification cracking, the high temperature ductility curve of G69A3UMN4M3 weld metal was investigated. The U-type hot cracking test was carried out. Two hot-wire laser welding was used to build up the weld metal to 40% dilution between SCMn3B and G69A3UMN4M3 filler wire. An experiment similar to the procedure mentioned above was performed.

6.2 Material and Specimen Used

6.2.1 Specimen Preparation for Modified 9Cr1Mo Weld Metal

Table 6.1 shows the chemical compositions of each material used. To make up a specimen, the welding process is carried out into two steps, namely buttering welding and butt welding with hot-wire laser welding.

Fig. 6.1 shows the experiment setup of buttering welding. During buttering welding, a particular chamber box was employed to pump in shielding argon gas so as to protect the molten pool from the outside atmosphere. As illustrated in Fig. 6.2, modified 9Cr1Mo steel plates of 5 mm in thickness are welded with buttering welding at one edge of the plate. Hot-wire laser welding was used to build up the ER90S-G weld bead due to the minimizing dilution effect from the base metal. Then, such welded plates were machined at the buttering side for a bevel groove of 10 degrees as illustrated in Fig. 6.3.

Next, with the bevel groove joint, such plates were jointed once more using butt hot-wire laser welding as illustrated in Fig. 6.4. For butt welding, the specimen was protected from the reactive atmosphere by the designed jig and the geometry of a fitting joint with a root gap width of 4 mm was applied as shown in Fig. 6.5. The standard size of a specimen for U-type hot cracking was $30^w \times 110^l \times 3^t$ mm as shown in Fig. 6.6. A high speed camera was used to visually observe adequate welding. Table 6.2 and 6.3 give the welding conditions for buttering and butt hot-wire laser welding, respectively.

Table 6.1 Chemical composition of materials used (mass %) for modified 9Cr1Mo weld metal

Material	C	Si	Mn	P	S	Fe	Cr	Mo	Nb	V	Cu
Base metal : Mod.9Cr1Mo	0.01	0.37	0.43	0.014	0.002	Bal.	8.55	0.98	0.08	0.19	0.02
Filler wire : (ϕ 1.2) ER90S-G	0.08	0.12	1.02	0.005	0.004	Bal.	8.99	0.90	0.04	0.18	0.12

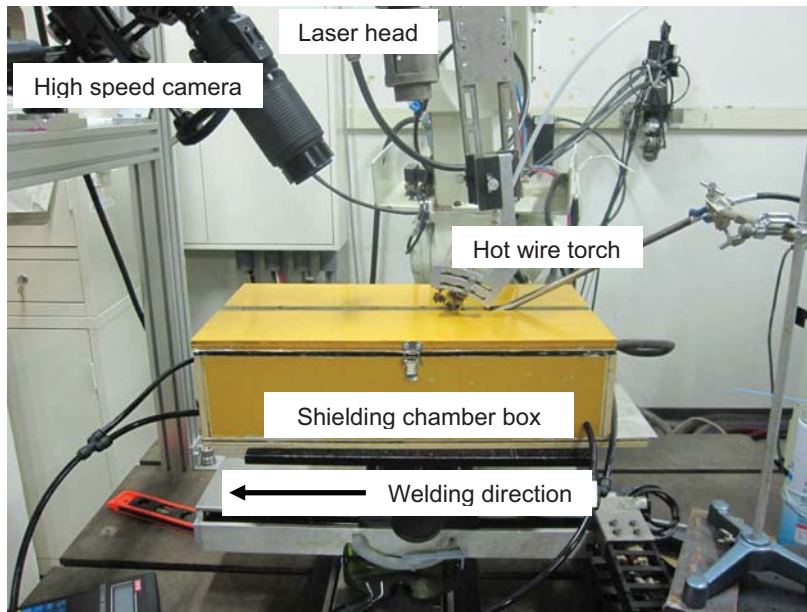


Fig. 6.1 Experimental setup of buttering welding.

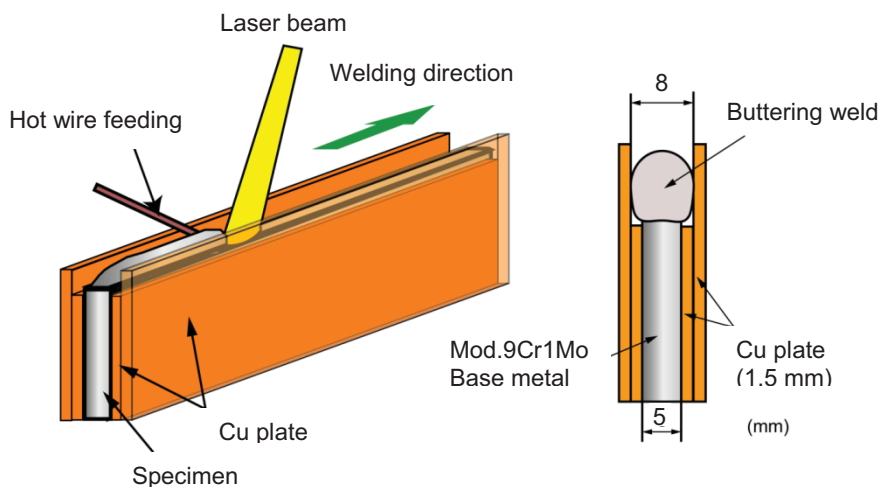


Fig. 6.2 Schematic illustration of buttering welding using hot-wire laser welding.

Achievement of high temperature ductility curve in modified 9Cr1Mo steel and cast steel welds using U-type hot cracking with In-situ observation

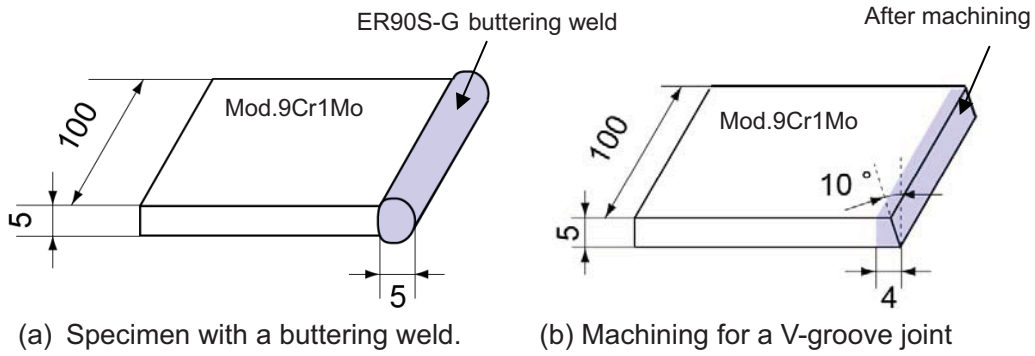


Fig. 6.3 Illustration of V-groove joint preparation.

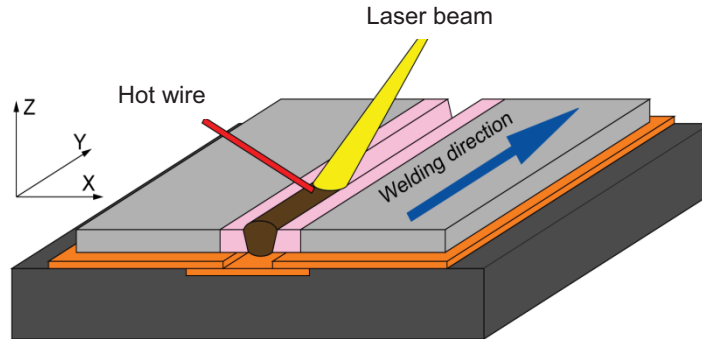
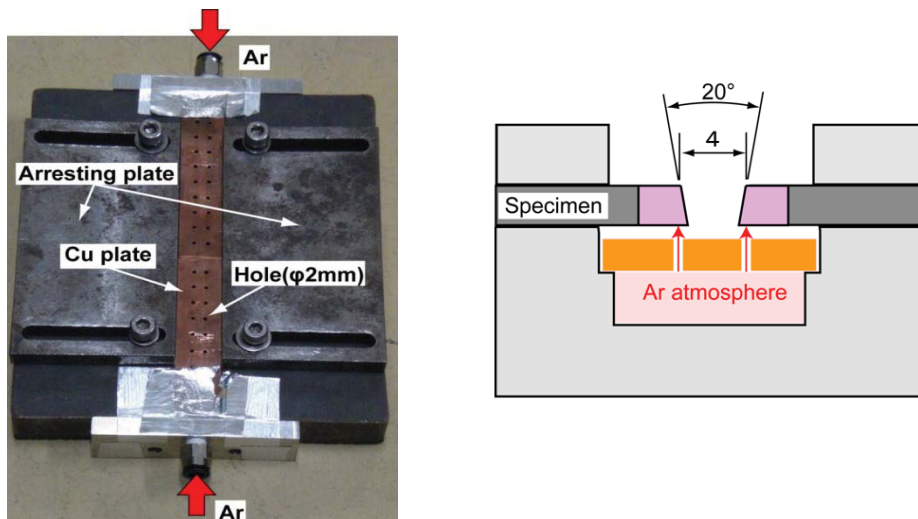


Fig. 6.4 Schematic illustration of butt welding using hot-wire laser welding.



(a) Image of clamping jig. (b) Cross section of shielding gas apparatus.

Fig. 6.5 Shielding gas method of butt welding.

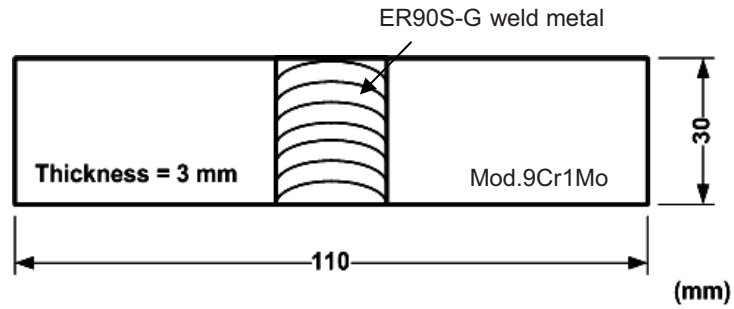


Fig. 6.6 Standard size of specimen for U-type hot cracking test. (Modified 9Cr1Mo weld metal)

Table 6.2 Welding parameters for buttering welding

Laser type	Fiber laser
Laser power (kW)	3
Welding speed (m/min)	0.2
Laser spot diameter (mm)	7
Irradiation angle (deg.)	5
Wire feeding speed (m/min)	5.4
Wire feeding angle (deg.)	70
Wire feeding position (mm)	2
Wire current (A)	82
Argon shielding gas (l/min)	
Chamber box	20
Holding time before welding (min.)	10

Table 6.3 Welding parameters for butt welding

Laser type	Fiber laser
Laser power (kW)	3
Welding speed (m/min)	0.2
Laser spot diameter (mm)	4
Irradiation angle (deg.)	5
Wire feeding speed (m/min)	5.4
Wire feeding angle (deg.)	70
Wire feeding position (mm)	2
Wire current (A)	82
Argon shielding gas (l/min)	10-20

6.2.2 Specimen Preparation for Cast Steel Weld Metal

In the case of the cast steel weld metal, a dilution ratio of 40% base metal is desired replicate the practical use in the U-groove weld cracking test. Table 6.4 shows chemical compositions of each material used. The welding processes are divided into two phases, namely buttering welding with two-hot wire laser welding and butt welding with two-wire GTA welding.

The first phase, Fig. 6.7, illustrates the use of two-hot wire laser welding to mark up the dissimilar welded joint for the U-type hot cracking test. The weld metal with 40% dilution between SCMn3B and G69A3UMN4M3 was built up on the mild steel SM490 using the buttering method with two-hot wire laser welding as illustrated in Fig. 6.8. The hot-wire laser welding provides the benefit of low heat input, minimizing the dilution effect from the SM490 base metal. As a result, the dilution ratio of SM490 base metal to the buttering weld metal is insignificant. The advantage of the two-wire feeding method is it provides the ability to control the dilution ratio in a weld joint. The preferred dilution ratio is obtained by adjusting the respective feeding speeds of two filler wires. In this case, Table 6.5 and 6.6 shows the welding conditions and the proportion of wire feeding speed between SCMn3B wire and G69A3UMN4M3 wire was 1.6 and 2.4 m/min. Figure 6.9 shows the positional setup related to laser irradiation and the wire feeding.

Table 6.4 Chemical composition of materials used (mass %) for G69A3UMN4M3 weld metal

Material	C	Si	Mn	P	S	Ni	Cr	Mo	Cu	V
Filler wire: SCMn3B (ϕ 1.2)	0.32	0.43	1.17	0.027	0.009	0.05	0.11	0.01	0.1	-
Filler wire :G69A3UMN4M3 (ϕ 1.2)	0.07	0.33	1.11	0.010	0.005	1.77	-	0.44	-	0.44
Base metal :SM490	0.07	0.02	1.31	0.017	0.005	-	-	-	-	-

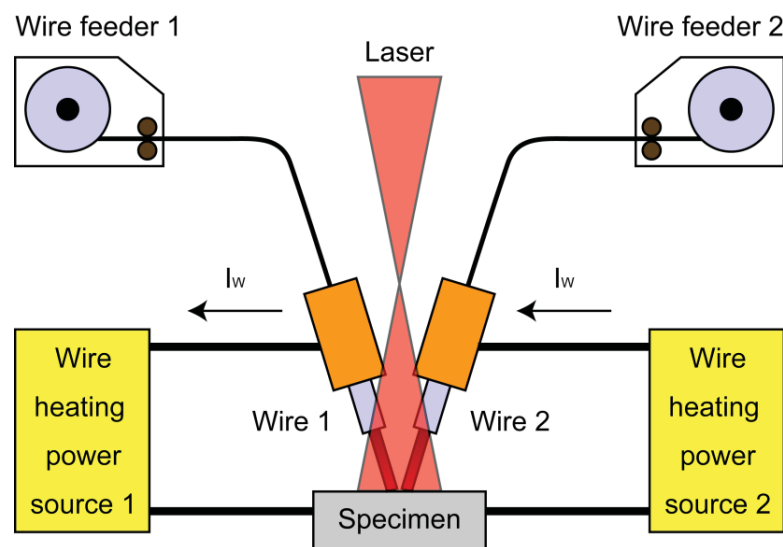


Fig. 6.7 Schematic illustration of two hot wire-laser welding system.

For the second phase, Fig. 6.10 illustrates how the buttered weld bead was machined for the groove joint preparation of two-wire GTA welding. At this time, to increase the efficiency of melting the two wires and sound welds, two-wire GTA welding was used to produce a weld joint with 40% dilution once again. Figure 6.11 presents the joint fitting for two-wire GTA welding. The tack welding with a tab plate of $30^w \times 110^L \times 3^t$ mm is performed at the two edge side of the specimen so as to fix the root gap width of 4 mm. Start and end welding was done at this tab plate in order to obtain a homogeneous weld bead specimen. Table 6.7 details the welding conditions for two-wire GTA welding. Shielding argon gas was used to protect it from the outside atmosphere. Figure 6.13 represents the standard size of the specimen for the U-type hot cracking test.

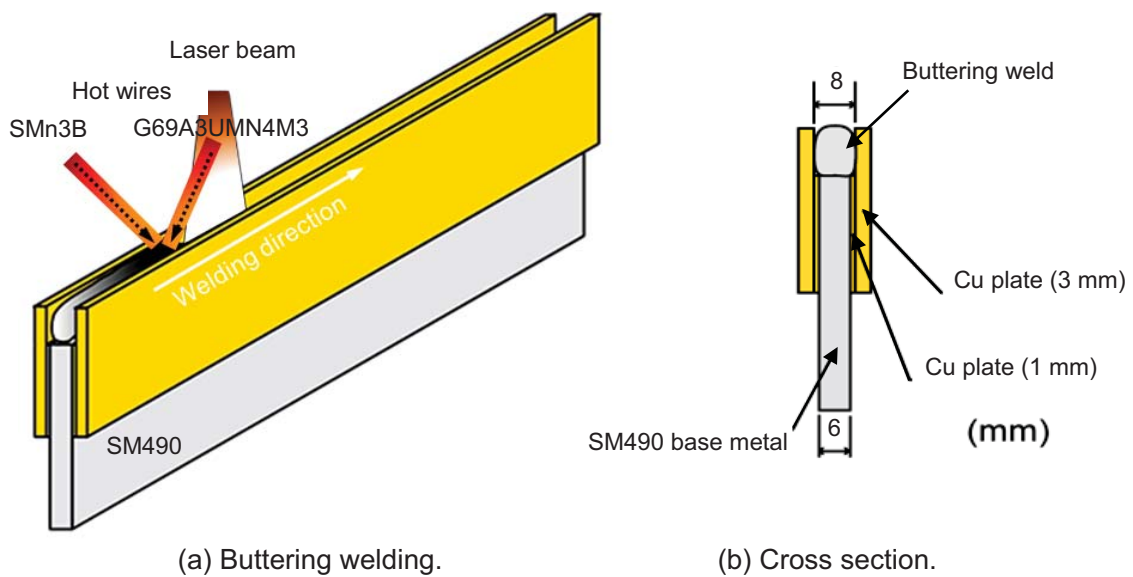


Fig. 6.8 Schematic illustrations of buttering welding with two hot-wires.

Table 6.5 Welding parameters for buttering two hot-wire laser welding

Laser type	Fiber laser
Laser power (kW)	3
Welding speed (m/min)	0.1
Laser spot diameter (mm)	7
Irradiation angle (deg.)	5
Wire feeding angle (deg.)	70
Argon shielding gas (l/min)	10-20

Achievement of high temperature ductility curve in modified 9Cr1Mo steel and cast steel welds using U-type hot cracking with In-situ observation

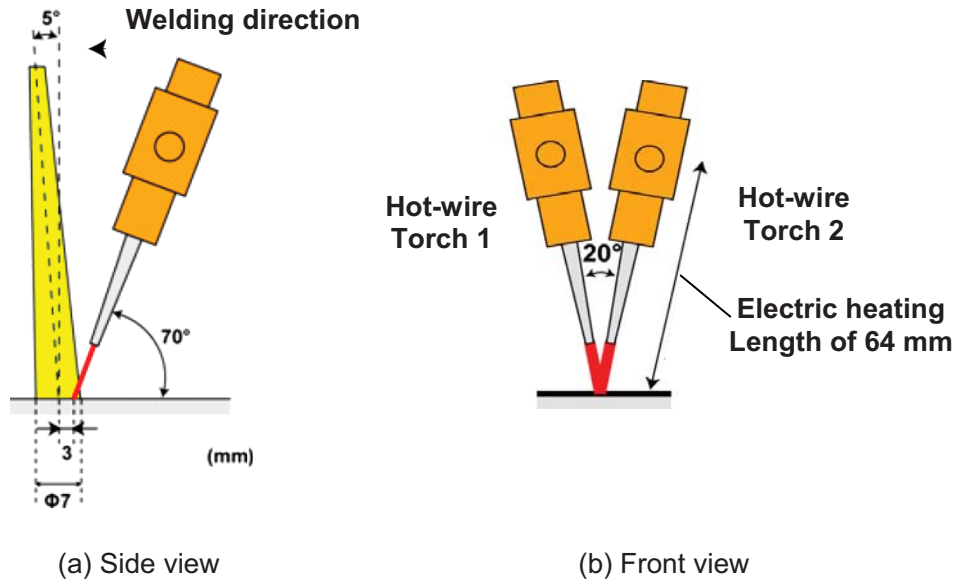


Fig. 6.9 Schematic illustrations of laser irradiation and wire feeding setup.

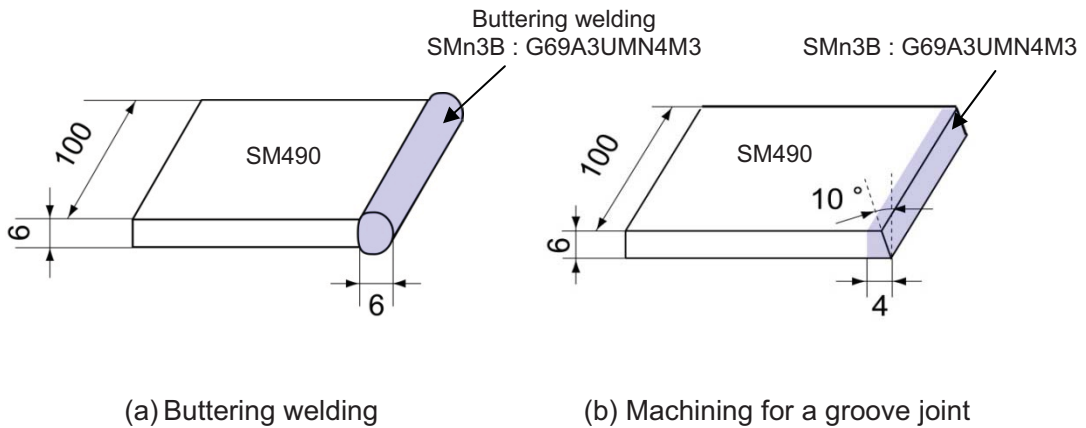
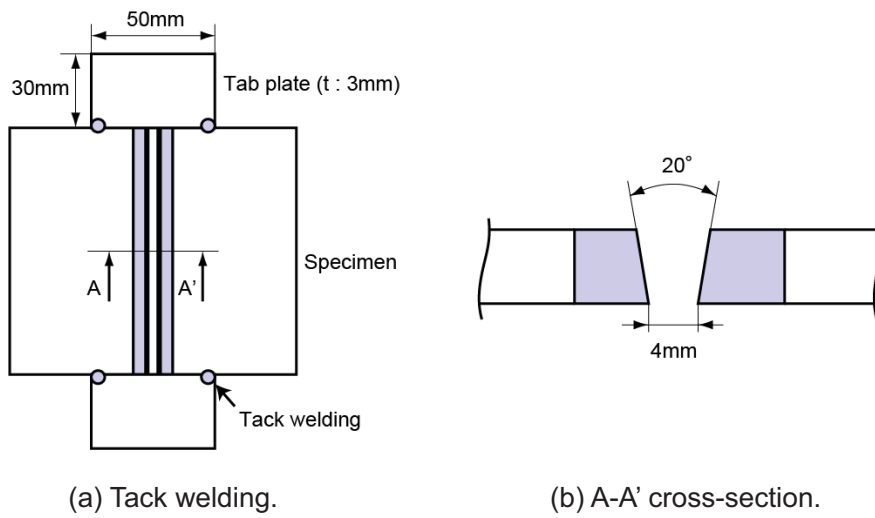


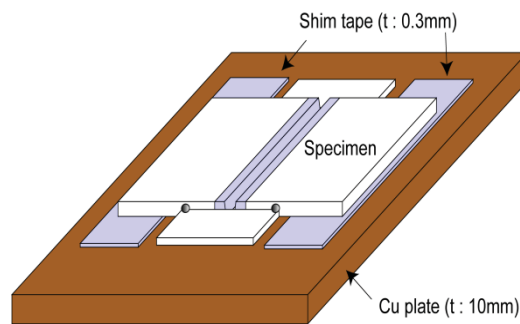
Fig. 6.10 Illustration of a V-groove joint preparation

Achievement of high temperature ductility curve in modified 9Cr1Mo steel and cast steel welds using U-type hot cracking with In-situ observation



(a) Tack welding.

(b) A-A' cross-section.



(c) Specimen setup

Fig. 6.11 Illustration of a joint fitting preparation for two-wire-butt GTA welding.

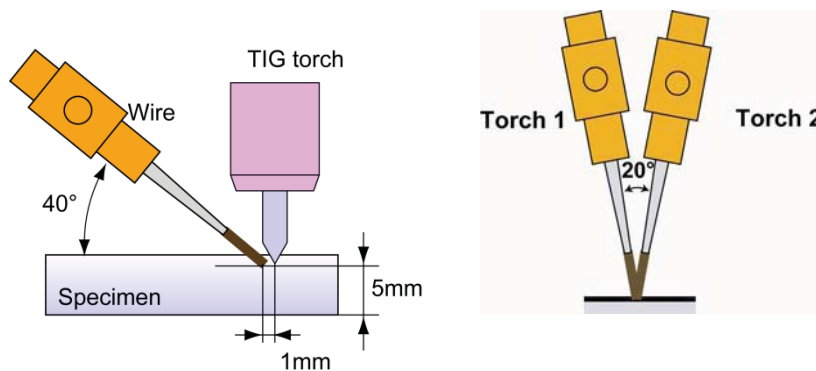


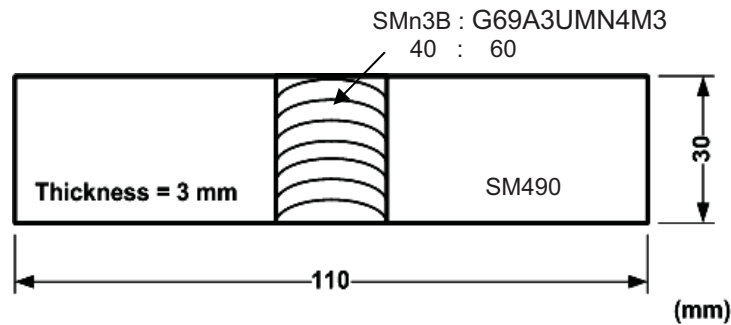
Fig. 6.12 Schematic illustrations of positional setting between GTA torches and two feeding wires.

Table 6.6 Welding conditions of filler wires

Dilution ratio	SCMn3B:G69A3UMN4M3 (40:60)	
Wire feeding speed (m/min)	1.6	2.4
Wire current (A)	85	102

Table 6.7 Welding parameters for two-wire-butt GTA welding

Arc current (A)	250
Arc length (mm)	5
Welding speed (m/min)	0.1

Fig. 6.13 Standard size of specimen for U-type hot cracking test.
SCMn3B:G69A3UMN4M3 (40:60)

6.3 Dilution Evaluation of Welds

In order to prove the dilution ratio of the specimen after buttering welding, a buttering welded plate was observed with a macrograph-cross section. The preparation for dilution observation included cutting the middle of a buttering weld bead and hot mounting in a thermosetting resin, then grinding with emery paper until grit no. 1500. After that, it was finely polished with diamond particles with a diameter of 1 μm and 3 μm . Ultrasonic cleaning was done beforehand. Last, chemical etching was used to reveal the macrostructure of the weld bead. The etchant formula for Modified 9Cr1Mo weld metal consists of a picric of 1 g, hydrochloric of 3 g and ethanol of 100 g. Nital 5% was used for YM70A weld metal. In the case of the weld bead, butt welding was carried out using the same procedure. The cross-sectional observation was visually examined with a microscope stereomicroscope (manufacturer: OLYMPUS, SZH10) and an optical microscope (manufacturer: NIKON, MU-21).

Figure 6.14 (a) and (b) illustrate the area of the weld metal (A_0) and the penetration zone in the base metal (A_1). A digital microscope (manufacturer: KEYENCE, VH-8000) was used for the area measurement. The dilution ratio was calculated as shown the following equation, 6.1.

$$\text{Dilution ratio} = \frac{A_1}{A_0} \times 100 \quad (\%) \quad (6.1)$$

Figure 6.15 represents the cross sections of modified 9Cr1Mo, together with the G69A3UMN4M3 buttering weld bead. The cross sections show a good sound weld and completed fusion between the weld metal and the base metal. It was found that the dilution ratio of Modified 9Cr1Mo is 1.7%, while the dilution ratio of G69A3UMN4M3 is 1.2%. It is obvious that hot-wire laser welding achieves very little penetration. Also, Fig. 6.16 shows the dilution ratio in both cases of butt welding. The Modified 9Cr1Mo is about 34.3% and G69A3UMN4M3 is about 30.1%. After calculating the gross dilution of the base metal into the weld metal, the Modified 9Cr1Mo is about 0.6%, while G69A3UMN4M3 is about 0.4% of the SM490 base metal. As a result, the base metal dilution does not drastically influence the weld bead.

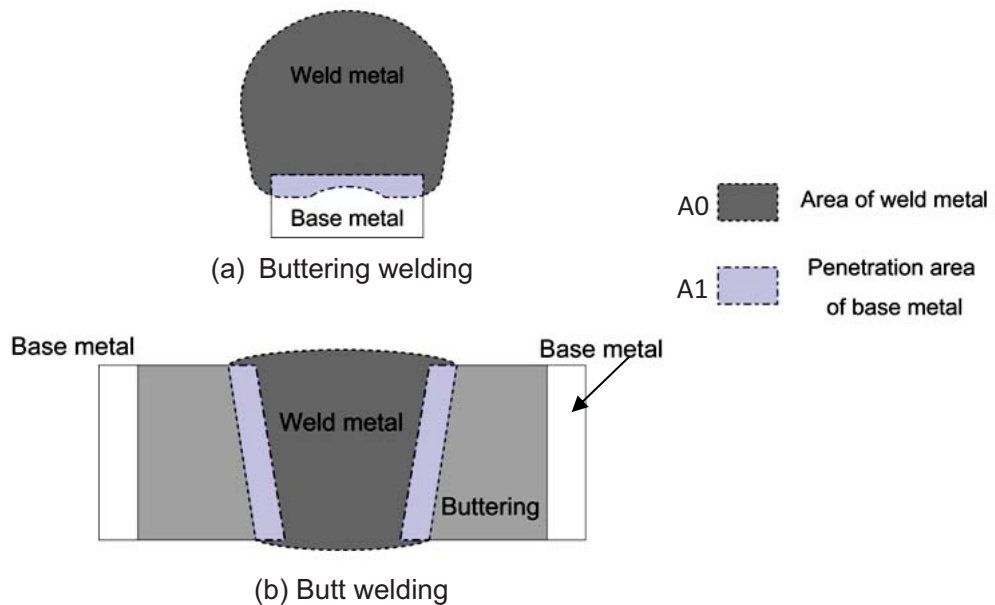


Fig. 6.14 Schematic illustration of weld metal and penetration area of base metal.

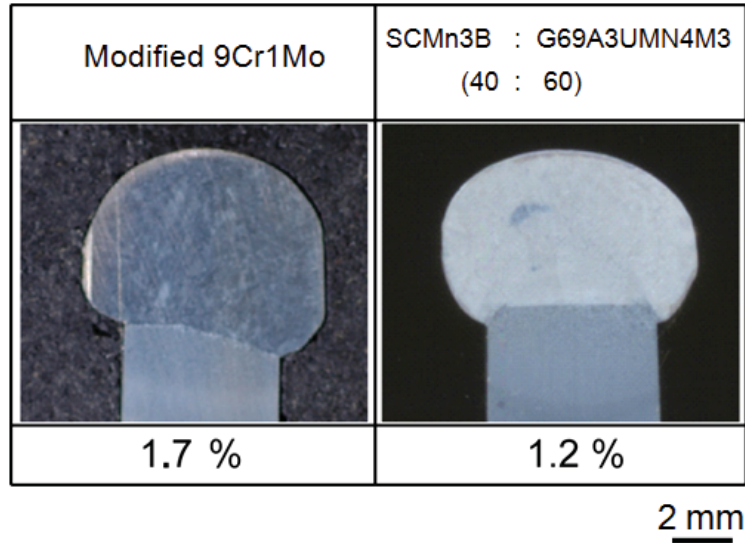


Fig. 6.15 Typical dilution ratio and cross sections after buttering welding.

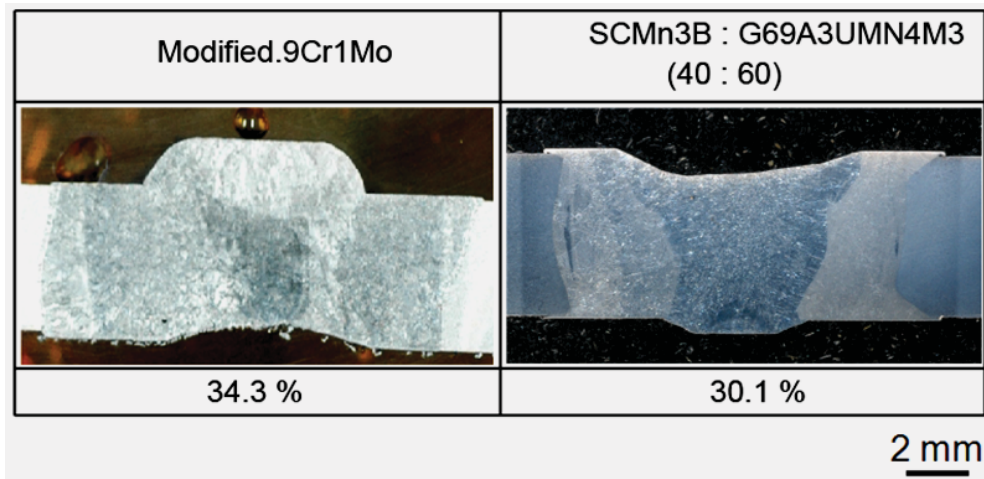


Fig. 6.16 Typical dilution ratio and cross sectional welds after butt welding.

6.4 U-type Hot Cracking Test with In-situ Observation

6.4.1 Method and Equipment

In accordance with the hot cracking test with in-situ observation which was first developed by Matsuda [63-64], the modified U-type hot cracking test was used to evaluate solidification cracking susceptibility during laser welding for this experiment. The developed jigs, so-called U-type 1 and U-type 2, were used to place an external tensile load on a specimen during laser welding. Their configurations are presented in Fig. 6.17 and 6.18. These U-type jigs are designed to serve as initial tensile loads with different stiffness. The loading direction is perpendicular to the welding direction so as to induce solidification cracking at the centerline of the weld bead. This provides an advantage in solidification cracking observation in practical laser welding.

The relation between the deflection of the restraint beam and the load applied to the specimen for U-type 1 and U-type 2 was determined and is derived as the following Equations 6.2 and 6.3, respectively.

$$\text{U-type 1} \quad F(\text{kN}) = 5.79 \times \delta \text{ (mm)} \quad (6.2)$$

$$\text{U-type 2} \quad F(\text{kN}) = 2.07 \times \delta \text{ (mm)} \quad (6.3)$$

Where F is the initial tensile load, δ is the total deflection of the two restraint beams. It was observed that U-type 2 can provide with larger deformation than U-type 1 when providing the same deflection of two restraint beams. The rollers in U-type 2 are useful for eliminating the bending deformation in the specimen.

The testing procedure as illustrated in Fig. 6.17 can be explained as follows. First, in Fig. 6.17 (a) and (b), the restraint beams are applied with an external load with an expected distance within the elastic limit.

Then, in Fig. 6.17 (c), the specimen is tightly clamped between the restraint beams using chucking plates.

Last, in Fig. 6.17 (d) and (e), the external load on the restraint beams is released. The total deflection of the two restraint beams (δ) is measured. At this stage, the initial tensile force (F) is applied to the specimen before welding. With the transverse tensile load during laser welding, solidification cracks occur in the centerline weld.

From step (a) to (b), the testing procedure is repeated once more with a diverse amount of tensile force. By this means, solidification cracking in different local strains can be obtained.

Achievement of high temperature ductility curve in modified 9Cr1Mo steel and cast steel welds using U-type hot cracking with In-situ observation

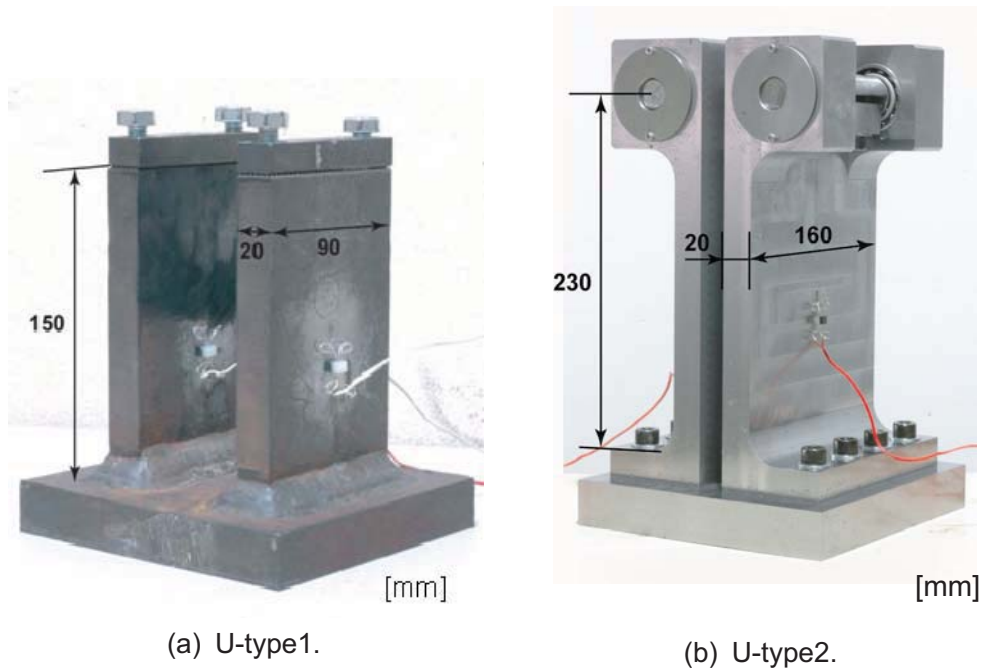


Fig. 6.17 U-type jigs used in U-type hot cracking test.

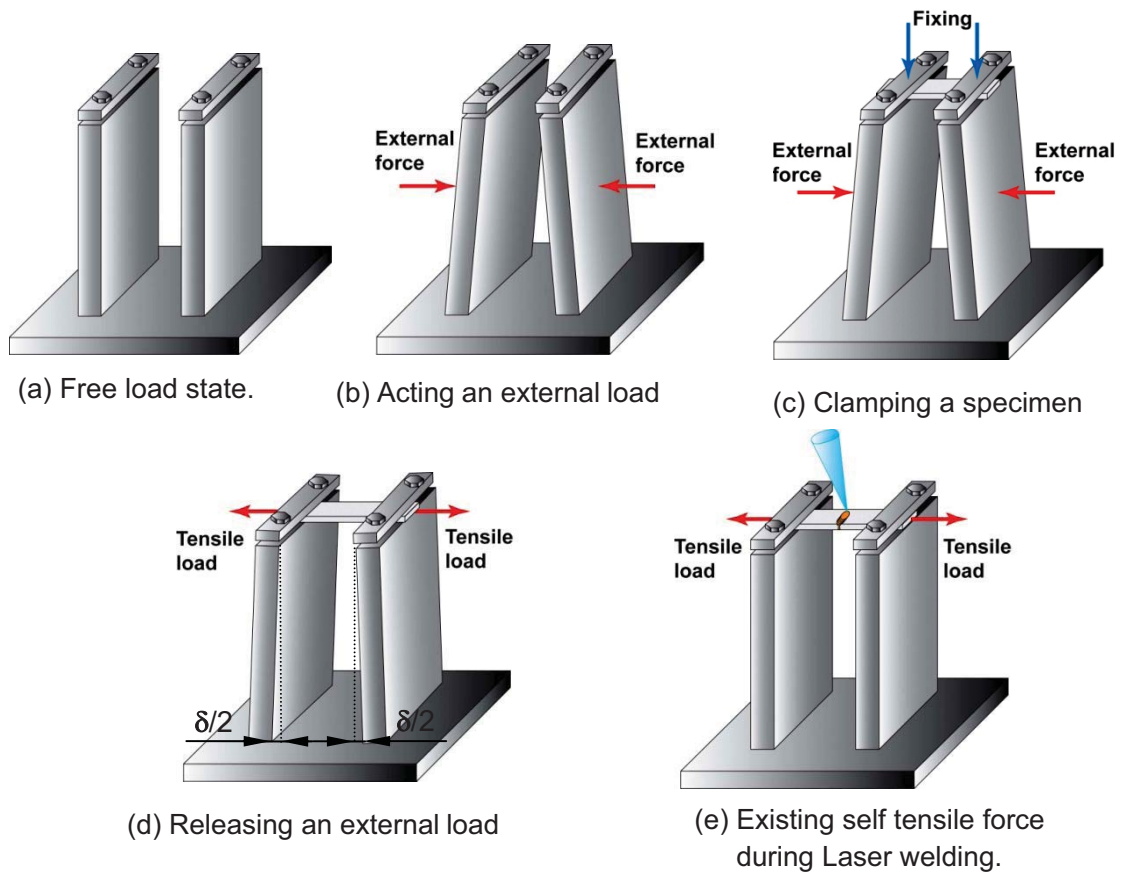
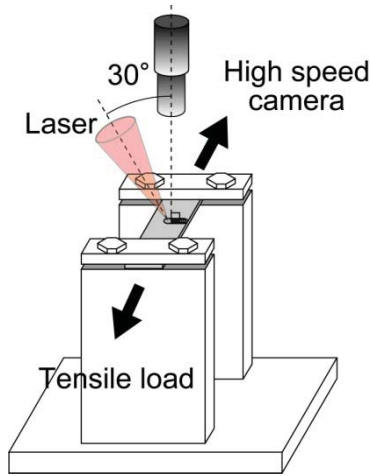


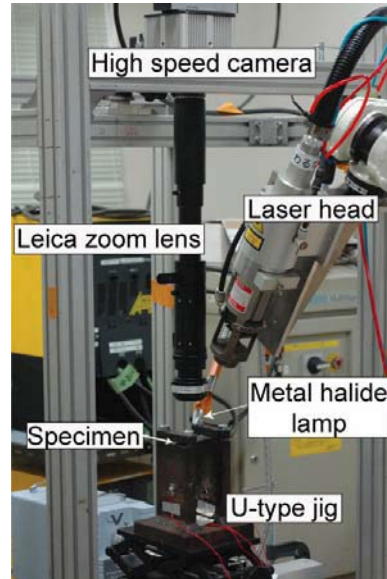
Fig. 6.18 Illustration of applied load in U-type hot cracking test.

Figure 6.19 shows the experimental setup of the U-type hot cracking test using an in-situ observation method. A fiber laser (IPG YLR3000) was used to provide the weld pool. The laser irradiation angle was set up with an incline of 30° , so that the laser irradiation did not reflect, causing damage to the camera. A high speed camera (nac, MEMRECAM Hx-3) was used to record the dynamic deformation at the trailing edge of the weld pool. A Macro lens (Nikon, 200 mmf/4D(IF)) with a close-up lens (Nikon, No. 6T) and zoom lens (Leica, Z16 APO) were used to obtain magnified observation. A metal halide lamp (Sumita, LS-M210) was used to provide enhanced lighting. This lighting illuminated the uneven surface of the weld bead and made concentrated light spots. In such a case, it helps with easily making an in-situ measurement of local strain.

Optical filters were installed in front of the magnified lens in order to clearly observe the trailing edge of the weld pool during laser welding. Fig. 6.20 shows the transmission conditions of the filters used. A near-infrared absorption filter (Sigma, CCF-50S-500C) was employed to filter out the reflecting laser beam (ray wavelength of 1070 nm) and other infrared rays from the weld pool. Thus, only the visible light could pass through the camera. A cold filter (Sigma, CLDF-50S) was used to absorb the excess heat and prevent heat damage to the near-infrared resonance filter. Moreover, the working distance between the lens and the weld pool is very close, so heat build-up can damage the cold filter. Therefore, a hot mirror (Edmund Optics, Mirror hot 0 DEG 50MM SQ) was used to reflect the infrared light and transfer the visible light. In the meantime, a protective lens was put in front of the filter lenses to prevent damage from spatter and metal vapor. Welding conditions and conditions of in-situ observation are detailed in Table 6.8 and Table 6.9.



(a) Schematic illustration of U-type hot cracking test using in-situ observation.



(b) Picture of U-type hot cracking test.

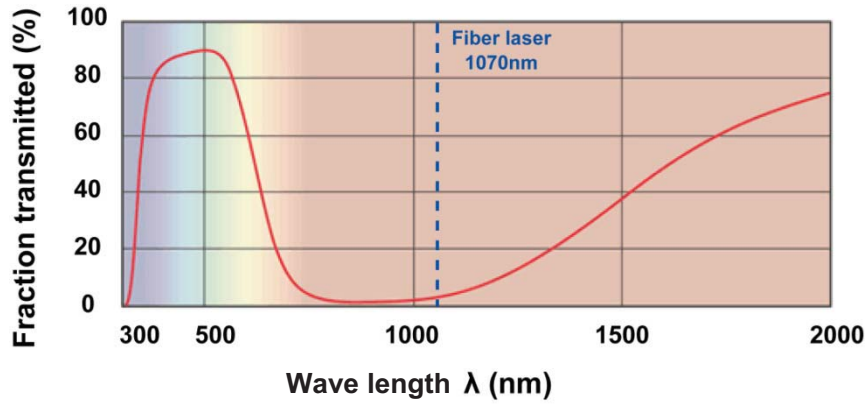
Fig. 6.19 Experimental setup of U-type hot cracking test.

Table 6.8 Welding conditions of U-type cracking test

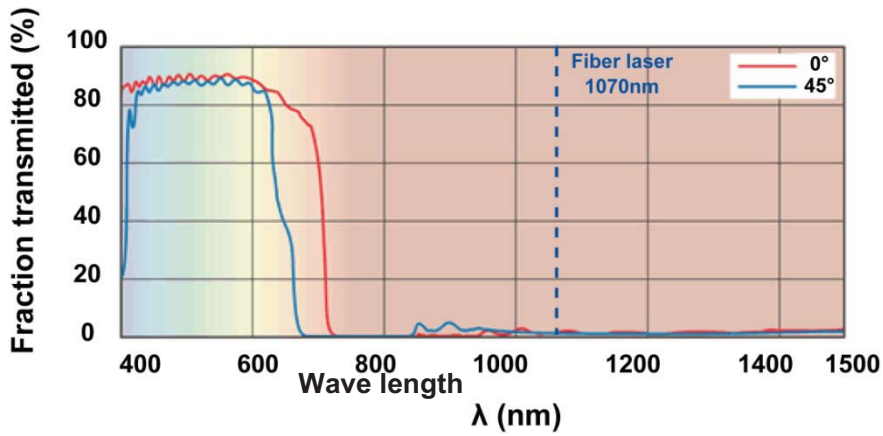
Laser type	Fiber laser
Laser power (kW)	
Modified 9Cr1Mo specimen	2.0
G69A3UMN4M3 specimen	1.6
Welding speed (m/min)	0.4
Laser spot diameter (mm)	0.4
Irradiation angle (deg.)	30
Penetration shape	Full
Argon shielding gas (l/min)	
Top side	50
Back side	15

Table 6.9 Conditions of in-situ observation

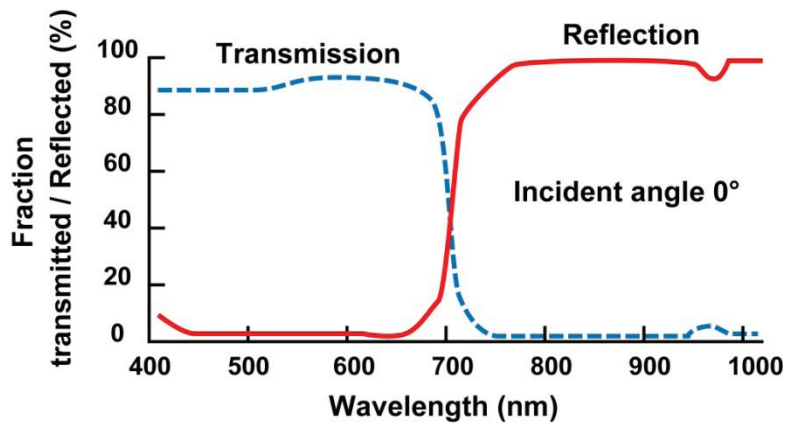
Frame rate, fps	1000
Shutter speed, sec.	1/1000
Optical magnification times	4.8(3.57 $\mu\text{m}/\text{pixel}$)
Aperture value	open
Lighting	Metal halide lamp
Optical filter	Near-infrared absorption filter, Cold filter, and Hot mirror



(a) Near-infrared absorption filter.



(b) Cold filter.



(c) Hot mirror

Fig. 6.20 Transmission conditions of optical filters used

6.4.2 Approach to Measuring Local Critical Strains

During the hot-type cracking test, occurrences of solidification cracking are observed and recorded through in-situ observation by means of a high speed camera. Thus, the initiation of solidification cracking can be detected. In order to measure the local critical strain, special image processing using tracking system software (Ditect, Dipp-Motion Pro2D) was performed so as to determine a dynamic deformation history at the trailing edge of the weld pool.

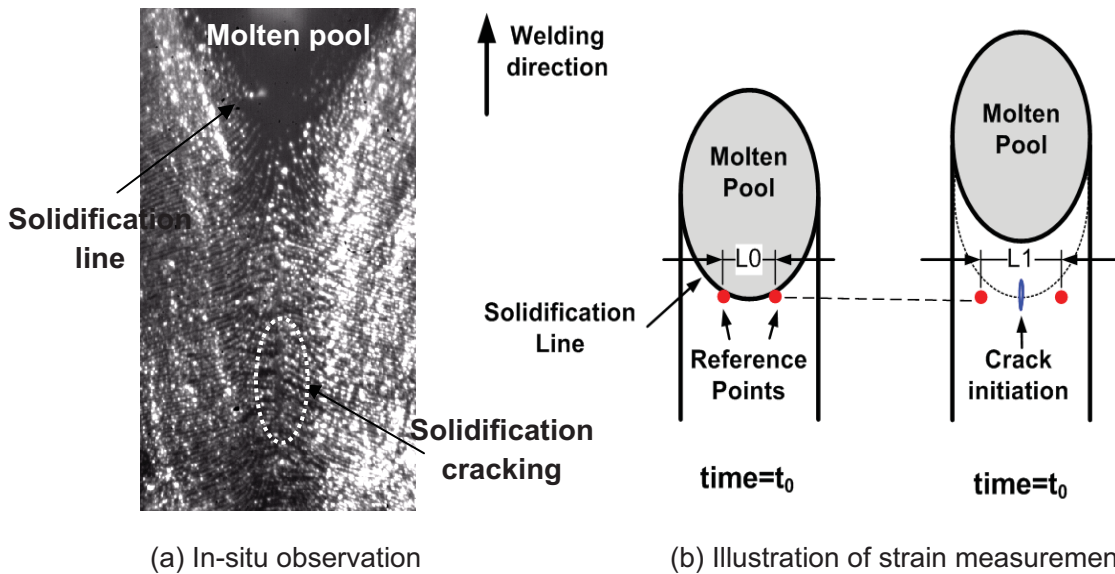


Fig. 6.21 Measurement of local critical strain.

As shown in Fig. 6.21, the in-situ observation image of the trailing edge of the weld pool can be considered as the start of the solidification. Stress and strain can be regarded as zero. First of all, the moment when cracking first occurs is determined. At this time (t_1), two reference points across the crack initiation are defined as L_1 . Then, the recorded movie is rewound to the moment when the reference points cross the end of the weld pool (t_0). The distance between the two reference points at this time is defined as L_0 or gauge length. By this means, the distance between the two reference points is altered along the tensile direction and the local strain (ϵ) is calculated as shown by Equation (6.4).

$$\text{Local strain } (\epsilon) = \frac{L_1}{L_0} \times 100 \quad (\%) \quad (6.4)$$

Where L_0 is Initial length, L_1 is Length at crack initiation

In this study, L_0 , or gauge length, was chosen to be about 1mm because it not only provided little scattering data but also reproducibility of critical strain measurement.

When compared with the traditional Trans-Varestraint test, this method not only determines the local strain concentration near the cracking, but also provides the strain at almost the exact instant the cracking occurs.

6.5 Measurement of Temperature History during Solidification

In order to achieve the high temperature ductility curve, it is necessary to obtain the temperature history when the critical strain occurs. Figure 6.21 provides an illustration of the measurement method of the temperature history near the solidification cracking. In this study, temperature measurement was performed using an optical fiber radiation thermometer (JFE Techno-Research Ltd, FIMTHERM-H) [98] in the weld metal due to its ability to obtain data during rapid cooling. Figure 6.20(a) provides an illustration of the measured temperatures. The thermometer was inserted at the trailing edge of the weld pool during laser welding. The guide jig was used to lead the thermometer directly into the designated position. At the time of $t=t_0$, the thermometer was dropped into the molten pool. The measured temperature exhibits a cooling curve that covers the solidification temperature range. In that way, using the time when crack initiation occurs, the temperature of the crack initiation can be obtained. The characteristics of the optical fiber radiation thermometer, as illustrated in Fig. 6.21(b), were sensor material made of indium gallium arsenide (InGaAs), a stainless steel protection tube with a diameter of 1.4 mm, quartz wire fiber with a diameter of 250 μm , and a detectable temperature range between 410-2000 $^{\circ}\text{C}$. The sampling rate of the data record was 1000 Hz.

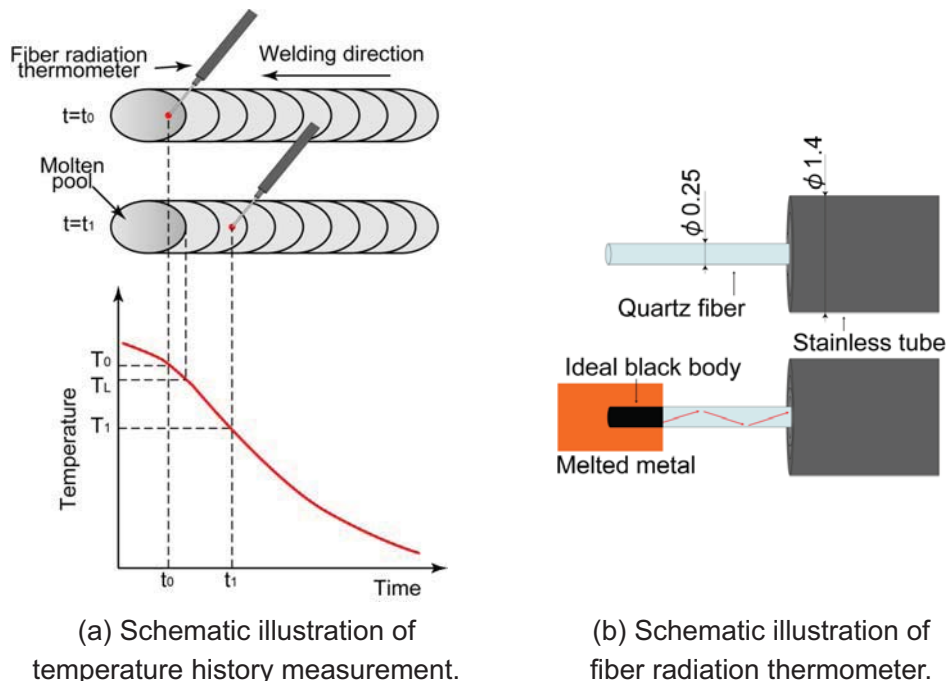


Fig. 6.21 Measurement of temperature history at the trailing edge of the molten pool.

6.6 Achievement of High Temperature Ductility Curve

6.6.1 Solidification cracking in U-type Hot Cracking Test

Figure 6.22 shows the top and back view of the Modified 9Cr1Mo specimens after the U-type hot cracking test. According to the magnitude of initial tensile load, U-type 1 and U-type 2 jigs were used to provide an initial load on the test specimens. As a result, no crack was found with an initial load of less than 3.1 kN. When increasing the initial load to a range of 4.0~7.0 kN, solidification cracking was induced, ranging from a small crack to an almost total fracture along the centerline of the weld bead.

Figure 6.23 shows the appearances of specimens of G69A3UMN4M3 with 40% base metal dilution after the U-type hot cracking test. From the results, solidification cracking did not occur in the initial load of 8.3 kN. When the initial load was varied in a range of 9.8~12.1 kN, solidification cracking could be observed. A small crack occurred at a position of about 25 mm from the welding start point.

Material: Modified 9Cr1Mo

Welding speed: 0.4 m/min

Laser power: 2.0 kW

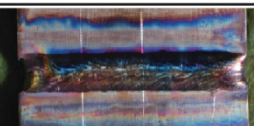
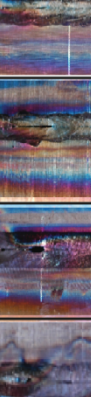

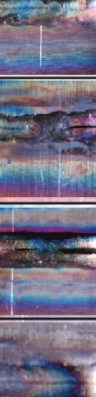











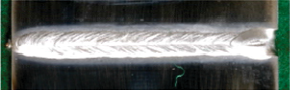
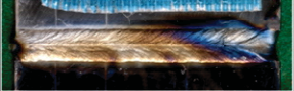

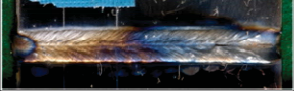





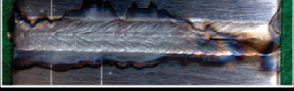


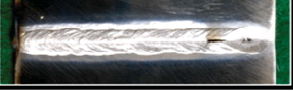
Jig type	Initial load	Topside	Backside
U-type1	4.4kN		
	5.0kN		
	5.9kN		
	6.7kN		
	7.0kN		
U-type2	4.0kN		
	3.1kN		

Fig. 6.22 Appearances of specimens after U-type hot cracking test (Modified 9Cr1Mo)

Material: G69A3UMN4M3

Welding speed: 0.4 m/min

Laser power: 1.6 kW

Jig type	Initial load	Topside	Backside
U-type1	8.3 kN		
	9.8 kN		
	10.1 kN		
	11.0 kN		
	12.1 kN		
U-type2	10.0 kN		
	11.3 kN		

5 mm

Fig. 6.23 Appearances of specimens after U-type hot cracking test (G69A3UMN4M3 with dilution of 40%)

6.6.2 Temperature History at the Trailing Edge of the Molten Pool

In this experiment, the optical fiber radiation thermometer was immediately dipped into the molten pool. The measurement position is the center weld line and also the tailing of the molten pool. Insertion accuracy was aided by a small hollow-tube guide. Along with measuring the temperature, the molten pool movement was directly observed with a high speed camera, and when the tailing of the molten pool was at the designated position, the thermometer was manually dipped into the molten pool. Figure 6.24 shows the sequent images captured while dipping the thermometer.

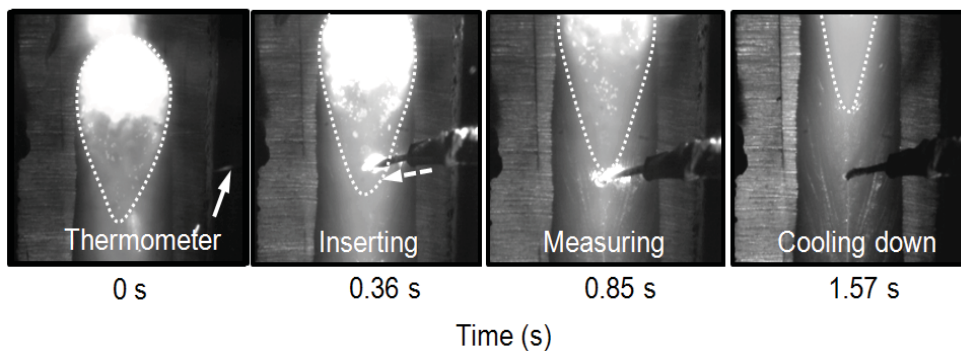


Fig. 6.24 Temperature history measurement by inserting thermometer.

Figure 6.25 (a) shows the cooling curve of Modified 9Cr1Mo weld metal. In order to estimate the liquidus and solidus temperatures, the cooling curve was converted into the differential curve as shown in Fig. 6.25 (b). Due to the effect of the latent heat during solidification, it can be seen that two common inflection points appear at 1501°C and 1448°C, which compare the temperature-time curve and the differential curve. Therefore, the solidification temperature range is regarded as being between 1501°C and 1448°C.

Also, Fig. 6.26 (a) and (b) shows the cooling curve and the differential curve of the dissimilar weld joint G69A3UMN4M3 with 40% dilution. Two common inflection points appear at 1490 °C and 1431°C. Therefore, these points are considered the liquidus and solidus temperatures, respectively.

Achievement of high temperature ductility curve in modified 9Cr1Mo steel and cast steel welds using U-type hot cracking with In-situ observation

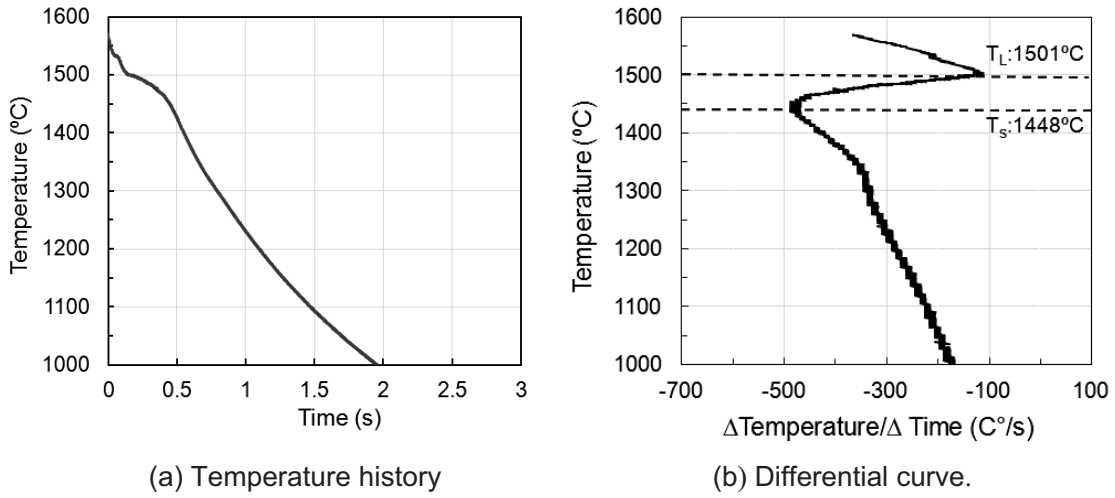


Fig. 6.25 Temperature history and differentiation curve. (Modified 9Cr1Mo)

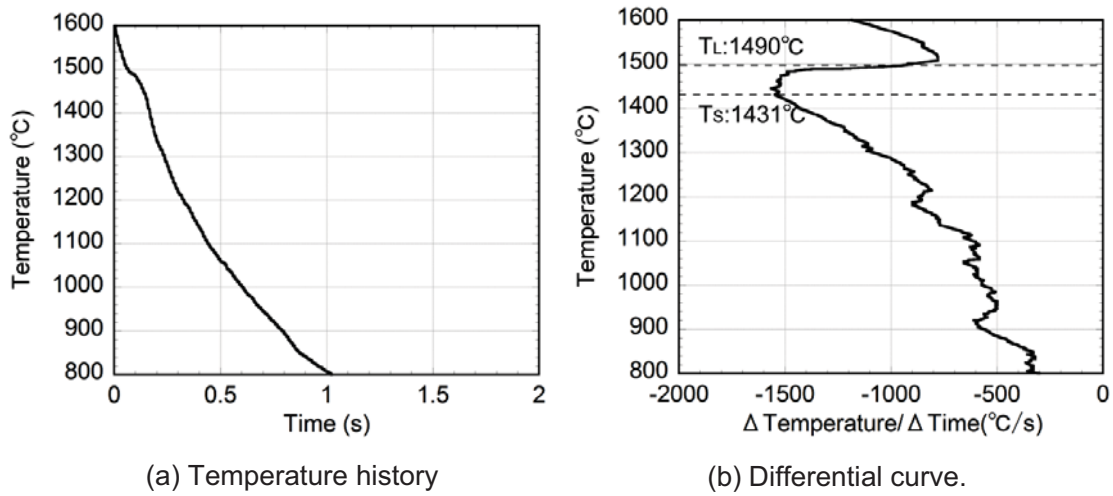


Fig. 6.26 Temperature history and differentiation curve. (G69A3UMN4M3 with dilution of 40%)

6.6.3 High Temperature Ductility Curves

As previously mentioned, regarding the measurement method of the local critical strain, the local strain as a function of time to crack initiation was measured in each initial load. Figure 6.27 shows the local strain histories of Modified 9Cr1Mo weld metal. From the results, it is seen that the maximum critical strain is not more than about 1.2% and there is a tendency for it to decrease with an increasing initial load. When applying an initial load of 3.1 kN, no cracking appears in the strain curve and it is rather constant. No cracking occurs at a strain level of about 0.3%.

For the cast steel weld joint G69A3UMN4M3 with 40% dilution, Fig. 6.28 shows its maximum critical strain is higher than the 9Cr1Mo weld metal. The maximum critical strain of the G69A3UMN4M3 weld metal is about 2.6%. Furthermore, critical strain tends to decrease with an increasing initial load. Critical strain does not occur in G69A3UMN4M3 weld metal when applying an initial load of 8.2 kN.

In order to obtain the high temperature ductility curve, the critical strain-time curve obtained by the U-type hot cracking test and the cooling curve (temperature-time) were used in order to draw the relationship of the critical strain as a function of temperature in a solidification range. Figure 6.29 illustrates the approach to achieve the high temperature ductility curve. For instance, the red-cross in Fig. 6.29 (a) represents the sample point of a certain critical strain depending on time. Subsequently, the time at which crack initiation occurs can be calculated to the exact temperature with the cooling curve in Fig. 6.29 (b). The cooling curve starts with the melting point of 1501°C and drops to the end at the solidus point of 1448°C. This step was performed repeatedly at every critical strain point as shown in Fig. 6.29 (c).

Figure 6.30 shows the achievement of the high temperature ductility curve of modified 9Cr1Mo weld metal. As a result, it is seen that the greater solidification cracking susceptibility was induced at the similar solidus temperature. The maximum critical strain occurs within 1.0% of its liquidus temperature. Meanwhile, the minimum critical strain value is around 0.3 %. Moreover, this critical strain level has a tendency to decline sharply when the temperature cools down close to the solidus temperature.

Figure 6.31 shows the high temperature ductility curve of the cast steel weld joint G69A3UMN4M3 with 40% dilution. In this case, the minimum critical strain is found within about 1.2% of the solidus temperature. Likewise, the critical strain tends to decrease close to its solidus temperature.

Comparing other materials using the same application, Fig. 6.32 exhibits the solidification cracking susceptibility of Modified 9Cr1Mo steel compared to other heat-resistant steels, namely SUS310S, and Inconel600 [99-100]. It can be seen that Modified 9Cr1Mo seems to be more susceptible than other materials. In addition, Fig. 6.33 presents a comparison of the high temperature ductility curves of SCMn3B base metal [23] and G69A3UMN4M3 weld metal with 40% dilution. The result clearly shows that cracking during welding is more likely to occur in

SCMn3B base metal. In other words, the SCMn3B base metal has more solidification cracking susceptibility than G69A3UMN4M3 weld metal.

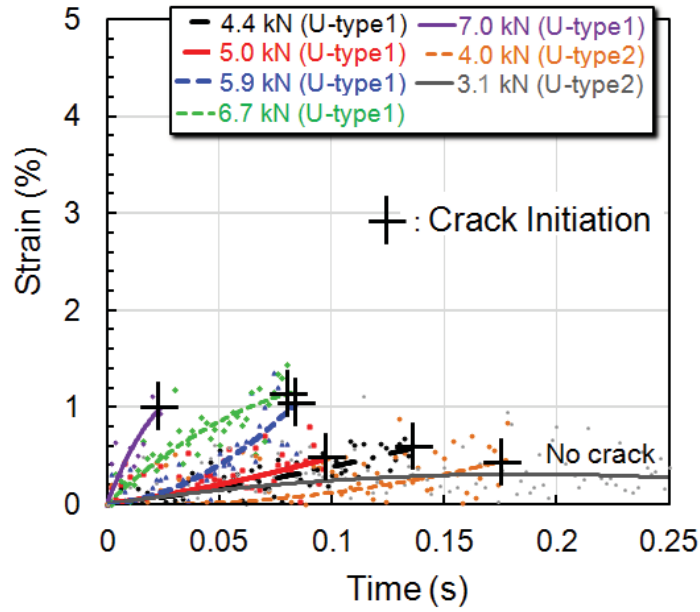
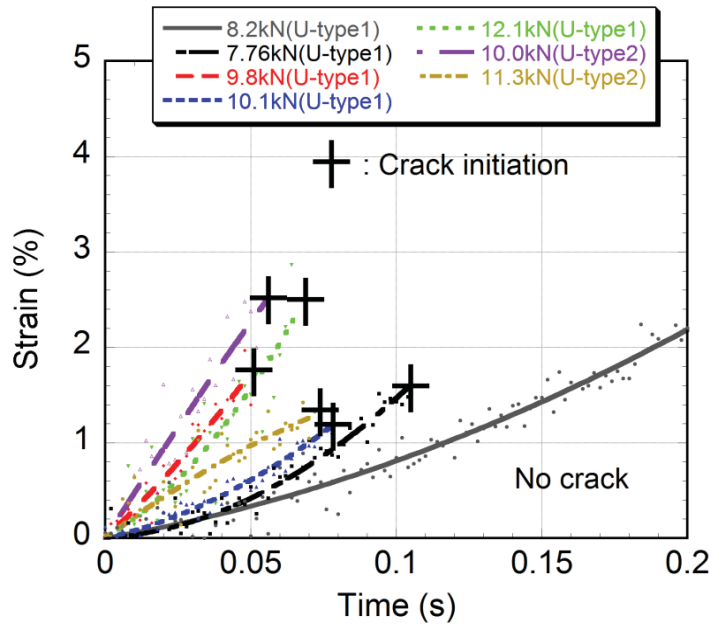


Fig. 6.27 Strain-time curve with crack initiation (Modified 9Cr1Mo weld metal).



Weld metal = G69A3UMN4M3, Welding speed=0.4 m/min,
Laser power=1.6 kW, Gauge length = 1 mm

Fig. 6.28 Strain-time to crack initiation (G69A3UMN4M3 with dilution of 40%).

Achievement of high temperature ductility curve in modified 9Cr1Mo steel and cast steel welds using U-type hot cracking with In-situ observation

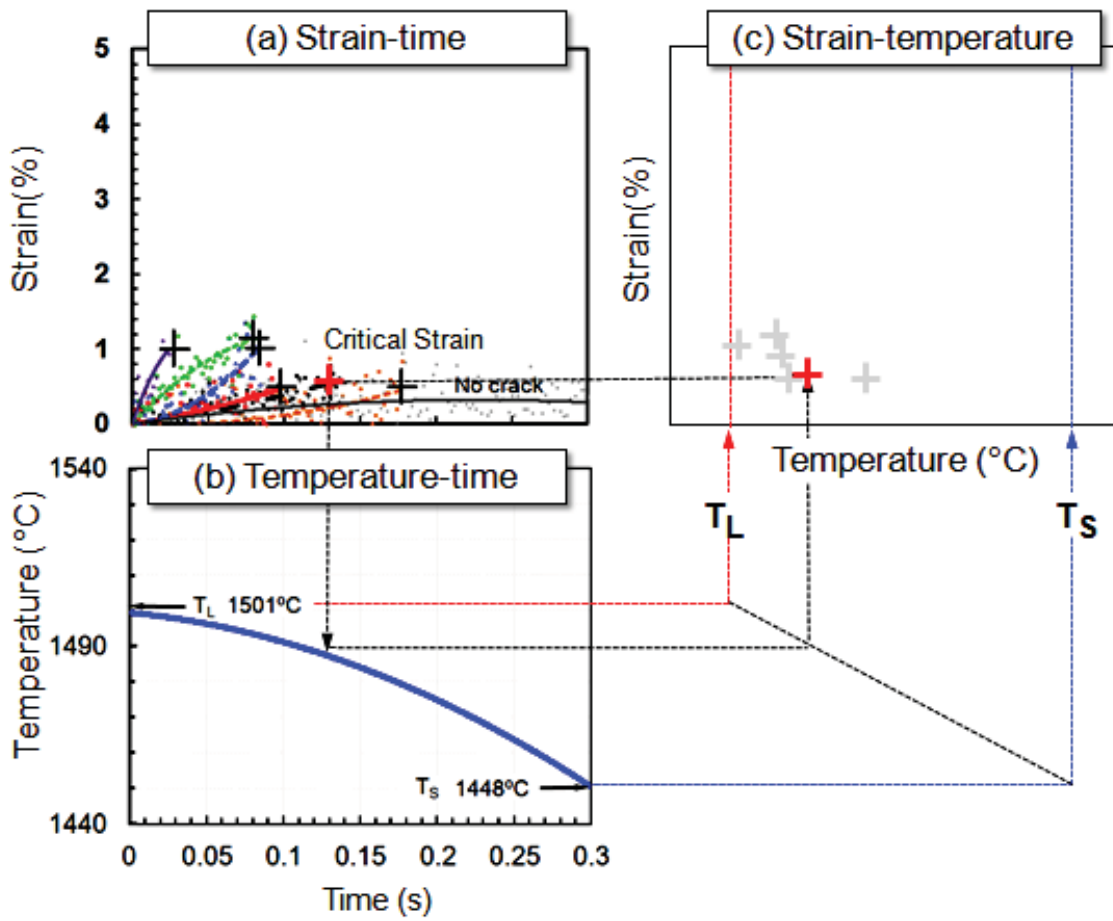


Fig. 6.29 Achievement of high temperature ductility curve.

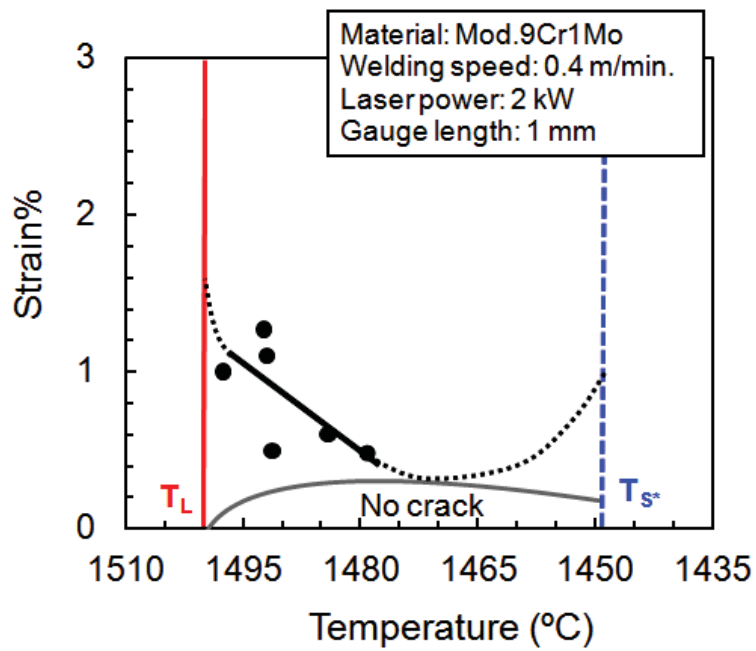


Fig. 6.30 High temperature ductility curve of modified 9Cr1Mo weld metal.

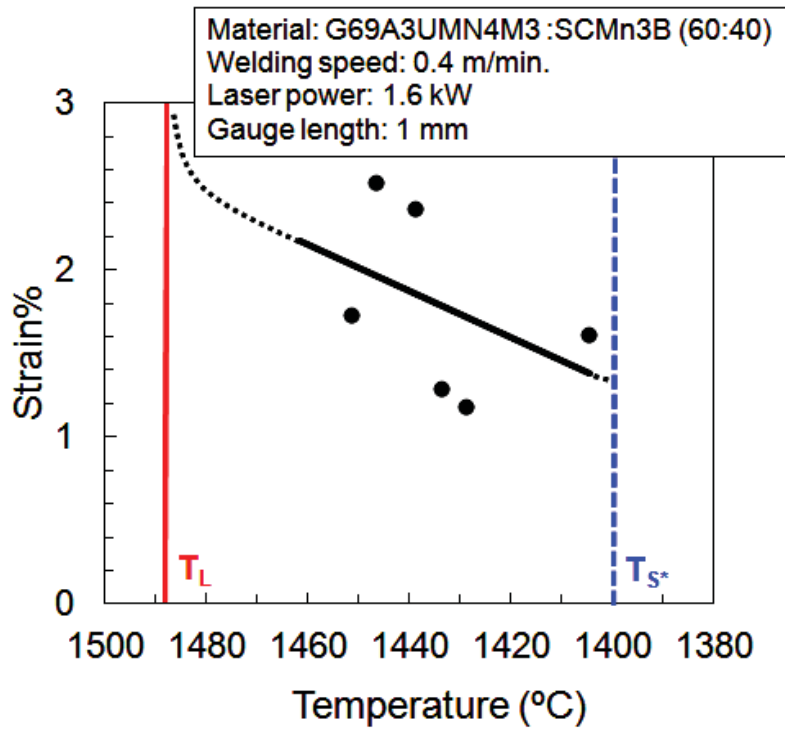


Fig. 6.31 High temperature ductility curve of G69A3UMN4M3 weld metal .

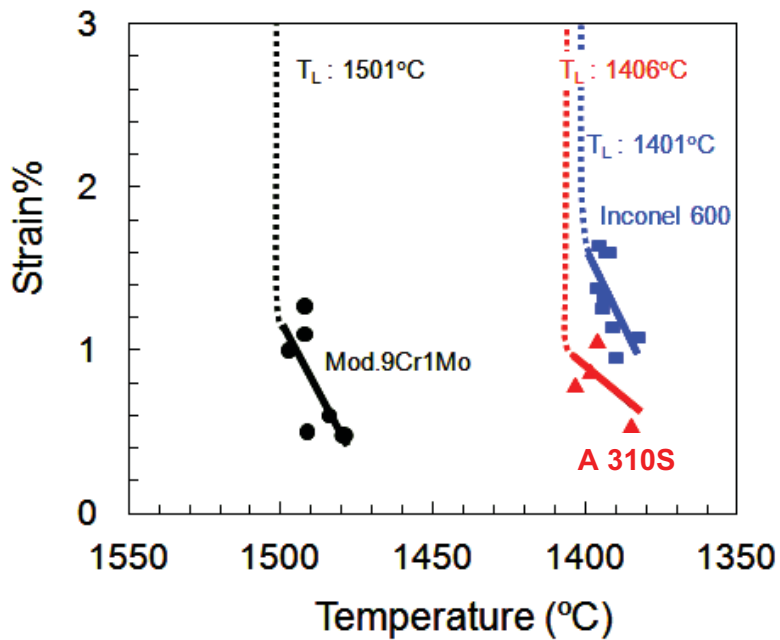


Fig. 3.32 Comparison of high temperature ductility curve with other heat resistant materials.

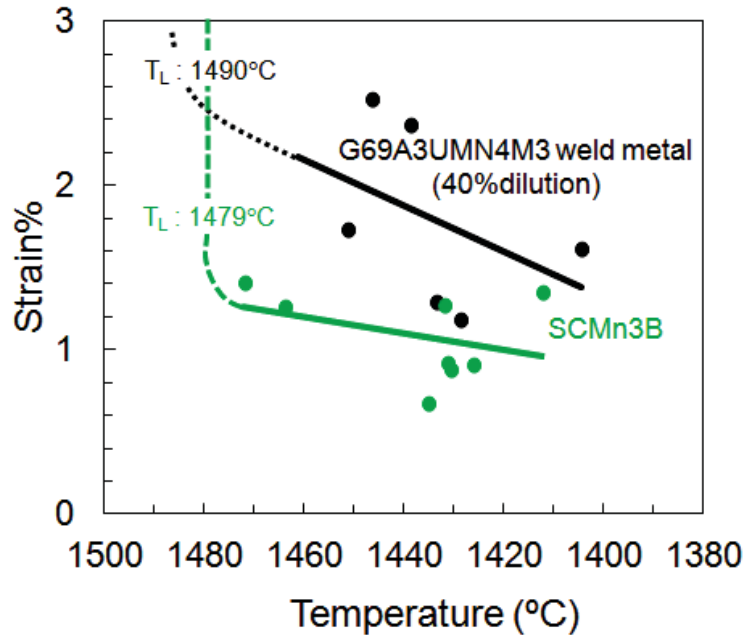


Fig. 33 Comparison of high temperature ductility curve with G69A3UMN4M3 weld metal with 40% dilution, and SCMn3B base metal.

6.7 Summary

In this chapter, a quantitative evaluation of solidification cracking in modified 9Cr1Mo weld metal and the dissimilar weld joint of G69A3UMN4M3 with 40% dilution was investigated by the achievement of high temperature ductility curves. The U-type hot cracking test with in-situ observation was carried out. The conclusions are as follows:

1. By using hot wire laser welding to make a specimen for the U-type hot cracking test, this method was able to produce a very low dilution ratio. This study particularly emphasized the weld metal, so it was very beneficial to avoid undesired compositions from the dilution effect of the base metal. Furthermore, the two-wire feeding method has the potential to provide a specified dilution ratio in the dissimilar weld joint. This could be accomplished in G69A3UMN4M3 weld metal with 40% dilution, which was built up on mild steel SM490.

2. The U-type hot cracking test with in-situ observation by means of the high speed camera was employed to determine the local critical strain to crack initiation. U-type 1 and U-type 2 testers were used to apply an initial tensile load on the specimens. With additional measurement of the temperature history at the weld pool using an optical fiber radiation thermometer, together special image processing by the tracking system software, the temperature-dependent local critical strain of each studied material was measured. Such an approach allowed this study to successfully evaluate the quantitative solidification cracking.

3. Using high temperature ductility curves, solidification cracking susceptibility was quantitatively evaluated. Modified 9Cr1Mo weld metal exhibited a minimum critical strain of about 0.3%, while G69A3UMN4M3 weld metal at about 1.2%. In both cases, there is a tendency towards greater solidification cracking susceptibility when the weld bead cools down close to its solidus temperature.

4. Compared with other materials in a similar application, Modified 9Cr1Mo weld metal exhibited greater solidification cracking susceptibility than other high-resistance steels such A 310S and Inconel600. Meanwhile, G69A3UMN4M3 weld metal with 40% dilution, which was used to weld the SCMn3B base metal in the U-groove weld cracking test, exhibited lower solidification cracking susceptibility.

Chapter 7

Computational Welding Simulation Approach for High Temperature Strain Analysis

7.1 Introduction

As previously described in Chapter 6, the high temperature ductility curves of modified 9Cr1Mo weld metal and G69A3UMN4M3 with 40% dilution has already been achieved. According to the principle of prediction of solidification cracking based on the dynamic between the high temperature ductility curve and strain rate during welding, this chapter therefore emphasizes the development approach to high temperature strain analysis in the weld bead during solidification. Computational welding simulation by means of finite element method (FEM) was employed. MSC .Marc software and a special subroutine program were applied in order to achieve the thermal distribution and strain calculation. All simulation results were validated based on experiments such as a cross-section weld, a temperature history and an elastic strain measurement. The implements of the calculation and the experimental validation were carried out as follows.

First, thermal and strain analyses related to hot-wire laser welding with a narrow groove were performed. As for the thermal analysis, temperature distributions are important in estimating the strain rate during welding, while the heat transfer phenomenon of hot-wire laser welding in a narrow groove is so complicated that the general equation of the heat source model cannot be applied. Therefore, such welding phenomenon was studied using high speed camera observation and then the development of a three-dimensional FEM with a moving heat source for hot-wire laser welding with a narrow-gap joint was proposed. The computational simulation was verified by comparing it with the experimental measurement in terms of the thermal history, peak temperature distribution close to the fusion zone, and the cross section of the weld bead. Temperature was measured using an optical-fiber radiation thermometer (JFE Mechanical Corporation) in the weld metal because it can acquire data during rapid cooling. Thermocouples were also set in the direction transverse to the weld. Furthermore, the longitudinal elastic strain at the side wall and the contraction of the groove width were compared as well in the mechanical analysis.

Second, the GMAW process regarding the U-groove weld cracking test with a full restraint type was calculated. A 3-D finite element model with Goldak's double ellipsoidal heat source was implemented. Actual welding was performed in the U-groove weld cracking test. Then, the simulation results, namely a cross-section of the weld shape, the thermal history at the bottom of the specimen nearby a weld pool, and also the longitudinal elastic strain at the specimen's side wall, were compared to the experimental measurements.

7.2 Computational simulation for Hot-Wire Laser Welding with a Narrow Groove Joint

7.2.1 Experimental Welding Procedure

This experiment was carried out to verify the FEM simulation. That is, Modified 9Cr1Mo steel was used as the base metal. The chemical compositions of the materials used are shown in Table 7.1. The dimensions of the sample plate as illustrated in Fig. 7.1 were 120^w mm × 75^l mm × 21^t mm. A U-shaped groove joint with a gap width of 3 mm was applied. Specimens were automatically welded using a Yb:YAG fiber laser power source with a six-axis robotic welder and a hot-wire feeding system. The laser beam utilized an operating wavelength of 1070 nm, with a beam parameter product of beam quality 5.4 mm·mrad. Welding conditions, as seen in Table 7.2, were set at a laser output power of 3 kW, a defocused laser beam diameter of 3 mm, a welding speed of 0.3 m/min, a wire diameter of 1.0 mm, and a feeding speed of 4.8 m/min. Argon was employed as a shielding gas to prevent an undesired reaction with the outside atmosphere.

Table 7.1 Chemical composition of materials used (mass %) in Modified 9Cr1Mo weld metal

Material	C	Si	Mn	P	S	Fe	Cr	Mo	Nb	V	Cu
Base metal : Mod.9Cr1Mo	0.01	0.37	0.43	0.014	0.002	Bal.	8.55	0.98	0.08	0.19	0.02
Filler wire : (φ1.2) ER90S-G	0.08	0.12	1.02	0.005	0.004	Bal.	8.99	0.90	0.04	0.18	0.12

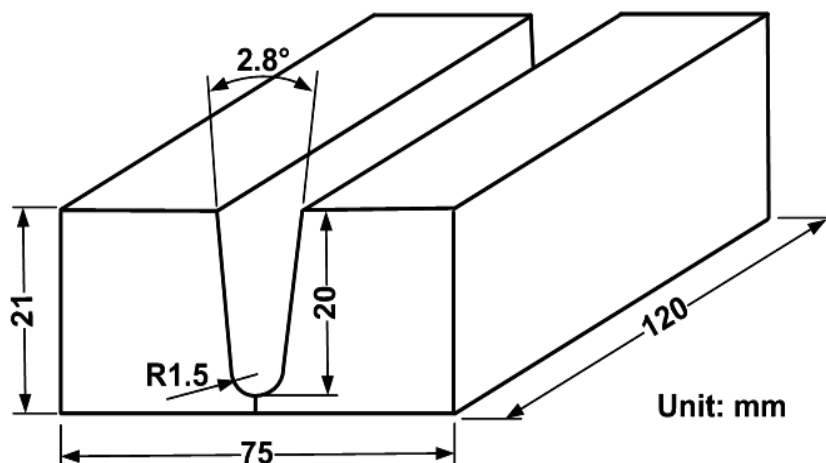


Fig. 7.1 Geometry of joint and test plate.

Table 7.2 Utilized welding parameters

Laser type	Fiber laser
Laser power (kW)	3
Traveling speed (m/min)	0.3
Defocused length (mm)	60
Laser spot diameter (mm)	3
Irradiation angle (deg.)	5
Wire feeding speed (m/min)	4.6
Wire feeding angle (deg.)	80
Wire feeding position (mm)	2
Wire current (A)	62
Argon shielding gas (l/min)	30

7.2.2 Finite Element 3-D Modeling

FEM by commercial codes MSC. Marc 2012 and a special subroutine program were applied in order to achieve a thermal distribution and a mechanical strain. Because of its symmetry along the weld centerline, one half of a sample plate was discretized with a 3-D thermo-mechanical solid element type of 8 node isoparametric hexahedral. The finer element size of 0.25 mm in the weld metal and 0.5 mm nearby the fusion zone were meshed in order to obtain precise results as shown in Fig. 7.2. The convection heat loss was defined to be a heat transfer coefficient of $45 \text{ W/m}^2/\text{C}$ at all of the plate surfaces except for the symmetrical plane, which was assumed to have an adiabatic condition, while the radiation heat loss was negligible. In a mechanical restraint condition, all the nodes on the symmetrical surface of a welding bead along the longitudinal direction are fixed in a transverse welding direction, whereas the degree of freedom at the side edge of a work piece is constrained to prevent rotational movement.

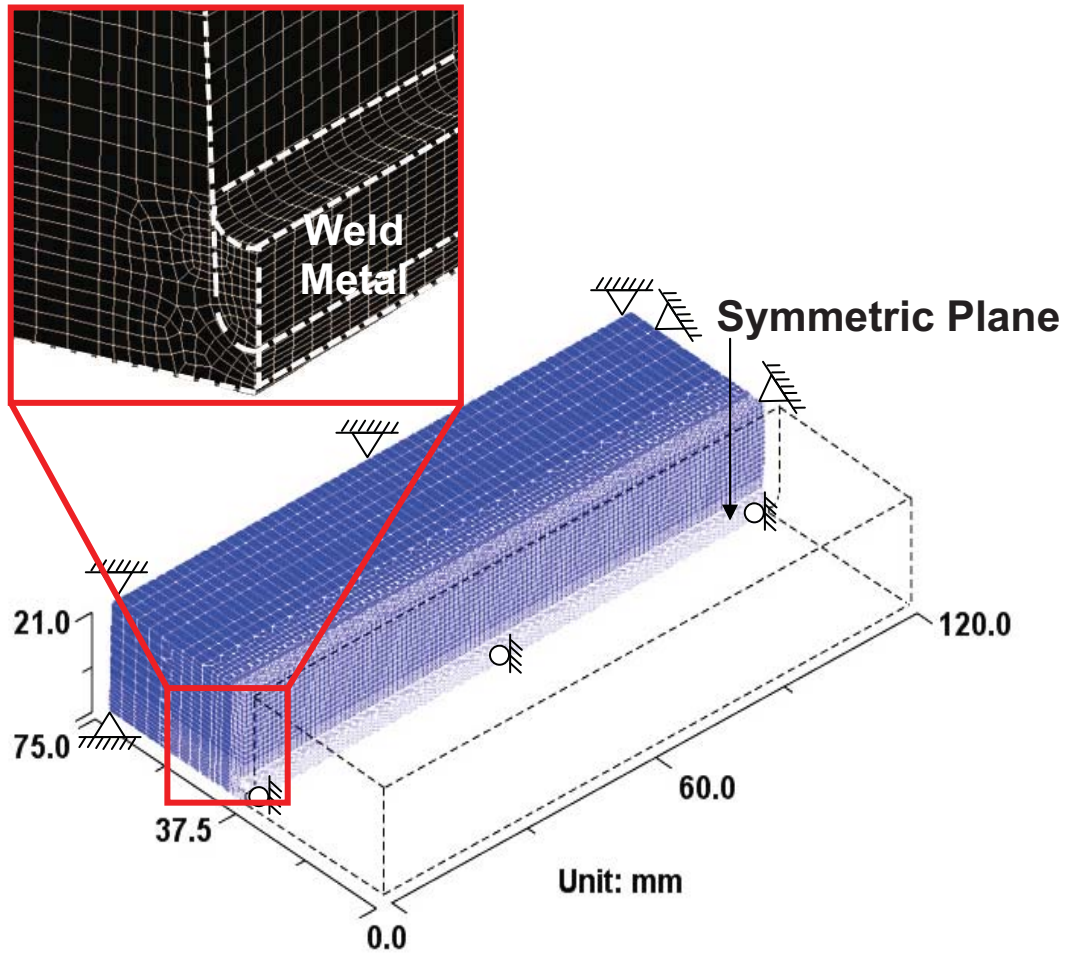


Fig. 7.2 Illustration of 3-D FEM model of a narrow welding.

7.2.3 Material properties

Thermo-mechanical material properties dependent on temperature such as thermal conductivity, specific heat, and thermal expansion were estimated with a thermodynamic approach through the application of commercial software, JMatPro. Poisson's ratio was assumed to be 0.29 with a mass density of 7750 kg/m^3 . Calculated solidus and liquidus temperatures were assigned as 1440°C and 1505°C , respectively. Yield strength and Young's modulus are taken from the literature review [101] as shown in Fig. 7.3.

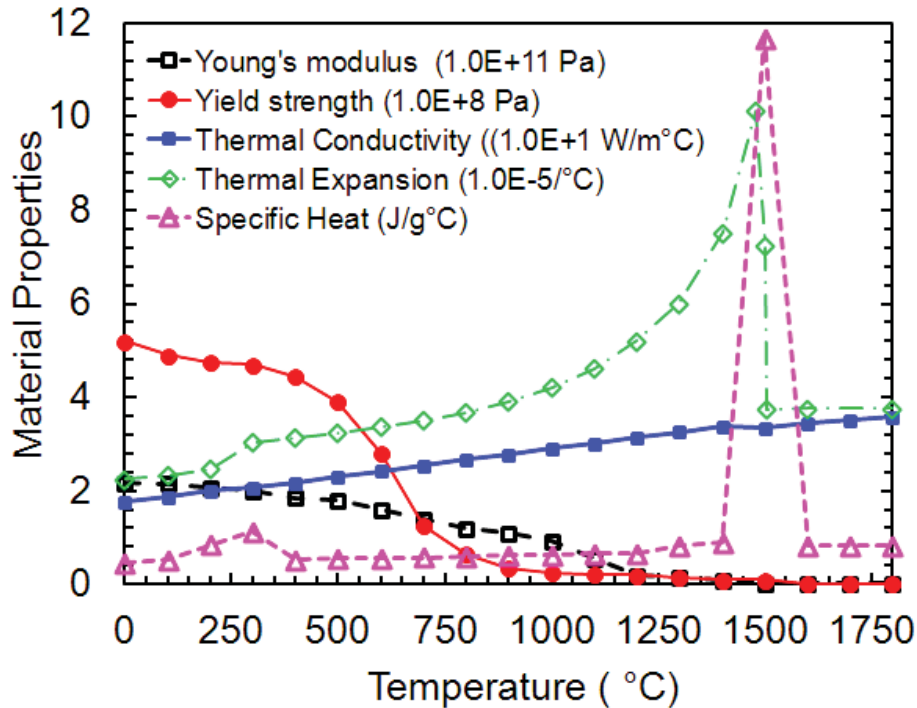


Fig. 7.3 Thermo mechanical material properties as a function of temperature.

7.2.4 Strategic FEM Approach for Welding Heat Source in Hot-Wire Laser Welding

To study the complex phenomenon of hot-wire laser welding with a narrow groove as represented in Fig. 7.4, the molten pool behavior was observed using a high speed camera as mentioned earlier in Chapter 3. Simply put, a hot-wire laser heat source consistent with such phenomenon was developed, as illustrated in Fig. 7.5. When taking into account the heat energy transfer during welding, the heat flow in hot-wire laser welding can be depicted, as seen in Fig. 7.6(a). Namely, the formation of a molten pool shape consists of a combination of three heat energy sources, namely hot-wire feeding (Q_1), a defocused laser beam (Q_2) and as an effect of a reflected laser irradiation (Q_3). According to the principle of conservation energy for control volume [102-103], heat transfer balance in the molten pool during welding can be written as equation (7.1):

$$\frac{dE}{dt} = \sum E_{in} - \sum E_{out} \quad (7.1)$$

Where dE/dt is the rate of energy change within the system, $\sum E_{in}$ is the total amount of energy entering the system and $\sum E_{out}$ is the total amount of energy leaving the system.

During hot-wire laser welding, hot-wire laser behavior can be considered to be the infinitesimal control volume shown in Fig. 7.6(b), with a steady state welding condition, hence

$$\sum E_{in} = \sum E_{out} \quad (7.2)$$

Therefore, the constant volume process can be rewritten in an explicit form as

$$Q_{hotwire} + Q_{laser} + Q_{Ref-laser} + \sum mass_{in} h_{in} = Q_{laser-loss} + Q_{con} + Q_{conv} + Q_{rad} + \sum mass_{out} h_{out} \quad (7.3)$$

Where,

- $Q_{hotwire}$ is the heat energy rate of hot-wire
- Q_{laser} is the heat energy rate of laser beam
- $Q_{Ref-laser}$ is the heat energy rate of laser reflection near a weld pool
- $Q_{laser-loss}$ is the heat loss rate of laser beam
- Q_{con} is the heat loss rate from conduction
- Q_{conv} is the heat loss rate from convection
- Q_{rad} is the heat loss rate from radiation
- $\sum mass_{in} h_{in}$ is the mass energy rate from a fed wire in a weld pool
- $\sum mass_{out} h_{out}$ is the mass energy rate leaving a weld pool

Let,

$$Q_{loss} = Q_{laser-loss} + Q_{rad} + Q_{cond} + Q_{conv}$$

Then,

$$Q_{hotwire} + Q_{laser} + Q_{Ref-laser} = Q_{loss} + \sum mass_{out} h_{out} - \sum mass_{in} h_{in}$$

As an assumption in this case, it is assumed that the change rate of the mass energy rate is equal to zero due to minimal spattering during welding. Radiation is not considered. Therefore, as can be seen in the equation above, there are three important heat energy sources in the hot-wire laser welding system, namely the heat sources generated through hot-wire feeding (Q_1), a defocused laser beam (Q_2) and as an effect of reflected laser irradiation (Q_3). The governing equation of energy conservation in heat conduction is shown as follows:

$$\frac{\partial(\rho cT)}{\partial t} = \frac{\partial^2(kT)}{\partial x^2} + \frac{\partial^2(kT)}{\partial y^2} + \frac{\partial^2(kT)}{\partial z^2} + q_{hotwire} + q_{laser} + q_{Ref.Laser} \quad (7.4)$$

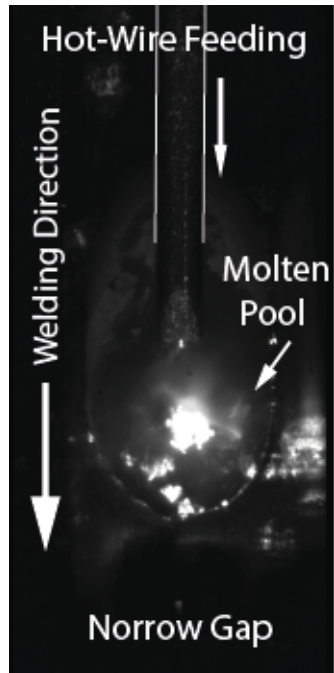


Fig. 7.4 Phenomena of hot-wire laser welding observed by high speed camera.

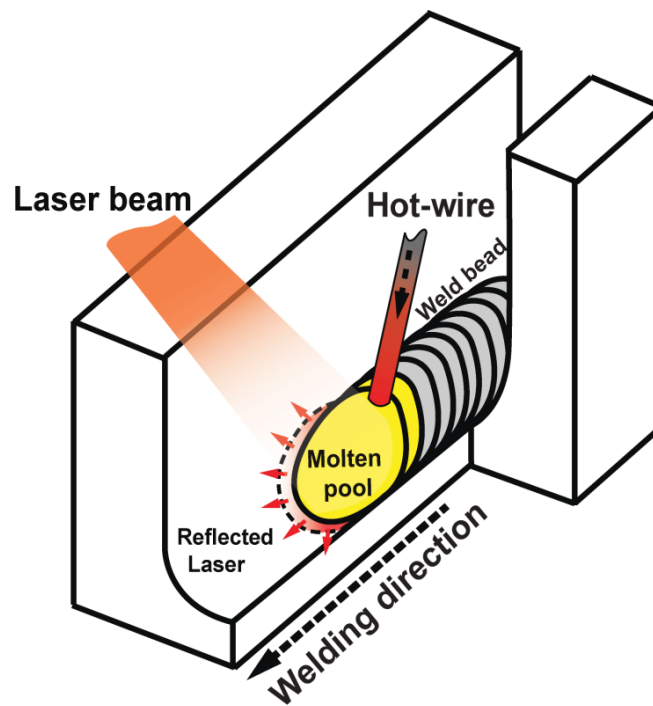
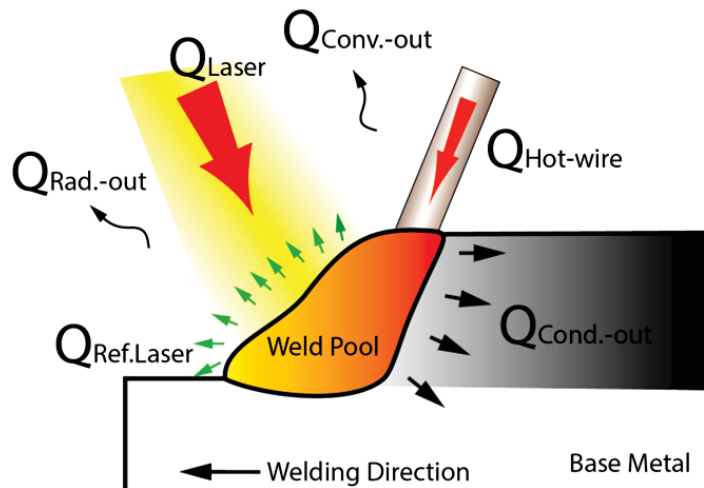


Fig. 7.5 Schematic illustration of hot-wire laser heat source.

As for the FEM strategic approach, at the start (time = 0) the deposition of the weld filler metal was generated using birth and death elements with an initial uniform temperature (Q_1) which was nearly equal to the wire's melting point (1436 °C). This method was applied at each time-step increment to imitate the weld deposition from feeding the hot-wire. Subsequently, the surface heat flux from the laser beam energy (Q_2) with an absorbed heat coefficient of 0.15 for a molten pool was uniformly distributed to the deposited elements in order to raise the temperature slightly in excess of the melting point. Furthermore, the energy of the reflected laser beam (Q_3) from the molten pool surface with an absorbed coefficient of 0.35 for a base metal transmits to the molten pool front and sidewall of the groove through the heat flux density applied around the weld pool. The ratio of heat energy between the reflected laser irradiation and the direct input power of laser irradiation was assigned at about 0.3. All of the energy produced an initial molten pool of the deposited elements.

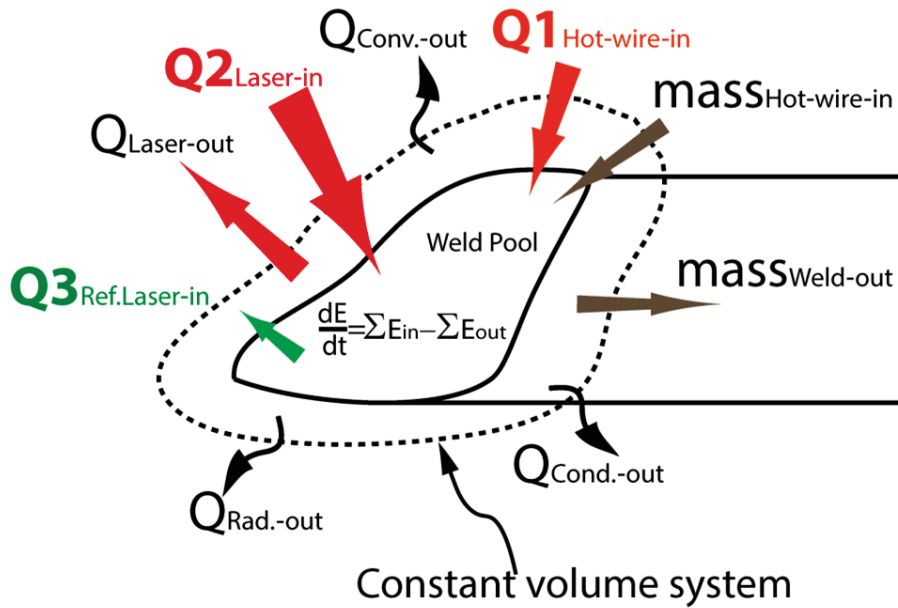
Subsequently, the heat source moved away from the start position (equal to welding speed). The original molten pool gradually changed through heat conduction loss and convection loss until it completely solidified (time = 1, 2, 3...n), while the rebirth-deposited elements were continuously filled at every time step. Therefore, the molten pool shape was naturally generated. The boundary of the molten pool was limited by the solidus temperature. In accordance with the steps mentioned above, the molten pool shape was stabilized throughout the welding.

In this case, since the calculation was mainly focused on strain analysis in mushy zone wettability, the fluid flow effect in the weld pool was not considered.



(a) Heat flow during hot-wire laser welding

Fig. 7.6 Schematic illustration of conceptual heat source model.



(b) Thermal energy balance in a molten pool based on constant volume system.

Fig. 7.6 Schematic illustration of conceptual heat source model.(continue)

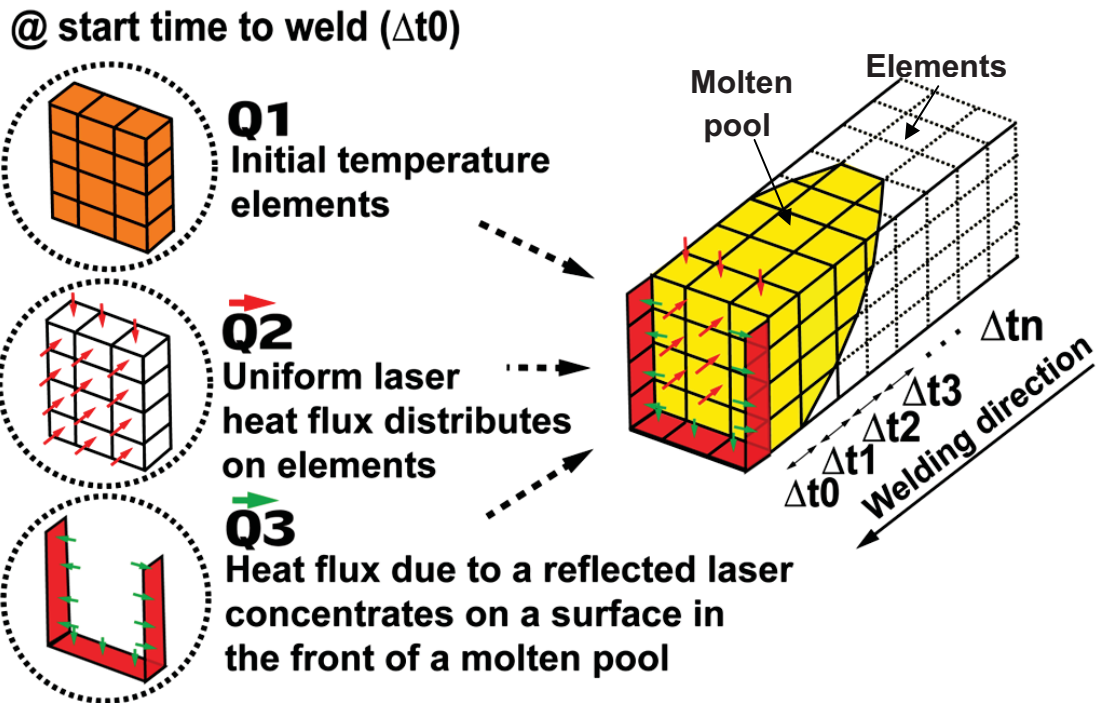


Fig. 7.7 Schematic illustration of FEM strategic approach.

7.2.5.2 Deformation and Elastic Strain History Measurement

In this section, the validity of the hot wire-laser welding simulation with a narrow groove joint, in terms of the mechanical analysis, is emphasized in particular. The contraction of the groove width, together with elastic strain history at the side wall during welding, was measured. In order to encourage an evident observation, the experiment was carried out with a thinner and smaller specimen. The dimensions of the specimen were 60^w mm x 24^l mm x 25^t mm, as presented in Fig. 7.9. This means allows greater deformation during welding. Modified 9Cr1Mo material was used as a base metal welded with ER90S-G filler wire. For narrow gap joint preparation, a U-shaped groove joint with a 3 mm gap was applied. A groove angle of 2.8° was provided. The filler wire had a diameter of 1.2 mm.

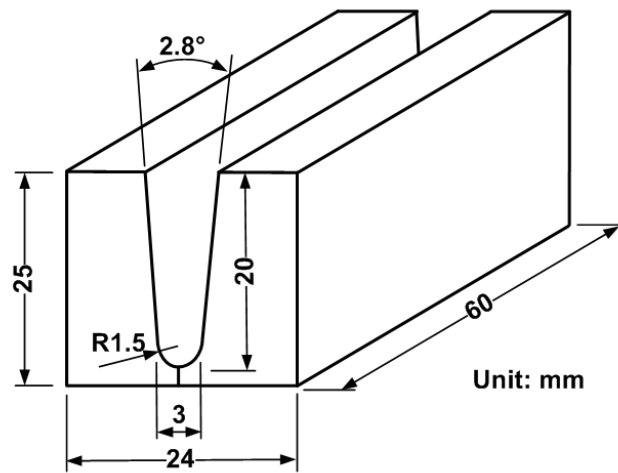


Fig.7.9 Illustration of specified specimen.

Welding conditions were the same as the thermal analysis experiment , namely, laser power of 3 kW, a defocused laser beam size of 3 mm in diameter, a welding speed of 0.3 m/min, and a feeding speed of 4.6 m/min. Argon was employed as a shielding gas to protect it from the outside atmosphere.

Figure 7.10 shows the experimental setup. To confirm the accuracy of the mechanical analysis, experimental measurement included displacements of the groove width, longitudinal elastic strain, and temperature history on the bottom side.

Figure 7.11 shows the elastic strain gauge was attached at the central point of the side wall. The longitudinal elastic strain was recorded. The type of strain gauge was KFU-5-120-C1-11H3M3 (Kyowa marker) which is made of highly heat resistant polyimide and the gauge element is made of NiCr alloy foil. Other characteristics included: the wide range of temperature application was $196\sim 350^\circ\text{C}$, a gauge length of 5 mm, and adaptable thermal expansion was 10.8 PPM/ $^\circ\text{C}$, specifically a gauge factor of 2.08 at room temperature and 1.85 at a

temperature of 350°C. Furthermore, the thermal history on the bottom side of the specimen at a distance of 0, and a spot 6 mm from the center line was measured with type R thermocouples 0.5 mm in diameter.

In addition, the specimen was placed on the particular fixture to allow movement readily during welding, as shown in Fig 7.12. This pin support fixture allows more contraction of groove width. Therefore, the displacement due to the contraction of the groove width during welding could be measured by a laser displacement instrument (LVDT) 2 mm below the top surface, as shown in Fig 7.13. The accuracy of measurement was specified by a characteristic of the instrument, namely a minimum displacement of 0.01 mm.

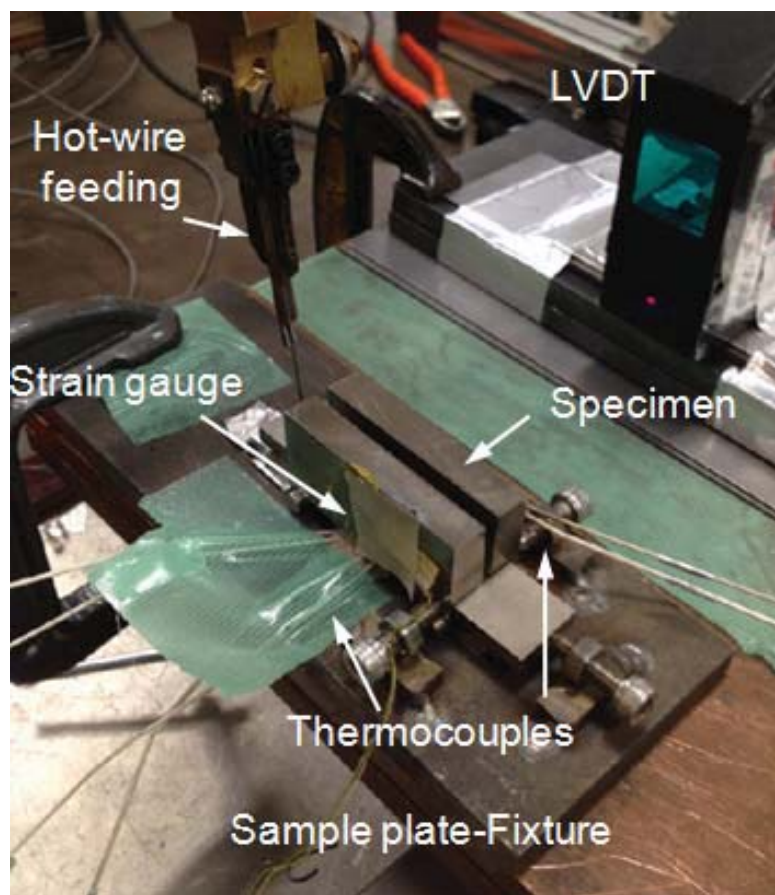
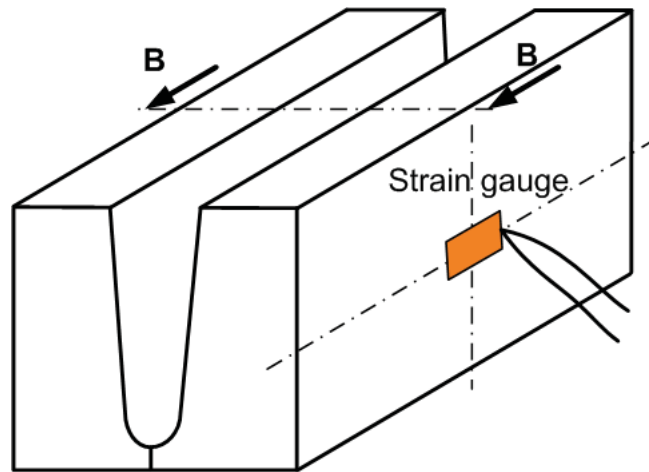
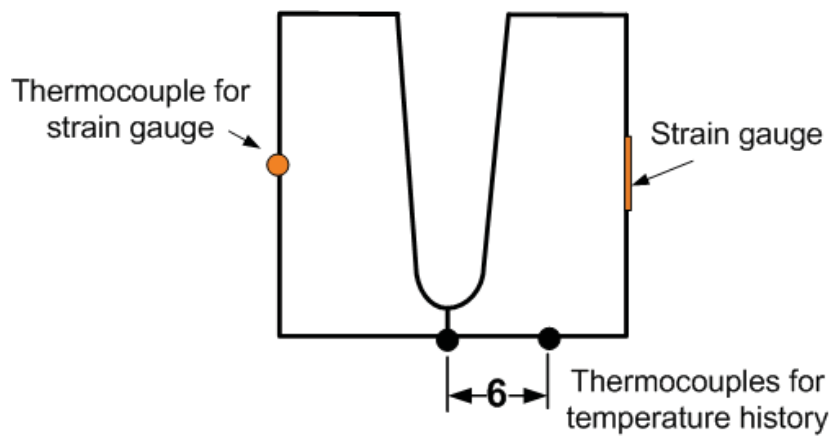


Fig.7.10 Experimental set-up of strain and displacement measurement.



(a) Strain gauge installation.



(b) Position of thermocouple measurement.

Fig.7.11 Illustration of strain gauge installation and thermocouple position.

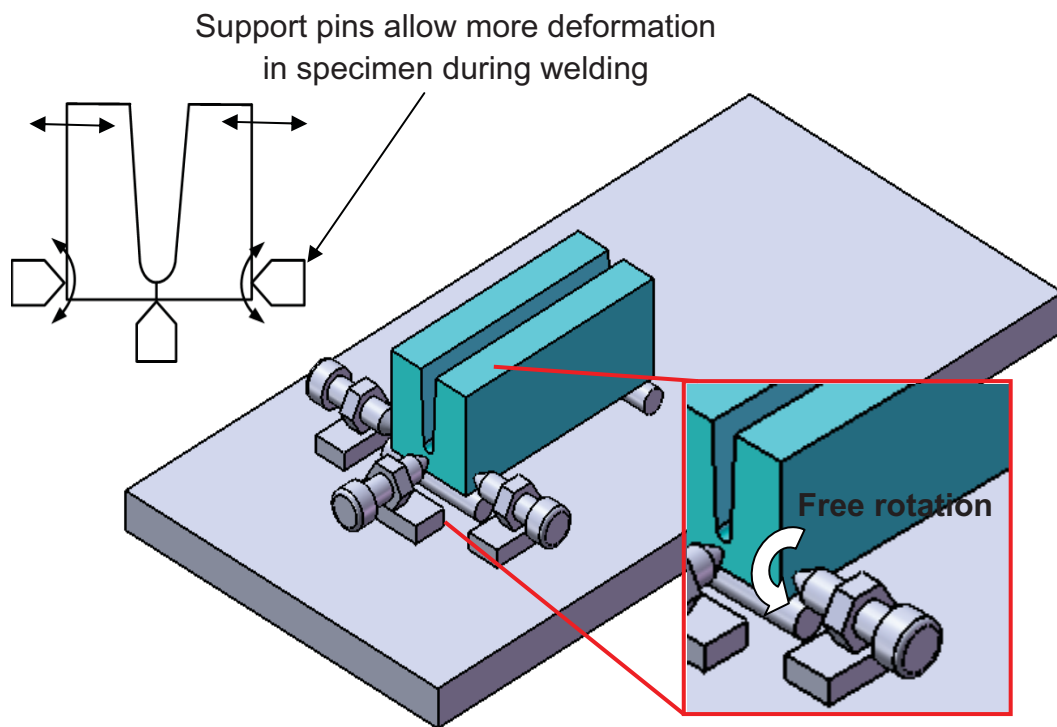


Fig.7.12 Illustration of a specimen placed on a pin support fixture.

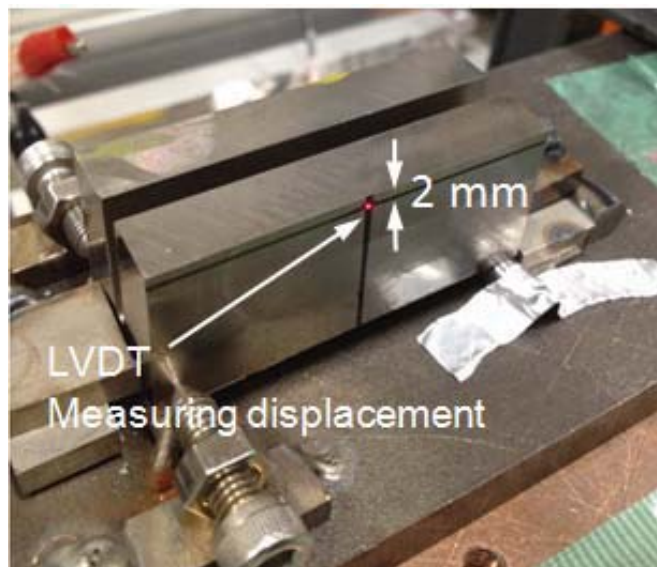


Fig.7.13 Image of a displacement measurement at a side wall.

7.2.5.3 FEM Model and Boundary conditions

Figure 7.14 shows the meshed model and its restrained condition. One half of a sample plate was discretized due to its symmetry along the weld centerline. The 3-D thermo-mechanical solid element type of 8 nodes isoparametric hexahedral was applied. The finer element size of 0.25 mm in the weld metal and 0.5 mm nearby the fusion zone were meshed in order to obtain precise results. During this time, the convection heat loss was defined for all of the plate surfaces except for the symmetrical plane, where an adiabatic condition was assumed while radiation heat loss was negligible. In the mechanical restraint condition, all nodes on the symmetrical surface of the welding bead along the longitudinal direction were fixed in a transverse weld direction, whereas the degree of freedom at the side edge of a work piece was constrained to prevent a rotational movement. Furthermore, the pin rods were taken to be a support at the bottom that allowed the model free movement.

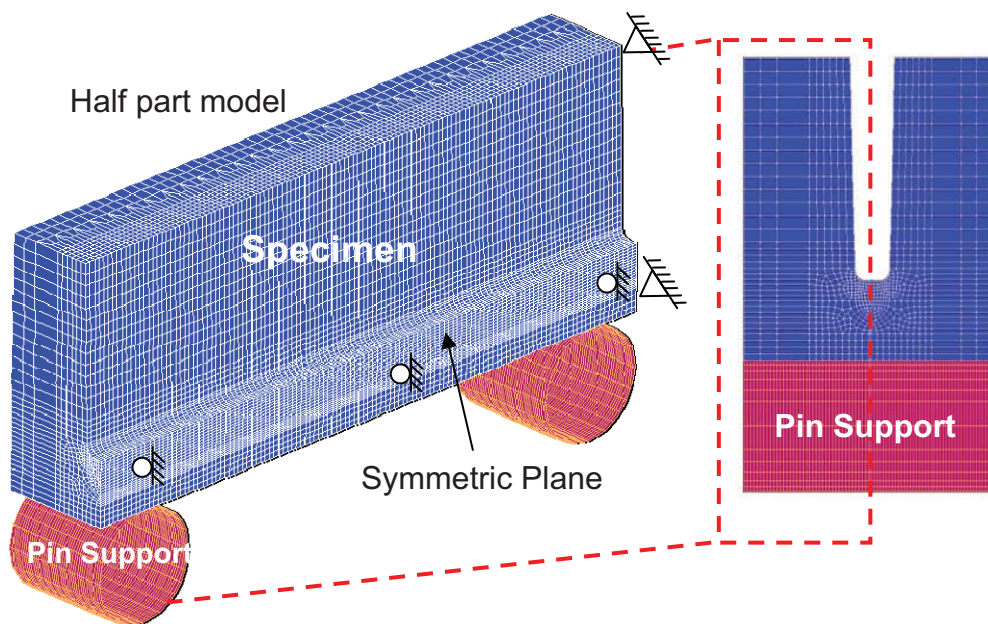


Fig.7.14 3D-FEM Model.

7.2.6 Simulation Result of Hot-Wire Laser Welding with a Narrow Groove Joint

7.2.6.1 Thermal Analysis

Figure 7.15 (a) presents the temperature distribution and the molten pool shape while moving the heat source throughout welding. Additionally, the vicinity of the forward molten pool exhibits a further fusion zone. It is caused by the heat flux of the reflected laser melting the area around the pool front and the side wall of the groove. In order to verify the suitability and validity of the model that was developed, the simulation results were compared in terms of thermal distribution, namely weld pool shape, peak temperature distribution, as well as thermal history.

As presented in Fig. 7.15 (b) the cross-section of the fusion zone was taken into account to confirm the accuracy of the simulation. As for the weld cross-section, it was found that the computed fusion zone with a temperature greater than the melting point ($1505\text{ }^{\circ}\text{C}$) was enhanced to satisfactorily match the experimental weld pool shape.

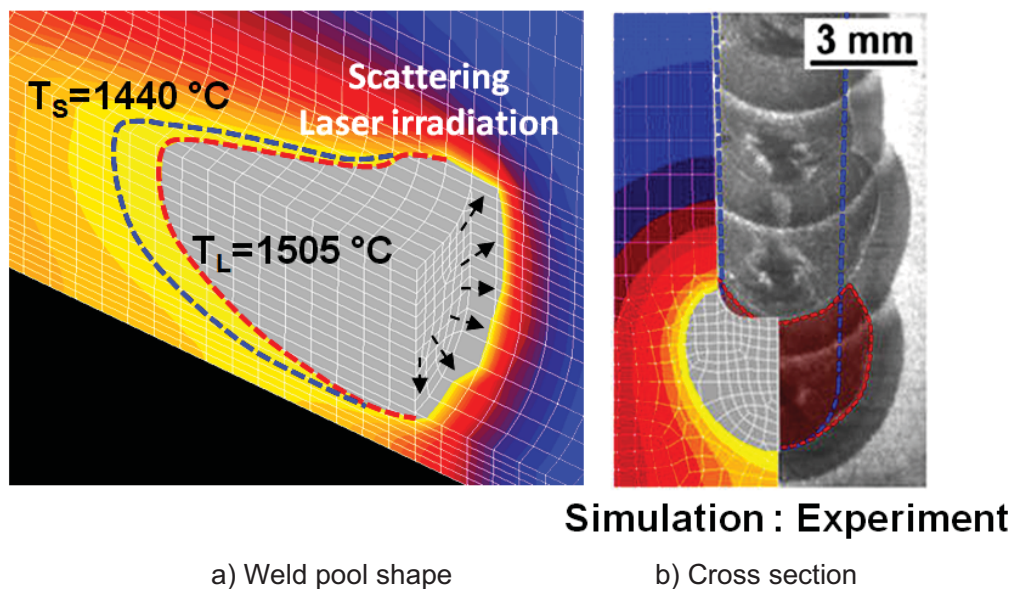


Fig. 7.15 Temperature distribution and cross section view.

Figure 7.16 shows the maximum temperature distribution along the distance from the centerline in the transverse welding direction for testing the temperature distribution of the calculation. Three measurement points with interval ranges of 1 mm are located and their regression line is also estimated. It can be observed that the comparison between the Computational simulation and the experimental results correspond well to each other.

Moreover, the temperature history from the thermal analysis is compared to the actual measurement value using an optical fiber radiation thermometer which was positioned in the fusion zone. Figure 7.17 presents the cross-sectional weld and the optical fiber thermometer location. As a result, it can be seen that the thermal cycle obtained from the simulation result coincides with the measured line as shown in Fig. 18.

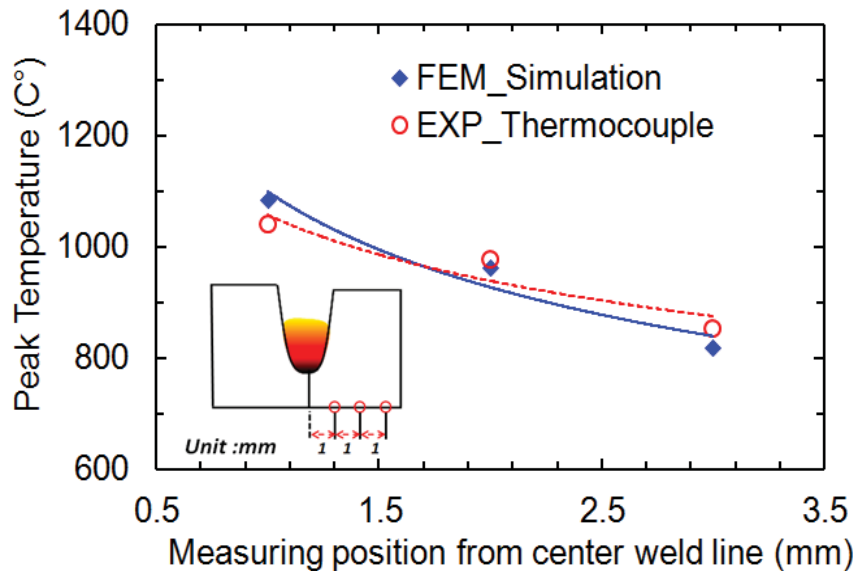


Fig. 7.16 Comparison of peak temperature between FEM and measurement.

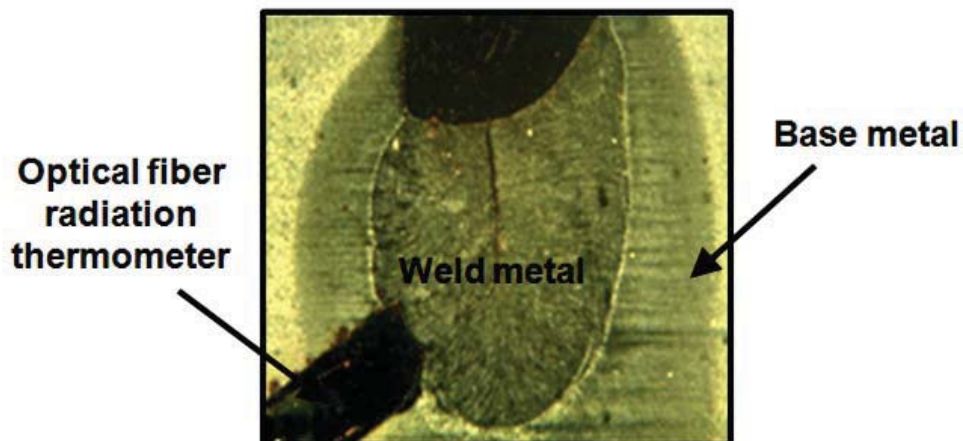


Fig. 7.17 Image of cross section of temperature history measurement.

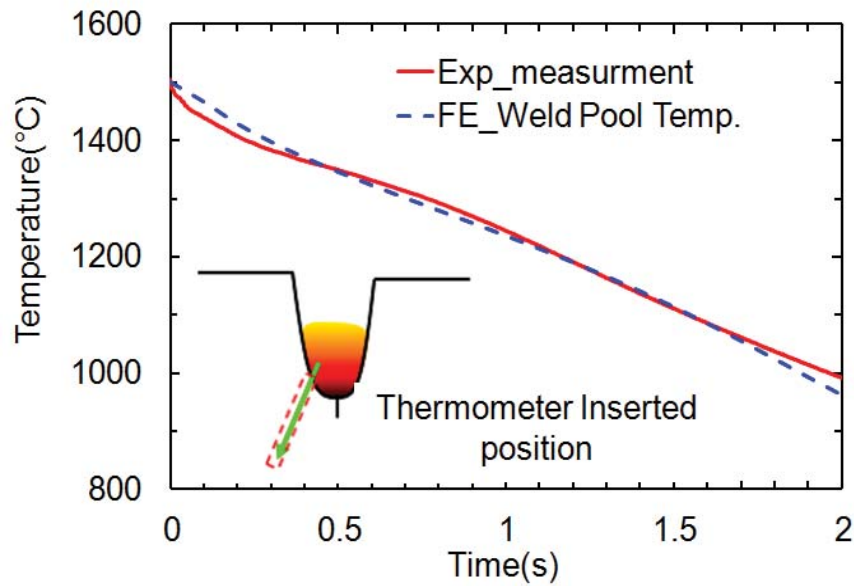


Fig. 7.18 Comparison of temperature history between FEM and measurement.

7.2.6.2 Thermo-Mechanical Analysis

Figure 7.19 is an image capture of contraction and expansion of the groove width during welding. The white arrow represents the original groove width. It can be seen that at the initiation time the groove expanded considerably and then eventually contracted due to weld bead shrinkage after the molten pool passed.

In this section, the simulation results are compared to the measurement in terms of elastic strain, displacement and temperature history. As Fig. 7.20 presents a comparison of the elastic strain history throughout and after the welding and the experiment's measurement and the FEM simulation, it is obvious that the strain history behavior in the simulated result was similar to the experimental curves. Firstly, the strain slightly increased in the tensile strain because of the weld metal's expansion. Next, when the molten pool had already passed the observation point, the temperature decreased below the melting point. Then, the shrinkage action of the weld bead would appear prominently afterward. After welding was completed, some plastic deformation in the weld took place during cooling which contributed to internal strain around the elastic zones.

However, the simulated strain curve after welding differs from the experimental measurement curve. This may be caused by somewhat less accurate mechanical material properties at the lower temperature.

In addition, Fig. 7.21 shows the displacement of the designated measuring point at the specimen's side wall compared to the simulation results. It can be observed that the simulation is similar in character to the experimental measurement. Nevertheless, the amount of displacement in the simulation is lower than the actual measurement, especially after welding.

Furthermore, the temperature at a distance 0 and 6 mm from the center line was measured by thermocouples. Figure 7.21 presents the temperature curves during welding and cooling. In conclusion, the simulation results are reasonably agree with the experiment's.

Initial groove width

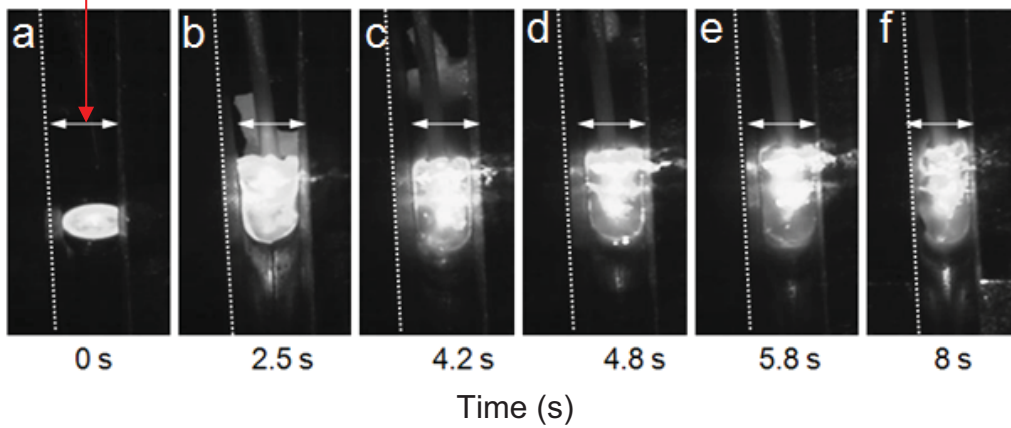


Fig. 7.19 Image capture of groove deformation during welding.

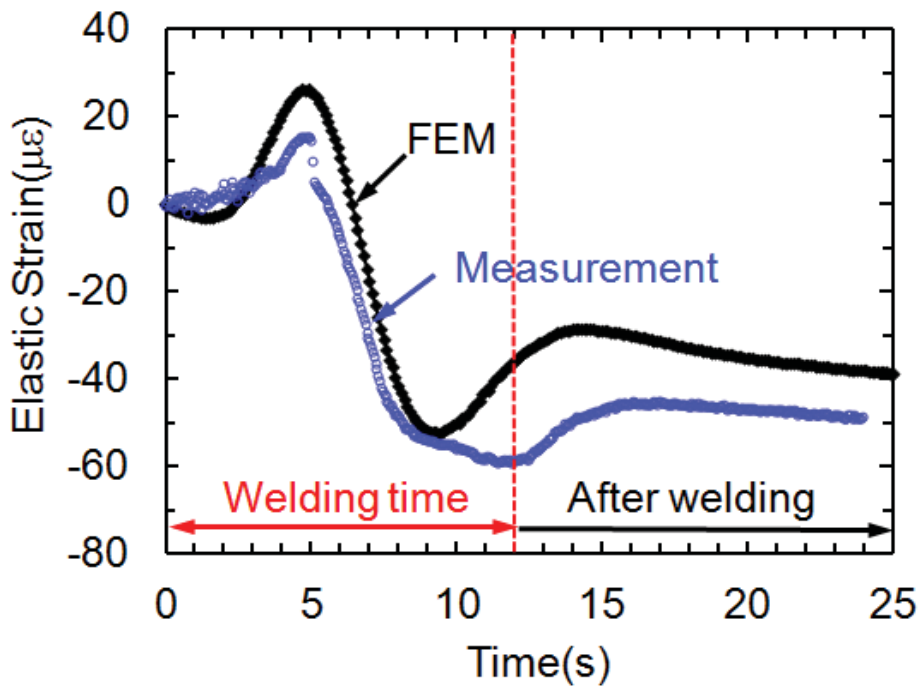


Fig. 7.20 Comparison of elastic strain between FEM and experiment.

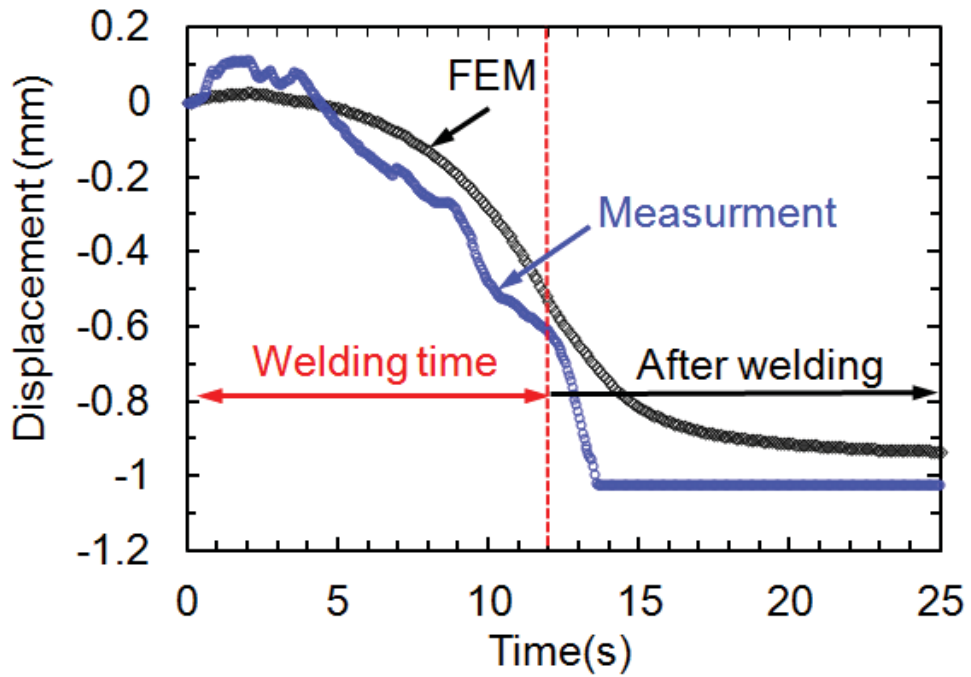


Fig. 7.21 Comparison of groove deformation between FEM and experiment.

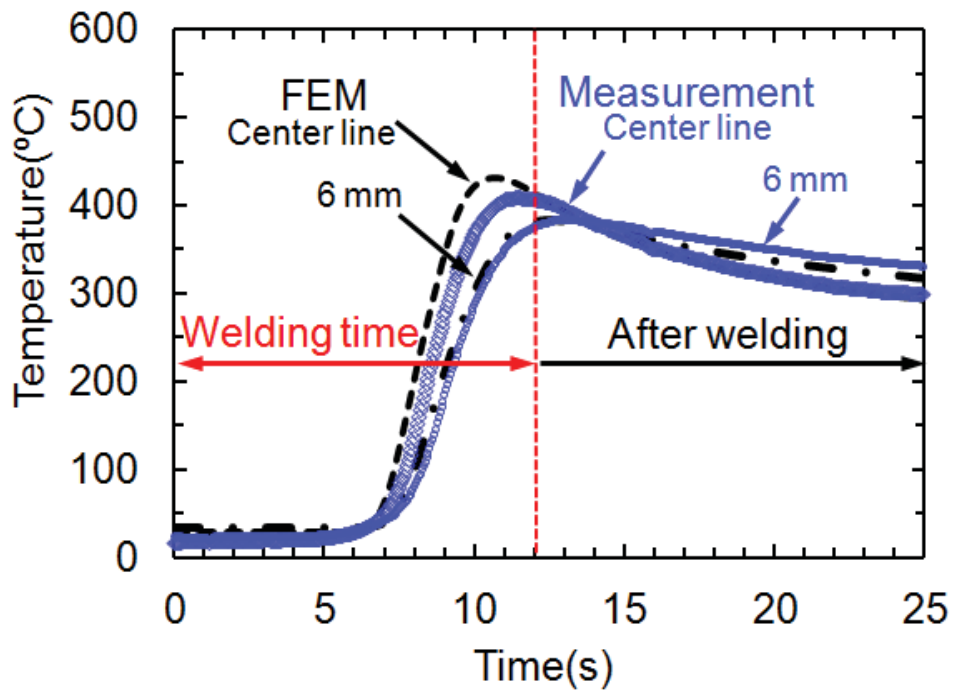


Fig. 7.22 Comparison of temperature history between FEM and experiment.

7.3 Computational GMAW Simulation of U-Groove Weld Cracking Test

This work is a study on the evaluation of the strain history in a U-shape weld test according to the JIS Z 3157 standard. GMAW is utilized. SCMn3B is employed as a base metal which is welded by G69A3UMN4M3 filler wire. A computational welding simulation is applied, through which finite element method 3D-FEM models are developed, including two features, namely a root gap of 0 and 2 mm. Thermo-mechanical properties dependent on temperature are considered in the calculation. As for the welding simulation, the approaches to the calculation are divided into two steps. Firstly, thermal analysis is performed to estimate the temperature distribution. The heat input from the moving welding arc is modeled as a double ellipsoidal heat source proposed by Goldak's equation. The validation of the adequacy of the simulation is implemented by comparing the experimental measurement with the computed results in terms of the weld bead shape, temperature distribution, and strain history. The important issues and the relevant details are described as follows.

7.3.1 Computer Simulation Procedure

7.3.1.1 Material Used and Welding Conditions

SCMn3B steel was used as a base metal. Fig. 2 illustrates the dimensions of a specimen according to the U-shape weld test JIS Z 3157 standard. A specimen size $150 \text{ mm}^w \times 200 \text{ mm}^l \times 80 \text{ mm}^t$, a U-shaped groove with a radius of 6 mm, a groove angle of 20° , and a root gap of 0 mm and 2 mm, were used. Such specimens were welded with G69A3UMN4M3 filler wire. The GMAW process was applied. Welding conditions were set at an arc current of 280 A, an arc voltage of 29 V, a welding speed of 0.22 m/min., a filler wire diameter of 1.2 mm, and a feeding speed of 8 m/min. as shown in Table 7.3.

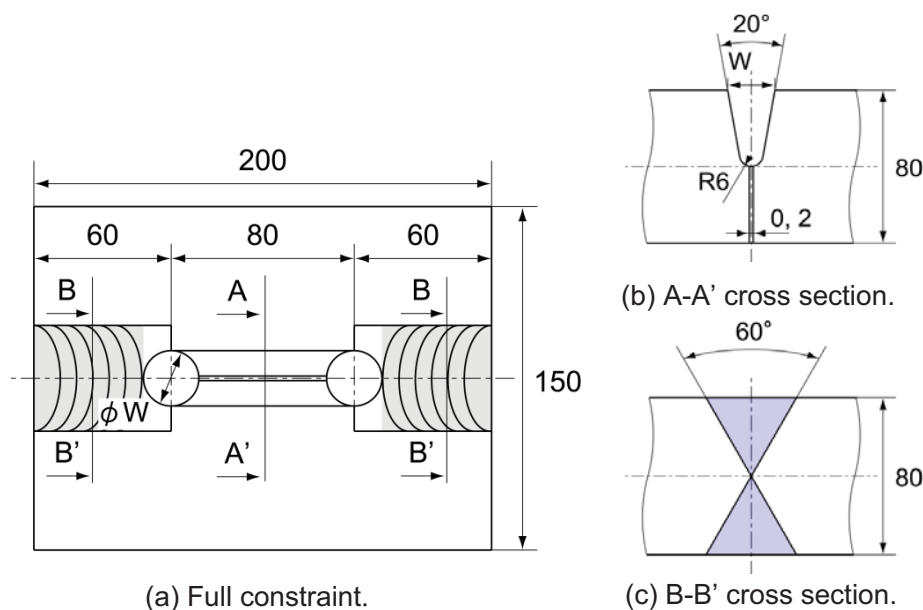


Fig. 7.23. Schematic illustration of a dimensional specimen.

Table.7.3 Welding conditions

Arc current, A	280
Arc voltage, V	29
Welding speed (m/min.)	0.22
Wire feeding speed (m/min.)	8

7.3.1.2 3D-Finite Element Model

As for the FEM analysis, commercial software, MSC.Marc 2012, with a developed user subroutine program was applied in order to achieve the thermal distribution and the occurrence of the local plastic strain during welding. In addition, a finite element technique to activate new elements, the so-called “birth and death element”, was also utilized to imitate the behavior of depositing a filler metal during welding. The simulation methodology is detailed as follows.

The FEM model of the welded plate test with a full constraint type according to ISO JIS Z 3157 was modeled, as shown in Fig. 3. Only half of the model was constructed due to its symmetry and to reduce calculation time. Meshing size was defined at 0.25 mm at the weld metal and 0.5 mm nearby the fusion zone in order to obtain precise results. Other parts were about 5-20 mm since they are not significant in the accuracy of the calculation. A meshed model was discretized with the 3-D thermo-mechanical solid element type of 8 nodes isoparametric hexahedral. The FEM model of a root gap of 0 and 2 mm consists of 153,324 elements and 149,512 elements, respectively.

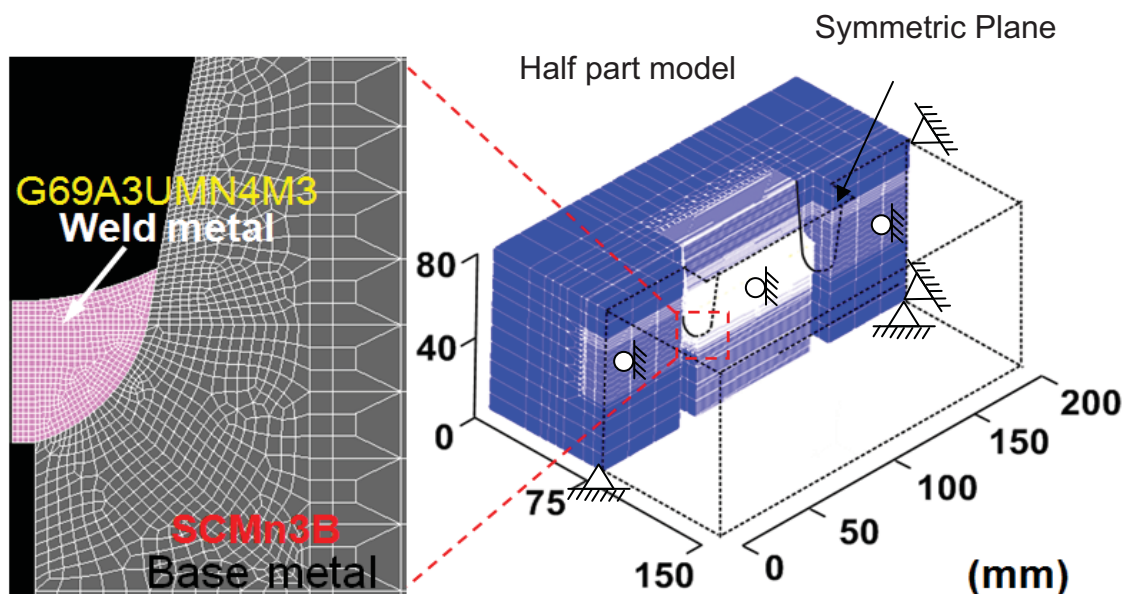


Fig. 7.24. 3D-Finite element model.

7.3.1.3 GMAW Heat Source Model

This study, according to the FEM analysis of GMAW in several reports, shows that the double ellipsoidal shape of a moving heat source was most likely to correspond with the experiments. Therefore, the approach to establish the heat source model in this study was performed as a double-ellipsoid volumetric heat flux distribution according to Goldak's equation [104].

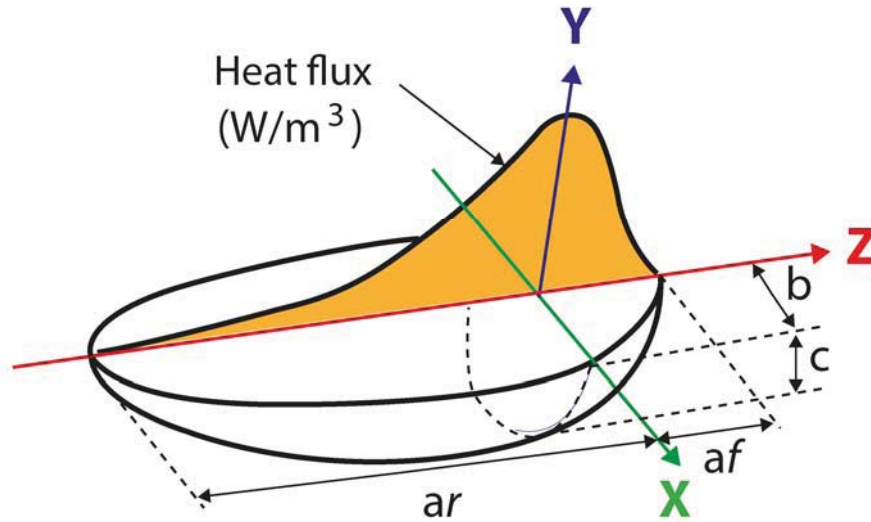


Fig. 7.25. Goldak's double ellipsoid heat source model [104].

The double-ellipsoid volumetric combines two different ellipses, namely one in the front quadrant of the heat source and the other in the rear quadrant. Figure 7.25 illustrates the shape parameters of the double ellipsoidal distribution according to Goldak's equation. The spatial heat distribution in a moving frame of reference can be expressed as the governing equations (7.5) and (7.6).

$$q_f = \frac{6\sqrt{3}\eta Q f_f}{\pi\sqrt{\pi a_f}bc} e^{-3\left(\frac{x^2}{a_f^2} + \frac{y^2}{b^2} + \frac{z^2}{bc^2}\right)} \quad (7.5)$$

$$q_r = \frac{6\sqrt{3}\eta Q f_r}{\pi\sqrt{\pi a_r}bc} e^{-3\left(\frac{x^2}{a_r^2} + \frac{y^2}{b^2} + \frac{z^2}{bc^2}\right)} \quad (7.6)$$

where,

- Q = Vxl, and $f_f + f_r$ is equal to 2
- Q is total heat input (W)
- V is welding voltage (V)
- I is welding current (I)
- η is heat transfer coefficient

In this simulation, the constant of the heat source shape parameters, such as a_f , a_r , b , and c , were defined at 1 mm, 8 mm, 9 mm, and 12 mm, respectively. The heat transfer coefficient was set as 0.87.

7.3.1.4 Boundary conditions

The convection heat loss was defined on all plate surfaces except for the symmetrical plane, which was assumed to have an adiabatic condition, while radiation heat loss was negligible. In the mechanical restraint condition, all nodes on the symmetrical surface of the weld bead along the longitudinal direction were fixed in the transverse welding direction, whereas the degree of freedom at the bottom edge of the model was constrained to prevent movement in the vertical and longitudinal welding direction.

7.3.1.5 Material properties

In the numerical simulation, the utilized model was assumed to contain isotropic material; the properties were independent directions. The plasticity behavior was defined as an isotropic strain hardening model. Furthermore, the particular properties of a base metal and a weld metal were specified separately, as presented in Fig. 7.24.

Thermo-mechanical material properties dependent on temperature, such as thermal conductivity, specific heat, and thermal expansion, were based on the international ASM standard as shown in Fig. 7.26 [105]. The remarkable mechanical properties such as yield strength and Young's modulus as a function of temperature were estimated using a thermodynamic approach through the application of JMatPro. Also, Poisson's ratio was assumed to be 0.29 and mass density was 7860 kg/m^3 as shown in Fig. 7.27.

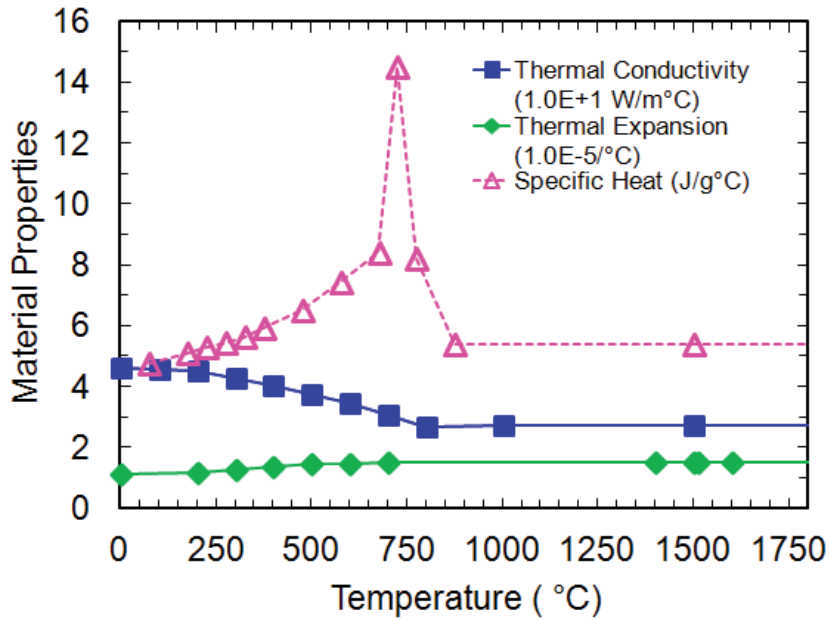


Fig. 7.26. Thermal properties as a function of temperature.

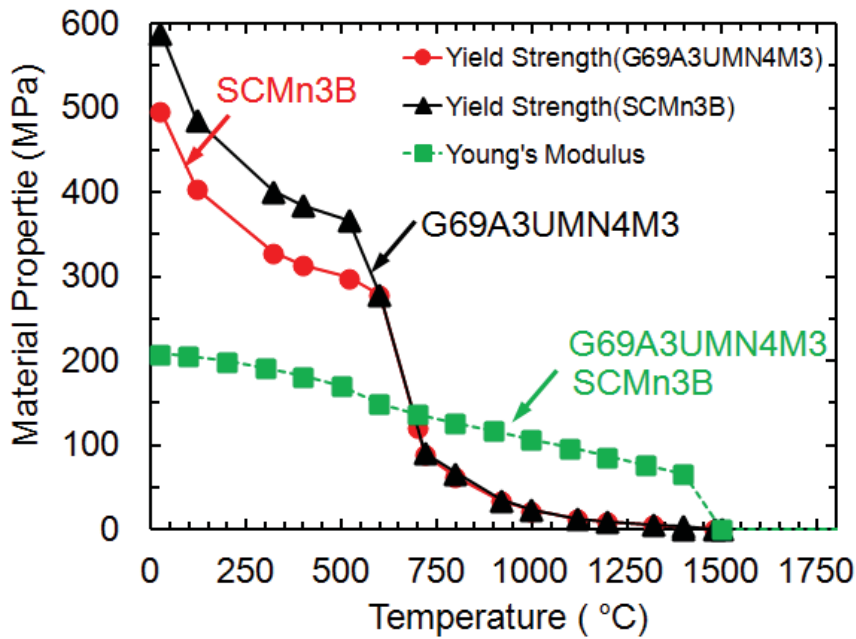
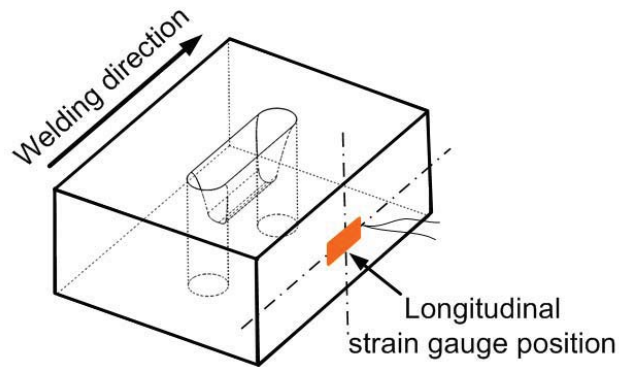


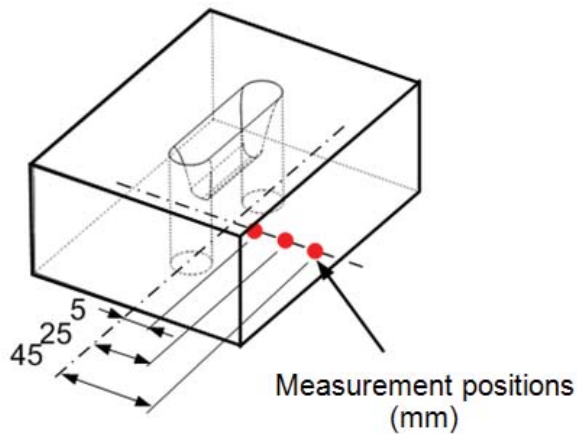
Fig. 7.27. Mechanical properties as a function of temperature.

7.3.2 Experimental Validation of GMAW Simulation of U-Groove Weld Cracking Test

The verification of the computational simulation was carried out through comparison with the actual experiment in terms of the thermal and strain history, together with a cross section of the weld bead. The specimen was welded with GMAW without preheating. The temperature measurement was performed using a thermocouple, while the measuring positions were installed on the back side of the specimen along the transverse weld direction. In the case of the strain history, a strain gauge was setup at the middle of the specimen's side wall in order to acquire a strain in a longitudinal welding direction, as shown in Fig. 7.28 (a). Three measurement points were assigned as the intervals from the center weld line of 5, 25, and 45 mm respectively, as can be seen in Fig. 7.28 (b).



(a) Strain gauge position.



(b) Temperature measurement.

Fig. 7.28. Illustration of strain gauge installation and thermocouple position.

7.3.3 Results of Validation in GMAW Simulation of U-Groove Weld Cracking Test

Figure 7.29 presents the temperature distribution and the molten pool shape while moving the heat source throughout welding. In order to verify the suitability and validity of the simulation, the computed results were compared in the cross-section of the fusion zone, as shown in Fig. 7.30 (a) and (b). As a result, it was found that the computed fusion zone with a temperature greater than the melting point (1497°C obtained from JMatPro database) was enhanced to satisfactorily match the experimental weld pool shape.

In addition to this, temperature and strain history were taken into account to confirm the accuracy of the simulation. As for the temperature history at the three measurement points, it can be seen that the thermal cycles obtained from the simulation result coincide with the experimental measurement presented in Fig. 7.30.

In addition, the strain history at the designated point between the experimental measurement and the simulation were compared to each other. As a result, it was found that the strain history using Goldak's heat source equation agrees well with the experimental measurement, as shown in Fig. 7.32.

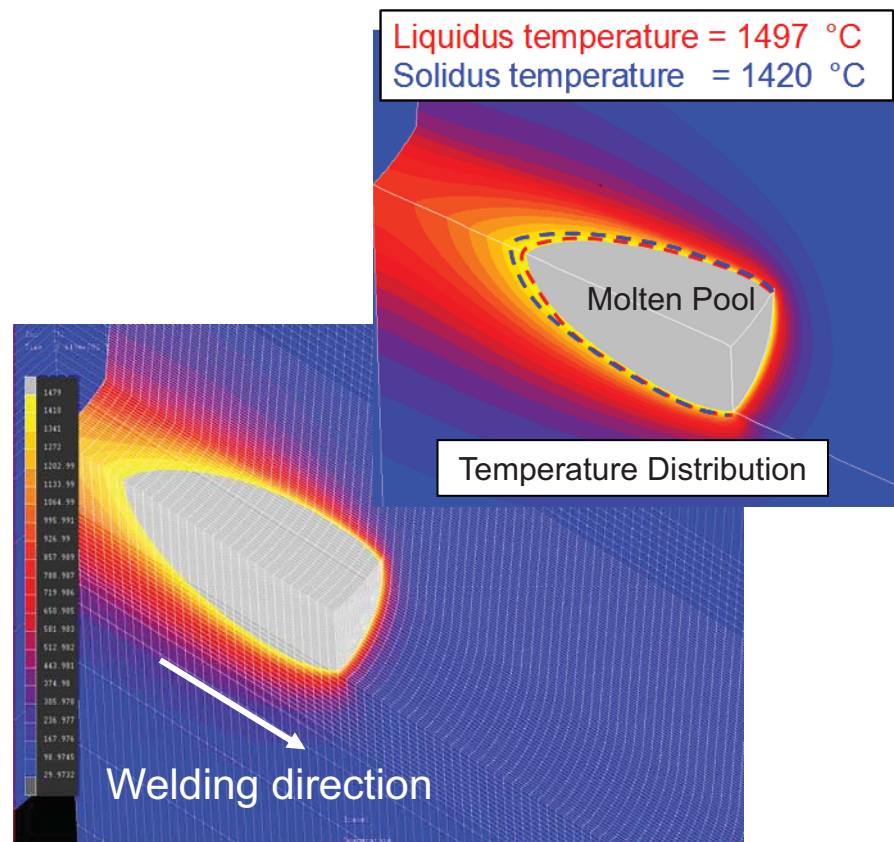
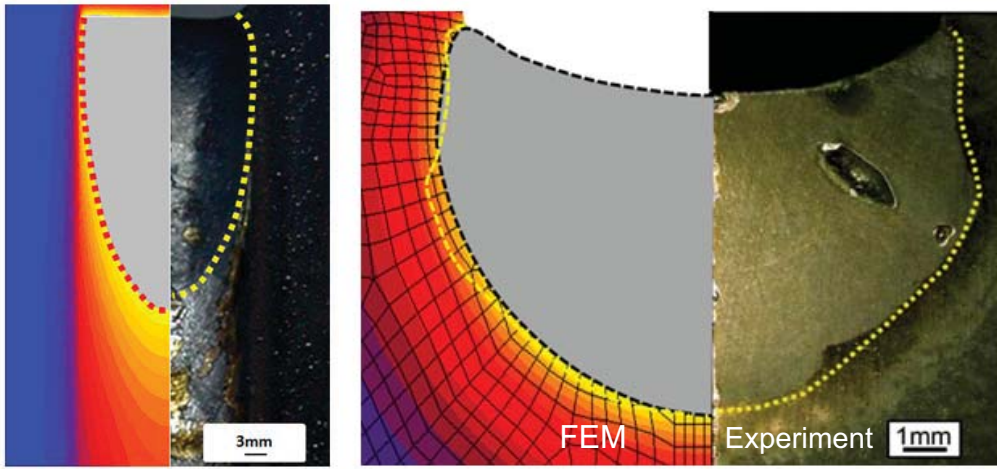


Fig. 7.29. Simulated temperature distribution.



a) Top view of model pool b) Cross section-Weld shape

Fig. 7.30 Comparison of weld shape between FEM and experiment.

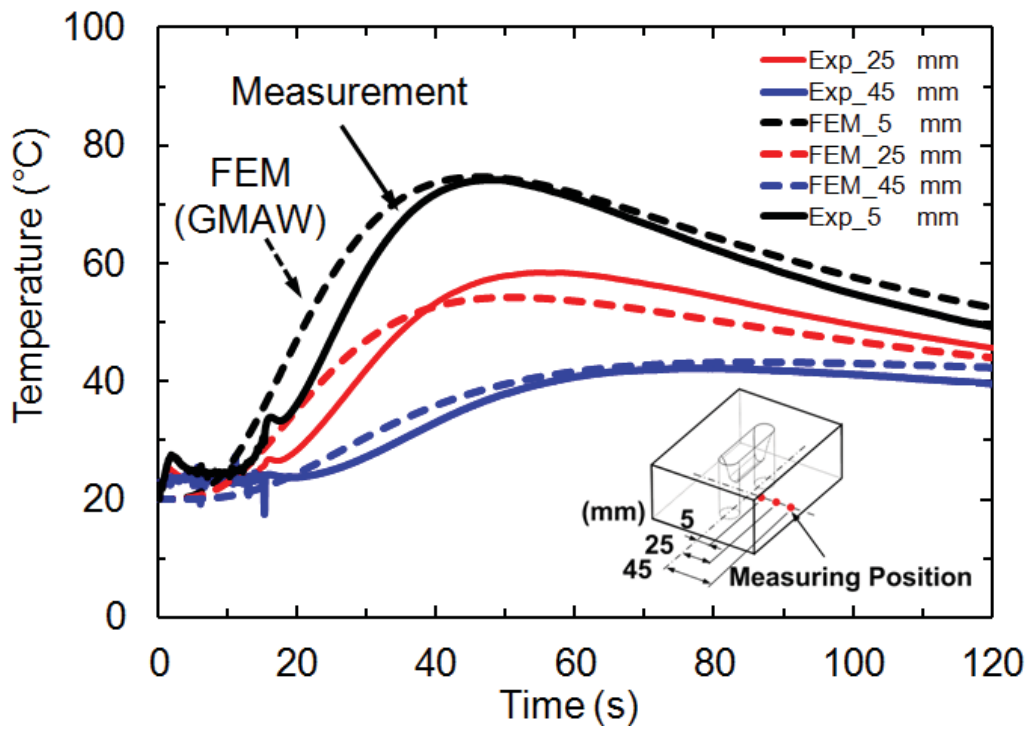


Fig. 7.31 Comparison of temperature history.

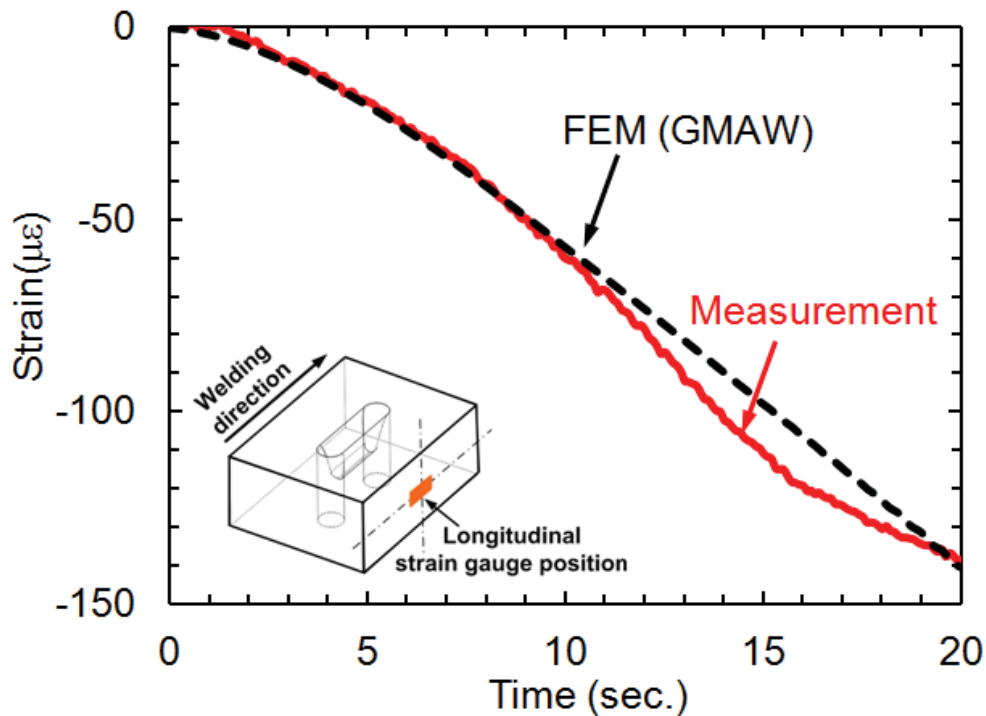


Fig. 7.32 Comparison of elastic strain history.

7.4 Summary

In this chapter, the computational welding simulation approach for hot-wire laser welding with a narrow groove was implemented, as well as a U-groove weld cracking test. 3-D FEM with a developed welding heat source model was proposed in order to achieve the thermal distribution and calculate the strain in hot-wire laser welding with a narrow groove. Meanwhile, Goldak's heat source model was used for the U-groove weld cracking test. All simulation results were validated based on the experiments. Conclusions are detailed as follows:

1. A particular heat source model of hot-wire laser welding with a narrow groove, which uses a general heat source model such as Gaussian heat flux and cannot be properly applied, was developed with special user subroutines. The simulation results were validated through comparison with the experimental measurement in terms of the thermal history, peak temperature distribution close to the fusion zone, and the weld shape. As a result, the thermal history and peak temperature distributed along the distance from the centerline in the transverse weld direction agreed well with the actual experiment. In mechanical analysis, the contraction of the groove width and the longitudinal elastic strain were compared. From the results, the comparison between the calculations and the measurement in terms of the strain history, the displacement, and the temperature history, it was found that the model was appropriately accurate during the welding.

2. According to GMAW with the U-groove weld cracking test, the computational simulation with the moving heat source model is consistent with Goldak's double-ellipsoidal model, so it was an appropriate approach in this study. The simulation was validated based on the experimental measurement of the cross sectional weld, the thermal history, and the elastic strain at the specimen's side wall. As a result, the simulation condition agreed well with the actual experiment.

From the results, the computational welding simulation approach exhibited the fact it has a tendency to accurately obtain the high temperature strain during solidification, which will be described in the next chapter.

Chapter 8

Prediction of Solidification Cracking by Integral Approach to Ductility Curves and FEM Analysis

8.1 Introduction

In Chapter 4 and 5, solidification cracking susceptibilities in Modified 9Cr1Mo and large cast steel welds were investigated. Chapter 6 then presented the high temperature ductility curves obtained from the U-type hot cracking test with an in-situ observation method. In order to gain the high temperature strain during welding, Chapter 7 proposed the approach of a computer welding simulation along with experimental validation.

In this chapter, so as to make clear the theoretical reason for solidification cracking susceptibility, 3D FEM is modeled to simulate hot-wire laser welding in a narrow gap groove, as well as GMA welding with the U-groove weld cracking test. Based on an integral systematic approach to high temperature ductility curves, the occurrence of solidification cracking is reasonably predicted by the intersection of the material resistance as a high temperature ductility curve and the high temperature strain calculated by the FEM analysis.

The prediction of solidification cracking is split into hot-wire laser welding with a narrow gap groove and GMA welding with the U-groove weld cracking test. As for a narrow gap groove, the effect of the depth-to-width ratio (D/W) of weld shape on solidification cracking was studied. In the case of the U-groove weld cracking test, it was considered in order to clarify the effect of root gap width.

8.2 Prediction of Solidification Cracking In Hot-Wire Laser Welding with a Narrow Groove Joint

8.2.1 Achievement of Appropriate Temperature for Initial Strain

Based on the mechanism of solidification cracking [52, 54], solidification cracking occurs at the terminal stage of solidification. In this stage, the concept of a coherent interlocking of the solid network is used to explain the transformation from solid to liquid metal. A coexistence of solid and liquid metal is referred to as a mushy zone. The solid network in the mushy zone is separated by continuous liquid films and is then broken out by tensile deformation.

From the study on stainless steels, Matsuda, et al. [106] revealed that the solid network forms significantly when the percentage of solid material is close to 50% in the mushy zone. On the one hand, when the solid material makes up less than 50%, there is a sufficient amount of liquid metal to continuously fill or heal the incipient crack. Therefore, solidification cracking is less likely to occur in this circumstance. On the other hand, when the solid network is solidified at greater than 50%, solidification shrinkage and thermal contraction can overcome the backfill ability of liquid metal. This tends to cause solidification cracking.

In this study, the relationship between the ratios of solid to liquid metal in a mushy zone was taken into account in the occurrence of an initial strain. In this case, the coherent temperature having a solid fraction (f_s) of 50% was defined as sufficient strain initiation. Thermodynamic theory and Scheil-Guiver's [3, 4] solidification model were utilized in the application of commercial JMatPro software to evaluate the temperature of the 50% solid fraction. The calculation result of the coherent temperature is shown in Fig. 8.1. In accordance with the JMatPro database, the temperature of the 50% solid fraction of modified 9Cr1Mo weld metal is approximated at 1495°C, while the G69A3UMN4M3 with 40% dilution's is 1480°C, as shown in Fig.8.2.

In the FEM calculation, the elements of the molten pool are defined as liquid metal when the temperature is greater than a temperature containing a solid fraction of 50%. A special subroutine program was specially developed to reset all the accumulated strain to zero. Then, when the temperature of the molten pool cooled down below the temperature containing a 50% solid fraction of 50%, the strain in the elements is increased to make a calculation in accordance with the elasto-plastic theory.

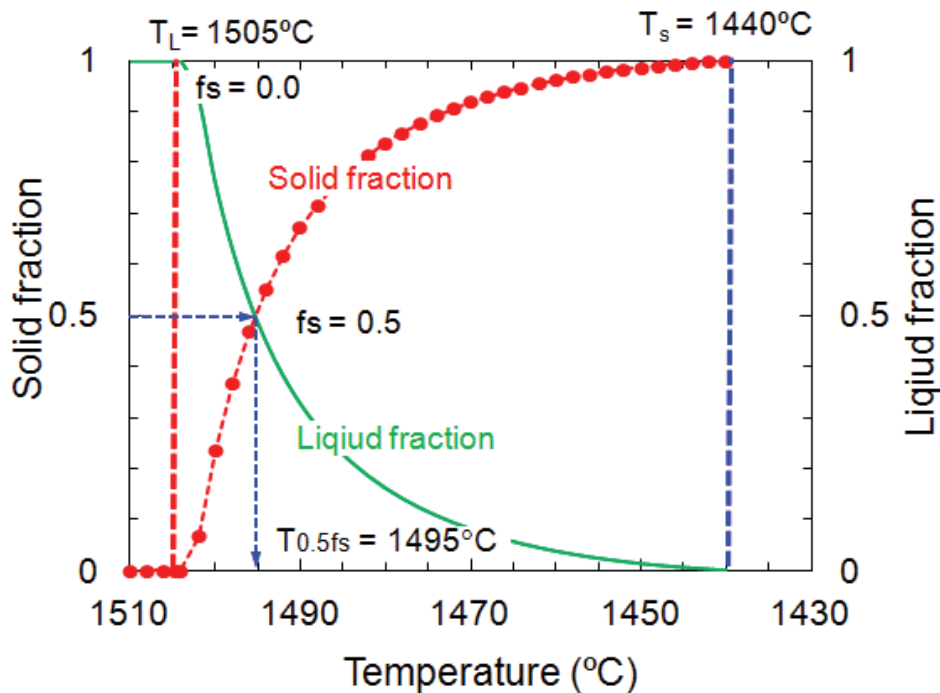


Fig. 8.1 Temperature against solid fraction to strain initiation.
(Modified 9Cr1Mo weld metal)

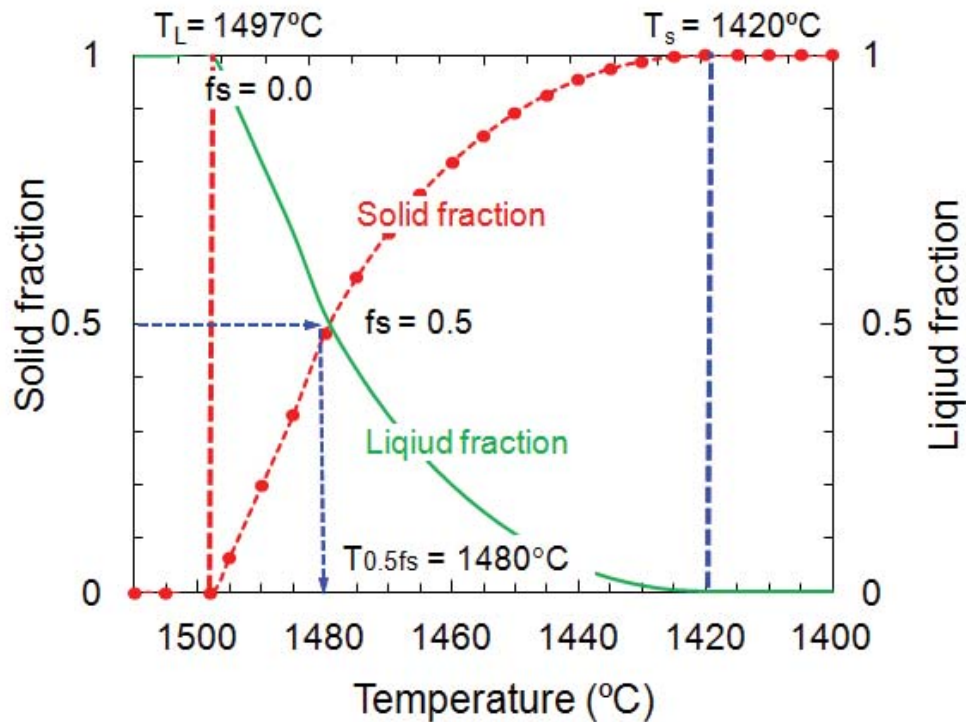


Fig. 8.2 Temperature against solid fraction to strain initiation.
(G69A3UMN4M3 with 40% dilution)

8.2.2 Determination of High Temperature Strain and Maximum Strain Rate

After measuring the temperature to strain initiation, this step explains the method to obtain the high temperature strain history in the mushy zone. For instance, Fig. 8.3 shows the simulation result of the hot-wire laser welding with a narrow gap groove. A groove width of 3 mm was used. Welding conditions are the same as the settings in Chapter 7, namely, a laser power of 3 kW, and a welding speed of 0.3 m/min. The fusion boundary is assigned as 1505°C, while the completely solidified temperature is 1440°C. This solidification temperature range is taken from the JMatPro database, as mentioned earlier. In this thesis, equivalent plastic strain was used because elastic strain has such little value when comparing the amount of equivalent strain between the plastic and the elastic. Thus, it is considered an insignificant strain type. Also, equivalent strain type is useful in evaluating driving force during solidification since such a strain type is a resultant of the three dimensional strains which correspond with three-axial solidification shrinkage in a molten pool and thermal contraction during welding. Strain initiation occurs at the coherent temperature of 1495°C.

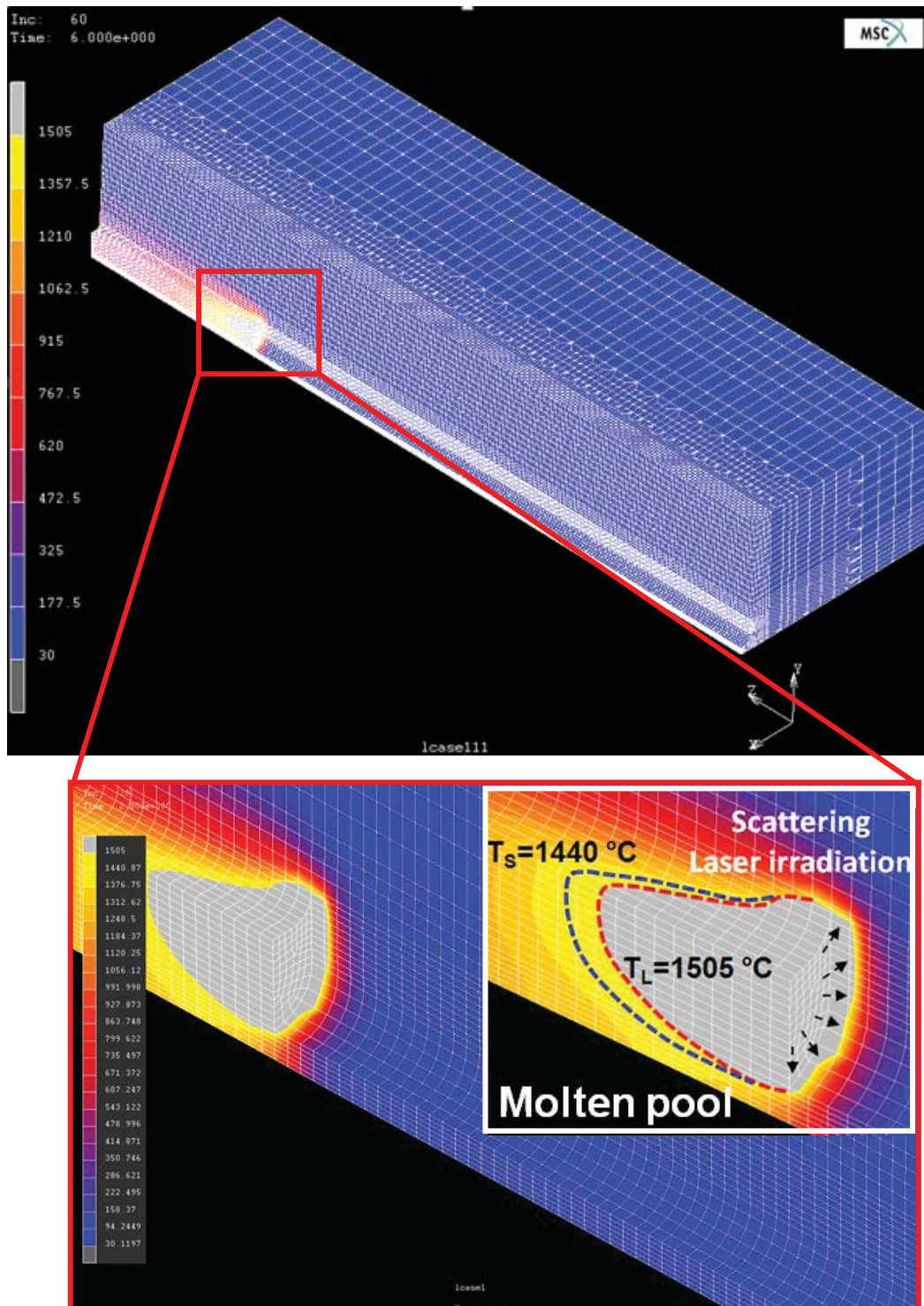


Fig.8.3 Simulation result of hot-wire laser welding with a narrow gap groove. (Groove width of 3 mm)

Thermal-elasto-plastic analysis followed because solidification cracking usually occurs at a center weld. Fig. 8.4 illustrates the calculation points (P1-P8) used to determine the strain history along the vertical center weld.

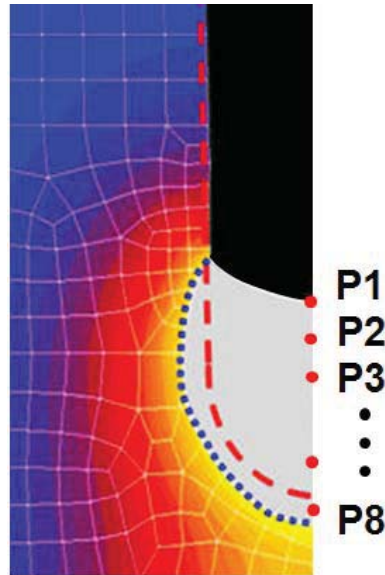
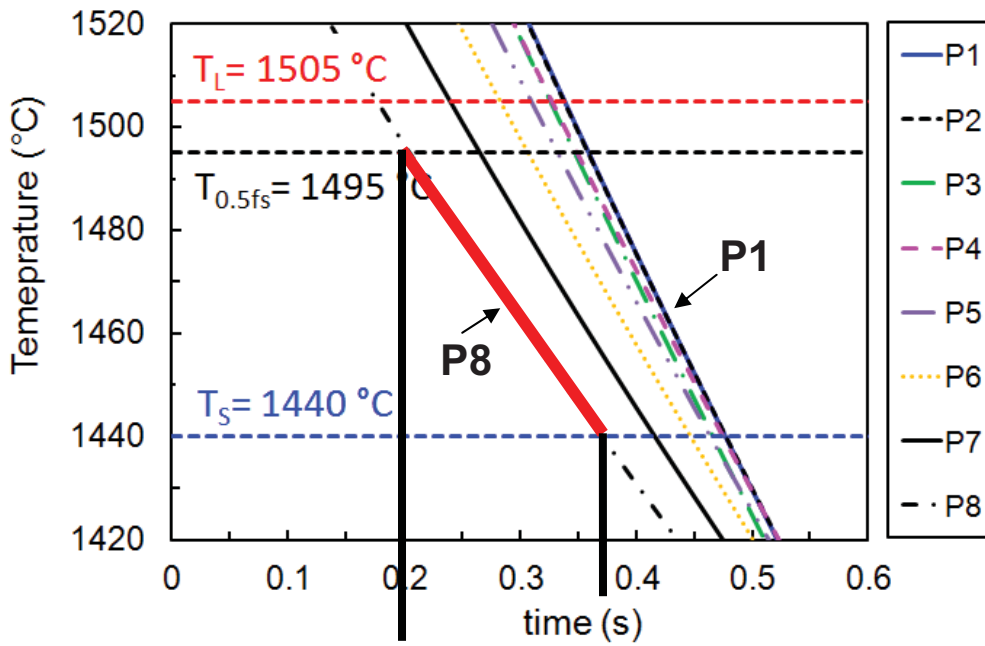


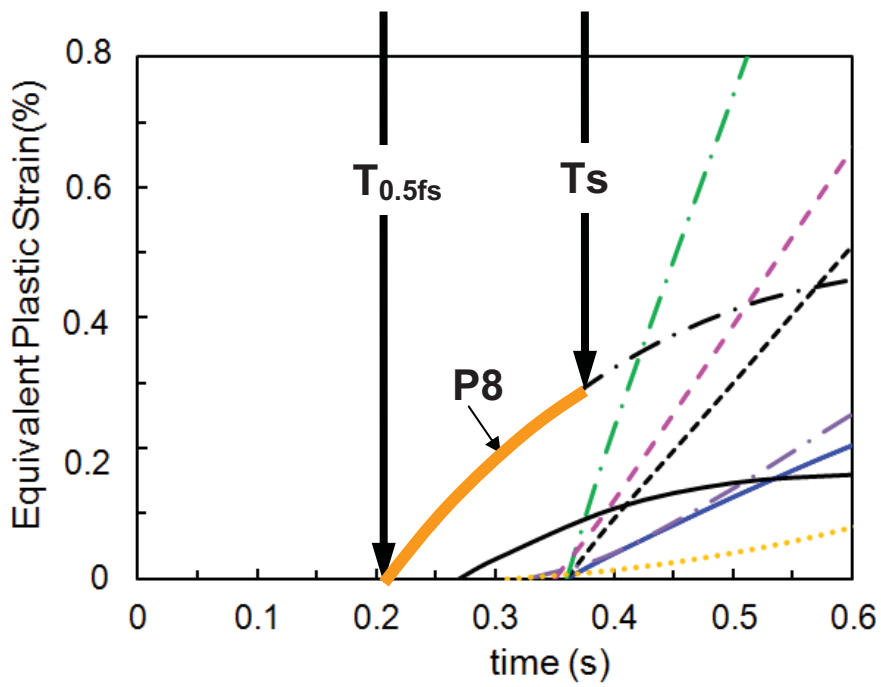
Fig.8.4 Calculation points of strain history.

To estimate the strain history during solidification, cooling curves and strain-time curves are calculated for every point from point P1 to P8, as shown in Fig. 8.5 (a) and (b). The solid red line in Fig. 8.5 (a) represents the cooling curve of point P8, while the solid orange line in Fig. 8.5 (a) indicates the amount of strain at the time. The relation between a cooling curve and a strain-time curve is employed to obtain a high temperature strain curve during weld pool solidification. By this means, strain-temperature curves in other locations are calculated with the same procedure, as mentioned above.

Figure 8.6 shows the high temperature strain curves of all points along the vertical axis of the weld bead. Consequently, all strain curves are compared to find the highest strain rate and its location. It shows that the point P3 presents the highest strain rate curve nearby the middle of the weld bead.



(a) Temperature against time.



(b) Equivalent plastic strain against time.

Fig.8.5 Method to obtain strain against temperature.

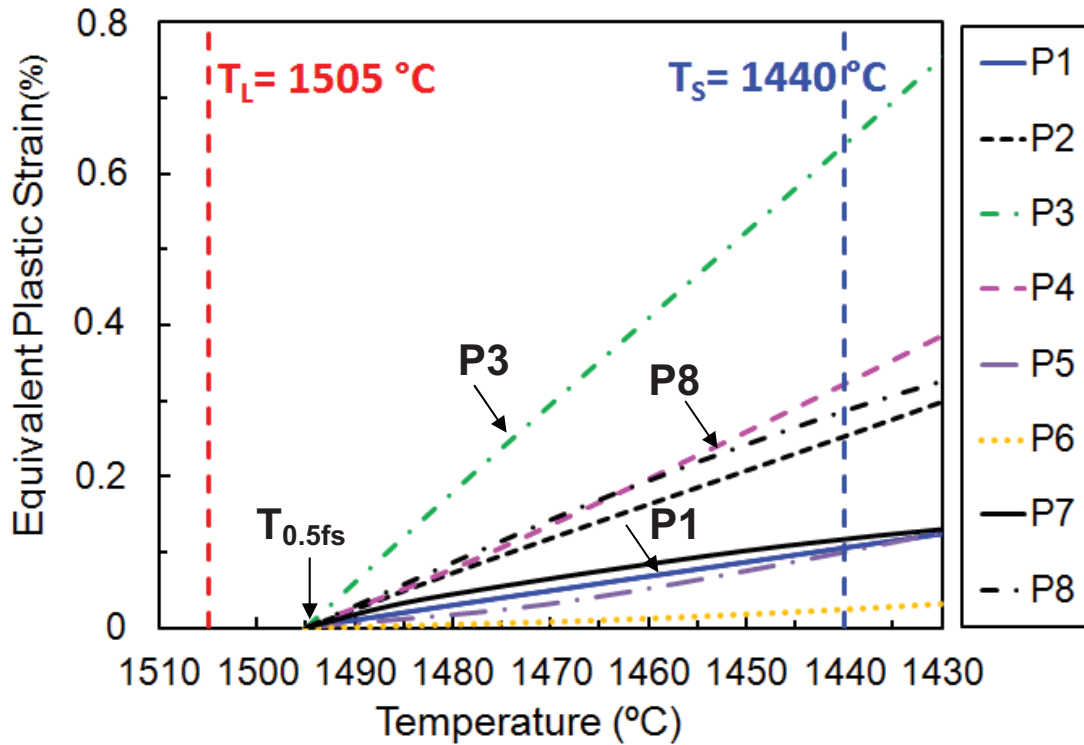
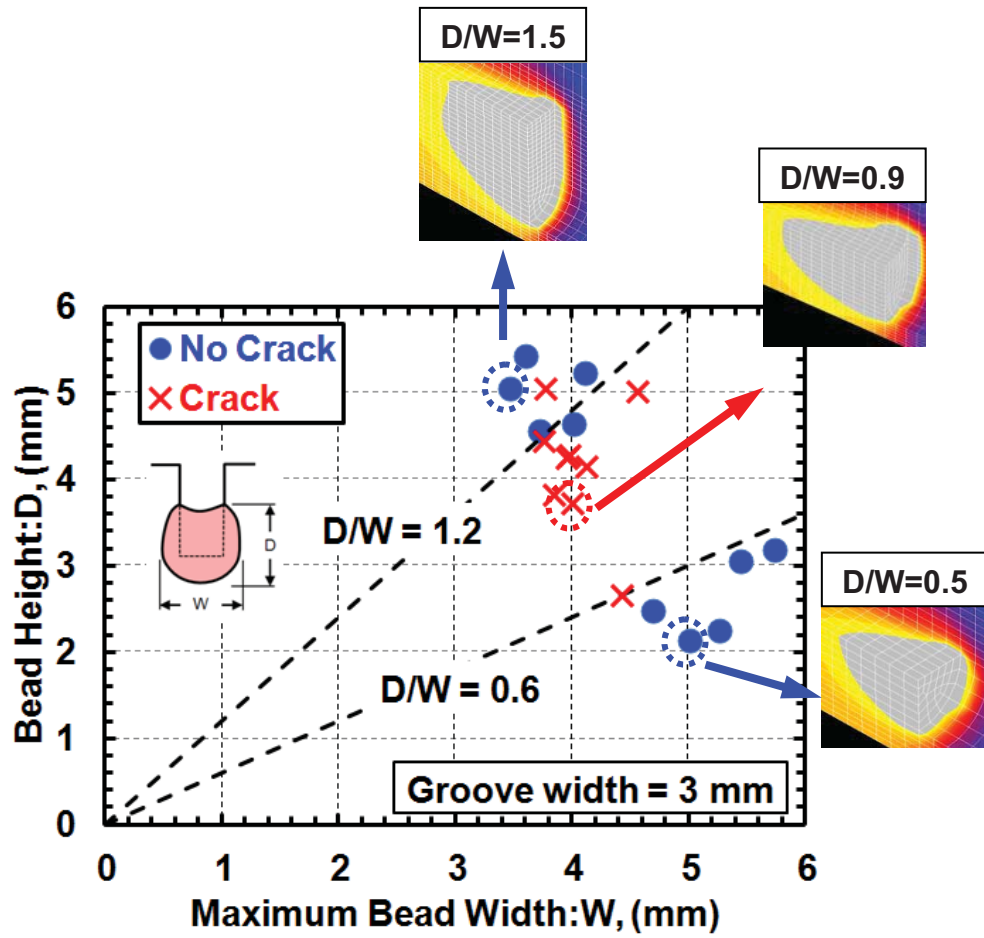


Fig. 8.6 Strain-temperature curves along the center weld.

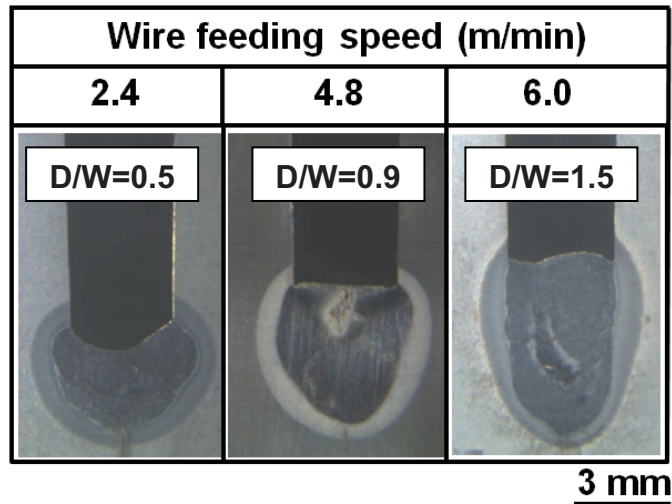
8.2.3 Prediction of Solidification Cracking at Different D/W Ratios

As previously described in Chapter 4, the influence of weld shape on solidification cracking susceptibility was investigated from the aspect of the D/W ratio. From the results with a groove width of 3 mm, solidification cracking did not occur when the D/W ratio was less than 0.6 or more than 1.2. Accordingly, solidification cracking is predicted in this section in order to make clear the effect of the D/W ratio on the susceptibility of solidification cracking from a, theoretical perspective.

Figure 8.7 (a) shows the relationship between the occurrences of solidification cracking and D/W ratios. Models of three different weld shapes, D/W of 0.5, 0.9, and 1.5, respectively, which correspond to the experiments, were created to investigate the aspect of the plastic strain history during solidification. Figure 8.7 (b) presents the actual cross section of the weld beads dependent on the D/W ratio. Welding conditions such as wire feeding rate and wire current were set as follows: wire feeding speed varied from 2.4, 4.8, and 6 m/min, while the wire current was set at 74, 105, and 118 A, respectively. A higher weld deposition led to an increase in the wire feed rate, while the wire current served to heat the temperature of the fed wire to an adequate and stable melting behavior before dipping it into the molten pool.



(a) Selected D/W covered solidification cracking zones.



(b) Experimental cross-section welds.

Fig. 8.7 D/W ratios of FEM strain analysis.

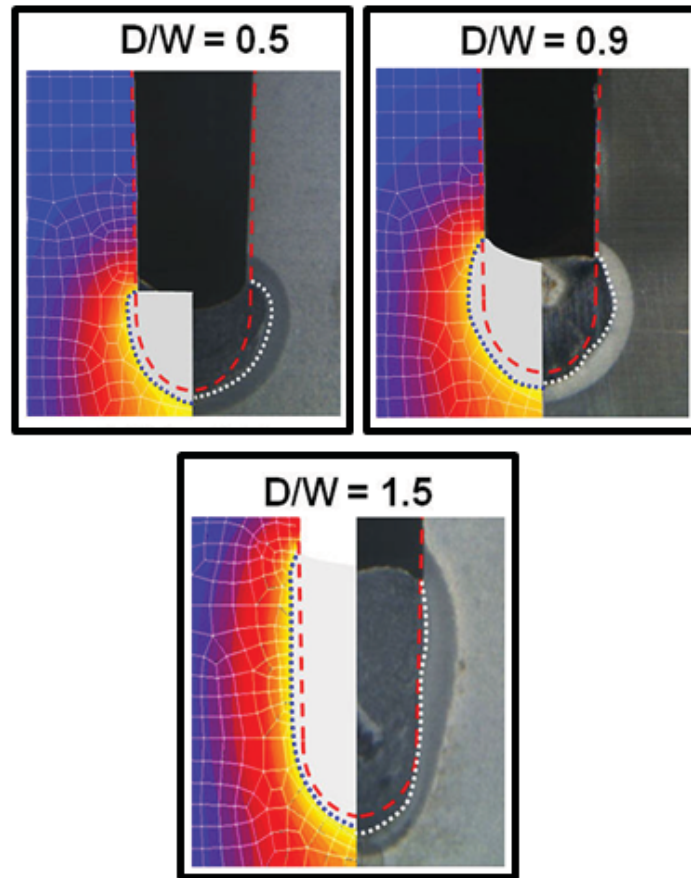


Fig. 8.8 Comparison of weld shapes between simulation and experiment.

Figure 8.8 shows the simulated weld pool shapes compared to experimental observations during the thermal analysis. It can be seen that the hot-wire laser process can be used to control the amount of penetration in a side wall. In particular, in a case where the D/W ratio is 1.5, it is not only a very small penetration but it also has a high deposition rate. In contrast, at a D/W ratio of 0.5 and 0.9 it melts, as well as having a larger fusion area.

Subsequently, the strain history as a function of temperature at each point along a centerline of a cross sectional weld was investigated to determine the maximum strain rate curve during solidification. Figure 8.9 presents the cross section at each D/W ratio where the highest strain rate position was initiated. It was found that such critical points occurred near the middle of the weld bead, as well as within the mushy zone.

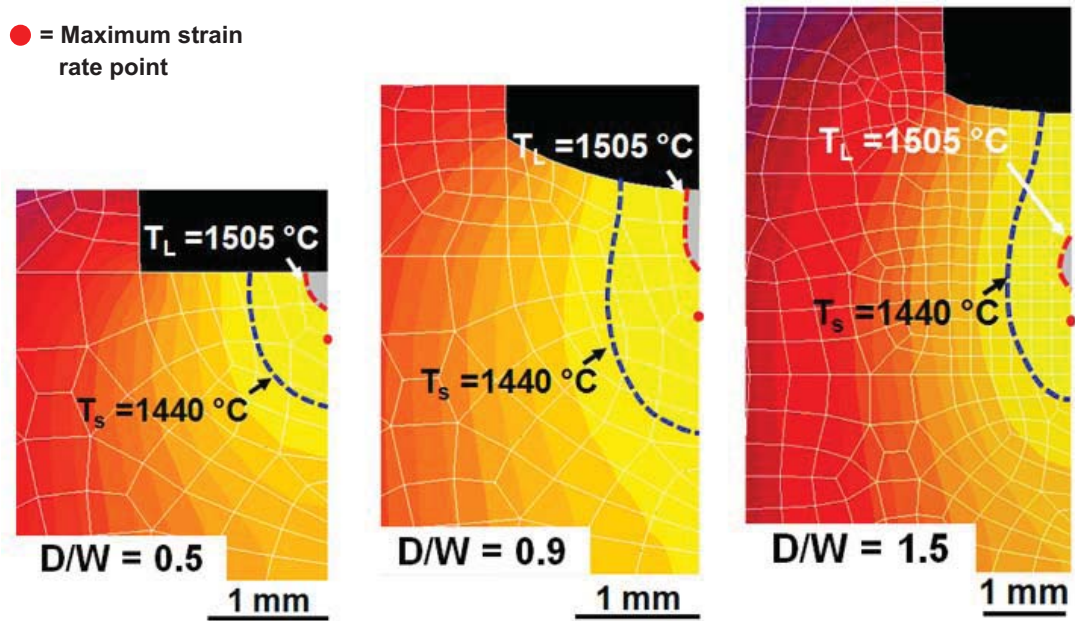


Fig. 8.9 Thermal distribution and critical strain rate position.

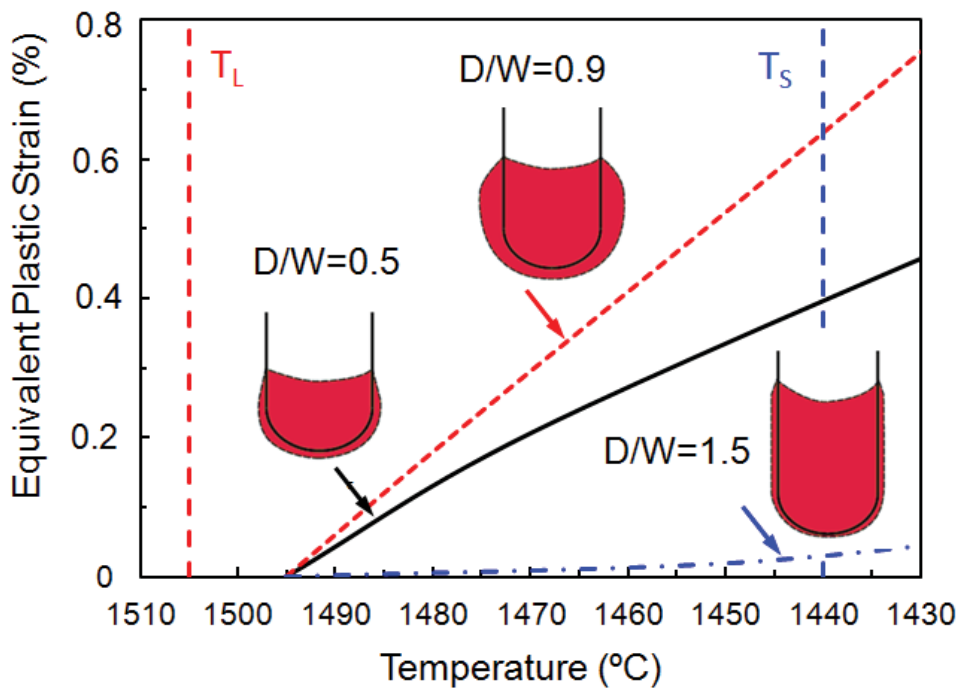


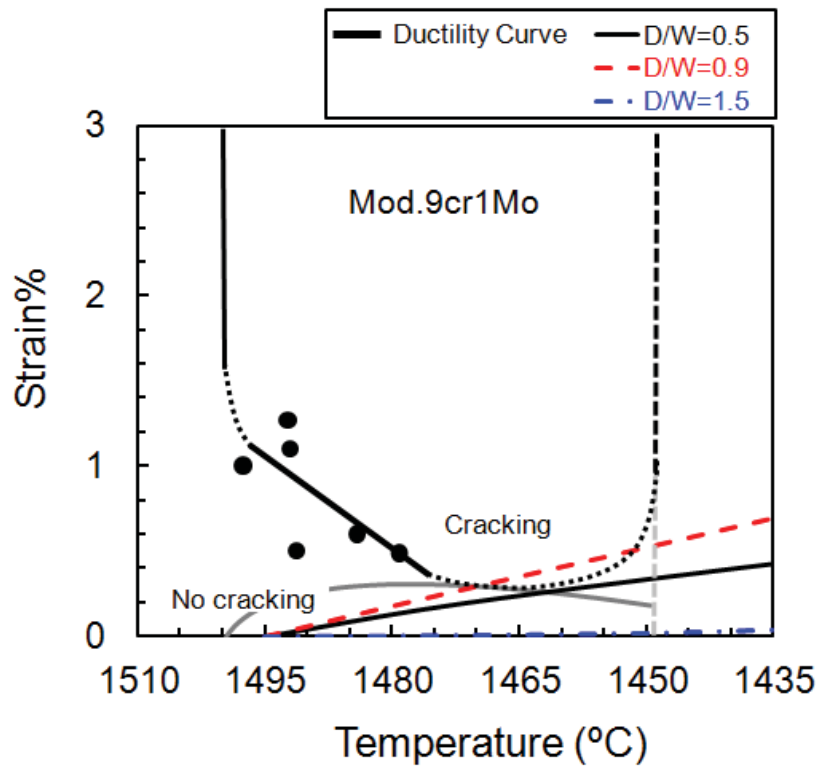
Fig. 8.10 Comparison of maximum strain history curves between D/W .

Additionally, it is important to consider the occurrence of strain history during solidification at each critical zone. Hence, as shown in Fig. 8.10, the computation results reveal a D/W ratio of 0.9 contributes to the highest strain rate and the next lower value is a D/W ratio of 0.5 and 1.5, respectively.

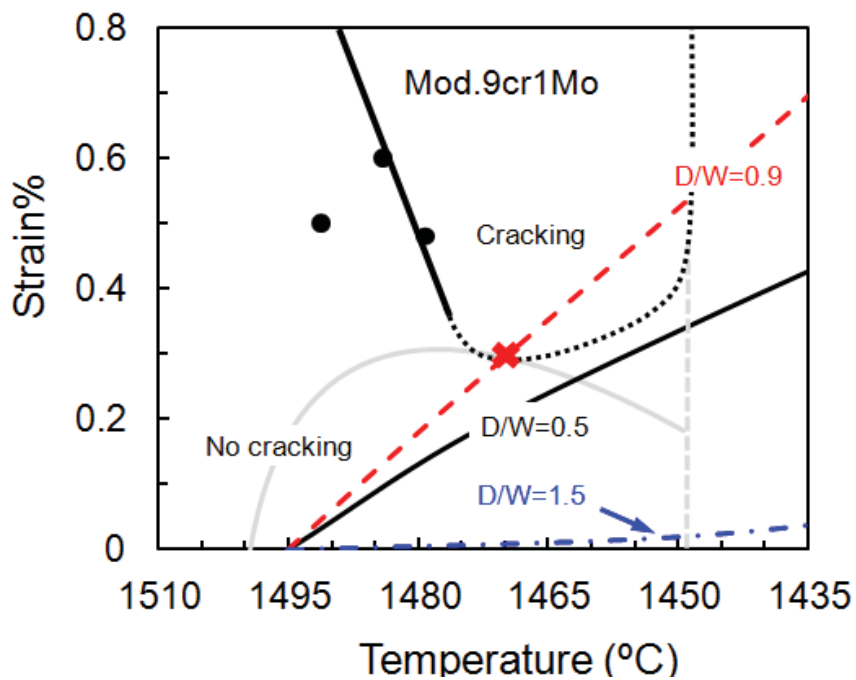
According to the principle of prediction of solidification cracking by the dynamic between a ductility curve and a high temperature strain calculated by FEM, the occurrence of solidification cracking can be predicted by comparing the strain rate with the ductility curves of the weld metal.

As seen in Fig. 8.11 (a), the ductility curve of modified 9Cr1Mo weld metal decreases sharply in the solidification temperature range because of the existence of a residual liquid film along the grain boundary. Strain history curves with different D/W ratios are compared with the ductility curve. For a clear observation, Fig. 8.10 (b) presents an enlarged view in a strain scale. As a result, it can be seen that a strain curve with a D/W ratio of 0.9 increases and then crosses the ductility curve, where the occurrence of solidification cracking is predicted. Meanwhile, strain curves with a D/W ratio of 0.5 and 1.5 do not cross the ductility curve. No solidification cracking is anticipated. In particular, notice that a unique weld bead shape, such as that with a D/W ratio of 1.5, produces a very low strain rate owing to the fact that the hot-wire laser welding method is able to provide little weld penetration in the groove side wall. Such an extraordinary weld shape results in less severe strain.

Comparing the actual experiment results, it was found that the prediction approach to solidification cracking generally corresponded. That is to say, solidification cracking occurred in a D/W ratio range of between 0.6 and 1.2. On the contrary, in a case of a D/W ratio greater than 1.2, it is evident that the hot-wire laser welding method is able to produce a weld without solidification cracking. The hot-wire laser process contributed to less risk of solidification cracking in the mechanical factor, while it is difficult to achieve this with conventional welding processes.



(a) Prediction of solidification cracking.



(b) Enlarged view of strain scale.

Fig. 8.11 Prediction of solidification cracking in each D/W ratio.

8.3 Prediction of Solidification Cracking in U-Groove Weld Cracking Test

8.3.1 Evaluation of High Temperature Strain Dependent on Root Gap Width

This work is an evaluation of the strain history in the U-shape weld test in accordance with the JIS Z 3157 standard. GMAW is utilized. SCMn3B is employed as a base metal, which is welded with G69A3UMN4M3 filler wire. A computer welding simulation was performed using 3D-FEM analysis. 3D-FEM models were developed, which included two features, namely, a root gap width of 0 and 2 mm. Thermal-mechanical properties dependent on temperature are considered in the calculation. Welding conditions were set with an arc current of 280 A, an arc voltage of 29 V, a welding speed of 0.22 m/min, a feeding speed of 8 m/min and a preheat temperature of 200°C.

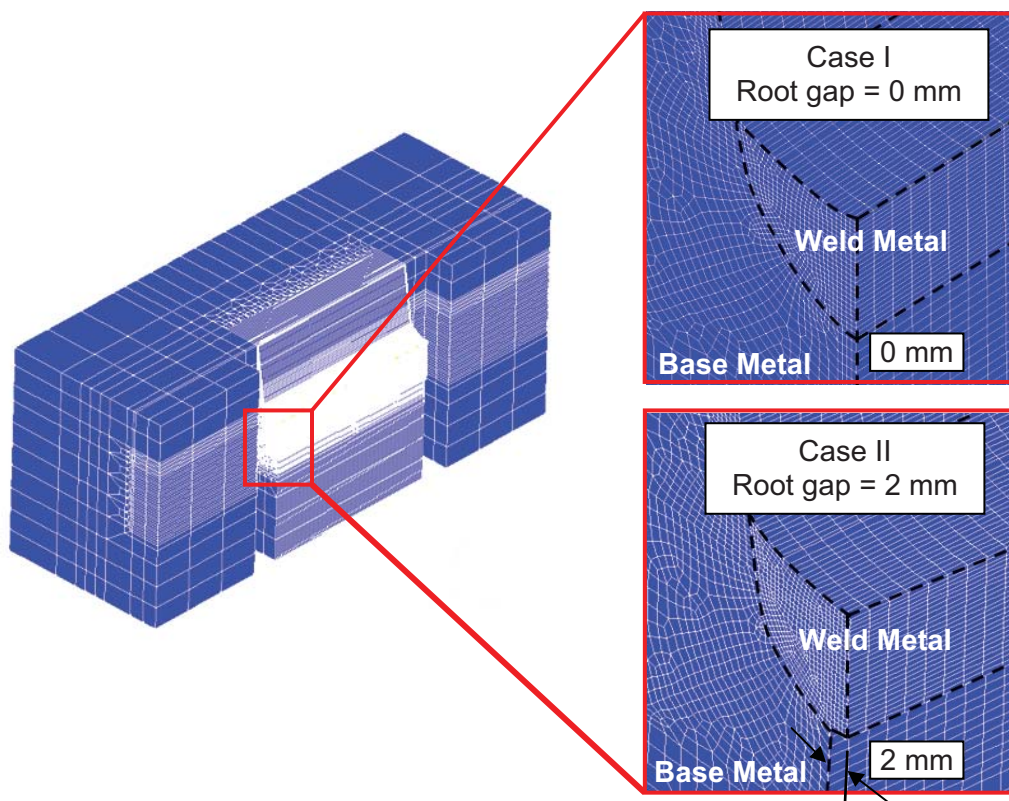


Fig. 8.12 3-D FEM models with a root gap of 0 mm and 2 mm.

As for the welding simulation, the calculation was divided into two steps. Firstly, the thermal analysis was performed to estimate the temperature distribution. The moving welding arc is modeled as a double ellipsoidal heat source proposed by Goldak's equation. Secondly, the thermal-elasto-plastic analysis was computed to estimate the high temperature strain in the solidification temperature range. The prediction of solidification weld metal cracks in the different root gap widths was studied. Figure 8.12 illustrates the FEM model with a root gap width of 0 mm and 2 mm.

Figure 8.13 shows the comparison of the simulated weld shape between a root gap width of 0 mm and 2 mm after performing the thermal analysis to achieve the temperature distribution in the welded specimen. The fusion boundary is given as 1497°C , taken from the JMatPro database. Because the solidification cracking in the first weld pass occurs outside of the center weld during the U-groove weld cracking test, the remarkable region where the anticipated occurrence of solidification cracking is specified for the calculation of the strain history. These regions are taken into account owing to the occurrences of cracking in the actual welds. The strain calculation regions are separated into two main zones, namely, the positions along the vertical axis of the weld bead and the gross area of the inside weld bead, as shown in Fig. 8.14. Figure 8.15 presents the positions where the maximum plastic strain rate was discovered on the centerline of the weld bead (point P1) and throughout the cross-section area (point P2) when the thermal-elasto-plastic analysis has already been computed. Both cases of root gap width induce the maximum strain rate in the similar position. Nevertheless, Fig. 8.16 (a) and (b) show the comparison of the maximum strain history curves in each root gap width. Fig. 8.16 (a) presents the maximum strain curves at the center welds, whereas Fig. 8.16 (b) compares the maximum strain curves between root gaps that occurred at inside welds. As a result, it can be seen that the inside weld region (P2) generates a higher strain rate than the center weld position (P1) in both cases of root gap width. Also and more importantly, the point P2 with a root gap width of 2 mm produces a drastically higher maximum strain rate than the center weld bead.

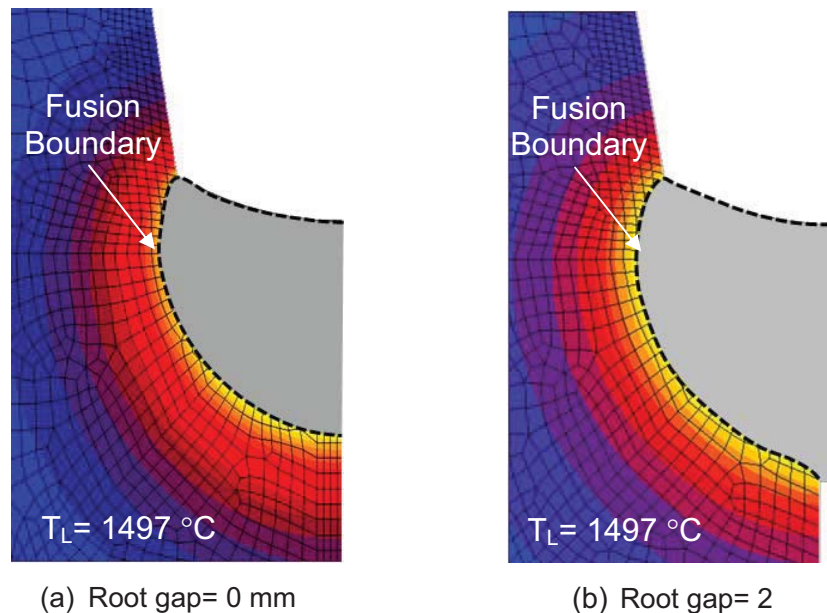


Fig. 8.13 Simulated weld shape with a root gap of 0 mm and 2 mm.

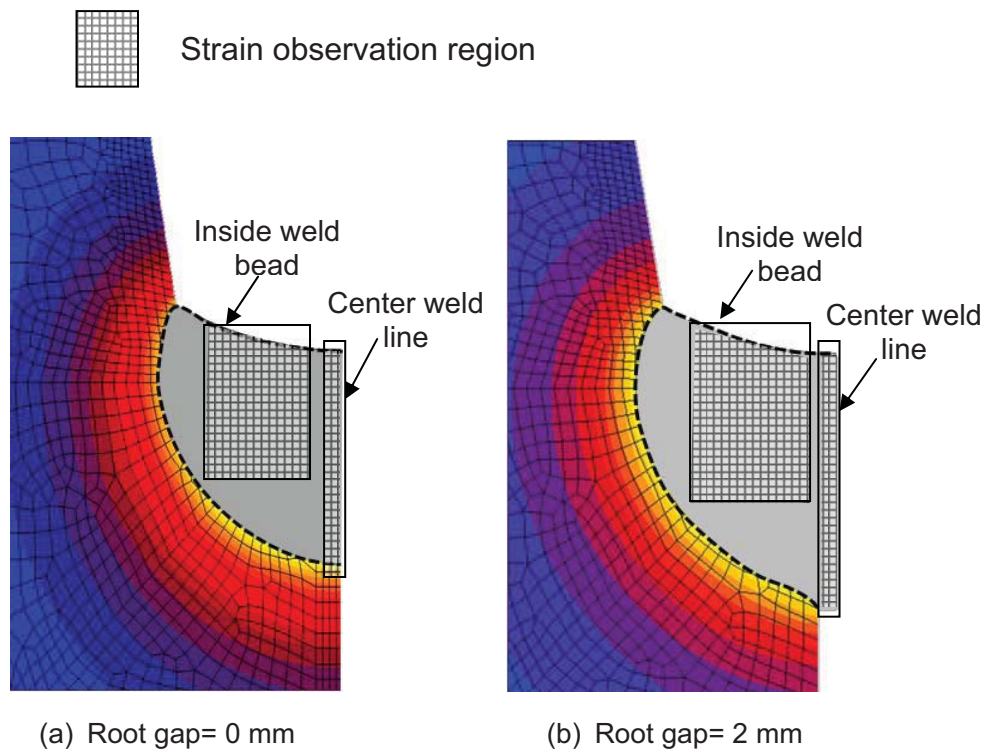


Fig. 8.14 Regions of strain calculation.

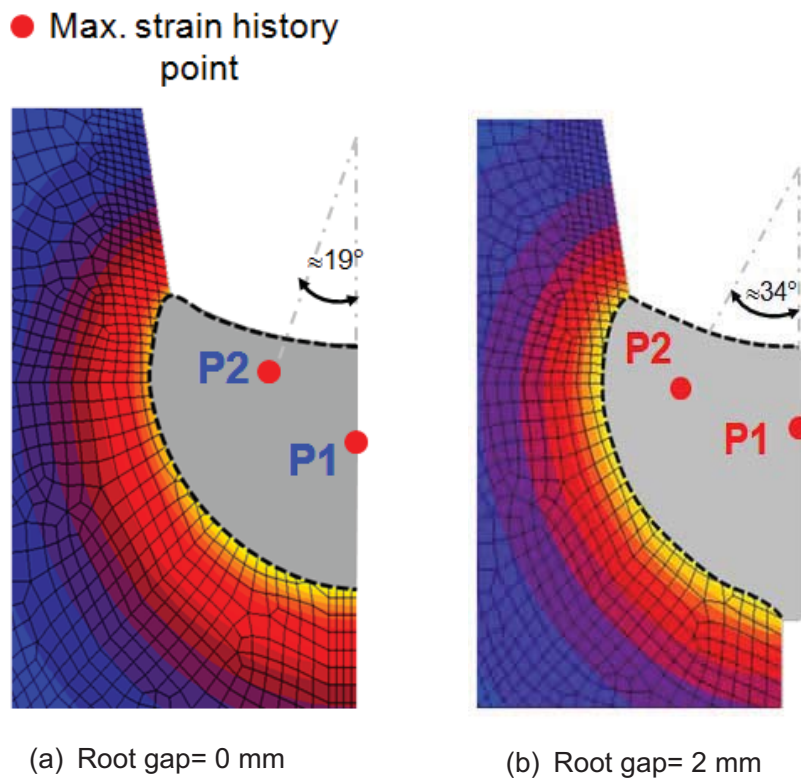
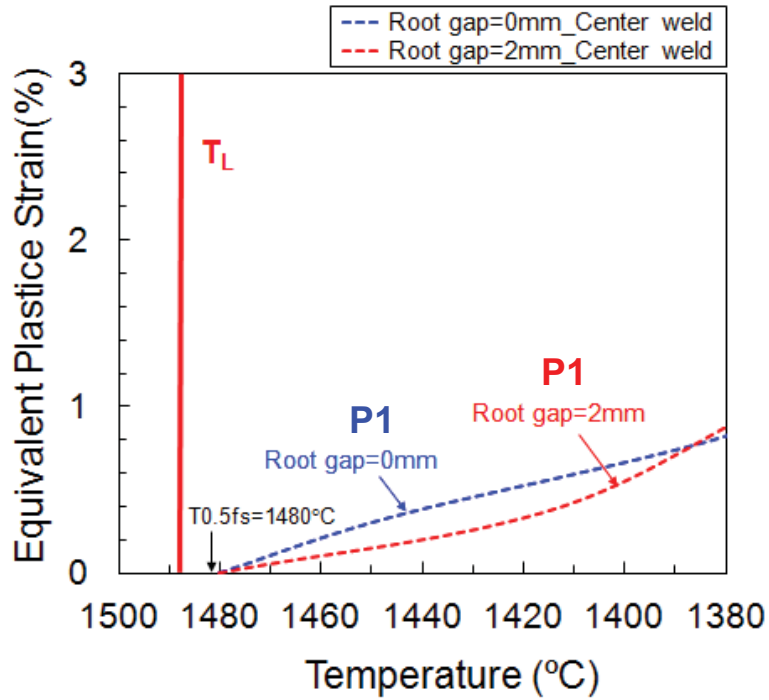
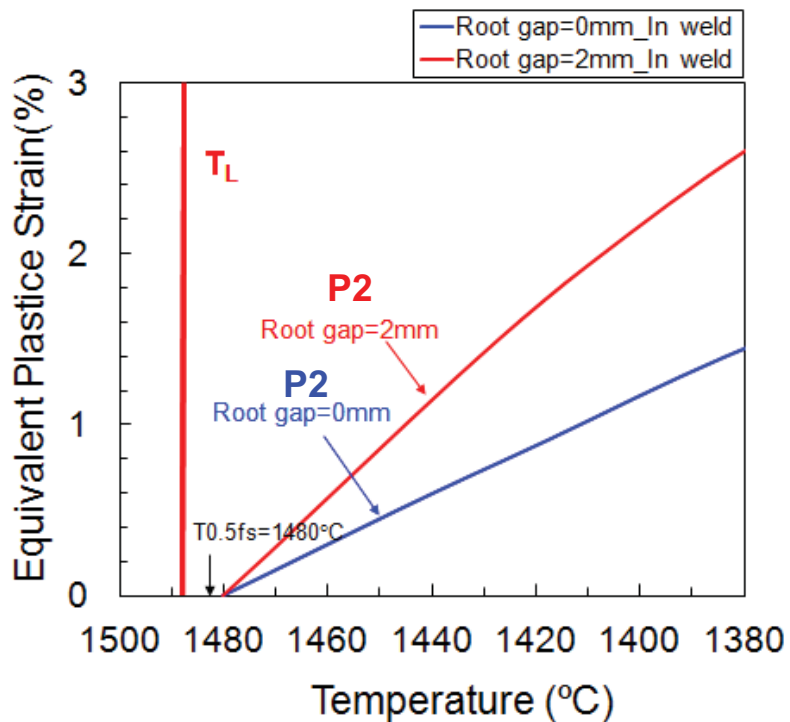


Fig. 8.15. Maximum strain history positions.



(a) Maximum strain history curves at the center welds.



(b) Maximum strain history curves at inside welds.

Fig. 8.16. Maximum strain history.
(Root gap width of 0 mm and 2 mm)

8.3.2 Prediction of Solidification Cracking in U-Groove Weld Cracking Test

The evaluation of solidification cracking susceptibility was investigated through the relationship between the high temperature ductility curve and the calculated equivalent plastic strain. The high temperature ductility curve of the weld metal (40% dilution) obtained by the U-type hot cracking test was compared to the equivalent plastic strain histories calculated with FEM. The relationship of these curves was interpreted in order to predict the occurrence of solidification cracking and its location.

Figure 8.17 shows a comparison between the ductility curve and the maximum strain history curves at the center weld (point P1). The blue and red dashed lines represent the strain history of the root gap width of 0 and 2 mm, respectively. It can be seen that those strain curves are not greater than the ductility curve. Thus, there was no solidification cracking at the center weld. In contrast, Fig. 8.18 shows the evaluation of solidification cracking at the inside weld (point P2). When compared with strain history curves at the center weld, the inside weld induces a sharply higher strain rate. In particular, solidification cracking has a strong tendency to occur in a 2 mm root gap because the strain rate exceeds the critical level of the ductility curve.

As for confirming the occurrence of solidification cracking, Fig. 8.19 presents a cross section of G69A3UMN4M3 weld metal with solidification cracking, comparing the locations of a maximum strain rate from the FEM calculation. Solidification cracking occurred considerably at the inside weld bead. Such a circumstance can be explained with an integral systematic approach to the prediction of solidification cracking. In other words, the calculated strain rate at the side weld bead after welding exceeded the high temperature ductility curve, in particular when the root gap had a width of 2 mm. Therefore, narrow gap welding of cast steel with a wide root opening increases solidification cracking susceptibility compared to welding without a root opening. Furthermore, the weld shape geometry affects the strain rate and the region where the solidification cracking occurs, as well.

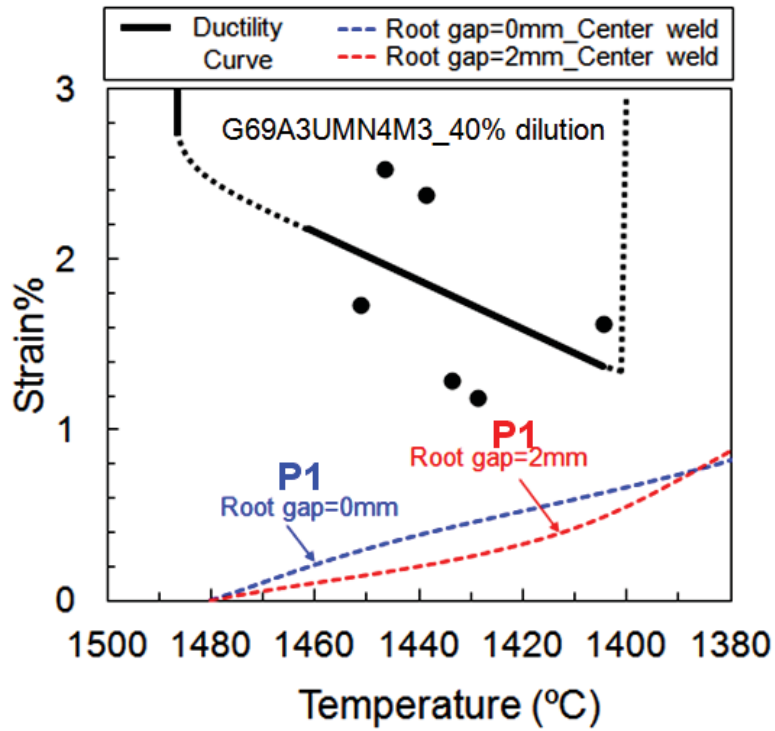


Fig. 8.17 Prediction of solidification at the center weld in each root gap width.

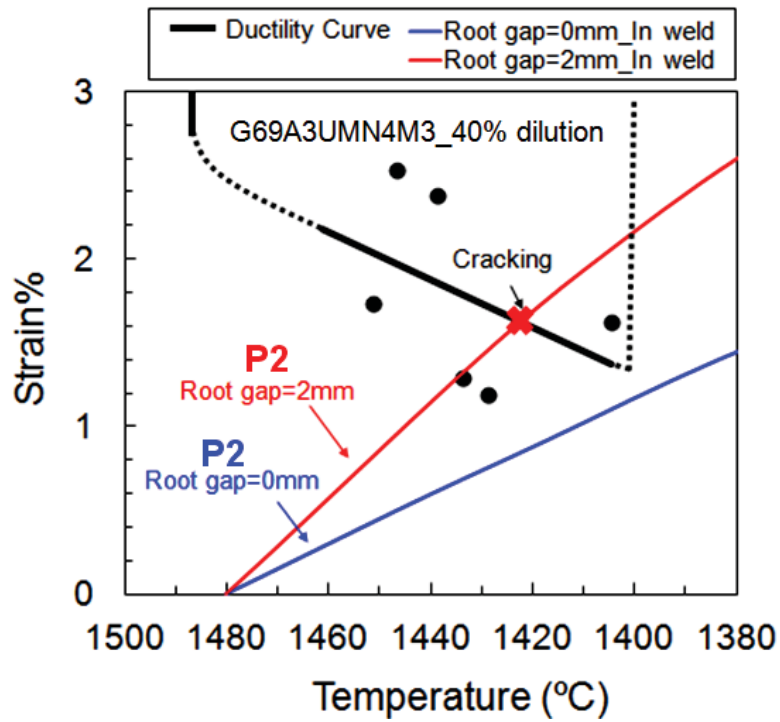


Fig. 8.18 Prediction of solidification at inside weld in each root gap width.

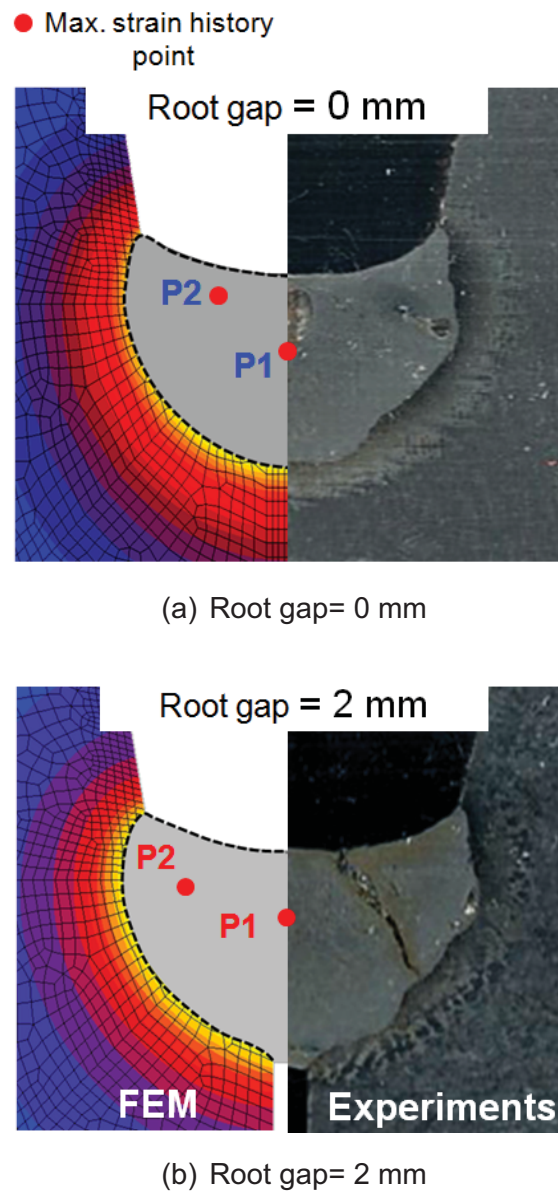


Fig. 8.19 Comparison between maximum strain points and cross-sectional welds.

8.4 Summary

In this chapter, an integral systematic approach to predicting solidification cracking in modified 9Cr1Mo weld metal and a dissimilar weld joint of G69A3UMN4M3 with 40% dilution was taken. By this means, a comparison between a ductility curve and a high temperature strain calculated with FEM analysis was utilized to anticipate the occurrence of solidification cracking. The main issues are as follows:

1. In hot-wire laser welding with a narrow gap joint for modified 9Cr1Mo weld metal, a strain calculation using 3-D FEM during weld pool solidification was performed in order to gain a thorough understanding of the effects of D/W ratios on the susceptibility of solidification cracking. D/W ratios such as 0.5, 0.9, and 1.5

were selected to evaluate strain rate in FEM analysis to correspond with the experiments. That is, for D/W ratios of more than 1.2 or less than 0.6, solidification cracking does not occur in a groove width of 3 mm. From the thermal-elasto-plastic analysis, it was found that at a higher D/W ratio, such as 1.5, presented a lower strain rate than other D/W ratios. In addition, the simulated cross section compared to the actual weld bead revealed a welding heat source from the hot-wire laser method produced little weld penetration in the groove sidewall. By this means, it is possible to decrease practically the amount of strain on a weld bead during solidification. Furthermore, the results predict solidification cracking in the different D/W ratios. Namely, a high temperature strain curve with a D/W ratio of 0.9 increases and then crosses the ductility curve; meanwhile, strain curves with a D/W ratio of 0.5 and 1.5 do not cross the ductility curve. The results agree reasonably well with the actual experiments.

2. In this study, a quantitative evaluation of the solidification cracking susceptibility of large-scale cast steel for construction machinery was undertaken. The comparison of the ductility curve and high temperature strain was interpreted in order to predict the occurrence of solidification cracking and its location. As a result, it revealed that the strain rate curves in the solidification temperature range at the central weld line in both root gap width conditions were lower than the ductility curve. That is, there is much less possibility of the occurrence of solidification cracking in the center of a weld line. On the contrary, it was clearly observed that after only the molten pool had solidified, the strain rate at the inside weld bead was higher than at the center of the weld line. Such an interesting occurrence took place under both conditions where the root gap was 0 mm and 2 mm. Moreover, it was clearly seen that in a root gap of 2 mm, there is a greater risk of solidification cracking occurring, particularly in the region of the side weld bead. When comparing the actual cross sections, the predictions generally agreed with the experimental results.

Chapter 9

Summary and Future Work

The main purpose of the present study is to evaluate and predict solidification cracking during narrow gap welding. An innovative hybrid process, so called hot wire laser welding, was developed for an extremely narrow gap joint. In accordance with the application to Modified 9Cr1Mo steel, the solidification cracking susceptibility owing to such a welding process was investigated. Furthermore, solidification cracking using GMAW for large-scale cast steel in construction machinery was also studied. By using the U-type hot cracking test with an in-situ observation method, the critical local strain to crack initiation at various temperatures during solidification was accurately measured, as well as the high temperature ductility curve. Using the 3D-FEM analysis, the high temperature strain during welding was reasonably estimated. Based on an integral systematic approach between the high temperature ductility curve and the calculated strain rate, the occurrence of solidification cracking during practical use could be understood comprehensively in both the material factor and the mechanical factor.

In the first part of the study, the background of the research and the objective and construction of the thesis were discussed. After that, the present research on solidification cracking, as well as related studies, was reviewed and summarized.

Next, the development of the hot wire laser welding for the narrow gap joints was described. Test pieces of ASTM A 304 stainless steel were welded with a tentative filler rod made of Inconel 600 alloy. The welding phenomena of the molten pool and the weld bead formation during welding were investigated with in-situ observation using a high-speed camera. Welding parameters such as the wire current, the wire feeding position, and the wire feeding angle were investigated to determine the appropriate conditions. An experiment on the laser beam reflection indicated that the laser beam reflected from the molten pool was a crucial phenomenon to explain the formation of the weld bead, especially in terms of melting the side groove wall of the base metal. Experimental results showed that the hot wire laser welding was able to produce a complete weld deposition with a very low dilution of the base metal. The welding parameters, as mentioned above, significantly affected the weld quality. The sufficiency of the bonding strength at the fusion boundary was examined using a tensile test. Metallurgical examination of the fracture surface revealed a rupture occurred in the weld metal and no defects, most likely because the fusion boundary was stronger than the weld metal.

Then, the hot wire laser welding with a narrow gap joint was applied to the Modified 9Cr1Mo steel. It was found that solidification cracking occurred in this material. Thus, the effect of the weld shape depth-to-width ratio (D/W) on the

solidification cracking susceptibility was investigated. With a groove width of 3 mm, solidification cracking did not occur with a D/W ratio of less than 0.6 or more than 1.2. The hot wire laser welding method with a narrow gap joint was efficient for practical use because the higher D/W condition was used without solidification cracking.

In addition, solidification cracking using GMAW on extra thick, large-scale cast steel parts for construction machinery, especially in the first weld pass of a narrow groove joint, was investigated by reproducing cracking behavior using the U-groove weld cracking test. The important factors in solidification cracking susceptibility were studied, namely, the degree of constraint, the root gap width, and the use of different filler wires. From the results, it was found that welding with G69A3UMN4M3 filler wire in a root gap width of 2 mm caused solidification cracking. It suggests that a wider root gap has a tendency to induce solidification cracking during welding.

In order to evaluate the material factor in solidification cracking, both the Modified 9Cr1Mo weld metal and the cast steel weld metal were experimented on to obtain high temperature ductility curves by means of the U-type hot cracking test using an in-situ observation method. In particular, for the cast steel weld metal, G69A3UMN4M3 weld metal with a 40% dilution ratio was used, due to it corresponding with the actual experiments. It was found that the Modified 9Cr1Mo weld metal had greater solidification cracking susceptibility than other high-resistance steels, such as SUS 310S and Inconel 600. Meanwhile, the G69A3UMN4M3 weld metal with 40% dilution, which was used to weld the SCMn3B base metal, had lower solidification cracking susceptibility.

Regarding the mechanical factor, 3D-FEM was simulated to estimate the high temperature strain in the weld metal during welding. According to the hot wire laser welding with a narrow gap joint, the high temperature strain was calculated in order to make clear the effect of D/W ratios on the susceptibility of solidification cracking in theory. The special heat source model consistent with the hot wire laser welding phenomenon was applied and validated based on the experimental measurements. The simulation results showed that a welding heat source using hot wire laser welding was able to produce a particular weld shape at a higher D/W ratio with a lower weld strain rate. Meanwhile, the FEM analysis of the U-groove weld cracking test using GMAW revealed that the inside weld induced a weld strain rate sharply higher than the centerline weld, particular in the case of a 2 mm root gap.

Finally, the prediction of solidification cracking by comparing the high temperature ductility curve and the calculated strain rate was analyzed. The occurrence of solidification cracking agreed reasonably well with the actual experiments. In a narrow-gap welding of the Modified 9Cr1Mo steel, it was found that a unique weld shape with a high D/W ratio can be achieved through hot wire laser welding. The FEM results showed that the high temperature strain rate was much lower than the ductility curve. Solidification cracking did not occur in such a unique weld shape. The prediction results corresponded to the relationship between D/W ratios and solidification cracking in the experiments.

In the narrow-gap GMAW of the cast steel, a wider root opening promotes greater solidification cracking susceptibility than a welding without a root opening. The weld strain calculated with FEM showed a higher level occurred at the inside weld rather than the centerline weld. Solidification cracking has a tendency to occur around that area. The prediction presented good agreement with the experimental results, as well. Furthermore, the geometry of the weld shape affects the amount of weld strain and the region where the solidification cracking occurs, as well.

This approach is of benefit to practically decrease the effect of weld shape on solidification cracking. In future studies, in order to further understand the occurrence of solidification cracking in Modified 9Cr1Mo, especially in a narrow-gap welding, the FEM approach should be improved to evaluate high temperature strain in multi-pass welding and groove width size.

Acknowledgements

I would like to express my sincere gratitude to Professor Kenji Shinozaki for his guidance, encouragement and insight throughout this study. He gave me full support not only with my research, but also with my life and career, and has played an important role in both my academic and personal development. I would like to thank Associate Professor Motomichi Yamamoto. He gave me so much positive help and instructive discussion in my study, and I have learned so much from him. Additionally, I extend many thanks to Professor Atsushi Sugata, Professor Gen Sasaki, and Professor Kazuhiro Matsugi for our precious discussions and their advice.

I would like to express my heartfelt thanks to Assistant Professor Kota Kadoi for helping my study. I would like to thank the past and present members of my research group: Mr. Akito Nishijima, Mr. Yamamoto Massayuki, Mr. Akira Fujinaga Mr. Hyoma Kengo, Mr Ryohei Nakamura. I would also like to thank all the past and present members of the Materials Joining Science and Engineering Laboratory, in the Department of Mechanical System Engineering, Hiroshima University, for their enthusiastic help to both my life and study.

I would like thank my parents for their support and encouragement from my youth to my time as a doctoral student. Their teaching is gratefully appreciated and has been invaluable in my life.

References

- 1) ASM INTERNATIONAL, ASM Handbook: Welding Brazing and Soldering, Vol. 6, US, 1993.
- 2) American Welding Society: Welding Hand Book, Vol. 1. Welding Science and technology. 9th ed., American Welding Society, USA (2001)
- 3) Sindo Kou.: Welding Metallurgy. 2nd. Wiley & Son, USA (2003)
- 4) B. Chalmers Principles of Solidification. John Wiley, (1964)
- 5) Cicero M.D. Starling , et al.,“ Statistical modelling of narrow-gap GTA welding with magnetic arc oscillation”, Journal of Materials Processing Technology 51 (1995) 37-49.
- 6) T.H.Hyde et al., “Assessment of creep behavior of a narrow gap weld”, International Journal of Pressure Vessels and Piping, 76(1999)515–525.
- 7) Pankaj Biswas et al.,“Analysis of welding distortion due to narrow-gap welding of upper port plug”, Fusion Engineering and Design 85 (2010) 780–788.
- 8) Cicero M. D. Starling, Paulo V. Marques and Paulo J. Modenesi: Statistical modeling of narrow-gap GTA welding with magnetic arc oscillation. J.Materials Processing Technology, 51, 37-49(1995)
- 9) I. Shinji, M. Masatoshi, and K. Yuji: Application of Narrow Gap Welding Process with High Speed Rotating Arc to Box Column Joints of Heavy Thick Plates. JFE technical report, 14, 16-21 (2009)
- 10)D. Yapp and S. A. Blackman: Recent Developments in High Productivity Pipeline Welding. J.the Braz. Soc. of Mech. Sci. & Eng, 26 -1,89-97(2004).
- 11)C. Liu, J.X. Zhang, C.B. Xue: Numerical investigation on residual stress distribution and evolution during multi pass narrow gap welding of thick-walled stainless steel pipes. J.Fusion Engineering and Design, 5681, 1-8(2011)
- 12)Nomura, Hirokazu, Sugitani,Yuji, Kobayashi, Yukio. “Narrow Gap MIG Welding Process with High Speed Rotating Arc” Journal of High Pressure Institute of Japan. 1984, vol. 22, no. 4, p. 186–193.
- 13)M. Yamamoto, K. shinozaki , K. Kadoi, D. Fujita, T. INOUE, M. Fukahori, and Y. Kitahara: Development of welding method for wide gap lap joint of steel sheet using laser welding with hot-wire. Transactions of JWRI, 39-2, 44-46(2010)
- 14)T. Okagaito, H. Watanabe, K. Shinozaki, M. Yamamoto, K. Kadoi, A. Nishijima, and R. Phaonaim: Development of Narrow Gap Hot-Wire Laser Welding Process for Heat-Resistant Steel Pipe for Boiler. National Meeting of Japan Welding Society,90(4), 200-201(2010)(in Japanese)
- 15)K. Shinozaki, M. Yamamoto, K. Kadoi, S. Tsuchiya, H. Watanabe, T. Nagashima: Investigation of Narrow Gap Hot-wire Laser Welding Phenomena”, National Meeting of Japan Welding Society, 87, 364-365 (2010) (in Japanese)

- 16) K. Shinozaki, M. Yamamoto, K. Kadoi, S. Kurachi, A. Nishijima, H. Watanabe, T. Nagashima : Development of Multi-pass Welding Technology using Narrow Gap Hot-wire Laser Welding Process for Nickel-based Superalloys”. National Meeting of Japan Welding Society, 87, 366-367 (2010) (in Japanese)
- 17) Miikka Karhu and Veli Kujanpää I: Experimental test set-up for studying hot cracking in multi pass laser hybrid welding of thick section austenitic stainless steel. Laser Materials Processing Conference, ICALEO, 535-544(2008)
- 18) M. Ono, Y. Shinbo, A. Yoshitake, and M. Ohmura: Development of Laser-arc Hybrid Welding. NKK technical review, 86,9-12(2002)
- 19) T. Maruyama, M. Yoshida, K. Kurokawa, Y. Kawahara, N. Otsuka: Development of Advanced Ultra Supercritical Fossil Power Plants in Japan: Materials and High Temperature Corrosion Properties, J. Materials Science Forum, 696, 236-241(2011).
- 20) H. Kimura, T. Sato, C. Bergins, S. Imano, E. Saito: Development of technologies for improving efficiency of large coal-fired thermal power plants, Hitachi review, 60(7), 365-371(2011).
- 21) Masakazu Shibahara, Shinsuke Itoh, Kohei Nakata, Shinji Takaba, Hisashi Serizawa, Koji Masaoka, Hidekazu Murakawa. “Prediction of Pear-shaped Bead Cracking under Full Penetration Welding of T-Joints Using Temperature Dependent Interface Element” QUARTERLY JOURNAL OF THE JAPAN WELDING SOCIETY, 2009, Vol.27, NO.1, p.73-80
- 22) J.L. Seran and et al.: “Development of 9-12 Cr martensitic steels for future nuclear system; weldability studied, mechanical characteristics and specification improvements, proceeding of 3rd international topical meeting on high temperature reactor technology (HTR), 1-10(2006).
- 23) K. Shinozaki, M. Yamamoto, K. Kadoi, K. Hyoma, H. Yamamoto, and T. Nakama ;” Evaluation of Solidification Cracking Susceptibility in Cast Steels : Evaluation of Hot Cracking Susceptibility on Large Scaled Cast Steel Part for Construction Machinery during GMA Welding (1st Report), National Meeting of Japan Welding Society, 89 (2011), p.20-21, [in Japanese]
- 24) K. Katada; “Construction Equipments and Machine Tools”, J. Japan Welding Society, 81(5), (2012), p.428-429, [in Japanese]
- 25) M. J. Cieslak and w. F. Savage; “ Weldability and Solidification Phenomena of Cast Stainless Steel”, Welding research supplement, (1980), p.136s-146s
- 26) Jae-Do Kim et al., “Repair welding of etched tubular components of nuclear power plant by Nd;YAG Laser”, Materials Processing Technology, vol. 114, 2001, pp. 51–56.
- 27) T. Branza et al., “Study and prevention of cracking during weld-repair of heat-resistant cast steels”, journal of materials processing technology, Vol. 209, (2009), pp 536–547.
- 28) K. Kimura, M. Tabuchi, Y. Takahashi, K. Yoshida and K. Yagi, "Long-term Creep Strength and Strength Reduction Factor for Welded Joints of ASME Grade 91,

- 92 and 122 Type Steels," International Journal of Microstructure and Material Properties, vol. 6, Nos. 1/2, pp. 72-90, 2011.
- 29) Dodko, D.A et al.; " Multi-pass welding of thick metal in the shield of carbon dioxide", automation Welding, V3, (1957), p. 58-59
- 30) R. P. Meister and D. C. Martin: Narrow Gap Welding Process, British Welding Journal, Vol.13 (1966) p.252-257.
- 31) Masao Ushio, Fukuhisa Matsuda, Isao Masumoto. "Narrow gap welding Review on NGW in Japan (Part 1)" Journal of the Japan Welding Society. 1985, Vol.54, No.6; p.358-365.[in Japanese]
- 32) Masao Ushio, Fukuhisa Matsuda, Isao Masumoto. "Narrow gap welding. Review on NGW in Japan. (Part 2)" Journal of the Japan Welding Society. 1985, Vol.54, NO.8; p. 451-455. [in Japanese]
- 33) G. A. Hutt : Narrow Gap Welding, Metal Construction, June (1984) p.355.
- 34) Claus Bagger and Flemming O. Olsen; "Review of laser hybrid welding", Journal of Laser Applications, Vol.17, 2005, doi: 10.2351/1.1848532
- 35) H. Nomura and Y. Sugitani; " Further improvements of narrow gap welding technique" , Journal of Metals, Vol 2, (1984), p. 73-85
- 36) V.Y. MALIN : The State of the Art of Narrow Gap Welding, Welding Journal, April (1983) p.22 and June (1983) p.37.
- 37) D. Bajic, G. Vladimirovich Kuzmenko, and I. Samardzic, " Welding of rails with new technology of arc welding", Journal of Metalurgija, V(52), (2013), p.399-402
- 38) Takeshi Shinoda, Katsuei Hoshino; Ryouichi Yamashita, Hidehiko Ono. "Development of solidification cracking test for MAG narrow gap welding. Effect of boron contents on solidification cracking" QUARTERLY JOURNAL OF THE JAPAN WELDING SOCIETY. 1990, Vol. 8, NO.1, PAGE.21-25;
- 39) Sadao Tsushima, Yukihiro Horii, Nobutaka Yurioka. "Development of AC-MIG welding process (Report 5). Application of AC-MIG narrow gap welding process for butt joints of 980MPa high strength steels" QUARTERLY Journal of the Japan Welding Society. 1994, Vol.12, NO.1, p.51-57
- 40) Katsuyoshi HORI and Mitsuaki HANEDA; "Narrow Gap Arc Welding", Journal of the Japan Welding Society. 1999, Vol.68, NO.3, p.41-62 [in Japanese]
- 41) M. Persson; " Fully Automation Welding of Thickwalled Pressure Vessel by the Narrow Gap Subaer Process", J. Materials and Design, Vol.6, No.5, (1985), 244-247
- 42) Chandel, R.S and Bala, S.R: " effect of welding parameters and groove angle on the soundness of root beads deposited by SAW process, Advance in Welding Science and Technology, ASM, (1983), p. 379-385
- 43) www.ametinc.com/.../AMET_Narrow_Gap_SAW
- 44) K Hori, H Watanabe, K Kusano, T Myoga, "Development of hot wire TIG welding methods using pulsed current to heat filler wire – research on pulse

- heated hot wire TIG welding processes” *Journal of Welding International*, 2004, Vol. 18, Issue 6, p. 456-468.
- 45) K Kusano, H Watanabe. “Recent trends in development of high-efficiency TIG welding; high deposition TIG welding and ultranarrow-gap TIG welding” *Journal of Welding International*, 2002, Vol. 16, Issue 12, p. 986-991.
- 46) Qing Jie Sun, Hai Feng Hu, Xin Yuan, Ji Cai Feng. “Research Status and Development Trend of Narrow-Gap TIG Welding” *Advanced Materials Research*, 2011, Vol. 308-310, p. 1170-1176.
- 47) Cicero M.D. Starling, et al., “Statistical modelling of narrow-gap GTA welding with magnetic arc oscillation”, *Journal of Materials Processing Technology* 51 (1995) 37-49.
- 48) S. Pike, C. Allen, C. Punshon, P. Threadgill, M. Gallegillo, and B. Holmes, J. Nicholas; Technical Report 09-05. “Critical Review of Welding Technology for Canisters for Disposal of Spent Fuel and High Level Waste”, TWI, Ltd., (2010)
- 49) Abdel Monem, El Batahy, “Effect of laser welding parameters on fusion zone shape and solidification structure of austenitic stainless steels” *Materials Letters*, 1997, Vol. 32, p. 155-163.
- 50) N. Coniglio, C.E. Cross, “Mechanisms for Solidification Crack Initiation and Growth in Aluminum Welding” *Metallurgical and Materials Transactions A*, 2009, Vol. 40A, p. 2718-2728.
- 51) F. Jalilian, M. Jahazi, R.A.L. Drew, “Microstructural evolution during transient liquid phase bonding of Inconel 617 using Ni-Si-B filler metal” *Materials Science and Engineering*, 2006, Vol 423 A, p. 269-281.
- 52) Borland, J.C 1960. Generalized theory of super-solidus cracking in welds. *British Welding journal*(Aug): 508-512
- 53) Borland, J.C 1961. Suggested explanation of hot cracking in mild and low alloy steel welds. *British Welding Journal*(Nov): 526-540
- 54) J.C. Borland; “Fundamentals of Solidification Cracking in Welds”. *J.Welding and Metal Fabrication*, (1979).p. 99-107
- 55) Tomita. S. 1988. Investigation of weld solidification cracking by MISO technique. Ph.D. Dissertation of Osaka University, Osaka Japan.
- 56) J.C. Lippold; “Recent Developments in Weldability Testing”, In: *Hot Cracking Phenomena in Welds*, Springer, 2005, p. 271-290.
- 57) Miikka Karhu and Veli Kujanpää, “Experimental test set-up for studying hot cracking in multi pass laser hybrid welding of thick section austenitic stainless steel”, *Laser Materials Processing Conference, ICALEO® 2008 Congress Proceeding*, pp. 535-544.
- 58) Akira matsunawa et al., “Mathematical Modeling of Fusion and solidification in Laser welding and Evaluation of Hot cracking Susceptibility”, *Welding Research Institute (JWRI)*, Vol. 25, 1996.
- 59) Yoshiaki Arata, Fukuhisa Matsuda, Seiji Katayama, “Solidification Crack Susceptibility in Weld Metals of Fully Austenitic Stainless Steels (Report I)- Fundamental Investigation on Solidification Behavior of Fully Austenitic and Duplex Microstructures and Effect of Ferrite in Microsegregation” *Transaction of JWRI*, 1976, Vol.5, No.2, p. 35-51.
- 60) Fukuhisa Matsuda, Hiroji Nakagawa, Seishiro Ogata, Seiji Katayama. “Fractographic Investigation on Solidification Crack in the Varestraint Test of Fully Austenitic Stainless Steel- Studies of Fractography of Welded Zone (III)” *Transaction of JWRI*, 1978, Vol.7, No.1, p. 59-70.

- 61) Fukuhisa Matsuda, Kazuhiro Nakata, Shoji Harada, "Moving Characteristics of Weld Edges during Solidification in Relation to Solidification Cracking in GTA Weld of Aluminum Alloy Thin Sheet" Transaction of JWRI, 1980, Vol.9, No.2, p. 83-93.
- 62) F. Matsuda). Hot Crack Susceptibility of Weld Metal. In: Advances in Welding Metallurgy, Miami, FL: Am. Welding Soc, Jap. Welding Soc., Jap. Welding Eng.Soc.: (1990), p.19-35.
- 63) Fukuhisa Matsuda, Hiroji Nakagawa, Kazuhiro Nakata, Hiroaki Kohmoto, Yoshiaki Honda, "Quantitative Evaluation of Solidification Brittleness of Weld Metal during Solidification by Means of In-situ Observation and Measurement (Report I)- Development of the MISO Technique" Transaction of JWRI, 1983, Vol.12, No.1, p. 65-72.
- 64) Fukuhisa Matsuda, Hiroji Nakagawa, Hiroaki Kohmoto, Yoshiaki Honda, Yasuhiro Matsubara. "Quantitative Evaluation of Solidification Brittleness of Weld Metal during Solidification by Means of In-situ Observation and Measurement (Report II)- Solidification Ductility Curves for Steels with the MISO Technique" Transaction of JWRI, 1983, Vol.12, No.1, p. 73-80.
- 65) Bochvar A.A. Rykalin N.N. Prokhorov N.N. Novikor I.I. and Movchan B.A. 1960. Welding production (10): 5-7.
- 66) Masakazu Shibahara. "Finite Element Simulation of Pear-shaped Bead Cracking in Narrow Gap Welding", Proceedings of The Thirteenth (2003) International Offshore and Polar Engineering Conference, USA, 2003, p.135-140
- 67) Masakazu Shibahara, Shinsuke Itoh, Hisashi Serizawa, Koji Masaoka, Hidekazu Murakawa "Development of 3D Finite Element Method for Hot Cracking Using Interface Element and Its Application for Pear-shaped Bead Cracking Under Narrow Gap Welding" QUARTERLY JOURNAL OF THE JAPAN WELDING SOCIETY, 2009, Vol.27, NO.1, p.81-88.
- 68) Weiping Liu. "Computational analysis and prediction of weld-solidification cracking" Computational Materials Science, 1995, Vol. 4, p. 211-219.
- 69) Jian-Qiang ZHANG et al ., "Numerical simulation of mechanical controlling parameters for TypeIV cracking on the welding joints of martensitic heat-resistant steel", Mater.Sci.China2010,4(2):210–216
- 70) Masato Yamamoto et al., "Applicability of C parameter in assessing TypeIV creep cracking in Mod. 9Cr–1Mo steel welded joint", Engineering Fracture Mechanics 77(2010)3022–3034
- 71) WEN Peng et al., "In-situ Observation of Solidification Cracking of Laser Dissimilar Welded Joint", 2009, p 134s-138s
- 72) Yanhong Wei et al., "Modeling the Trans-Varestraint test with finite element method", Computational Materials Science, Vol. 35, 2006, pp. 84–91.
- 73) H. Murakawa, H. Serizawa, M. Shibahara (2003). Prediction of Welding Hot Cracking using Temperature Dependent Interface Element. In: Mathematical Modelling of Weld Phenomena 7, Maney: 539-554.
- 74) Zhibo Dong, Yanhong Wei, Yanhi Xu, "Predicting weld solidification cracks in multipass welds of SUS310 stainless steel" Computational Materials Science, 2006, Vol. 38, p. 459-466.
- 75) Z.B. Dong, Y.H. Wei, "Three dimensional modeling weld solidification cracks in multipass welding" Theoretical and Applied Fracture Mechanics, 2006, Vol. 46. P. 156-165.

- 76) Wei Y.H. and Liu R.P. 2003. Science and technology of welding and joining 8(5): 325-333.
- 77) J. A. Goldak, M. Akhlaghi, Computational Welding Mechanics, Springer Science + Business Media, Inc , 2005
- 78) J. A. Goldak, A. Chakravarti, M. Bibby, 1984, A finite element model for welding heat sources, Metallurgical Transactions B, Vol. 15B, pp. 299-305
- 79) D. Radaj: "Heat effects of welding", Springer-Verlag, Berlin, 1992
- 80) V. A. Karkhin and A. Yu. Pilipenko: " Modeling thermal cycles in the weld metal and the heat affected zone in beam methods of welding thick plates" ,Welding International, 1997, Vol.11, 401-403;
- 81) P. L. Mangonon, M. A. Mahimkar: "A three-dimensional heat transfer finite element model of submerged arc welding of HSLA steels", Advances in Welding Science and Technology - TWR '86: Proceedings of an International Conference on Trends in Welding Research, Gatlinburg, USA, 1986
- 82) Yu. Luo, H. Murakawa, Yu. Ueda: "Prediction of welding deformation and residual stress by elastic FEM based on inherent strain", Trans. JWRI, Vol. 26, 1997, No. 2, p. 467-475
- 83) C. D. Wu, H. g. Wang, and Y. M. Zhang; "A New Heat Source Model for Keyhole Plasma Arc Welding in FEM Analysis of the Temperature Profile", Welding Journal, 2006, p. 284s-291s
- 84) C. Liu, J.X. Zhang, C.B. Xue: Numerical investigation on residual stress distribution and evolution during multi pass narrow gap welding of thick-walled stainless steel pipes. J. Fusion Engineering and Design, 5681, 1-8(2011).
- 85) Masakazu Shibahara, Shinsuke Itoh, Hisashi Serizawa, Weiping Liu, Hidekazu Murakawa "Finite Element Simulation of Pear-shape Bead Cracking in Narrow Gap Welding" Proceeding of The Thirteenth International offshore and Polar Engineering Conference, Honolulu, Hawaii, USA, 2003, May 25-30, p. 135-140.
- 86) Masato Yamamoto et al., "Applicability of C parameter in assessing TypeIV creep cracking in Mod. 9Cr-1Mo steel welded joint", EngineeringFractureMechanics77(2010)3022-3034
- 87) T. Massé, Y. Lejeail; Creep mechanical behavior of modified 9Cr1Mo steel weldments: Experimental analysis and modeling, J. Nuclear Engineering and Design, 254, 97-110 (2013).
- 88) B. Fourniera, F. Dallea, M. Sauzaya, J. Longoura, M. Salvia, C. Caësa, I. Tourniéa, P.-F. Giroux, S.-H. Kim: Comparison of various 9-12%Cr steels under fatigue and creep-fatigue loadings at high temperature, J. Materials Science and Engineering A 528, 6934-6945(2011)
- 89) T. Maruyama, M. Yoshiba, K. Kurokawa, Y. Kawahara, N. Otsuka: Development of Advanced Ultra Supercritical Fossil Power Plants in Japan: Materials and High Temperature Corrosion Properties, J. Materials Science Forum, 696, 236-241(2011).
- 90) H. Kimura, T. Sato, C. Bergins, S. Imano, E. Saito: Development of technologies for improving efficiency of large coal-fired thermal power plants, Hitachi review, 60(7), 365-371(2011).
- 91) Fukuhisa Matsuda et al., "Solidification Crack Susceptibility in Weld metals of Duplex Stainless Steel", Welding Research Institute (JWRI), Vol. 15, No.1, 1986, pp. 99-112.

- 92) I. Varol and W.A. Baselack., "characterization of weld solidification cracking in duplex stainless steels", *Metallography*, vol.23, 1989, pp. 1-19.
- 93) Abdulhamid S. Al-Akel et al., "Effect of preheating on hot cracking susceptibility of welded austenitic stainless steels", *The 6th Saudi Engineering Conference, KFUPM, Dhahran, December 2002*, pp. 243-255.
- 94) Arantes and R.E. Trevisan, "Experimental and theoretical evaluation of solidification cracking in weld metal", *Achievements in Materials and Manufacturing Engineering, F.M.L. VOL. 20*, 2007, pp. 407-410
- 95) V. SHANKAR et al., "Solidification cracking in austenitic stainless steel welds", *S^{adha}n*, India, Vol.28, 2003, pp. 359–382.
- 96) Verena Petzet et al, "Elimination of Hot Cracking in Laser Beam Welding", *PAMM · Proc. Appl. Math*, vol. 10, 2004, pp. 580–581.
- 97) K. Shinozaki, M. Yamamoto, A. Kawasaki, T. Tamura, Peng Wen: "Development of evaluation method for solidification cracking susceptibility of inconel600/sus347 dissimilar laser weld metal by in-situ observation", *J. Mater. Sci. Forum*, 580-582(2008), 49-52.
- 98) Y. Ueno, S. Ishii, Z. Yamanaka: Measurement of weld metal temperature with an immersion-type optical-fiber radiation thermometer without correcting emissivity, *J. Japanese Welding Society*, 81(7), 17-21 (2012). (in Japanese)
- 99) K. Kadoi, Akira Fujinaga, Motomichi Yamamoto, and Kenji Shinozak; "The effect of welding conditions on solidification cracking susceptibility of type 310S stainless steel during laser welding using an in-situ observation technique", *J.Weld World*, Vol. 57, (2013), p. 383–390
- 100) Akira Fujinaga ; "Evaluation of Solidification Cracking Susceptibility using In-situ Observation Technique", Master thesis, Mechanical system engineering, Hiroshima University, 2011
- 101) D. Deng, H. Murakawa: Prediction of welding residual stress in multi-pass butt-welded modified 9Cr-1Mo steel pipe considering phase transformation effect, *J. Computational Mater. Sci.*, 37 (2006), 209-219.
- 102) Frank P. Incropera and David P. DeWitt; "Introduction to Heat Transfer", 4th edition, Wiley & Son, USA (2002)
- 103) M. Necatio OZISIK; "Heat Transfer; A basic approach", International Edition, McGraw-Hill, (1985)
- 104) J. Goldak, A. Chakravarti, and M. Bibby; "A New Finite Element Model for Welding Heat Sources", *J. Metallurgical Transactions B*, Vol. 15B, (1984), p.299-305
- 105) American Society for Metals. Reference Publications : (ASM metals reference book) (1981), p.164-178
- 106) Matsuda. F., Nakagawa. H., Tomita. S., and Sorada. K. 1988. Behaviors of solidification front, initiation and propagation of solidification crack- Investigation of weld solidification cracking by MISO technique (Report I), *Quarterly Journal of the JWS*, 6-3, 394-400

Published or Submitted Papers in Regards to This Thesis

1. **R. Phaonaim**, K. Shinozaki, M. Yamamoto, and K. Kadoi, and A. Nishijima: “Development of a highly efficient hot-wire-laser hybrid process for narrow-gap welding; welding phenomena and their adequate conditions”, Journal of welding in the world, (2013),p.607-613 (chapter 3)
2. **R. Phaonaim**, M. Yamamonto, K. Shinozaki, M. Yamamoto, and K. Kadoi: “Development of Heat Source Model for Narrow Gap Hot-wire Laser Welding Method”, Quarterly Journal of the Japan Welding Society, (2013),.Vol.31, No.4, p.82s-85s (Chapter 7 and 8)
3. **R. Phaoniam**, K. Shinozaki, M. Yamamoto, K. Kadoi, A. Nishijima, and M. Yamamoto: “Solidification cracking susceptibility of modified 9Cr1Mo steel weld metal during hot-wire laser welding with a narrow gap groove”, Journal of welding in the world, (2013). (Submitted) (Chapter 4, 8, and 7)
4. **R. Phaoniam**, K. Shinozaki, M. Yamamoto, K. Kadoi, A. Nishijima, and M. Yamamoto: “Solidification cracking susceptibility of modified 9Cr1Mo steel weld metal during hot-wire laser welding with a narrow gap groove”, International institute of welding (IIW), 66th Annual Assembly 2013,Doc. Doc. IV-1125-13. (Chapter 4, 8, and 7)
5. M. Yamamoto, **R. Phaonaim**, K. Shinozaki, M. Yamamoto, K. Kadoi, and A. Nishijima, and S. Tsuchiya: “Development of high efficient hot-wire laser welding for narrow gap joint”, Proceeding of the International symposium on Visual-JW 2012, (2012), p.73-74. (Chapter 3)

Presentations

1. **P. Rittichai**, M. Yamamoto, K. Shinozaki, M. Yamamoto, and K. Kadoi: "Heat Source Model for Hot-wire Laser Narrow Gap Welding Process; Effects of Welding Conditions on High-temperature Strain Initiation, Modeling of Thermal Elastic Plastic Analysis for Hot-wire laser Narrow Gap Welding Process (Part 2)", National Meeting of Japan Welding Society, 93(4) (2013), p.212-213
2. **R. Phaoniam**, R. Nakamura, K. Shinozaki, M. Yamamoto, K. Kadoi H. Yamamoto, and T. Nakajima: "Evaluation of solidification cracking susceptibility based on high-temperature strain analysis, Evaluation of hot cracking susceptibility on large scaled cast steel part for construction machinery during GMA welding (2nd report), National Meeting of Japan Welding Society, 93(4) (2013), p.210-211
3. Masayuki Yamamoto, **Phaoniam Rittichai**; Kenji Shinozaki; Motomichi Yamamoto; Kota Kadoi: "Development of High Efficient Hot-wire Laser Welding for Narrow Gap Joint", 7th Asia Pacific IIW International Congress, (2013), Document number: ICRA-2013-SING.211.
4. **P. Rittichai**, A.Nishijima, M.Yamamoto, K.Shinozaki, M.Yamamoto, and K.Kadoi: "Heat Source Model for Hot-wire Laser Narrow Gap Welding Process; Modeling of Thermal Elastic Plastic Analysis for Hot-wire laser Narrow Gap Welding Process (Part 1)", National Meeting of Japan Welding Society, 91(4) (2012), p.18-19
5. M. Yamamoto, **R. Phaonaim**, K. Shinozaki, M. Yamamoto, K. Kadoi, and A. Nishijima, and S. Tsuchiya: "Development of high efficient hot-wire laser welding for narrow gap joint", The International symposium on Visualization in Joining & Welding Science through Advanced Measurements and Simulation (Visual-JW 2012), Joining and Welding Research Institute Osaka University, 2012, Osaka, Japan, V(1), p.73-74.
6. T. Okagaito, H. Watanabe, K. Shinozaki, M. Yamamoto, K. Kadoi, M. Yamamoto, and **R. Phaonaim**: "Strength evaluation of narrow gap hot wire laser welding joint of heat-resistant steel for boiler", National Meeting of Japan Welding Society, 91(4) (2012), p.16-17.
7. T. Okagaito, H. Watanabe, K. Shinozaki, M. Yamamoto, K. Kadoi, A. Nishijima, and **R. Phaonaim**: "Development of Narrow Gap Hot-Wire Laser Welding Process for Heat-Resistant Steel Pipe for Boiler", National Meeting of Japan Welding Society, 90(4) (2010), p.200-201.